



HAL
open science

Prévisions de l'évolution micro structurale jusqu'à fin de vie sous irradiation d'alliages ferritiques par simulations numérique : vers une simulation quantitative et la prise en compte des hétérogénéités

Céline Paré

► To cite this version:

Céline Paré. Prévisions de l'évolution micro structurale jusqu'à fin de vie sous irradiation d'alliages ferritiques par simulations numérique : vers une simulation quantitative et la prise en compte des hétérogénéités. Autre. Centrale Lille Institut, 2022. Français. NNT : 2022CLIL0033 . tel-04076160

HAL Id: tel-04076160

<https://theses.hal.science/tel-04076160v1>

Submitted on 20 Apr 2023

HAL is a multi-disciplinary open access archive for the deposit and dissemination of scientific research documents, whether they are published or not. The documents may come from teaching and research institutions in France or abroad, or from public or private research centers.

L'archive ouverte pluridisciplinaire **HAL**, est destinée au dépôt et à la diffusion de documents scientifiques de niveau recherche, publiés ou non, émanant des établissements d'enseignement et de recherche français ou étrangers, des laboratoires publics ou privés.

CENTRALE LILLE
THESE

Présentée en vue
d'obtenir le grade de

DOCTEUR

En

Spécialité : Chimie des matériaux

Par

Céline Paré

DOCTORAT DELIVRE PAR CENTRALE LILLE

Titre de la thèse :

Prévisions de l'évolution micro structurale jusqu'à fin de vie sous irradiation d'alliages ferritiques par simulations numériques - vers une simulation quantitative et la prise en compte des hétérogénéités

Soutenue le 13 décembre 2022 devant le jury d'examen :

Présidente	Cristelle PAREIGE , Professeur à l'Université de Rouen Normandie, Groupe de Physique des Matériaux, UMR 6634 CNRS
Rapporteure	Anne HEMERYCK , Chargée de Recherche Classe Normale - HDR, au Laboratoire d'Analyse et d'Architecture des Systèmes, CNRS-UPR 8001, Toulouse
Rapporteure	Cristelle PAREIGE , Professeur à l'Université de Rouen Normandie, Groupe de Physique des Matériaux, UMR 6634 CNRS.
Membre	Christophe DOMAIN , Ingénieur R&D à EDF lab Les Renardières
Directrice de thèse	Charlotte BECQUART , Professeur à Centrale Lille Institut, Laboratoire Unité Matériaux et Transformation, CNRS UMR 8207
Invité	Julien VIDAL , Ingénieur R&D à Philip Morris International

Thèse préparée dans le Laboratoire Unité Matériaux et Transformation
Ecole Doctorale SMRE 104

Remerciements

Je veux remercier tout particulièrement ma Directrice de thèse, Charlotte BECQUART, ainsi que Julien VIDAL et Christophe DOMAIN, mes co-encadrants EDF, pour leur grande capacité d'écoute, leur disponibilité et leurs nombreuses et précises explications. Ils ont su, en m'accordant leur confiance et en prenant de leur temps, m'encadrer, me guider et en même temps me faire partager leurs compétences scientifiques au travers de nombreux échanges enrichissants.

Je tiens à remercier également mes deux rapporteurs Mme Anne HEMERYCK et Mme Cristelle PAREIGE pour avoir accepté de s'impliquer dans ma thèse et de relire ce manuscrit.

Je tiens également à remercier Julien STODOLNA et Bertrand CHASSIGNOLE, Ingénieurs Chercheur, chefs du groupe Métallurgie du département Matériaux et Mécanique des Composants, à EDF lab. les Renardières durant mes 3 ans de thèse, pour m'avoir accueilli dans leur groupe.

Ce travail faisant partie du projet EDF R&D PRIMA et du projet Européen SOTERIA, il a été en partie supervisé par Adrien GUERY et Nhu Cuong TRAN, chefs successifs de ce projet, que je remercie pour leur implication et participation.

Un grand merci également à Philippe BARANEK, Ingénieur Chercheur à EDF Lab Saclay, pour sa gentillesse, ses précieux conseils et son soutien constant tout au long de ma thèse.

Mes remerciements vont également aux différentes personnes d'EDF Lab. Les Renardières qui m'ont consacré de leur temps et apporté conseils et sympathie : Valérie KERVARGANT, Gilles ADJANOR, Sonia VIOLIER, Andreas SCHUMM, Laurent PETIT, Yanick NZIAKOU, Dominique LOISNARD, Emeric BRANTUS, Alexandre BALAN, Adèle ASTORG, Romain BADYKA, Frédéric DELABROUILLE, Audrey DELOTS et Miroslav FOKT.

Enfin, j'adresse mes remerciements à mes collègues actuels d'EDF DI, tout particulièrement Pierre GUÉRIN, Marine GAILLARD, Guillaume BECK, Dorian MONCHECOURT, Thierry FAURE, Romain JONCHIERE et tous les membres du pôle Tuyauterie Composants : Daphné MENSAH, Aurélia TOK, Stéphane RAGOBERT, Romain ARTEIL, Manuel POMMIER, Jonatan DATCHANAMOURTY, Guillaume SAGOT, Bruno FAREZ, François AMAZAN, Sabire EL RHOUL, Cyril RUE, Laurent ULPLAT, Mikael POTTIER, Rémi SCHOUTTETEN, Caglar ECKER, Abdallah EL SAADI, Marie-Anaïs LEMARCHAND, Alexis TRIALLOUP, Michel FOATA, Hamza GUELIL et Hakim TALHADJT pour leur accueil, leurs encouragements et bonne humeur quotidienne pendant ma dernière année de thèse.

Ma reconnaissance va à chacune de ces personnes pour avoir rendu ma thèse passionnante et permis de développer mes compétences dans une ambiance particulièrement chaleureuse.

Je remercie évidemment mes proches, ma mère et mon frère pour le soutien qu'ils m'accordent depuis toujours.

Je dédie cette thèse à mon père Étienne PARÉ et mes grands-parents Jeannine et Robert BONNEAU.

« Tu n'es plus là où tu étais, mais tu es partout là où je suis »

Victor Hugo

Glossary

AEM: Analytical Electron Microscopy

AES: Auger Electron Spectroscopy

AFS: Angular Fourier Series

ANN: Artificial Neural Network

APT: Atom Probe Tomography

ART: Activation Relaxation Technique

ACSF: Atom-Centred Symmetry Function

BM: Base Material

BOP: Bond-Orientational order Parameter

BWR: Boiling Water Reactors

CDP: Concentration Dependent Pairs

CE: Cluster Expansion

CGHAZ: Coarse Grain Heat Affected Zone

CM: Coulomb Matrix

CVN: Charpy V-notch

CSL: Coincidence Lattice Site

DBTT: Ductile-Brittle Transition Temperature

DFT: Density Functional Theory

Dpa : displacement per atom

DSC: Displacement Shift Lattice

EBS: Electron Back Scatter Diffraction

EDXS: Energy Dispersive X-ray Spectroscopy

EELS: Electron Energy Loss Spectroscopy

EM2VM: Etude et Modélisation des Mécanismes de Vieillessement des Matériaux

EP: Empirical Potential

ESCA: Electron Spectroscopy for Chemical Analysis

FIM: Fragilisation par Irradiation Moyenne

FIS : Fragilisation par Irradiation Supérieure

GB: Grain Boundary

GGA: Generalized Gradient Approximation

HAGB: High Angle Grain Boundary

HAZ: Heat Affected Zone

HRTEM: High Resolution Transmitted Electron Microscopy

IGF : Intergranular Fracture

KMC: Kinetic Monte Carlo

LAGB: Low Angle Grain Boundary

LDA: Local Density Approximation

MBTR: Many Body Tensor Representation

MC: Monte Carlo

MD: Molecular Dynamic

ML: Machine Learning

MMC: Monte Carlo Metropolis

MS: Molecular Static

NBE: Nudged Elastic Band

NN: Nearest Neighbour

NPP: Nuclear Power Plants

PAW: Projector Augmented Wave

PD: Point Defect

PERFECT: Prediction of Irradiation Damage Effects in Reactor Component

PERFORM: Prediction of the effects of radiation for reactor pressure vessel and in-core materials using multi-scale modelling

PES: Potential Energy Surface

PKA: Primary Knock-on Atom

PRIMA: PRévision de l'Influence de la Microstructure des mAtériaux

PSI: Programme de Surveillance à l'Irradiation

PWR: Pressurized Water Reactor

RCC-M: Règles de Conception et de Construction des Matériels Mécaniques des Ilôts Nucléaires REP.

RPV: Reactor Pressure Vessel

RSE-M: Règles de Surveillance en Exploitation des Matériels Mécaniques des Ilots Nucléaires REP.

SEAKMC: Self-Evolving Atomistic Kinetic Monte Carlo

SEM: Scanning Electron Microscopy

SIMS: Secondary Ion Mass Spectroscopy

SOAP: Smooth Overlap of Atomic Positions

SOTERIA: Safe LOng-TERm operation of light water reactors based on Improved understanding of radiation effects in nuclear structural mAterials

STGB: Symmetric Tilt Grain Boundaries

TEM: Transmitted Electron Microscopy

TKD: Transmission Kikuchi Diffraction

UHV: Ultra High Vacuum

WM: Weld Metal

XPS: X-ray Photoelectron Spectroscopy

Résumé substantiel

Le but principal de cette thèse était de modéliser l'évolution de la microstructure de l'acier ferritique faiblement allié 16MND5 sous irradiation avec plus de précision, pour mieux tenir compte des hétérogénéités présentes dans les aciers des réacteurs à eau pressurisée (REP).

L'un des éléments les plus importants influençant fortement de nombreuses propriétés des matériaux **sont les joints de grain (JG)** – défauts cristallins planaires. Dans les alliages industriels tels que les aciers des réacteurs à eau pressurisée, qui contiennent plus d'un élément, les JGs sont généralement décorés par des solutés : la ségrégation des solutés influence de manière assez significative les propriétés macroscopiques du matériau. Les effets néfastes induits par ce processus de ségrégation peuvent réduire la ténacité et la ductilité d'un matériau. Ainsi, une attention particulière dans cette thèse a été accordée aux JGs et à la ségrégation de solutés sur ces JGs. **La modélisation de l'évolution de la microstructure nécessite une bonne représentation des JGs.** Une grande partie de cette thèse a donc été consacrée à la construction des JGs les plus stables afin d'étudier et de quantifier la ségrégation de solutés sur ces JGs.

La majorité des microstructures connues des JGs concerne les JGs de flexion à symétrie élevée (par exemple $\Sigma 3$ et $\Sigma 5$). **Dans ce travail, six JGs de torsion différents**, dont les microstructures par définition sont plus complexes que pour les JGs de flexion, possédant des géométries de haute et basse symétrie pour le fer ont été construits et étudiés. En raison de leur structure complexe, les états d'énergie minimum sont difficiles à déterminer.

→ **Dans un premier temps, deux méthodologies de construction de JGs utilisant le potentiel empirique d'Ackland [1] ont été développées** dans cette thèse pour atteindre les configurations de plus basse énergie. Ces deux méthodes utilisent 3 traitements atomiques différents :

- la translation de la partie supérieure du JG dans la direction X et Y (se déplaçant ainsi sur la γ -surface). Cette étape n'est effectuée qu'une seule fois, juste après que le JG a été construit en utilisant la méthode CSL.
- l'insertion d'interstitiel (SIA) et le choix de la position pour laquelle le SIA a l'énergie de liaison la plus élevée avec le JG, conduisant ainsi à la plus faible énergie de formation du JG.
- le recuit et la trempe

Tous ces événements atomiques appliqués séquentiellement permettent d'atteindre un état de plus basse énergie (**Figure 1**).

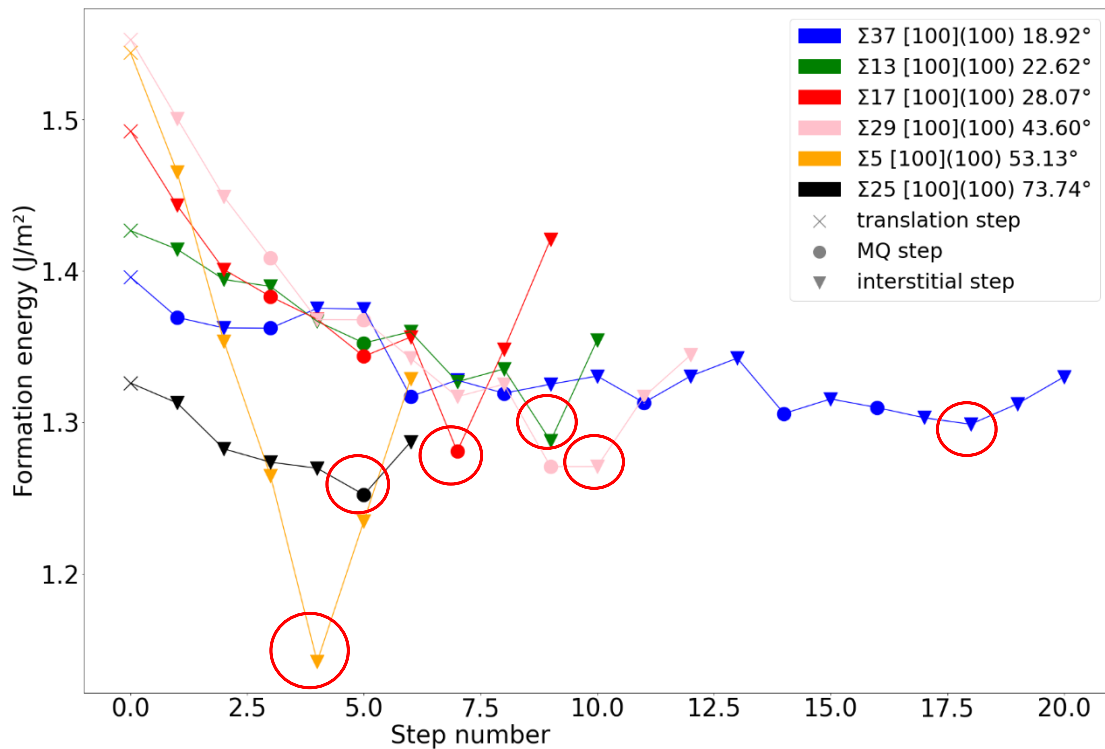


Figure 1 : Energie de formation en J/m² en fonction de l'évènement atomique appliqué pour les différents angles de désorientation testés avec la méthode **MQ_method**. Les configurations avec le nombre de SIA optimum sont entourées en rouge.

La première méthodologie « **All_trans_method** », que nous avons développée, considère l'addition séquentielle d'interstitiels sur des positions octaédrales, pour toutes les configurations possibles déterminées avec la méthode γ surface (**Figure 2**).

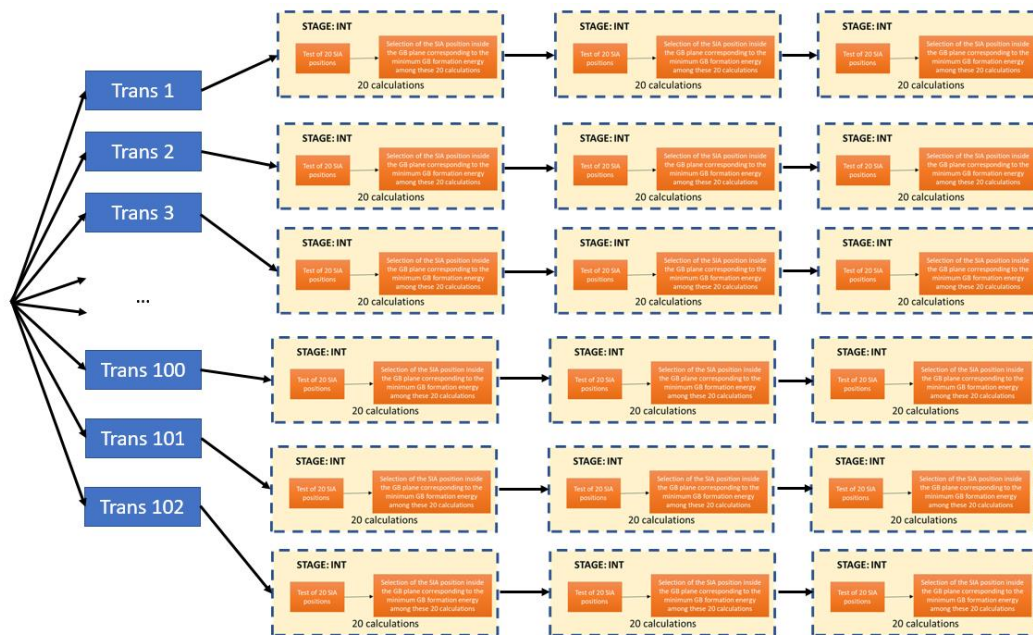


Figure 2 : Vue schématique de la méthode All-Trans. L'ajout séquentiel de 3 interstitiels est représenté ici, mais plus d'interstitiels peuvent être introduits.

En revanche, la deuxième méthode appelée « **MQ_method** » correspond à une combinaison d'un recuit puis d'une trempe et de l'ajout de SIA comme traitements séquentiels sur un JG généré avec la méthode de γ surface (**Figures 3 et 4**).

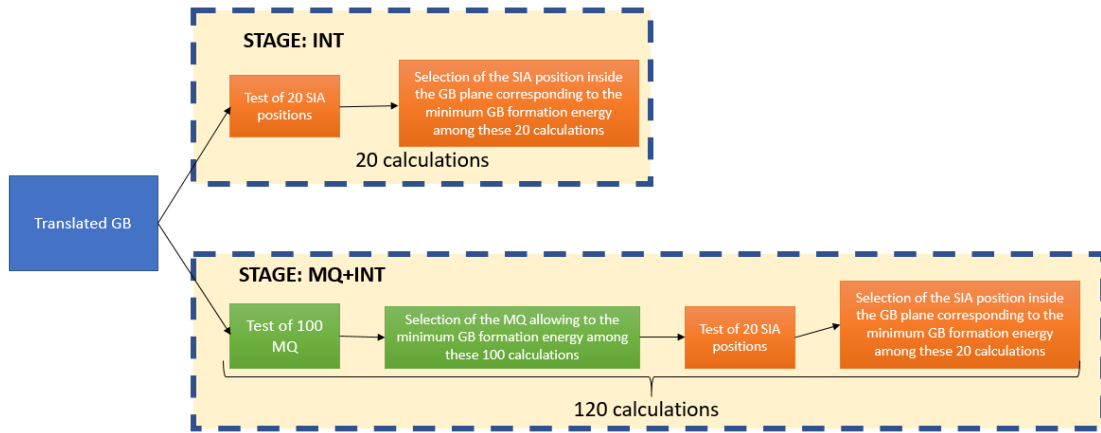


Figure 3 : Description des premières étapes de la méthode MQ. Les deux étapes possibles sont encadrées en bleu.

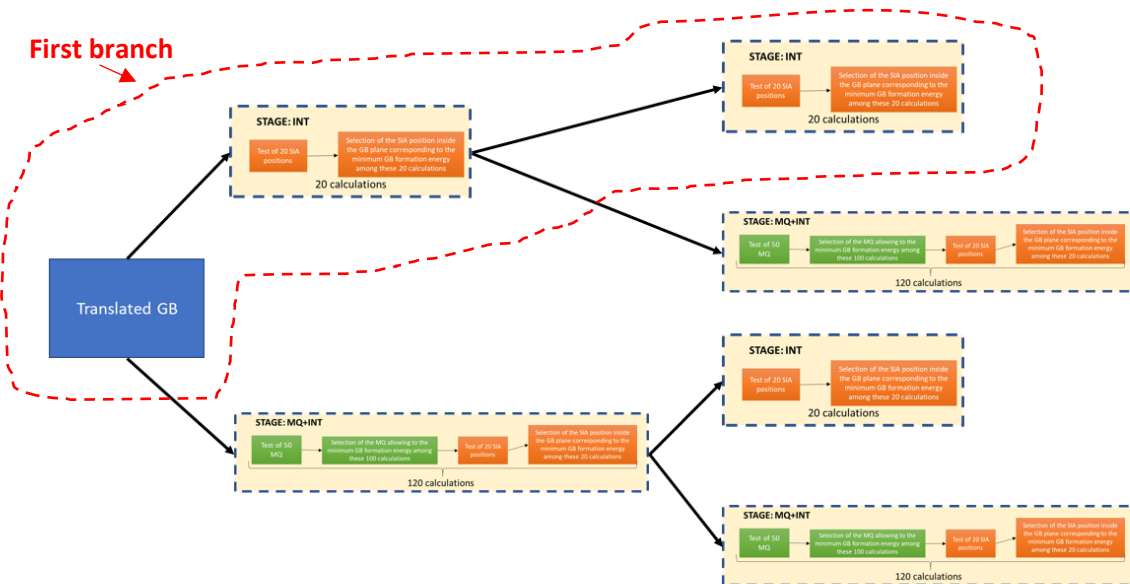


Figure 4 : Vue schématique de la **méthode MQ** après deux itérations et les quatre branches correspondantes. Les étapes répétées pour explorer l'espace des phases des JG sont encadrées en bleu. La première branche représentée ici encadrée en rouge est similaire aux branches obtenues avec la **méthode All_trans**.

Ces deux méthodologies conduisent à la construction de JGs de torsion équivalents. Le nombre d'interstitiels qui doit être ajoutés à proximité du plan du JG est le même quelle que soit la méthode choisie : de 4 à 11 interstitiels. Les microstructures obtenues ainsi que les énergies de formation associées sont représentées **Figure 5**.

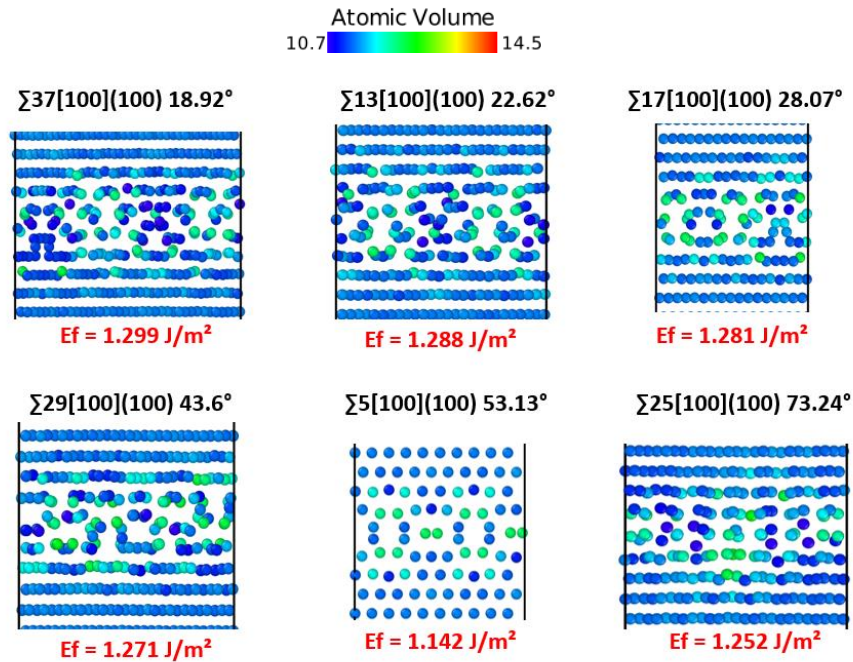


Figure 5 : Microstructures finales de plus basse énergie et énergies de formation associées en J/m^2 .

La méthode **All_trans_method** bien que plus rapide est moins efficace que la méthode **MQ_method** qui est plus lente pour atteindre le minimum d'énergie (**Table 1**). L'ajout de SIA sur les positions octaédriques et l'application de traitements thermiques permet d'explorer la surface d'énergie potentielle afin de trouver des états énergétiques de plus basse énergie. L'application d'une translation telle qu'elle est effectuée avec la γ -method n'est donc pas nécessaire ; tous les JGs translattés semblent converger vers le même état de plus basse énergie. Cependant, seulement 20 positions de SIA près du plan JG ont été testées, donc l'introduction de plus de 20 positions rendra peut-être la méthode **All_trans_method** plus efficace pour trouver la configuration de plus basse énergie. Pour deux JGs ($\Sigma 25$ et $\Sigma 29$), 60 positions de SIA ont été utilisées à chaque étape de construction, les résultats obtenus sont encourageants : l'augmentation du nombre de positions de SIA testées permet dans certains cas d'augmenter le pourcentage de JGs de plus basse énergie recherché.

JG	Angle (°)	All_trans_method		MQ_method	
		% structures d'énergie minimale	Temps réel (h)	% structures d'énergie minimale	Temps réel (h)
$\Sigma 37$	18.92	1	2.18	39	255
$\Sigma 13$	22.62	30	1.11	57	32
$\Sigma 17$	28.07	60	0.46	48	1.35
$\Sigma 29$	43.6	5	0.98	61	8.75
$\Sigma 5$	53.13	100	0.53	97	1.35
$\Sigma 25$	73.74	2	0.67	34	1.35

Tableau 1 : Pourcentage de JG de plus basse énergie et temps de calcul pour les méthodes **All_trans_method** et **MQ_method** en fonction de l'angle de désorientation testé.

La relaxation DFT des structures de JG générées avec **MQ_method** et **All_trans_method** conduit au même schéma de construction JG (le même nombre d'interstitiels) pour $\Sigma 17$, $\Sigma 29$ et $\Sigma 5$. Toutefois, pour les microstructures plus complexes pour lesquelles aucun modèle visuel géométrique clair en fonction du volume atomique n'a pu être mis en évidence. Pour les JGs $\Sigma 37$ et $\Sigma 13$, le nombre d'étapes est différent des résultats obtenus en potentiel empirique. En outre, même si **MQ_method** et **All_trans_method** conduisent à la même énergie de formation en potentiel empirique, **MQ_method** et **All_trans_method** convergent vers une énergie de formation différente pour ces deux JGs complexes en DFT. Les résultats énergétiques en potentiel empirique et en DFT sont en bon accord avec la littérature et leur énergie de formation attendue est toujours inférieure aux valeurs rapportées dans la littérature (**Figure 6**). Ces deux méthodes de construction permettent donc d'obtenir des structures de JGs plus stables par rapport à ce qui a déjà été développé dans la littérature.

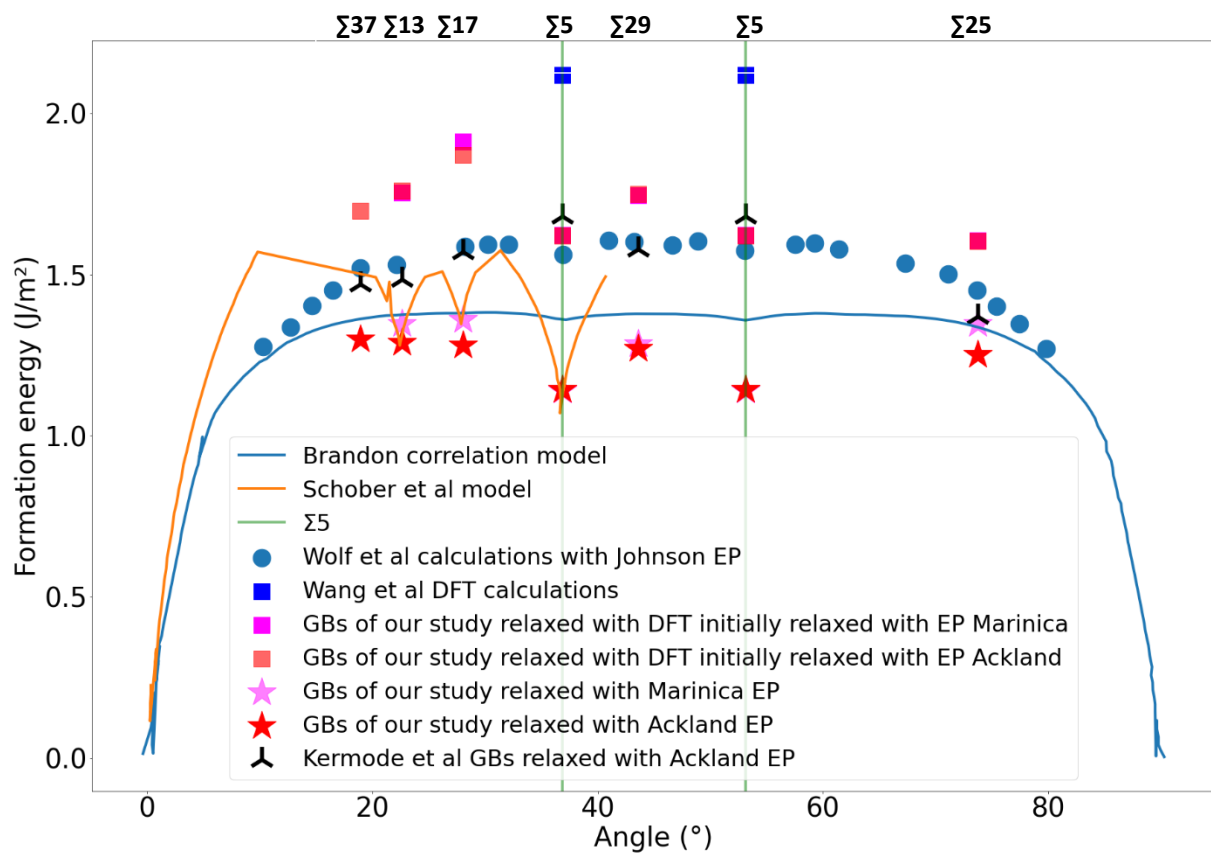


Figure 6 : Energie de formation en fonction de l'angle de désorientation. Puisque les résultats obtenus avec le potentiel empirique Ackland sont les mêmes quel que soit la méthode choisie, la méthode utilisée n'est pas précisée. Pour les calculs DFT, les états de plus basse énergie ont été choisis parmi les résultats obtenus avec **All_trans_method** et **MQ_method**. Les résultats obtenus avec le potentiel empirique Marinica [2] (en DFT ou en potentiel empirique) sont présentés uniquement avec les résultats obtenus avec la méthode MQ.

→ Dans un second temps, une attention particulière a été accordée à l'impact de la ségrégation du phosphore sur ces JGs ; le phosphore étant principalement impliqué dans la fragilisation non durcissante provoquant le phénomène de fracture intergranulaire. L'interaction d'un JG de torsion avec le phosphore comme ségrégant substitutionnel a été calculée et analysée en fonction de différents descripteurs atomiques. Le modèle de ségrégation de White Coghlan [3], permettant une étude de la ségrégation à l'échelle atomique, a été utilisé pour quantifier la ségrégation du phosphore.

La comparaison entre les résultats expérimentaux et la simulation est difficile car les mesures expérimentales correspondent généralement aux teneurs moyennes de ségrégation, tandis que les simulations atomistiques fournissent une image plus détaillée en tenant compte de la position précise du soluté dans le JG.

Le taux de couverture estimé du phosphore est supérieur à celui de la littérature et des valeurs expérimentales pour les JGs symétriques : entre 3.2 et 11.1 atomes/nm² à 873 K et 923 K (Figure 7). Ces valeurs sont plus élevées que les résultats MET de V.HSU avec 2.6 atomes/nm² [4] et les valeurs obtenues en sonde atomique tomographique d'Akhatova avec 1,6 atomes/nm² [5] et de Zhang *et al* [6] avec 0.6 atomes/nm² à 873 K et 923 K. Cependant, les interactions entre solutés n'ont pas été prises en compte dans les simulations réalisées. En effet le modèle White-Coghlan ne permet pas de tenir compte des interactions possibles entre solutés dans le calcul du taux de couverture de soluté sur le JG. Un modèle White-Coghlan prenant en compte ces interactions doit être introduit pour modéliser la co-ségrégation. Cela fera l'objet d'un futur travail. De plus les JGs testés par ces auteurs ne correspondent pas à des JGs de torsion mais à des JGs mixtes.

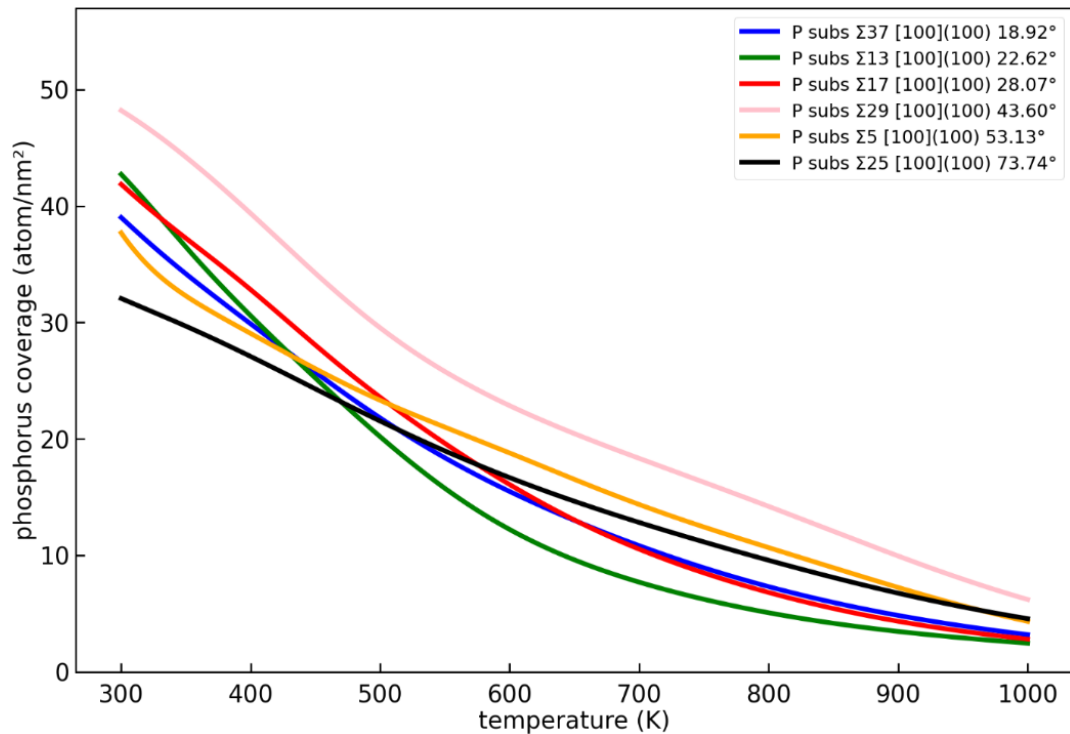


Figure 7 : Taux de couverture de phosphore exprimé en atomes/nm² en fonction de l'angle de désorientation du JG et de la température en Kelvins.

L'énergie de ségrégation n'est pas homogène dans le JG. La ségrégation est un processus anisotrope qui dépend fortement de la structure JG et des caractéristiques du ségrégant (la taille, l'espèce chimique...). Certains sites dans ou près de GB sont plus favorables à interagir avec un ségrégant que d'autres. Les distributions d'énergie de liaison pour chaque angle de désorientation testé sont toutes différentes.

Il est difficile de trouver des corrélations entre les descripteurs atomiques et l'énergie de liaison. Le graphique de corrélation de Spearman montre une corrélation forte-moderée entre SOAP et CS avec l'énergie de liaison quel que soit l'angle d'orientation choisi. Cependant, **aucune corrélation évidente entre l'énergie de liaison et les descripteurs atomiques n'a été mise en évidence.** Le nombre de données utilisées pour construire une étude statistique de corrélation de Spearman n'est pas suffisant pour tirer une conclusion générale.

→ **La ségrégation sur des JG twists est difficile à comprendre, mesurer et prédire** : la ségrégation sur les JGs dépend de nombreux facteurs physiques. La grande variété des structures de JG rend difficile l'établissement d'un modèle général de ségrégation. Le nombre de données nécessaires à la mise en place d'une bonne représentation de la ségrégation aux JGs est important, un élargissement de la base de données de JG d'EDF des aciers ferritiques est donc nécessaire. Des JG twist ont été générés avec les méthodes **MQ_method** et **All_trans_method**, cependant, pour un JG donné, de nombreux états métastables proches les uns des autres peuvent être atteints. Il faut donc en tenir compte pour réaliser une étude exhaustive de la ségrégation du phosphore avec une base de données suffisamment grande. **Une meilleure compréhension de la ségrégation GB nécessite une meilleure description des sites atomiques JG**, la génération d'une plus grande base de données de ségrégation JG et le développement de modèles précis de prédiction de la ségrégation sur la base de la description physique à l'échelle atomique des JGs.

L'intégration de l'impact du comportement de ségrégation du phosphore sur l'évolution de la microstructure dans les simulations de Monte Carlo Cinétique fera l'objet de futures études. Ces avancées permettront d'envisager des simulations plus quantitatives dans des conditions d'irradiation de type REP sur plusieurs décennies d'exploitation, et de mieux comprendre les mécanismes de dommages des alliages ferritiques à différentes échelles.

Bibliographie

- [1] G. J. Ackland, M. I. Mendeleev, D. J. Srolovitz, S. Han, et A. V. Barashev, « Development of an interatomic potential for phosphorus impurities in alpha-iron », *Journal of Physics: Condensed Matter*, vol. 16, n° 27, p. 1-14, 2004.
- [2] L. Malerba *et al.*, « Comparison of empirical interatomic potentials for iron applied to radiation damage studies », *Journal of Nuclear Materials*, vol. 406, n° 1, p. 19, 2010.
- [3] C. L. White et W. A. Coghlan, « The Spectrum of Binding Energies Approach to Grain Boundary Segregation », *Metallurgical transactions A*, vol. 8A, p. 1403-1411, 1977.
- [4] C.-Y. Hsu, J. Stodolna, P. Todeschini, F. Delabrouille, B. Radiguet, et F. Christien, « Accurate quantification of phosphorus intergranular segregation in iron by STEM-EDX », *Micron*, vol. 153, p. 103175, 2022.
- [5] A. Akhatova, « Méthodologie instrumentale à l'échelle atomique pour une meilleure compréhension des mécanismes de ségrégation intergranulaire dans les aciers : application au phosphore. », Université de Rouen Normandie, 2018.
- [6] L. Zhang, « Ségrégation intergranulaire du phosphore dans les aciers des cuves des REP », Université de Rouen Normandie, 2018.

Contents

Remerciements	2
Glossary	3
Résumé substantiel	6
Introduction	16
1. Industrial context.....	16
2. EDF project	28
3. Purpose of this work.....	30
4. Manuscript organisation.....	31
5. Bibliography.....	32
Chapter I: Numerical methods and models	35
I-1. Cohesive models	35
I-1.1 Ab initio methods	36
I-1.2 Empirical cohesive models	39
I-1.3 Energetic property calculations.....	43
I-2. Conclusion	45
I-3. Bibliography	46
Chapter II: GB descriptions	49
II-1. GB crystallographic definition and description	49
II-1.1 Crystallographic description.....	49
II-1.2 General framework to construct GBs.....	52
II-2. Energetic description of GBs	56
II-2.1 Dislocation model and low angle GB description	56
II-2.2 Limitations of the dislocation model for high angle GB	57
II-2.3 CSL meaning and relationship with GB energy.....	58
II-3. Atomistic description of GBs	62
II-3.1 Definition of physical descriptors	62
II-3.2 Towards specific iron bcc GB segregation descriptors	65
II-4. Conclusion	68
II-5. Bibliography	69

Chapter III: development of atomistic methods to construct twist GB	71
III-1. Atomistic construction of GBs, literature overview	72
III-1.1 GB representations	72
III-1.2 Translations parallel to the GB plane and deletion of overlapping atoms	75
III-1.3 GB density variation	76
III-1.4 Melt and quench (MQ).....	77
III-2. Development of effective methodologies to construct twist GBs in α-iron	79
III-2.1 Computational details	79
III-2.2 Grain boundary construction methodologies	79
III-2.3 Iterative GB construction processes developed.....	109
III-3. Comparison of EP results with other potentials and DFT.....	133
III-3.1 Comparison between EP and DFT	133
III-3.2 Impact of the choice of EP	144
III-3.3 Comparison with literature	147
III-4. Conclusion.....	149
III-5. Bibliography	150
Chapter IV: Segregation of P on twist GBs	155
IV-1. Phosphorus GB segregation	155
IV-1.1 Macroscopic and microstructural results.....	156
IV-1.2 Synergetic segregation.....	167
IV-2. Equilibrium GB segregation models	170
IV-2.1 McLean models.....	170
IV-2.2 Improvement of McLean model	173
IV-2.3 Towards more realistic segregation models	177
IV-3. Study of P segregation on twist GBs in α-iron	184
IV-3.1 Methodology adopted	184
IV-3.2 Phosphorus segregation results.....	188
IV-4. Conclusion	204
IV-5. Bibliography	206
Conclusion and perspectives	210
Annexes.....	214

Introduction

1. Industrial context

The main source of electricity in France comes from nuclear energy: 18 power stations and 56 nuclear power plants (NPP) produce 69%¹ of electricity. All currently operating NPPs in France use the pressurized water reactor technology (PWR) presented **Figure 1**. For these reactors, three independent loops are needed. Once heat has been generated through fission of the core within the reactor pressure vessel, a primary cooling loop ensures the transport of heat to the steam generator. Then, the thermal energy is transferred to a secondary loop and leads to the production of steam which is carried to the turbine of a generator that produces the electricity. Finally, the steam is converted back into water in the condenser. In contrast to other types of reactors such as boiling water reactors (BWR), PWR reactors prevent the water from boiling to steam. The pressure is maintained at 15 MPa by a "pressurizer", which keeps the water in the liquid form at 325°C to allow greater power output and high thermal efficiency.

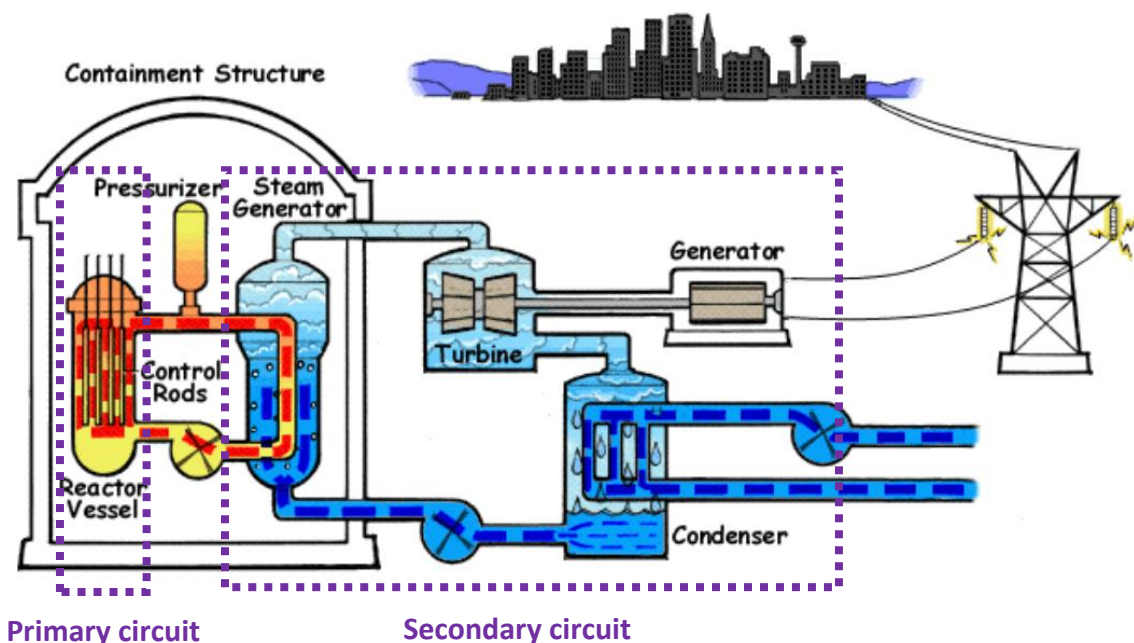


Figure 1: Primary and secondary circuit of a typical pressurized water reactor (taken from (U.S.NRC)).

The reactor pressure vessel (RPV) (**Figure 2**) is subjected to the pressure and temperature conditions (pressure: 12 –18 MPa, temperature: 270 –325 °C) of the primary cooling loop, as well as to the neutron irradiation generated by the nuclear reactions (neutron fluence after 40 years: 10^{18} – 2×10^{24} n.m⁻²) that occur in the core. It constitutes the second containment barrier of protection to the irradiation (the first is the fuel cladding and the third is

¹ RTE bilan électrique 2021 https://assets.rte-france.com/prod/public/2022-02/CP_RTE_Bilan-electrique-2021_1.pdf

containment) made of steel and composed of ferrules (C1 and C2), rings, flanges, pipes and caps. The RPV beltline region partly composed of ferrules is the most critical region.

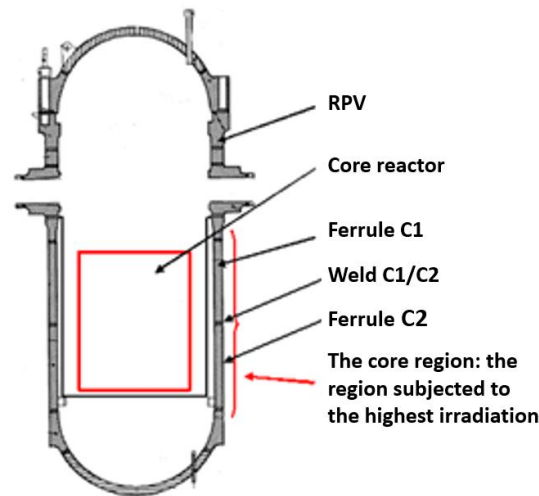


Figure 2: RPV components[1]

NPP safety is subject to very stringent regulations and is ensured on a day-to-day basis by a safety culture that is continuously being improved. Unlike other primary loop components, like steam generators, **replacing the RPV is not possible**. This component constituted of low-alloy ferritic steels containing Mn, Ni and Mo solutes and some impurities such as Cu, P or Si. Its composition is optimized to maintain the structural integrity throughout the expected operation time period. Alloying elements can improve the mechanical properties of the steel and thus refine its microstructure. For example, gammagen elements such as Mn and Ni improve the hardenability of steel by lowering the temperature of transformation of austenite to ferrite, thus promoting the germination of fine grains; carbide-forming alloying elements like Mo and Cr have a hardening effect and impurity elements such as P and S lead to a decrease of the cohesive strength at GBs and thus promote intergranular fracture (these elements are not voluntarily added, they are considered as trace elements). Typical ranges of solute content found in French RPV steels (low alloyed 16MND5 steel) are given in table 1:

Cu	Mn	Ni	Si	Mo	Cr	P	C
max 0.18	1.16-1.57	0.48-0.77	0.2-0.6	0.24-0.33	max 0.27	max 0.014	max 0.92

Table 1: Range of typical solute content present in 16MND5 RCC-M2111 forging for the reactor core region (at.%) [2]

The service lifetime of the NPP is directly impacted by the vessel integrity, which may thus, be ensured and justified in all operating situations of the reactor and for the time of its operation.

The **vessel structural integrity** is determined based on three main elements:

- the **fracture toughness** which is a measure of a material resistance to failure in the presence of a flaw (crack) and a stress. This physical property is quantified by the stress intensity which corresponds to the relationship between the flaw (or crack) and the stress. The operating environment (neutron fluence and flux, neutron spectrum, and irradiation temperature) constitutes one of the main influencing parameter.
- the **mechanical and thermal stresses** experienced during normal operating and severe accident transients.

- the **size and potential growth of defects** postulated (or measured) to be present in the RPV.

The neutron irradiation environment can create significant changes in material toughness and tensile properties (i.e. reduction of material fracture toughness and an increase in the yield strength of the RPV steel, which can have second- or third-order effects on the actual loads and growth of defects), such that structural integrity needs to be assessed periodically as the properties change.

Changes in material properties and in particular fracture toughness are monitored and predicted through an Irradiation Monitoring Program (IMP). More precisely, the purpose of this program is to anticipate the evolution of the mechanical properties of the vessel steel by carrying out mechanical tests on representative samples of the RPV and welds placed on the core shell. Fracture mechanics integrity evaluations are performed to ensure sufficient margin against failure.

Structural integrity of RPV steels depends on the evolution during operation of the material under irradiation and thermal aging, in particular on the microstructural evolution of the material that leads to mechanical changes of RPV steels. **Under irradiation**, radiation-induced nanometer-size objects are formed (point defects (PD), solute clusters, dislocation loops ...); they come from the successive interactions of neutrons with the material that take place after the fission reaction. An important number of energetic neutrons (with energy of the order of MeV) is produced during the fission reaction, which interacts with surrounding materials. Thermal neutrons² are able to produce atomic displacements because of the recoil of the nucleus that results from γ ray emission in radiative capture of neutrons, and also because the resulting γ rays can produce displaced atoms via Compton recoil electrons [3]. The interaction of a neutron with a target lattice atom, in the case of an elastic interaction, results in a transmission of a certain amount of energy E . If the energy transmitted to the target atom (referred to as the primary knock-on atom (PKA)) is higher than a critical value E_d (this value is equal to about 40 eV in Fe [4]), called the threshold displacement energy, a Frenkel pair is formed, i.e. the creation of one vacancy and one interstitial. If the kinetic energy of the PKA is high enough (higher than about $2E_d$), it becomes a projectile itself and can cause new displacements. This phenomenon illustrated in **Figure 3** is called a displacement cascade and is the origin of a point-defect oversaturation in the material under irradiation. Displacement cascades can be decomposed into two distinct phases [5]: a collision phase where the maximal number of point defects is reached and a recombination phase where the number of point defects decreases. Above a certain PKA energy (30-50 keV), which depends on the material, the cascade breaks down into separated subcascades[6].

² thermal Neutrons are free neutron with a kinetic energy of about 0.025 eV (about 4.0×10^{-21} J or 2.4 MJ/kg, hence a speed of 2.19 km/s) which corresponds to the most probable energy) for Maxwellian distribution at temperature of 290 K. It constitutes the most important spectrum part in thermal reactors.

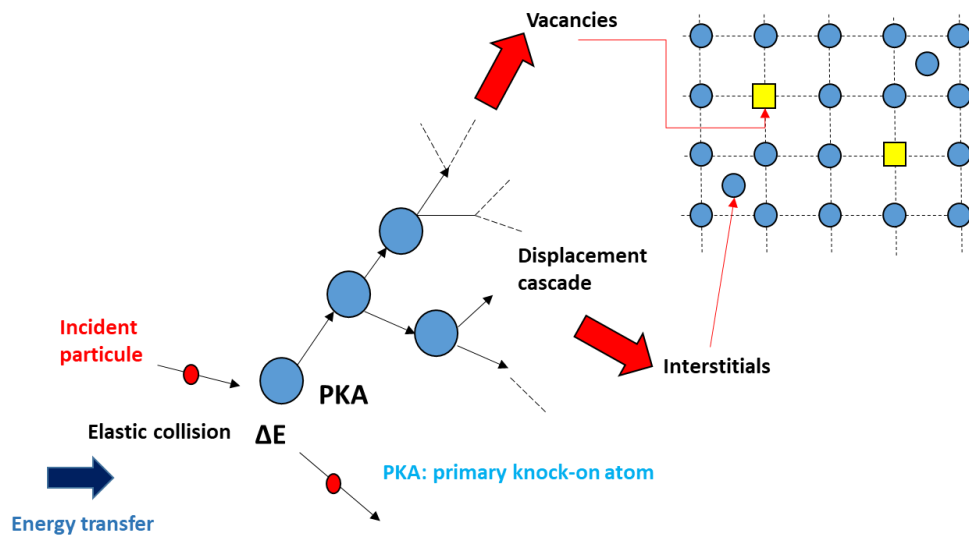


Figure 3: Illustration of the formation of a displacement cascade after the impact of a neutron

The radiation damage is often quantified by the number of displacements per atom (dpa). This number corresponds to the average number of times an atom has been displaced from its crystallographic site. The dpa is usually estimated using the Norgett–Robinson–Torrens NRT [7] dpa for engineering applications as recommended by the ASTM [ASTM1993]. In this model the number of number of Frenkel pairs generated by the PKA is expressed as:

$$N_d = \frac{0.8T_{DAM}}{2E_d}$$

where T_{DAM} is the kinetic energy transferred to the PKA and E_d is the threshold displacement energy (e.g. 40 eV for Fe [ASTM1994]).

Radiation damage leads thus to the creation of a large number of self-interstitial atoms (SIAs) and vacancies. This oversaturation of point-defects results in the formation of point defect clusters: when one PD encounters another PD of the same type, it can agglomerate to form a dimer, then other point defects can agglomerate with the dimer, thereby increasing the size of the aggregate and forming a point defect cluster such as a cavity or a vacancy/interstitial dislocation loop.

The PD oversaturation directly affects the kinetic evolution of the material as diffusion of most solutes takes place via the motion of the point defects:

- Radiation-accelerated diffusion, diffusion can take place and makes the system return faster to its equilibrium state³. This phenomenon refers to as radiation-enhanced diffusion in the literature [8].
- Solute-defect flux like solute segregation at grain boundaries (GBs) or depletion of solutes at sinks can occur: the PDs tend to eliminate on sinks (e.g. dislocations, GBs, surfaces), the concentration of PD near the sinks is then lower than the average concentration and thus leads to concentration gradients inducing a flow of PD nearby sinks. The solute flux can point in the same direction as the PDs flux involving a possible solute segregation at sinks if there is an affinity between solute atoms and PD; whereas in the absence of affinity between solute atoms and PDs, the solute flux and the PD flux can point to opposite directions (resulting in a possible solute depletion at sinks). Nano-features formed by these processes are denoted as radiation-induced.

³ many alloys are out of balance in real life: under normal temperature conditions they should not evolve.

Therefore, the evolution of the microstructure under irradiation can be divided into three contributions:

- The matrix damage which corresponds to the formation of cavities and vacancies/interstitial dislocations loops.
- The formation of solute-rich clusters (illustrated in **Figure 4**)

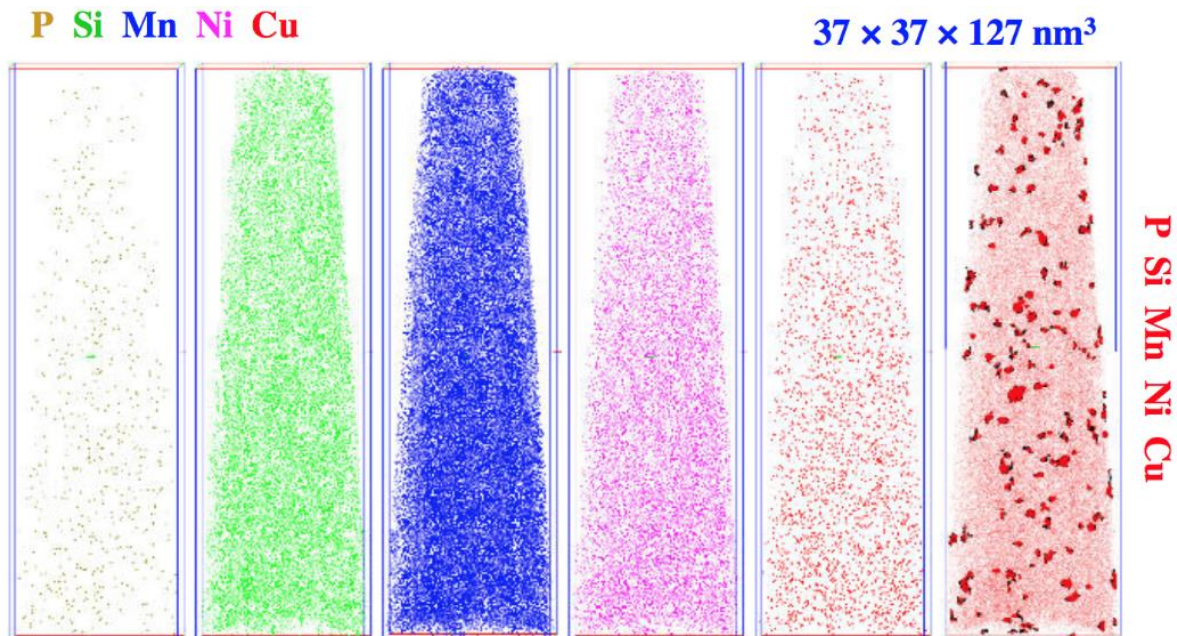


Figure 4: Solute-rich clusters observed by Atom Probe Tomography (APT) in a RPV steel irradiated at $11.4 \cdot 10^{23} \text{ n.m}^{-2}$ [9]. The solute atoms are displayed in different colors.

- The solute segregation on GBs (illustrated in **Figure 5**)

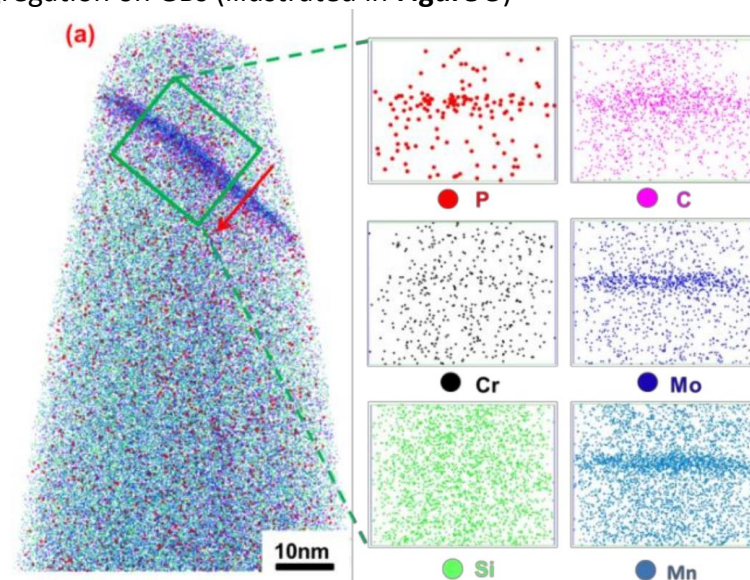


Figure 5: APT maps of RPV steels studied [10], [11]

All these atomic contributions lead to radiation embrittlement (**Figure 6**).

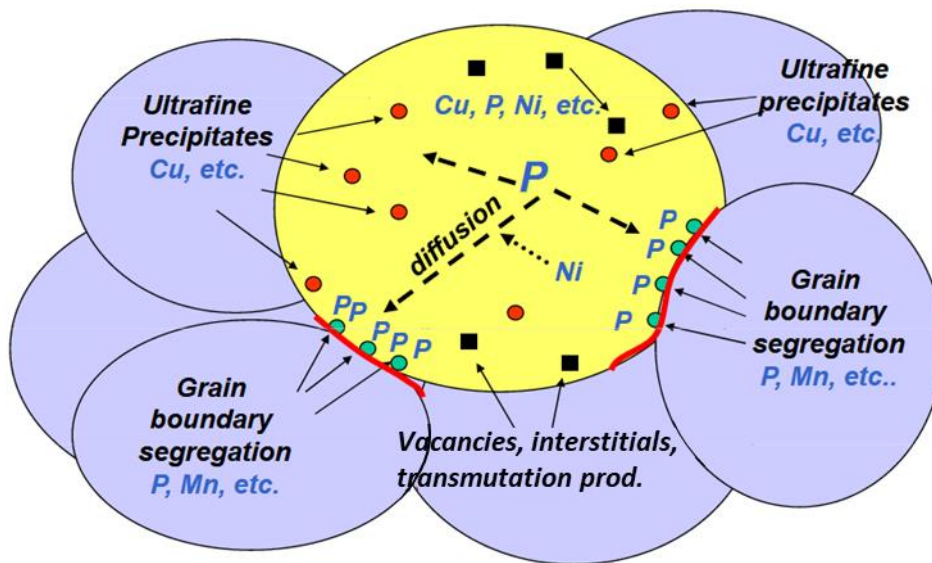


Figure 6: Schematic radiation embrittlement processes [12]

We can distinguish two main embrittlement mechanisms:

- **The hardening** embrittlement causing intragranular cleavage fracture in the matrix is partly due to the formation of nanometer size solute clusters which are created under irradiation [13].
- **The non-hardening** embrittlement refers to a typical thermal ageing phenomena for ferritic steels (even outside of the field of nuclear energy) caused by the intergranular segregation (i.e. the gathering of solutes or impurity atoms at GB) causing intergranular fracture [14]. The presence of segregated impurities such as phosphorus to the former austenitic grain boundaries results in embrittlement leading to a brittle intergranular fracture mode. This may involve cleavage across the boundary and produce a fracture surface which appears essentially transgranular; it proceeds as follows (**Figure 7**):
 - 1) Approach of the cleavage crack to the boundary
 - 2) Nucleation of new cracks on cleavage planes in the second grain
 - 3) Fracture of the triangular ligaments in the boundary plane
 - 4) Propagation of the perturbed crack front

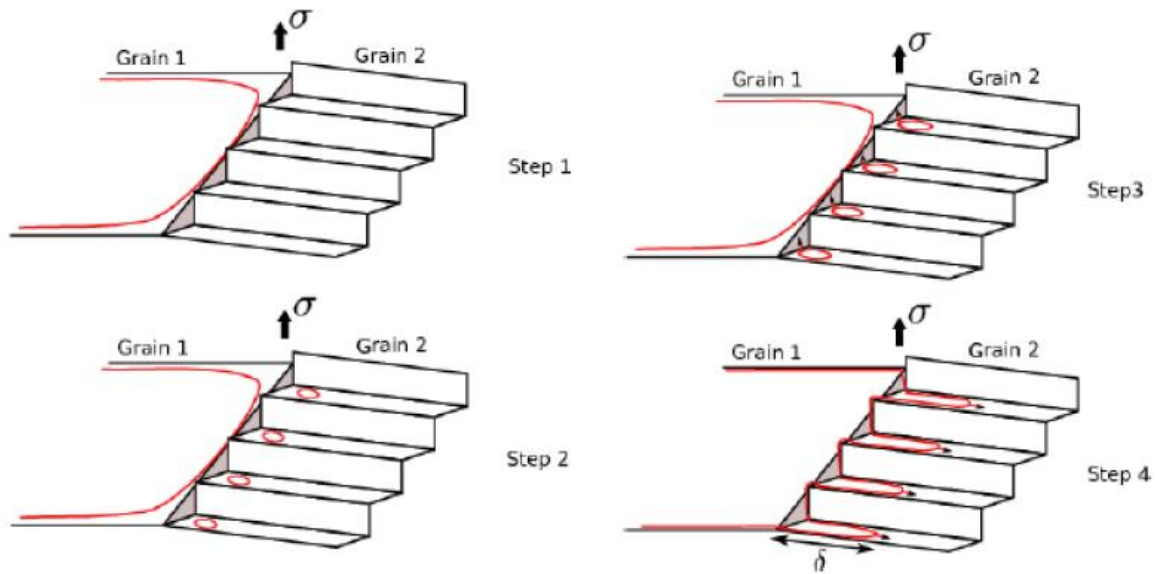


Figure 7: Transfer of a cleavage crack across a twist boundary [15]

Under thermal ageing conditions, the tensile strength of the steel may not be concurrently affected, so this phenomenon is often described as a ‘non-hardening’ embrittlement mechanism. However, radiation effects are supposed to impact the solute transport toward the GB and can lead to an acceleration or a slowdown of non-hardening embrittlement [16].

These embrittlement mechanisms result in changes in mechanical properties of RPV constitutive steels. Relative to various measures of toughness, the **Charpy V-notch (CVN)** impact test is the most commonly used technique (ASTM E23, EN 10045-1 and ISO 148-1). A pendulum is dropped towards the material to break it. The **energy absorbed (fracture energy)** by the material is calculated from the difference between the start and end angles of the swing with the known striker mass and pendulum arm length. The default specimen type has a V-notch and dimensions of 10×10×55 mm (sub-sized specimens with reduced thickness are also common). For bcc metals the fracture energy strongly depends on the test temperature. High energy absorbed at high temperature results in a great plastic deformation.

One of the embrittlement fingerprints induced by neutron irradiation is an increase of Ductile-Brittle Transition Temperature (DBTT). In other words, the material is brittle at higher temperatures in the irradiated case than the as-received condition. **Figure 8** illustrates the shift of this transition temperature $\Delta T T$ which is a measure of the embrittlement of the material. The current provisions for determination of the upward temperature shift of the lower-bound

static fracture toughness curve due to irradiation of reactor pressure vessel steels are based on the assumption that they are the same as for the Charpy 41 -J shifts as a consequence of irradiation. Thus, the 41 J temperature (T41J) corresponding to Charpy impact energy of 41 J, °C is used as the index for transition temperature shift.

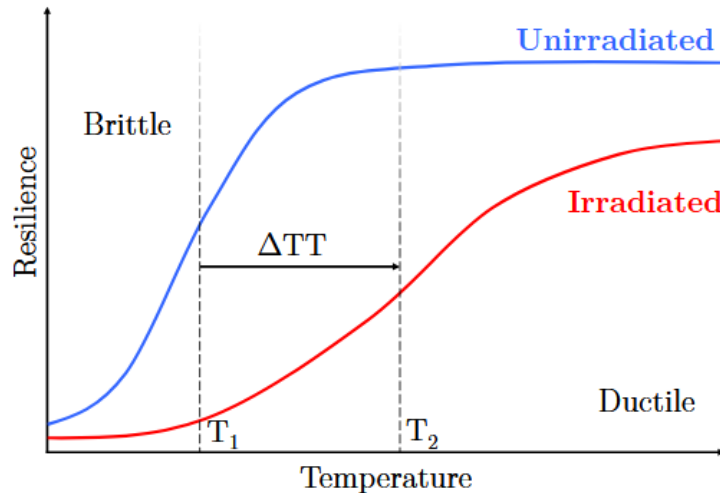


Figure 8: schematic illustration of the DBTT shift under irradiation [17]

Predicting ΔTT over time is a significant issue for the nuclear industry, therefore formulas which are called “correlation embrittlement models”, have been developed based on data collected from the surveillance program (Irradiation Monitoring Program) of irradiated microstructures characterized using various techniques that cover the macroscopic to the atomic scales which are connected to the embrittlement mechanisms (for example copper rich precipitate formation and matrix damage mechanisms).

The prediction of ΔTT is generally based on correlations of measured surveillance CVN transition temperature shifts with specific chemistry variables (generally Cu, Ni, P, Mn and Si) and fluence for the materials of interest. Current correlation embrittlement models are the result of successive improvement for more than 40 years. At the beginning, the effects of neutron fluence and the chemical elements were the primary concerns; indeed, in the late 1980s and early 1990s, harmful chemical variables have been revealed and then widely incorporated in the embrittlement correlation methods: copper and phosphorus were identified as significant elements for embrittlement, the synergetic effect of copper and nickel was highlighted. In the 1990s, environmental variables such as irradiation temperature and neutron flux were included into the embrittlement correlation method. From the mid-1990s to the early 2000s the flux effect has been taken into account in the embrittlement correlation, even if it was not necessarily a common practice. Since 2000, the embrittlement of low-copper materials is better understood and is thus included in correlation formula. The effect of high neutron fluences has attracted also considerable attention because of the necessity for long term operations beyond 40 or 60 years.

Even if these correlation formulas are originally based on the statistical analysis of the available databases concerning the steels used in RPV manufacture with individual terms not strictly associated with a particular mechanistic contribution to hardening, by the time, the size of the database and general understanding of embrittlement mechanisms had both increased, thus the forms of the terms used in the correlation were based on both mechanistic understanding and statistical significance. **Figure 9** highlights the significant factors that have impacted the evolution of the embrittlement correlation formula.

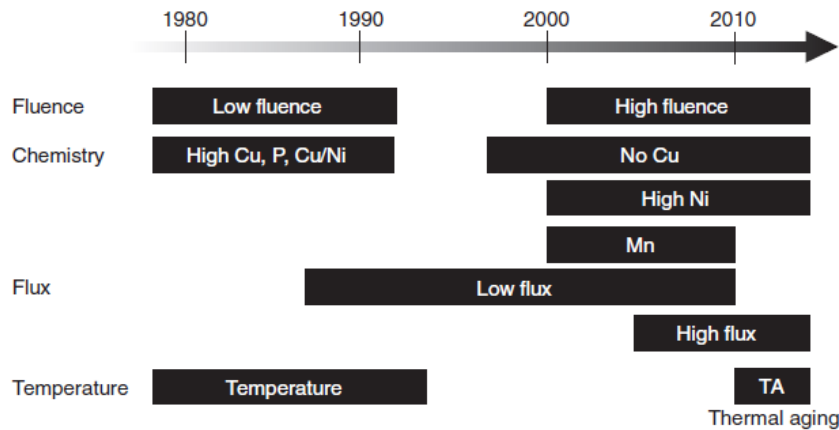


Figure 9: Transition of interests for embrittlement correlation methods [15].

Furthermore, these models are valid only in a limited range of chemical compositions and operation conditions. In the French models (the RCC-M Code⁴ for design and the RSE-M Code⁵ for surveillance), the effects of Cu, P, Ni and the fluence are included. One of the formula is given by the FIM (Fragilisation par Irradiation Moyenne) formula [18]:

$$\Delta TT = (17.3 + 1537. (P - 0.008) + 238. (Cu - 0.08) + 191. Ni^2. Cu). \Phi^{0.35} \text{ (eq 1)}$$

where:

- P, Cu and Ni contents are expressed in wt%
- $P - 0.008 = 0$ if $P \leq 0.008\%$ and $Cu - 0.08 = 0$ if $Cu \leq 0.08\%$
- The fluence Φ ($E > 1\text{MeV}$) is expressed in $10^{19} \text{ n.cm}^{-2}$

The FIS (Fragilisation par Irradiation Supérieure) formula is very similar, but has margin built in to bound the predictions[18]:

$$\Delta TT = 8 + (24 + 1537. (P - 0.008) + 238. (Cu - 0.08) + 191. Ni^2. Cu). \Phi^{0.35} \text{ (eq 2)}$$

In these French formulae, it should be noticed that Ni and Cu have a synergistic effect, the efficiency of P is significantly greater than that of Cu, and the fluence exponent is close to 1/3. Due to the accumulation of new data including high fluence data during 30 years of operation, a comparison between the prediction of the FIS model and the surveillance data has been carried out; some deviations have been found: an overestimation at the low fluence region and an under-estimation at the high fluence region have been identified.

Therefore, in order to anticipate the RPV life extension beyond 40 years, Todeschini *et al* [15], [19] developed ten years ago, a new embrittlement correlation model. By performing a fitting to the database they identified the possible influential parameters on the residuals: Ni has an effect only in the presence of Cu, Mn has some effect on welds but the increase of Mn makes the degree of embrittlement smaller, Si has a very weak effect and Cu and P have a strong effect on both base and weld metals.

⁴ RCC-M (2002), *Design and construction rules for mechanical components of PWR nuclear islands*, RCC-M, AFCEN, Paris.

⁵ RSE-M (2007), *In-service inspection rules for mechanical components of PWR islands*, RSEM, AFCEN, Paris.

Mn and Si provide smaller effects than other identified effect thus only Cu, P and a cross-term of Cu and Ni have been included in the new correlation formula. The effects of product form and flux within the French database is not supported by this test. Concerning the temperature effect, a temperature term correction has been introduced due to the constant value of irradiation temperature of French surveillance data [15]. Based on these considerations, Todeschini *et al* [19] keep the same equation as the one used in the FIS model but changed the constants in it. Their microstructural observations of the continuous increase in the number density of irradiation-induced solute atom clusters containing very small amount of Cu atoms give rise to another feature model of the FIS formula for the French database:

$$\Delta TT = A \cdot (1 + 35.7 \cdot (P - 0.008)_+ + 6.6 \cdot (Cu - 0.08)_+ + 5.8 \cdot Ni^2 \cdot Cu) \cdot \Phi^{0.59} \text{ (eq 3)}$$

where A is 15.4 for forgings and standard reference material, and 15.8 for welds, and (X)₊ means that the value of the term is zero when X is negative. The exponent value for fluence is changed from 0.35 in the FIS model to 0.59 in the present model. This large exponent contributes to improved accuracy at the high fluence region.

In equations 1, 2 and 3, P is anticipated to have predominantly hardening effect. **However, P is known to be the cause of non-hardening embrittlement in thermally aged ferritic steels.**

The segregation of phosphorus at GBs and associated intergranular fracture (IGF) has been identified in different ferritic steels: base material (BM), weld metal (WM), Heat Affected Zone (HAZ) and Coarse Grain Heat Affected Zone (CGHAZ). The coarse-grain regions of the weld HAZ constitute more susceptible zones to GB embrittlement than the other zones of the NPP [20]–[22]. Naudin *et al* [23] find out a quantitative relationship between grain boundary phosphorus segregation and critical intergranular fracture stress : the amount of intergranular fracture increases with phosphorus monolayer coverage.

Several studies have confirmed the embrittling potency of P as an increase of phosphorus segregation at grain boundary is correlated to an increase of the DBTT:

- Song *et al* [24], highlighted an empirical linear relation between the DBTT and GB concentration of phosphorus in a 2.25Cr-1Mn steel doped with phosphorus and isothermally aged at temperatures from 480°C to 650°C.

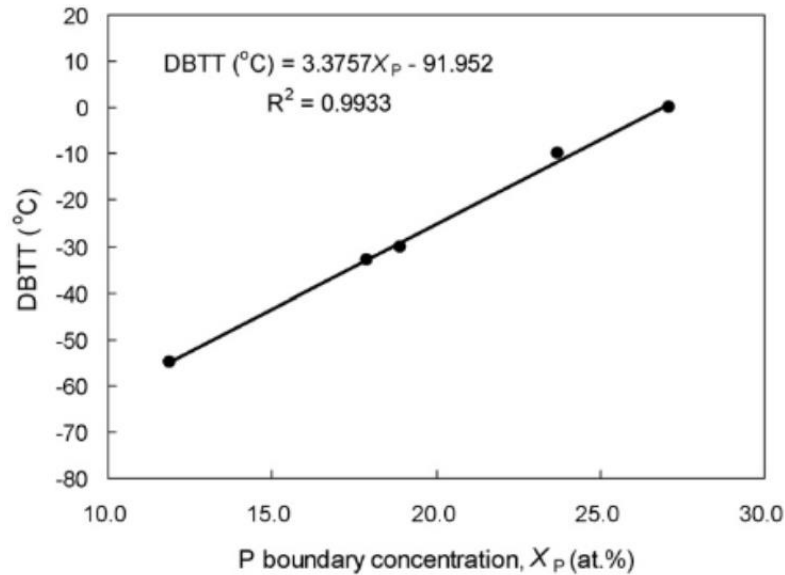


Figure 10: Dependence of DBTT to the GB concentration of phosphorus in thermally aged 2.25Cr-1Mn steel [24]

- Druce *et al.* [20], have thermally aged CGHAZ composed of low alloy steel (type A508) in the temperature range 300-500°C and have performed the quantification of P GB segregation by AES. They identified a linear correlation between DBTT and P concentration at the GB. In another study [25], Druce *et al.*, studied thermally aged HAZ in the temperature range 300–550°C for durations up to 20000 h. The results also show that the DBTT is proportional to the P GB segregation.

Thus, non-hardening embrittlement appears to dominate embrittlement in the thermal ageing samples.

Based on experimental data on P-doped 3.5%Ni 1.7%Cr steels aged at 480°C, Takayama *et al.*[26] developed an equation to calculate DBTT of steels as a function of three variables : the grain size, hardness, and intergranular segregation:

$$\Delta TT = -120 + 4.8P_p + 2(H - 20) + 0.15(7 - G)P_p + 0.23(H - 20)P_p + 0.036(7 - G)(H - 20)P_p \quad (eq\ 4)$$

where P_p is the AES $P_{120}=Fe_{730}$ peak height ratio in %, H is the Rockwell hardness⁶, G is the ASTM grain size number of previous austenite grain.

However, this formula leads to little deviations of measured value of transition temperature with predicted values for various combinations of hardness, grain size, and P peak height ratio.

⁶ The Rockwell test measuring the depth of penetration of an indenter under a large load compared to the penetration made by a preload.

These discrepancies can stem from the modification of the embrittling potency of the impurity by a co-segregated element.

Radiation embrittlement is generally due to hardening; however, it is currently not clear whether non-hardening embrittlement may occur in addition to hardening embrittlement. Understanding the contribution of the non-hardening embrittlement mechanism due to the parallel irradiation-induced processes such as hardening-effect of defect clusters and solute-rich cluster is difficult. In an industrial material subjected to irradiation, there are many competing effects, for example the decrease in the concentration of phosphorus available in solid solution due to their capture by solute clusters and the presence of other solutes at the GB with a cohesive effect. It is not certain that there is any non-hardening embrittlement effect on industrial steels.

The limited data concerning fractography and grain boundary composition in association with embrittlement measurement about irradiated steels lead to use trends in embrittlement alone to assess the importance of non-hardening embrittlement in RPV steels. As hardening will be responsible for some embrittlement, the ratio of hardening to embrittlement ($\Delta T/\Delta\sigma_y$) is often used to detect the presence of non-hardening embrittlement and to its part of embrittlement. This ratio should be higher than the average ratio calculated with all steels experiencing non-hardening embrittlement. The Charpy shift versus hardness change data were examined for evidence of non-linearity or non-zero intercepts, which might indicate non-hardening embrittlement effects.

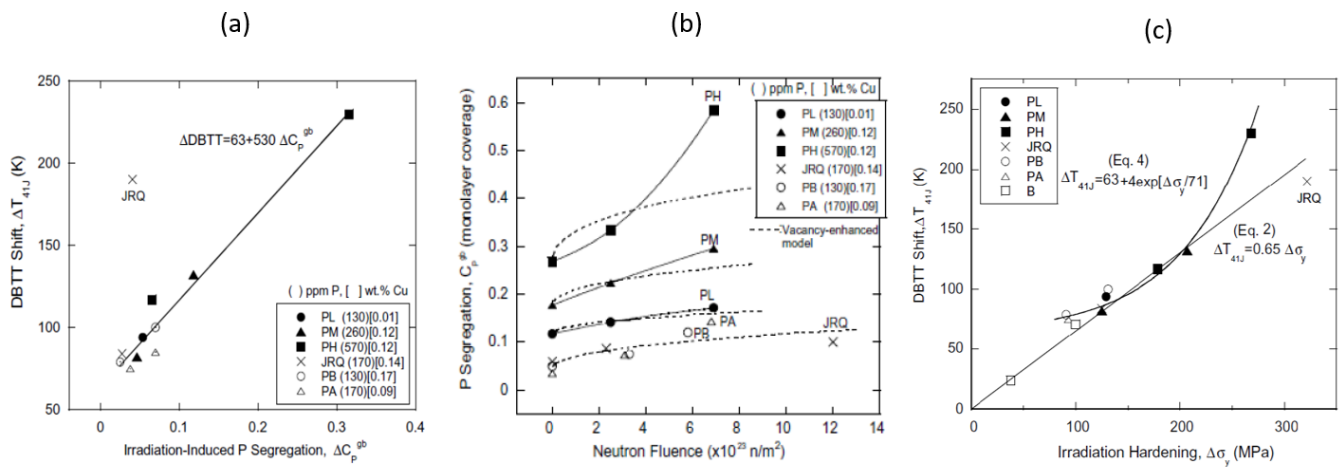


Figure 11: (a) DBTT correlation with Irradiation-induced P segregation, (b) segregated P at GB (in monolayers) as a function of neutron fluence, (c) DBTT correlation with irradiation hardening [26]

Nishiyama and co-workers [25] have studied MnMoNi steels with levels of P between 0.004 wt.% and 0.057 wt.% irradiated by neutrons with energy > 1 MeV in a range of neutron fluence from 2.3 to 12×10^{23} neutrons.m⁻² at 290°C. The minimum of phosphorus content (130 ppm) in the steel is called PB, the maximum phosphorus concentration (570 ppm) is named PH steel (**Figure 11abc**). The CVN tests as a function of AES measures revealed a linear dependence of DBTT from intergranular phosphorus segregation (**Figure 11a**).

According to **Figure 11c and 11b**, they have identified a constant embrittlement to hardening ratio for a P GB segregation about 0.3 monolayers. This linear correlation between DBTT and irradiation hardening suggests that an embrittlement effect of phosphorus is associated with the hardening mechanism. Only the PH sample corresponding to a P GB segregation about 0.6 monolayers deviate drastically from the embrittlement to hardening ratio of 0.65. This observation means that **non-hardening embrittlement** caused by intergranular segregation of phosphorus was observed only in HP steel irradiated to high neutron fluence ($2.6 \times 10^{23} \text{ nm}^{-2}$). The combined influence of intergranular P segregation and hardening on irradiation embrittlement and the threshold level of segregated P required for the occurrence of intergranular embrittlement have been investigated in another study [27].

Despite these progresses in predicting embrittlement, the contribution of the non-hardening mechanisms is still not completely understood. It is one of the reasons why in complement to IMP, a better understanding of the microstructure contribution including both hardening and non-hardening to the embrittlement is necessary.

2. EDF project

Due to the complexity and the large number of processes that occur during the microstructure evolution under irradiation, a numerical approach can help complement experimental studies.

A multi-scale approach for the RPV and core internals evolution under irradiation has been developed by EDF in collaboration with Lille University and other partners, for more than 20 years, in the framework of European projects: PERFECT⁷ (Prediction of Irradiation Damage Effects in Reactor Component), PERFORM 60⁸ (Prediction of the effects of radiation for reactor pressure vessel and in-core materials using multi-scale modelling – 60 years foreseen plant lifetime), SOTERIA (Safe LOng-TERM operation of light water reactors based on Improved understanding of radiation effects in nuclear structural mAterials) [28], [29] The work of this PhD is part of SOTERIA⁹.

⁷ This project was the first of its kind in Europe, and most probably in the world, to adopt a multiscale approach for assessing radiation damage in materials. This project aimed at developing and building predictive tools for quantifying the effects of neutron irradiation damage on Reactor Pressure Vessels and Internal structures. The major challenge was to introduce a physical description at the atomic scale of the effect of alloying elements of RPV steels with the objective of assessing quantitatively their effect on the macroscopic behaviour of the material.

⁸ Relying on the existing PERFECT project, PERFORM 60 was launched to develop similar tools that would allow simulation of the combined effects of irradiation and corrosion on internals, in addition to a further improvement of the existing tools which model irradiation effects in RPV bainitic steels.

⁹ Building on the achievements made by the previous European projects (PERFECT, PERFORM60), SOTERIA integrates progressively more complex parameters from material studies, such as microstructure defects and heterogeneities

The present work also contributes to the EDF R&D project PRIMA - **PRévision de l'Influence de la Microstructure des mAtériaux** - whose main objective is to improve the representativeness of the microstructure modelling, the understanding of the degradation mechanisms and thus the strength of the resulting analysis, to meet the main challenges of the nuclear fleet:

- Support the operating nuclear fleet and the new nuclear plants with a consolidation of the IMP
- Extending the life of the RPV with the building of a physics-based embrittlement model and controlling the potential intergranular embrittlement at high doses and possible co-segregation effects.

A bottom-up strategy consisting in developing a numerical predictive tool by chaining models describing different scales has been chosen: starting from the lowest time/scale, the results obtained with one scale are used as input data for the higher scale models. This method starts from first principles electronic structure calculations to finite element studies at the scale of the component. **Figure 12** presents a schematic representation of the multiscale approach used in the SOTERIA project. A platform composed of a chain of different codes allows to compute the hardening/fracture properties of a specific alloy from the knowledge of the PKA spectrum [30]. This thesis work takes place mainly at the atomistic scale

It can be noted that all the links between the different simulation steps need to be validated by dedicated experiments; therefore, keeping interactions and exchanges between modelling work and experimental work is crucial. In this framework, EDF, Lille University and Rouen University have formed a joint Laboratory EM2VM (Étude et Modélisation des Mécanismes de Vieillessement des Matériaux).

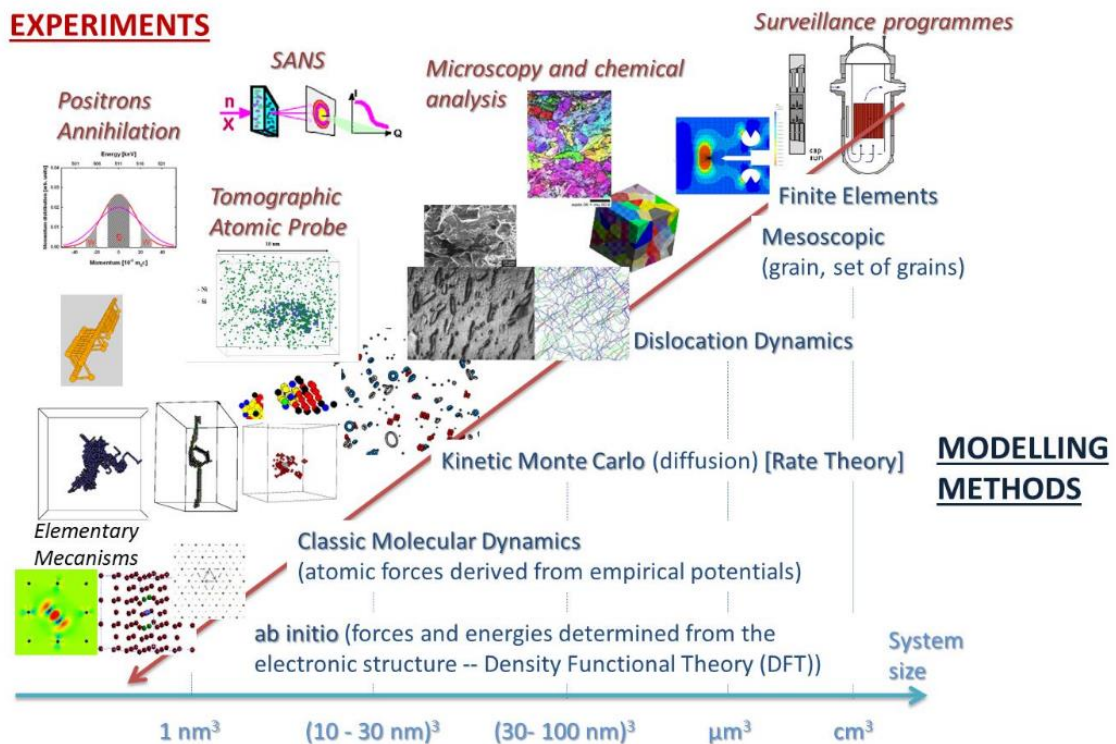


Figure 12: Schematic representation of the links between the different simulation techniques from nano- to macro scales with a strong link between the developed modelling tools and experimental characterisation techniques used in SOTERIA to simulate the microstructural evolution of RPV steels¹⁰.

3. Purpose of this work

The main goal of this work is to model the evolution of the microstructure of the low-alloy ferritic steel 16MND5 under irradiation more accurately by taking better account of the heterogeneities present in RPV steels. More precisely, this thesis focuses on non-hardening embrittlement, in particular on GB chemical composition under irradiation. The aim is to construct the most stable GBs in order to study and quantify the segregation on these GBs. A particular attention has been paid on the effect of phosphorus segregation, which is mainly implicated in the non-hardening embrittlement causing intergranular fracture. We use, for that purpose, empirical potentials and ab initio methods.

¹⁰ Picture from Soteria website: <http://www.soteria-project.eu/page/en/about/concept-approach.php>

4. Manuscript organisation

The manuscript is organized **in four chapters**. **In the first chapter**, the numerical methods and models used in this thesis will be presented in a general way as well as cohesive models such as ab initio methods and empirical methods. Monte-Carlo methods will then be introduced briefly. In order to develop a more accurate description of RPV steels, a better consideration of some heterogeneities, like GBs is necessary to make precise simulations. Therefore, **the second chapter** will be dedicated to a literature review on grain boundary features; a particular attention will be paid on GB atomic description. Due to the lack of data about twist GBs, we chose to study this type of GBs. The methodologies that have been developed during this PhD to construct stable twist GBs will be presented in **the third chapter**. Because of the significance of the intergranular segregation in RPV steels embrittlement, **the last chapter** will expose in a first part a bibliographic study of GB segregation and in a second part segregation results obtained on GBs that have been constructed during this thesis.

5. Bibliography

- [1] B. Laponche, « Quatrième visite decennale des réacteurs de 900 MW, la tenue des cuves », 2019. [En ligne]. Disponible sur: https://www.global-chance.org/IMG/pdf/b.laponche_vd4_cuves_20190504.pdf
- [2] International Atomic Energy Agency, « Assessment and Management of Ageing of Major Nuclear Power Plant Components Important to Safety: Steam Generators ». 2011.
- [3] L. E. Rehn et R. C. Birtcher, « Freely-Migrating Defects », *Trans Tech Publications Ltd*, vol. 97, p. 43-58, 1992.
- [4] « Standard Practice for Characterizing Neutron Exposures in Iron and Low Alloy Steels in Terms of Displacements Per Atom (DPA) », *ASTM E693*, 1994.
- [5] R. E. Stoller, « Primary Radiation Damage Formation », *Comprehensive Nuclear Materials*, vol. 1, n° 11, p. 293-332, 2012.
- [6] R. E. Stoller et L. R. Greenwood, « Subcascade formation in displacement cascade simulations: Implications for fusion reactor materials », *Journal of Nuclear Materials*, vol. 271, p. 57-62, 1999.
- [7] M. J. Norgett, M. T. Robinson, et I. M. Torrens, « A proposed method of calculating displacement dose rates », *Nuclear Engineering and Design*, vol. 33, p. 50-54, 1975.
- [8] B. Radiguet, « Etude de la formation d'amas diffus de solutés sous irradiation dans des alliages modèles ferritiques », Université de Rouen Normandie, 2004.
- [9] H. Huang, « Influence de l'irradiation aux neutrons sur le vieillissement des aciers de cuves des réacteurs nucléaires à eau pressurisée », Université de Rouen Normandie, 2012.
- [10] L. Zhang, « Ségrégation intergranulaire du phosphore dans les aciers des cuves des REP », Université de Rouen Normandie, 2018.
- [11] L. Zhang, B. Radiguet, P. Todeschini, C. Domain, T. Shen, et P. Pareige, « Investigation of solute segregation behavior using a correlative EBSD/TKD/APT methodology in a 16MND5 weld », *Journal of Nuclear Materials*, vol. 523, p. 434-443, 2019.
- [12] L. Debarberis, « Effect of radiation embrittlement to reactor pressure vessel steels and its surveillance ». Institute for Energy, 2009. [En ligne]. Disponible sur: <http://indico.ictp.it/event/a08149/session/9/contribution/6/material/0/0.pdf>
- [13] E. Meslin, B. Radiguet, P. Pareige, et A. Barbu, « Kinetic of solute clustering in neutron irradiated ferritic model alloys and a French pressure vessel steel investigated by atom probe tomography », *Journal of Nuclear Materials*, vol. 399, p. 137-145, 2010.
- [14] P. D. Styman, J. M. Hyde, K. Wildford, A. Morley, et G. D. W. Smith, « Precipitation in long term thermally aged high copper, high nickel model RPV steel welds », *Progress in Nuclear Energy*, vol. 57, p. 86-92, 2012.
- [15] N. Soneta, *Contribution of Materials Investigations to Improve the Safety and Performance of LWRs*, Woodhead Publishing Series in Energy., vol. 26. 2015.

- [16] K. Ebihara et T. Suzudo, « Atomistic Simulation of Phosphorus Segregation to sigma 3 (111) Symmetrical Tilt Grain Boundary in alpha-iron », *Modelling and Simulation in Materials Science and Engineering*, vol. 103122.R1, p. 1-16, 2018.
- [17] B. Pannier, « Towards the prediction of microstructure evolution under irradiation of model ferritic alloys with an hybrid AKMC-OKMC approach », Thèse de Doctorat, Université de Lille, 2017.
- [18] P. Petrequin, « Ames Report No 6 ». 1996.
- [19] P. Todeschini, Y. Lefebvre, H. Churier-Bossennec, N. Rupa, G. Chas, et C. Benhamou, « Revision of the irradiation embrittlement correlation used for the EDF RPV fleet », *Proceedings of Fontevraud 7: Contribution of Materials Investigations to Improve the Safety and Performance of LWRs*, vol. A084-T01, 2010.
- [20] S. G. Druce, G. Gage, et G. Jordan, « Effect of ageing on properties of pressure vessel steels », *Acta Metallurgica*, vol. 34, p. 641-652, 1986.
- [21] Z. Zhai, Y. Miyahara, H. Abe, et Y. Watanabe, « Segregation behavior of phosphorus in the heat-affected zone of an A533B/A182 dissimilar weld joint before and after simulated thermal aging », *Journal of Nuclear Materials*, vol. 452, p. 133-140, 2014.
- [22] A. Akhatova, « Méthodologie instrumentale à l'échelle atomique pour une meilleure compréhension des mécanismes de ségrégation intergranulaire dans les aciers : application au phosphore. », Université de Rouen Normandie, 2018.
- [23] C. Naudin, J. M. Frund, et M. Pineau, « Intergranular fracture stress and phosphorus grain boundary segregation of a Mn-Ni-Mo steel. », *Scripta Materialia*, vol. 40, n° 9, p. 1013-1019, 1999.
- [24] S. H. Song, H. Zhuang, J. Wu, L. Q. Weng, Z. X. Yuan, et T. H. Xi, « Dependence of ductile-to-brittle transition temperature on phosphorus grain boundary segregation for a 2.25Cr1Mo steel », *Material Science and Engineering A*, vol. 486, p. 433-438, 2008.
- [25] Y. Nishiyama *et al.*, « Effects of neutron-irradiation-induced intergranular phosphorus segregation and hardening on embrittlement in reactor pressure vessel steels », *Acta Metallurgica*, vol. 56, p. 4510-4521, 2008.
- [26] S. Takayama, T. Ogura, S. C. Fu, et C. J. McMahon, « The calculation of transition temperature changes in steels due to temper embrittlement », *Metallurgical transactions A*, vol. 11, p. 1513-1530, 1980.
- [27] C. English, S. Ortner, G. Gage, W. Server, et S. Rosinski, *Review of Phosphorus Segregation and Intergranular Embrittlement in Reactor Pressure Vessel Steels*, S. Rosinski, M. Grossbeck, T. Allen, A. Kumar., vol. Eff. Radiat. Mater. 20th Int. Symp. 2001.
- [28] J. P. Massoud, S. Bugat, B. Marini, D. Lidbury, et S. V. Dyck, « PERFECT - Prediction of Irradiation Damage Effects on Reactor Components: A summary », *Journal of Nuclear Materials*, vol. 406, p. 2-6, 2010.
- [29] A. Al Mazouzi, A. Alamo, D. Lidbury, D. Moinereau, et S. Van Dyck, « PERFORM 60: Prediction of the effects of radiation for reactor pressure vessel and in-core materials using multi-scale modelling – 60 years foreseen plant lifetime », *Nuclear Engineering and Design*, vol. 241, p. 3403-3415, 2010.

[30] G. Adjanor, S. Bugat, C. Domain, et A. Barbu, « Overview of the RPV-2 and INTERN-1 packages: From primary damage to microplasticity », *Journal of Nuclear Materials*, vol. 406, p. 175-186, 2010.

Chapter I: Numerical methods and models

In this chapter, we will present the numerical methods and models used during the Ph.D. to describe the thermodynamics and segregation in ferritic steels. We will present cohesive models used to describe the interactions among the atoms, in order to determine energetic properties. The focus will be made on the cohesive models, i.e. the different approaches used in this thesis to obtain the total energy of a system of atoms in order to study local elements (i.e. twist grain boundaries (GBs)) of ferritic steels microstructure at the atomic scale: ab initio methods and empirical potentials. The energetic properties extracted in this work will be also presented in a sub-section.

I-1. Cohesive models

Atomistic modelling is a set of simulation methods using an atomistic description (i.e. atomic positions and chemical nature of the atoms) to simulate a solid, liquid or gas phase. The main ingredient of such simulations is the description of the electronic interactions between atoms or more generally the knowledge of the dependence of the total energy of the system on the position of the atoms. Despite the very small-scale nature of this type of simulation, it is possible to estimate macroscopic quantities of interest for industrial applications. The accuracy of the model describing interactions between atoms obviously influences the quality of the results of the overall simulation and its complexity determines the computational time necessary to obtain the result.

Two different approaches are possible:

- **The ab initio method** models the interactions and the atomic structure with no a priori knowledge of the behaviour of a material in its stable state. Ab initio methods solve the Schrodinger equation after series of approximations and are based upon the determination of the ground state electronic structure. This method referred to as first-principles is the most accurate but is computationally expensive; thus, its use is limited to small systems (a few hundreds of atoms).
- **The empirical cohesive models** allow simulating systems containing more atoms but are often less accurate. Firstly, there are empirical or semi-empirical potentials, adjusted on carefully chosen physical properties of the system studied. These potentials are adjusted on experimental data and/or ab-initio calculation results for a given system; they provide a mathematical expression of the potential energy of an atom according to the position of the neighbouring atoms in the system. However, this method is limited to simple systems (unary or binary alloys) and cannot be used for RPV alloys because of the number of solute species one has to account for. Thus, simpler models based on strong approximations, such as pair interaction models or more complex models based on the cluster expansion method [1] with rigid lattices have been developed enabling a decrease of the computational time. In order to specifically take into account the effect of the local atomic environment, another model has been developed recently for the particular case of RPV steels: the **concentration dependent model** [2].

In section 1.1, ab initio methods are described, then in section 1.2, empirical cohesive models are presented. Finally, the expressions for the energetic properties calculated in this thesis are given in section 1.3.

I-1.1 Ab initio methods

I-1.1.1 Generalities

First principle methods are based on the resolution of the Schrödinger equation and permit to determine the energy of a collection of atoms. The common objective of all ab initio techniques is to solve the Schrödinger equation for the Hamiltonian of a system containing m atoms and n electrons:

$$\widehat{H}\psi(r_1, r_2, \dots, r_n, R_1, R_2, \dots, R_m) = E\psi(r_1, r_2, \dots, r_n, R_1, R_2, \dots, R_m) \quad (\text{eq I-1})$$

where ψ denotes the wave function of a system composed of m atoms and n electrons, r_n corresponds to the position associated to the electron n, R_m is the position of atom m and E is the total energy of the system. The Hamiltonian \widehat{H} describes the interactions between all nuclei and electrons $\widehat{H} = \widehat{T}_N + \widehat{T}_e + \widehat{V}_{e-e} + \widehat{V}_{e-N} + \widehat{V}_{N-N}$ (eq I-2), where:

- $\widehat{T}_N = -\frac{\hbar^2}{2} \sum_{I=1}^m \frac{\nabla_I^2}{2M_I}$ (eq I-3) corresponds to the kinetic energy of nuclei, where M_I is the mass of nucleus I
- $\widehat{T}_e = -\frac{\hbar^2}{2m_e} \sum_{i=1}^n \nabla_i^2$ (eq I-4) corresponds to the kinetic energy of electrons, where m_e is the electron mass
- $\widehat{V}_{e-e} = \sum_{i=1}^n \sum_{i>j}^n \frac{e^2}{|r_i - r_j|}$ (eq I-5) denotes the *potential of the electron-electron interaction*
- $\widehat{V}_{e-N} = \sum_{I=1}^m \sum_{i=1}^n \frac{e^2 Z_I}{|r_i - R_I|}$ (eq I-6) denotes the *potential of the electron-nuclei interaction, where Z_I is the nucleus charge.*
- $\widehat{V}_{N-N} = \sum_{I=1}^m \sum_{J>I}^m \frac{e^2 Z_I Z_J}{|R_I - R_J|}$ (eq I-7) denotes the potential of the nuclei-nuclei interaction

\hbar is Planck constant and e is the elementary charge.

However, the many body Schrödinger equation is too complicated to be directly solved for systems of relevant size, thus the approximation of a non-interacting system permits to divide this unique equation into a system of equations easier to solve. In this context, a certain number of approximations are necessary:

- **The Born Oppenheimer approximation** or adiabatic approximation decouples the motion of electrons from the one of the nucleus owing to the fact that electrons have a mass much lower than protons and neutrons. Therefore, in many problems, this approximation allows to treat the electrons as moving in the potential generated by motionless nuclei, which is considered fixed. The corresponding Hamiltonian is called the electronic Hamiltonian and is given by:

$$\widehat{H}_{elec} = \widehat{T}_e + \widehat{V}_{e-e} + \widehat{V}_{e-N} \quad (\text{eq I-8})$$

where \widehat{T}_e is the kinetic energy of the electrons, \widehat{V}_{e-e} the potential energy between electrons and \widehat{V}_{e-N} the potential energy between electrons and nucleus.

The objective is to solve therefore:

$$\widehat{H}_{elec}\psi_{elec}(r_n, R_m) = E(R_m)\psi_{elec}(r_n, R_m) \quad (\text{eq I-9})$$

The eigenvalue $E(R_m)$ depending parametrically on the positions of the nuclei The one electron approximation simplifies the all electron Hamiltonian into a sum of independent mono-electronic Hamiltonians $\widehat{h}_{e,l}$ as:

$$\widehat{H}_e = \sum_{i=1}^n \widehat{h}_{e,i} \quad (\text{eq I-10})$$

where n is the number of electrons in the material.

I-1.1.2 Variational principle

The variational method is one of the main methods used in quantum mechanics. Compared to perturbation theory, the variational method can be more robust in situations where it is hard to determine a good unperturbed Hamiltonian (i.e., one which makes the perturbation small but is still easily solvable). It allows an **approximation of the wave function of the ground state ψ_0** . The resolution of the Schrödinger equation consists in minimizing the matrix element $\frac{\langle \psi | \widehat{H}_{elec} | \psi \rangle}{\langle \psi | \psi \rangle}$. The basic idea is to guess a "trial" wavefunction, which consists of some adjustable parameters.

These parameters are adjusted until the energy of the trial wavefunction is minimized. It is necessary to test all the wave functions ψ_{trial} satisfying the antisymmetrical property of the wave function as well as the fact it must be normalized ($\langle \psi | \psi \rangle = 1$). The computed energy using ψ_{trial} is then higher than E_0 the energy of the ground state for $\psi_{trial} \neq \psi_0$.

$$\langle \psi_{trial} | \widehat{H}_{elec} | \psi_{trial} \rangle = E_{trial} \geq E_0 = \langle \psi_0 | \widehat{H} | \psi_0 \rangle \quad (\text{eq I-11})$$

It is important to notice that the total energy E_0 of the system is defined as a functional of ψ_{trial} . Then the objective is to find:

$$E_0 = \min E [\psi_{trial}] = \min(\langle \psi_{trial} | \widehat{T}_e + \widehat{V}_{e-e} + \widehat{V}_{e-N} | \psi_{trial} \rangle) \quad (\text{eq I-12})$$

The resulting trial wavefunction and its corresponding energy are variational method approximations to the exact wavefunction and energy. Obviously, it is not possible to search among all eligible functions. The Hartree Fock approximation takes into account only the exchange interaction in electron electron interactions. This approximation is restricted to the calculation of a single determinant i.e the wavefunction solution is developed on atomic orbitals basis, and determined due to the asymmetrical property of the wave-function, by the calculation of a single Slater determinant:

$$\psi_e(r_1, r_2, \dots, r_n) = \frac{1}{\sqrt{n!}} \begin{bmatrix} \chi_1(r_1) & \chi_2(r_1) & \dots & \chi_n(r_1) \\ \chi_1(r_2) & \chi_2(r_2) & \dots & \chi_n(r_2) \\ \dots & \dots & \ddots & \dots \\ \chi_1(r_n) & \chi_2(r_n) & \dots & \chi_n(r_n) \end{bmatrix} \quad (\text{eq I-13})$$

Where n is the number of crystal electrons, ψ_e is the wavefunction of the system or molecular orbital and χ_n are the associated mono-electronic wavefunction.

I-1.1.3 Density functional theory

Developed in the framework of solid state electronic theory, the **density functional theory (DFT) initially** based on the principles of Thomas [3], postulates that electronic properties of an homogenous N-body system can be described as a **functional of the electronic density**. This theory relies on the knowledge of the **ground state electronic density**: Hohenberg and Kohn [4] have shown that the ground state energy depends only on the electronic density and the total energy of the system can be expressed as a functional of the electronic density. Then, one electron approximation coming from **Kohn et Sham equations** [5] (which are solved by a self-consistent scheme and rely on Hohenberg and Kohn theorem) expresses the electronic density as the sum of squares of mono-electronic plane-wave functions and contains all the information necessary to determine the properties of an electronic system *i.e.* the energy functional can be expressed as a function of the electronic density ρ as:

$$E[\rho] = T_s[\rho] + V_{e-N}[\rho] + J[\rho] - E_{XC}[\rho] \text{ (eq I-14)}$$

where T_s is the kinetic energy of the non-interacting system, V_{e-N} the electron-nuclear interaction, J the Coulomb term and E_{XC} the exchange and correlation energy.

The density of a system of interacting particles can be calculated exactly as the density of an auxiliary system of non-interacting particles. The complex N body problem is reduced into a one-body problem: the particles are considered as independent particles moving in an effective potential V_{eff} created by all other electrons, which is expressed as a sum of the external potential, V_{ext} (the potential from the nuclei), V_H , the Coulomb potential and V_{xc} , the exchange correlation potential.

The total energy of the system of particles can thus be obtained and any physical properties that is related to the total energy or differences between total energies, can be calculated (equilibrium lattice constant, energy minimum, forces, as the derivative of the energy with respect to position (Hellman 1937, Feynman 1939), the stress as the derivative of the energy with respect to strain, elastic constants as second derivatives of the energy, vibrational properties as the derivative of the forces with respect to displacements).

The approximated Schrödinger equations are rewritten according to electronic density. Quantum correlation energy correction terms $E_{XC}[\rho(r)]$ are introduced to account for many body interactions. The self-consistent scheme¹¹ uses the variational principle to obtain the ground state electronic densities. The issue, in this approach, lies in the lack of exact knowledge of the correlation energy function associated with the system. Thus, the reliability of the DFT depends on the ability of finding a relevant functional $E_{XC}[\rho(r)]$ that contains all quantum interactions. Many approximations exist, and the functions have to be chosen

¹¹ The effective potential V_{eff} depends on the electronic density itself depending on ψ_i

according to the intrinsic properties of the material studied. In practice, the functional has to resort to physically motivated approximations, such as

- Local-density approximation (LDA): the real electron density at a certain spatial point can be locally approximated by that of the free-electron gas.
- Generalized-gradient approximation (GGA, PBE) is an extension to the LDA where the local gradient of the electron density is taken additionally into account.
- Hybrid functionals (B3LYP, PBE0) is a mix of local or semi-local functionals with exact exchange contributions.

Even though ab initio calculations are not strictly exact, since they are based on a certain number of approximations, their use represents, at the moment, the most reliable approach to obtain the total energy for a given atomic distribution. We chose this method for the study of twist GBs in complement with empirical potential calculations presented in the next section.

I-1.2 Empirical cohesive models

I-1.2.1 Empirical potentials

DFT certainly offers flexibility in its use in terms of transferability (very few fitting parameters) and provides an excellent predictive power in solids by giving accurate results, but this method implies a high computational cost compared to semi-empirical methods and empirical potentials (EP). In the EP approach, the cohesive energy of the system is usually approximated as an explicit function of the atom positions. More precisely, the interatomic interaction potential is a function $U(r_1, r_2 \dots)$ of the positions of the nuclei, which represents the potential energy of the system when the atoms are arranged according to a specific configuration. This function is invariant with respect to translations and ensemble rotations and is usually constructed from the relative positions of atoms rather than from their absolute positions.

The forces on the atoms are then obtained by calculating the potential gradient with respect to the atomic displacements. The development of such potentials is usually performed in two steps: first, usually one chooses the analytical form of the function (which often depends on the type of interactions involved), which contains adjustable parameters and secondly adjusts the function to a certain number of wisely chosen physical properties - cohesive energy, elastic constants, defect formation energy, surface energies, interface energy, phonon spectrum, Pressure-Volume relationship ... - depending on the field of application.

The earliest simulations used simple pair potentials where the total energy of the system is calculated as a sum over interactions between isolated particles:

$$U(r_1, r_2, \dots, r_N) = \sum_i \sum_{j>i} V(|\vec{r}_i - \vec{r}_j|) \quad (\text{eq I-15})$$

Such potentials cannot describe correctly the formation of surfaces vacancies among other properties for metallic systems. As a consequence, in the early 1980s, a number of N-body potentials models emerged. The total energy of the system is usually obtained as a pair contribution $\phi(r_{ij}) = \frac{1}{2}V_{ij}(|\vec{r}_i - \vec{r}_j|)$ which models the repulsion generated by the nuclei at short distance and a many body term $U(\Omega)$ which models the cohesion brought by the electron sea:

$$E = \sum_i \sum_j \phi(r_{ij}) + U(\Omega) \quad (\text{eq I-16})$$

One of the most commonly method used is the Embedded Atom Method (EAM) developed by Baskes and Daw [6]. This method is based on a simplified description of the electronic density. This approach includes embedding energies F which depend on the local electron density ρ_i seen through a host atom which would replace atom i but without its contribution.

The potential energy of an atom of the system is composed of two terms and is given by:

$$E_i^{EAM} = \sum_{j \neq i} \phi(r_{ij}) - F(\sum_{j \neq i} \rho_j(r_{ij})) \quad (\text{eq I-17})$$

The first term corresponds to the repulsive part which is described by a pair interaction term. The second term denotes the attractive part which is defined by a function of the local environment, F . In order to adjust this model to metals and to obtain the results closest to experiments, many releases of this potential exist. In the original form of EAM, the atomic reference environment is limited to the first atomic neighbours and the calculation of the interaction term does not take into account the screening effect on the interaction between two atoms. The Modified-EAM (MEAM) method permits to overcome these issues by taking into account the atomic screening effect and the second nearest neighbours [6]. Atomistic simulations of alloys at the empirical level face the challenge of correctly modelling basic thermodynamic properties. Another release of EAM method has been developed by Ouyang *et al* [7]: in order to fit a negative Cauchy pressure, especially in the case of binary bcc alloys comprising chromium, a modified term of energy was introduced in the EAM model. These improvements gave rise to an analytic EAM model representing the interaction between atoms in a wide range. This new approach permits to calculate the self-diffusion properties of bcc transition metals (the dilute-solution enthalpies and formation enthalpies of binary alloys of bcc transition metals V, Nb, Ta, Cr, Mo, W and Fe), with results in good agreement with experiments [8]–[11].

In the case of Fe-Cr, an EAM dependent on concentration has been proposed by Caro *et al* [12] to take into account the change of sign of the mixing energy. Another EAM version is the two band potential developed by Olsson *et al* [13]. They added two contributions in the embedding function which depends on the local environment of the atoms: a first contribution for the s band and a second for the d band. Taking into account these two contributions in the embedding function by adjusting the model on DFT mixing energy calculations, enabled them to reproduce the change of mixing energy sign for low concentration of Cr.

Other N-body potentials in the same spirit as the EAM approach have been developed at the same time: the second-moment approximations of the strong-bond method with the potentials of Finnis and Sinclair [14], those of Ducastelle and Cyrot-Lackmann [15], those of Rosato, Guillopé and Legrand [16], the effective medium theory (Effective Medium Theory) of Norskov and coauthors [17], the "glue model" by Ercolessi, Tosatti and Parinello [18] ... The difference between these methods stems from the physical interpretation and the way of choosing the parametric functions.

The empirical potential complexity increases with the number of elements modelled: currently empirical potentials with up to 4 different atomic species not including iron are available to model typical RPV steels [19].

Regarding the case of phosphorus in iron, the only empirical potential (EP) available is **Ackland *et al.***[20], **potential which has been** fitted on ab initio data. Its use for studying the behaviour of P is adapted for the study of low phosphorus content in low alloy α -iron steels. This EP also adapted for the study of GBs has been chosen in the PhD to construct and study the segregation of phosphorus on twist GBs.

While the traditional potentials presented here are constructed on a particular set of properties i.e. lattice constant, cohesive energy, elastic constants, point defect formation and migration energies, surface energies, generalized stacking fault energies... one should bear in mind that other methods using machine learning permits the construction of a new class of potentials called machine learning (ML) potentials. In contrast to traditional potentials, ML potentials [21] map the 3 N-dimensional configurational space of the system onto its potential energy surface (PES) and then used a high-dimensional mathematical regression to interpolate between the reference energies. Based on these two techniques a third intermediate class of potential emerges which mixes physics based interatomic potentials and letting a ML regression predict its parameters according to each atom's local environment. These two latter classes of potentials improve the accuracy of the results in comparison with classical potentials. However, they require a very large amount of data to fit on, and the reliance for human is weaker. That is why we use classical EP in this work for the study of GBs in *Chapters III and IV*.

DFT calculations suffer from high computational cost while empirical methods cannot be used for RPV alloys because of their high number of atomic species. Thus, simpler models based on strong approximations typically associated with rigid lattices have been developed. One of this method, the cluster expansion method and the concentration dependant model are presented briefly in the next subsection.

I-1.2.2 The cluster expansion approach

The cluster expansion approach [1] provides a formalism to derive Hamiltonian based on a decomposition of the interactions into pairs ε_{ij} , triplets ε_{ijk} , quadruplets ε_{ijkl} , quintuplets and so on. The interest of this model applied on a rigid lattice is that it permits to overcome the absence of interatomic potential when the chemical complexity of a system of atoms is too high.

The total energy of the system can thus be written as a sum of n-uplet interactions:

$$E_{tot} = \sum_i \varepsilon_i + \sum_i \sum_{j<i} \varepsilon_{ij} + \sum_i \sum_{j<i} \sum_{k<j} \varepsilon_{ijk} + \sum_i \sum_{j<i} \sum_{k<j} \sum_{l<k} \varepsilon_{ijkl} \quad (\text{eq I-18})$$

The first simulations in metals used pair interaction models for which the energy of a system of particles is obtained as the sum of interactions between pairs of particles [22].

Using the on-lattice Hamiltonian with a pair interaction approximation, the total energy of N particles can be expressed as the sum of pair interactions between lattice sites:

$$E_{tot} = \sum_{k=1}^M \sum_{i=1}^N \sum_{j \neq i}^N \varepsilon_{ij}^k \quad (\text{eq I-19})$$

where ε_{ij}^k denotes the pair interactions between sites i and j. M denotes the range of the pair interaction employed in the model.

I-1.2.3 Concentration dependent model (CDP)

In order to account for the effect of the local environment in the pair interaction model described above, Senninger *et al* [23] developed an energetic model in which the dependence on the local Cr concentration in the Fe-Cr pair interaction is taken into account in order to reproduce the asymmetrical mixing energies in the Fe-Cr alloys. The pair interactions are defined as:

$$\varepsilon_{Fe-Cr}^{(n)}(c) = \frac{1}{2} \left(\varepsilon_{Fe-Cr}^{(n)}(c_{Fe}) + \varepsilon_{Fe-Cr}^{(n)}(c_{Cr}) \right) \quad (\text{eq I-20})$$

where the local concentration c_x in the bcc lattice is:

$$c_X = \frac{N_{Cr}^X(1) + N_{Cr}^X(2) + \delta_{XCr}}{15} \quad (\text{eq I-21})$$

where $N_{Cr}^X(1)$ and $N_{Cr}^X(2)$ denotes the number of Cr atoms around the X atom at 1NN distance and at 2NN distance respectively. δ_{XCr} corresponds to the Kronecker symbol which is equal to 1 if the X site is occupied by a Cr atom.

I-1.3 Energetic property calculations

I-1.3.1 Empirical potential and DFT calculations

The molecular statics (MS) and molecular dynamics (MD) calculations presented in this work have been performed with the DYMOKA code [24]. The neighbor search is done through a link cell approach combined with a Verlet list. The newtonian equations of motion are integrated using a fifth-order Gear predictor corrector algorithm. Forces applying to atoms are calculated and new positions of the atoms are calculated accordingly to reach a more favourable energetic state. The number of steps for MS calculations needed to obtain the energy convergence is about 10000. GBs are constructed with Fe-P Ackland *et al.* [20] empirical many-body potential which is adapted to study GBs in low alloy α -iron steels.

An energy minimization method algorithm called quench molecular dynamics (QMD) derived after [25], [26] is also included in DYMOKA. The purpose of quenching is to rapidly relax the system to the current local minimum potential energy. In contrast to conventional DYMOKA relaxation, quenching sets the atomic velocities to zero whenever the total potential energy rises relative to the preceding time step. It is used in addition to a conventional DYMOKA relaxation described before to construct GBs. More details about twist GB construction will be presented in *Chapter III*.

DFT calculations were performed using the projector augmented wave (PAW) method as implemented in the Vienna Ab initio Simulation Package (VASP) [27]–[31]. To describe the electron-ion interactions, we used the PAW potentials including '3d' and '4s' electrons of Fe in the valence. The pseudopotentials were taken from the VASP library. The exchange correlation energy was described by the spin-polarized generalized gradient approximation (GGA) with the Perdrew-Burke-Ernzerhof (PBE) functional [32]. The wavefunction was expanded using a plane-wave basis with a cut-off energy of 300 eV. The error induced by this lower cutoff energy was checked to be negligible. Periodic boundary conditions and the supercell approach were used for all calculations. The Brillouin zone integration was performed using the Monkhorst-Pack (MP) scheme [33]. By this method, the equilibrium lattice parameter (a_0) for bcc Fe obtained is 2.83 Å which is in good agreement with theoretical values of 2.83-2.87 Å [34]–[37] and the experimental value of 2.867 Å [38]. All the calculations were done at constant volume fully relaxing the atomic positions in the supercells. The atomic relaxation according to the Hellman-Feynman forces was performed using the quasi-Newton method.

I-1.3.2 Formation energy

The formation energy E_f represents the energy required to dissociate the material into its individual components. *The formation energy* of a defect is defined as a function of the total energy of a cell containing n_i atoms of species i as follows:

$$E_f = E_{tot} - \sum_i n_i \mu_i \quad (\text{eq I-22})$$

Where E_{tot} is the total energy of the system with the defect and μ_i is the chemical potential of species i , determined by the energy per atom from a reservoir in equilibrium with the defective crystal. For instance, the GB formation energy corresponds to the energy required to introduce a GB in a system. It can be determined simply by comparing the total energies of pure systems with and without a GB. The GB formation energy E_f^{gb} for a supercell containing a GB is calculated as follows:

$$E_f^{gb} = \frac{(E_{tot} - E_{surf})}{A_{surf}} \quad (\text{eq I-23})$$

Where E_{tot} is the total energy of the system with the GB, E_{surf} is the total energy of the system without the GB and A_{surf} is the GB area (which depends on the size of the supercell). The supercell considered is composed of only one GB.

I-1.3.3 Binding energy

The binding energy between two elements or objects A and B represents the energy gain or loss when one brings the two objects within a distance where some interaction occurs. The binding energy between “microstructural objects” characterizes the interaction strength of these objects. The total binding energy between n objects, i.e., solutes, vacancies, self-interstitial atoms, GB etc. is the energy difference between the configuration where all the objects interact, and the configurations where the objects are isolated and non-interacting.

The total binding energy is expressed as follows:

$$E_b(P_1, P_2, \dots, P_n) = \sum_{i=1, \dots, n} E(P_i) - [E(P_1 + P_2 + \dots + P_n) + (n - 1)E_{ref}] \quad (\text{eq I-24})$$

where E_{ref} is the energy of the supercell without any defects, $E(P_i)$ is the energy of the supercell with a defect P_i which is for instance a GB, a solute a self-interstitial or a vacancy and $E(P_1 + P_2 + \dots + P_n)$ is the energy of the cell containing all interacting defects. All the supercells contain the same number of sites, $(n - 1)E_{ref}$ represents the contribution of the perfect supercell without any defect. All the supercells have the same size: the number of atoms is conserved to be consistent in terms of energy. With this definition, positive values are binding (or attractive) configurations.

I-1.3.4 Segregation energy

The GB segregation energy, which characterizes the tendency of atoms to segregate at GBs, is defined as the difference of energy for a solute atom located in the GB and in the bulk. Thus, with respect to the previously defined binding energy, **the segregation energy is the opposite of the binding energy.**

Note that, for all calculations (segregation energy, binding energy, formation energy), the calculations have been performed at $T = 0$ K: the free energy is equivalent to the enthalpy, which can be broken down according to the internal energy, the pressure and the volume: $G = H = U + PV$. Entropy effects are neglected, even though entropy effects exist, it is difficult to account for such effects in our simulations due to the computational burden it represents. In this work no calculation considers entropy effects. The variation ΔPV is also negligible, thus, the variation of the free energy or the reaction free energy is equal to the variation of internal energy: $\Delta G = \Delta U$.

A particular attention in this PhD has been paid to phosphorus GB segregation, since the temperature dependence $[T \ln X_S^*]$ for phosphorus in α -iron seems to be constant with the temperature according to Lejcek *et al* [39], the effect of the entropy is considered negligible. X_S^* is the solute solubility limit in the matrix. More details about GB segregation will be presented in *Chapter IV*.

I-2. Conclusion

Modelling the microstructure evolution of alloys is a difficult task for multicomponent alloys with multiple solutes and/or several point defects. An accurate description of the evolution (during irradiation, thermal ageing ...) requires an accurate description of the energetics of the system which is given by cohesive models.

DFT method gives an accurate description of the energetic interactions but at a high computational cost. Empirical potentials, even if they are more adapted to bigger systems, raise the problem of transferability i.e. the ability of the method to correctly model the desired material under conditions far from the conditions used when adjusting the parameters. On the other hand, the development of empirical potential is time-consuming, in particular for complex alloys like RPV steels. However, these methods are adapted for the study of local element in RPV steels such as GBs which are developed in *Chapter III and IV*.

I-3. Bibliography

- [1] J. M. Sanchez, F. Ducastelle, et D. Gratias, « Generalized cluster description of multicomponent systems », *Physica*, vol. 128A, p. 334-350, 1984.
- [2] B. Pannier, « Towards the prediction of microstructure evolution under irradiation of model ferritic alloys with an hybrid AKMC-OKMC approach », Thèse de Doctorat, Université de Lille, 2017.
- [3] L. H. Thomas, « The stopping of alpha-particles in heavy atoms », *Proc. Cambridge Phil. Soc.*, vol. 23, p. 713, 1927.
- [4] P. Hohenberg et W. Kohn, *Physical Review*, vol. 136, p. 864, 1964.
- [5] W. Kohn et L. J. Sham, *Physical Review*, vol. 140, p. 1133, 1965.
- [6] M. I. Baskes, « Modified embedded-atom potentials for cubic materials and impurities », *Physical Review B*, vol. 46, p. 2727, 1992.
- [7] Y. Ouyang, B. Zhang, S. Liao, et Z. Jin, « A simple analytical EAM model for bcc metals including Cr and its application », *Zeitschrift für Physik B Condensed Matter*, vol. 101, p. 161-168, 1996.
- [8] R. Hultgren, P. D. Desai, D. T. Hawkins, M. Gleiser, et K. K. Kelley, « Selected values of the thermodynamic properties of binary alloys. », *Metals Park: American Society for Metals*, 1973.
- [9] O. Kubaschewski, H. Probst, et K. H. Geioer, « The Thermochemical Properties of Solid and Liquid Iron-Vanadium Alloys », *Z. Phys. Chem. Neue Folge.*, vol. 104, p. 23, 1977.
- [10] S. C. Singhal et W. L. Worrell, « A high-temperature thermodynamic investigation of the nb-mo system », *Metallurgical transactions A*, vol. 4, p. 1125-1128, 1973.
- [11] C. Colinet, A. Beesound, et A. Pasturel, « Theoretical determinations of thermodynamic data and phase diagrams of BCC binary transition-metal alloys », *Journal of Physics F: Metal Physics*, vol. 18, p. 903, 1988.
- [12] A. Caro, D. V. Crowson, et M. Caro, « Classical Many-Body Potential for Concentrated Alloys and the Inversion of Order in Iron-Chromium Alloys », *Physical Review Letters*, vol. 95, p. 075702, 2005.
- [13] P. Olsson, J. Wallenius, C. Domain, K. Nordlund, et L. Malerba, « Two-band modeling of alpha-prime phase formation in Fe-Cr », *Physical Review B*, vol. 72, p. 214119, 2005.
- [14] M. W. Finnis et J. E. Sinclair, « A simple empirical N-body potential for transition metals », *Philosophical Magazine A*, vol. 50, p. 45-55, 1984.
- [15] F. Ducastelle et Cyrot-Lackmann, « Moments developments: II Application to the crystalline structures and the stacking fault energies of transition metals », *J. Phys. Chem. Solids*, vol. 32, p. 285, 1971.
- [16] V. Rosato, M. Guillopé, et B. Legrand, « Thermodynamical and structural properties of f.c.c. transition metals using a simple tight-binding model », *Philosophical Magazine A*, vol. 59, p. 321, 1989.
- [17] J. K. Norskov, « Interatomic interactions in the effective-medium theory », *Reports on Progress in Physics*, vol. 53, p. 1253, 1990.
- [18] F. Ercolessi, E. Tosatti, et M. Parinello, « Au (100) reconstruction in the glue model », *Surface Science*, vol. 177, p. 314, 1986.

- [19] B. Jelinek *et al.*, « Modified embedded atom method potential for Al, Si, Mg, Cu, and Fe alloys », *Physical Review B*, vol. 85, p. 245102, 2012.
- [20] G. J. Ackland, M. I. Mendeleev, D. J. Srolovitz, S. Han, et A. V. Barashev, « Development of an interatomic potential for phosphorus impurities in alpha-iron », *Journal of Physics: Condensed Matter*, vol. 16, n° 27, p. 1-14, 2004.
- [21] Y. Mishin, « Machine-learning interatomic potentials for materials science », *Acta Materialia*, vol. 214, p. 116980, 2021.
- [22] E. Vincent, « Simulation numérique à l'échelle atomique de l'évolution microstructurale sous irradiation d'alliages ferritiques », Thèse de Doctorat, Université de Lille, 2006.
- [23] O. Senninger, « Ségrégation et précipitation dans les alliages fer-chrome hors et sous irradiation », Université de Grenoble, 2013.
- [24] C. S. Becquart, C. Domain, A. Legris, et J. C. Van Duysen, « Influence of the interatomic potentials on molecular dynamicssimulations of displacement cascades », *Journal of Nuclear Materials*, vol. 280, p. 73-85, 2000.
- [25] C. H. Bennett, « Exact calculations defects in model substances », in *Diffusion in Solids, Recent Developments*, New York, 1975, p. 85.
- [26] J. R. Beeler et G. L. Kulcinski, « Interatomic Potentials and Simulation of Lattice Defects », New York, p. 735, 1972.
- [27] G. Kresse et J. Furthmüller, « Efficient iterative schemes for ab initio total-energy calculations using a plane-wave basis set », *Physical Review B*, vol. 54, p. 11169, 1996.
- [28] G. Kresse et J. Furthmüller, « Efficiency of ab-initio total energy calculations for metals and semiconductors using a plane-wave basis set », *Computational Materials Science*, vol. 6, n° 1, p. 15-50, 1996.
- [29] G. Kresse et J. Hafner, « Ab initio molecular dynamics for liquid metals », *Physical Review B*, vol. 47, p. 558, 1993.
- [30] G. Kresse et D. Joubert, « From ultrasoft pseudopotentials to the projector augmented-wave method », *Physical Review B*, vol. 59, p. 1758, 1999.
- [31] P. E. Blöchl, « Projector augmented-wave method », *Physical Review B*, vol. 50, p. 17953, 1994.
- [32] J. P. Perdew, J. A. Chevary, S. H. Vosko, K. A. Jackson, M. R. Pederson, et C. Fiolhais, « Atoms, molecules, solids, and surfaces: Applications of the generalized gradient approximation for exchange and correlation », *Physical Review B*, vol. 46, p. 6671, 1992.
- [33] H. J. Monkhorst et J. D. Pack, « In the original Monkhorst and Pack scheme, the k-point mesh is always symmetric around the cpoint, whereas very often in our calculations we adopted grids centered at the cpoint », *Physical Review B*, vol. 13, p. 5188, 1976.
- [34] M. Cak, M. Sob, et J. Hafner, « First-principles study of magnetism at grain boundaries in iron and nickel », *Physical Review B*, vol. 78, n° 5, p. 054418, 2010.
- [35] E. G. Moroni, G. Kresse, et J. Hafner, « Ultrasoft pseudopotentials applied to magnetic Fe, Co, and Ni: From atoms to solids », *Physical Review B*, vol. 56, n° 24, p. 15629, 1997.

- [36] D. E. Jiang et E. A. Carter, « Diffusion of interstitial hydrogen into and through bcc Fe from first principles », *Physical Review B*, vol. 70, n° 6, p. 064102, 2004.
- [37] Y. Tateyama et T. Ohno, « Stability and clusterization of hydrogen-vacancy complexes in α -Fe: An ab initio study », *Physical Review B*, vol. 67, n° 17, p. 174105, 2003.
- [38] R. Kohlhaas, P. Dunner, et N. Schmitz-Prange, « Über die temperaturabhängigkeit der gitterparameter von eisen, kobalt und nickel im bereich hoher temperature », *Zeitschrift für Angewandte Physik*, vol. 23, p. 245-249, 1967.
- [39] P. Lejcek, L. Zheng, S. Hofmann, et M. Sob, « Applied Thermodynamics: Grain Boundary Segregation », *Entropy*, vol. 16, p. 1462-1483, 2014.

Chapter II: GB descriptions

A GB can be considered as a transition region between two grains where the atoms might be displaced from their regular lattice position to accommodate discontinuities in crystallographic direction. It is an important feature of the microstructure of metals in particular because it may limit the cohesion of the materials. A robust theoretical description of GBs is necessary to understand physical mechanism involving GBs. Different approaches, at different scales, have been developed to describe these systems and will be detailed in this Chapter.

II-1. GB crystallographic definition and description

II-1.1 Crystallographic description

Technologically relevant materials are composed of **grains** which are separated from one another by **GB**. GBs are usually represented as a **crystallographic discontinuity** with an average width less than two atomic diameters [1]–[3]. This means that a transition region is formed where the atoms might be displaced from their regular lattice position. A GB can be viewed from a macroscopic (the material is described by a set of grains delimited by GB) and atomistic point of view (each GB is distinguished and is described as a specific arrangement of atoms) as illustrated in **Figure II-1**.

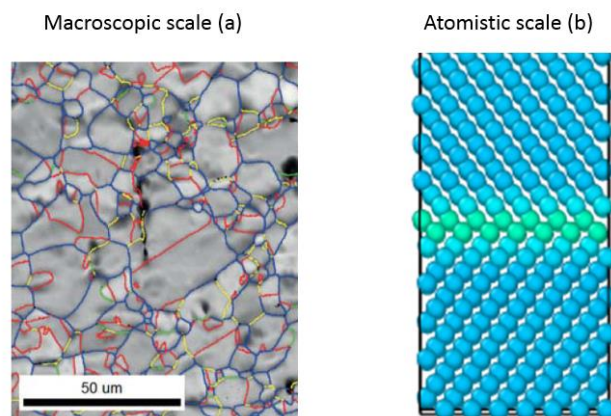


Figure II- 1: GB illustration: (a) Electron back scatter diffraction (EBSD) image¹² representing the “macroscopic scale” of Fe-Mn-C alloy, blue lines correspond to high angle GB (HAGB), green lines to low angle GB (LAGB), red lines to $\Sigma 3$ GBs, and yellow lines to other GBs, [4], (b) atomistic scale of $\Sigma 3[110]$ GB.

¹² Microscopic techniques equipped with electron backscatter diffraction (EBSD) camera provide access to GB plane orientation from the incident beam diffracted by crystal plane (more details in part II)

Five macroscopic independent degrees of freedom which are thermodynamic state variables, in addition to the conventional state variables such as temperature, pressure, and bulk composition, are used to describe the **crystallographic structure of GB**. They are split into two groups:

- Three degrees of freedom are used to define the mutual misorientation between the two crystals. Two parameters must be considered: the misorientation angle θ which corresponds to one degree of freedom and two direction cosines for the rotation axis, $c = [h_0, k_0, l_0]$ which correspond to the two remaining degrees of freedom.
- Two degrees of freedom are used to define the GB normal planes $(h_{nA}k_{nA}l_{nA})$ and $(h_{nB}k_{nB}l_{nB})$ which are associated to a normal vector to the GB plane.

The GB is then fully described as $\theta^\circ [h_0k_0l_0] (h_{nA}k_{nA}l_{nA})/(h_{nB}k_{nB}l_{nB})$. If the two grains present the same grain orientation, the GB is described by the notation: $\theta^\circ [h_0k_0l_0] (h_{nA}k_{nA}l_{nA})$, and is called a symmetric GB.

Three other microscopic parameters characterise the rigid body translation of both grains relative to one another. They are represented by a translation vector \mathbf{t} , which can be expressed as a sum of the parallel and perpendicular component to the GB plane:

$$\mathbf{t} = \mathbf{p} + \mathbf{e} \text{ (eq II-1)}$$

where \mathbf{p} corresponds to the parallel component to the GB plane related to the parallel move of one grain with respect to the other preserving the perfect crystal density and the lattice periodicity of GB layers. The second component \mathbf{e} represents the normal displacement of both grains, which involves the creation of an **excess volume**. In order to keep a GB volume constant, this volume change is compensated by an **elastic deformation**. The interspatial spacing increases but it is compensated by a strain field which spreads over a little volume near the GB [5].

It should be noticed that only few mutual translations may exist for each GB under external conditions (temperature, pressure and chemical composition) which are directly linked to energetic considerations of GB. Indeed, according to Pond *et al* [5], computer simulations of aluminium periodic GB, show that rigid body translation plays an important role in the energetic stabilization with a dominant contribution to relaxation not simply related to boundary periodicity.

The relationship, as illustrated in **Figure II- 2**, between the rotation axis \mathbf{c} and the GB normal \mathbf{n} , leads also to the definition of different types of GBs:

- **Symmetric tilt grain boundaries (STGB):** tilt boundary, \mathbf{c} is perpendicular to the GB normal \mathbf{n} , the normal GB plane is the same in both grains (**Figure II- 3**). Thus, the mirror symmetry is described by the same Miller indices $(h_{nA}k_{nA}l_{nA}) = (h_{nB}k_{nB}l_{nB})$ and the twist angle is equal to zero. It is the most studied GB.

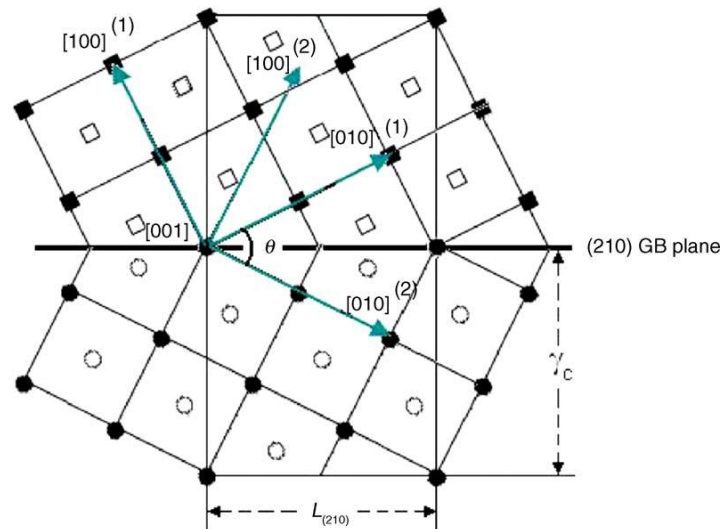


Figure II- 2: Projection plot of the (2 1 0) STGB onto (0 0 1) plane [6]

- **Twist grain boundaries:** c is parallel to the GB normal n .

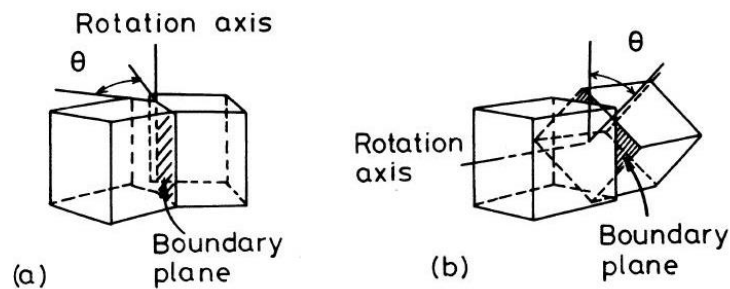


Figure II- 3: Tilt (a) and Twist (b) GB [7]

- **Random/mixed GB:** the indices $(h_{nA}k_{nA}l_{nA}) \neq (h_{nB}k_{nB}l_{nB})$ and the twist angle is different from zero. A **mathematical description** represents a GB structure as a product of a rotation matrix M of a grain along a specific crystallographic direction for the three axes of the crystal (yielding the rotation angle and axis) and a translation matrix vector T for the three-translation axis.

$$M' = TM \text{ (eq II-2)}$$

Misorientation angle distributions allow a comparison on either side of the GB, which leads to the determination of the GB character. Therefore, supported by both theoretical and experimental studies and based on **dislocation models**, two significant GB groups may be defined, low angle GB (LAGB) and (HAGB) high angle GB.

GB is a crystallographic discontinuity between two grains. The parameters most commonly used to describe a GB are the misorientation angle and the GB orientation plane. Based on these characteristics, a wide range of GB exists but the most studied is the STGB.

II-1.2 General framework to construct GBs

Three independent variables are necessary to specify a **misorientation** and therefore providing either the angle or axis alone corresponds to an incomplete description. Thus, large efforts have been devoted to create a simple geometrical classification to characterise and classify usually high angle GB which can be associated to a repetition of structural units.

1.2.1 Coincidence Site Lattice (CSL)

GBs can be **described by the Coincident Site Lattice (CSL)** approach with the concept of **Kronberg and Wilson** (Kronberg and Wilson 1949). The CSL refers to a geometrical construction where the lattices cannot actually overlap, the atomic positions are not accounted for and the boundary structure is expected to be more regular than a general boundary. In this model, **the rotations** are limited to values that bring a lattice point from one grain into coincidence with a different point in the second grain producing a **surface of lattice points**, separating the two grains. These surfaces contain a number of positions, where the sites where atoms in both grains are in coincidence are called **coincidence sites**.

The relation between the number of lattice points in the unit cell of a **CSL** and the number of lattice points in a unit cell of the generating lattice is given by Σ . It corresponds to the inverse ratio of the area of coincidence site unit cell to the elementary unit cell i.e.: the inverse of coincidence density of sites. It is given by:

$$\Sigma = \frac{\text{total number of all lattice sites in elementary cell}}{\text{number of coincidence sites in an elementary cell}} \text{ (eq II-3)}$$

A high Σ value involves a low density of coincidence lattice sites, whereas a low Σ value refers to a high density of coincidence lattice sites and a preferential low interfacial energy as it will be seen in the next subsection.

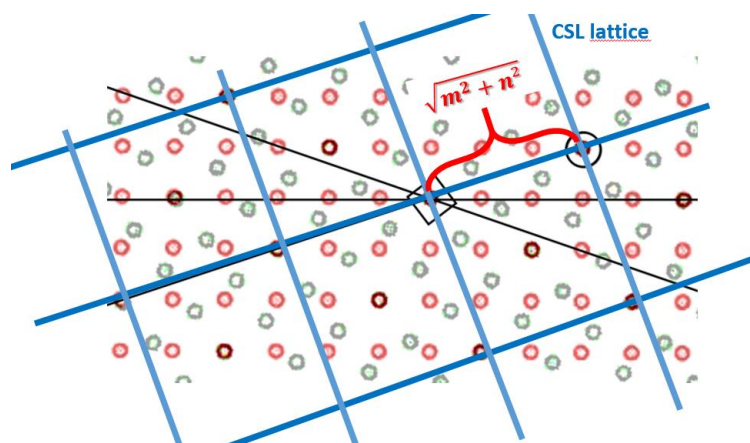


Figure II- 4: Representation of a CSL lattice

The angle of rotation can be determined from the lattice geometry (**Figure II- 5**). In a cubic lattice for (100) GB plane:

$$\theta = 2 \tan^{-1} \left(\frac{n}{m} \right) \text{ (eq II-4)}$$

where (m,n) are the coordinates of the superimposed point considering that a coincident site is located at (0,0), m is measured parallel to the mirror plane and n perpendicular to the mirror plane.

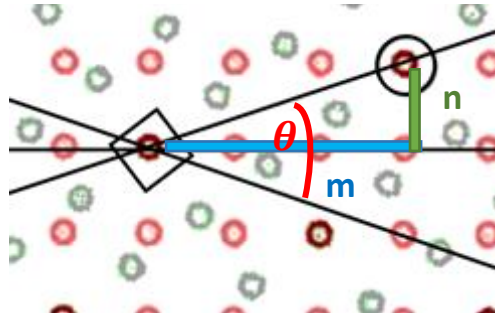


Figure II- 5: Definition of the rotation angle

Depending on the plane choice, the GB is a tilt, a twist or a mixed GB.

In a **square lattice for a (100) GB plane**, the unit cell for the coincidence site lattice (**Figure II- 5**) is a square where each side is $\sqrt{(m^2 + n^2)}$ long. Thus, the area of the cell is m^2+n^2 . The range of m and n is restricted such that $m < n$. If $n = m$ then all points coincide, and $m > n$ does not produce any new lattices. Since, Σ denotes the ratio of the area of coincidence site lattice to the regular lattice, finally:

$$\Sigma = \delta(m^2 + n^2) \text{ (eq II-5)}$$

where $\delta = 1$ if $(m^2 + n^2)$ is odd and $\delta = 1/2$ if $(m^2 + n^2)$ is even.

The calculation of density of coincidence lattice sites can be extended to the general case. Any rotation vector can be characterized by an axis r and a rotation angle α with $R(r, \alpha)$ its “axis-angle” representation. A convenient method to express this rotation angle is to use the Rodrigues vector representation (**Figure II- 6**) ρ_{RF} which instead scales r by the tangent of the semi-angle $\alpha/2$:

$$\rho_{RF} = r \cdot \tan \left(\frac{\alpha}{2} \right) \text{ (eq II-6)}$$

Rodrigues rotational vector is generated, where $m < n$, m,n, being integer, and h, k, l being Miller indices of the GB plane. The rotation angle can be expressed for any lattice by the following expression:

$$\tan\left(\frac{\theta}{2}\right) = \frac{m}{n} \sqrt{(h^2 + k^2 + l^2)} \text{ (eq II-7)}$$

Area of CSL cell can be thus transformed as:

$$m^2 + n^2 = n^2 \left(1 + \left(\frac{n}{m}\right)^2\right) = n^2 \left(1 + \tan^2\left(\frac{\theta}{2}\right)\right) \text{ (eq II-8)}$$

Finally, Σ extended to general case is expressed by Miller indices:

$$\Sigma = n^2 + \delta m^2 (h^2 + k^2 + l^2) \text{ (eq II-9)}$$

Where $\delta = 1$ if $(h^2 + k^2 + l^2)$ is odd and $\delta = 1/2$ if $(h^2 + k^2 + l^2)$ is even. In cubic systems, all Σ values are odd.

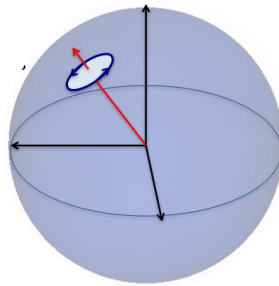


Figure II- 6: Rodrigues representation, rotation axis in red[8].

CSL is a geometrical construction which represents the lattice formed by the positions where atoms are in coincidence after a specific rotation. Depending on the plane choice, the GB is a tilt, a twist or a mixed GB. Each CSL for a given rotation is characterized by a certain density of coincidence sites which is linked to the misorientation angle.

1.2.2 Displacement shift lattice (DSC)

Even if high angle tilt GBs occupy only an infinitely small portion of the five-dimensional geometric GB phase space [9], they are frequently observed experimentally [10], [11]. Therefore, they are the most studied theoretically as they are also easy to build. [12]–[14].

The CSL concept is useful to approximate some correlations between the symmetric GB structure and the energy. However, this method is not powerful enough to describe any GB structures. Indeed the CSL description characterises exclusively the mutual misorientation of two adjoining crystal and does not give any information about the change of GB orientation. For example, there are 24 ways to describe a single misorientation for cubic crystal symmetry [15].

Despite these drawbacks, the CSL model remains the most useful approach to deal with symmetric geometrical structures obtained by a rotation between two grains around a given axis which leads to special orientations between grains. **Its strength and weakness arise from its independence of the GB position/orientation inside the material.**

Relaxations can introduce some **small deviations** from a perfect lattice coincidence orientation. Thus, displacement shift lattice (DSC) was created to account for these deviations. It corresponds to the lattice of all possible shift vectors which preserve the **CSL and the structure of the GB**. Displacing one grain by a vector from corresponding DSC lattice preserves the structure of the boundary by keeping the symmetries of the **CSL**, while, any arbitrary shift of CSL which do not correspond to DSC lattice will destroy the CSL.

The DSC lattice comes from the O-lattice representation which corresponds to a generalisation of the CSL theory [3], [16]. Any **O**-point from an O-lattice can be taken as the origin for the rotation transforming crystal **A** into crystal **B**. The lattice A can be formed from the other (B lattice) by a homogeneous linear transformation \mathcal{S} performed about the point O as the origin. Each point \mathbf{r}' of one lattice is derived from a corresponding point \mathbf{r} of the other lattice by the relation:

$$\mathbf{r}' = \mathcal{S}\mathbf{r} \text{ (eq II-10)}$$

In other words, the lattice A can be shifted by any vector pointing to an equivalence point in the **O**-lattice without changing the periodic pattern of the **O**-lattice. Finally, it just changes the rotation origin which leaves the periodic pattern of the **O**-lattice unchanged.

Any arbitrary shift of CSL destroys the CSL and the density of coincidence lattice sites is not preserved. In that situation and for small relaxations of the CSL, the GB can be represented by a DSC lattice

II-2. Energetic description of GBs

GB can feature a lot of different atomic configurations and their corresponding energy is directly linked to the geometry of the interface structure and preferential deformation. Yet, GB energy is found to be a **function of the misorientation angle (Figure II- 7a)**.

Singular GB corresponding to a minimal GB energy arises at some given misorientation angle. For example, in **Figure II-7 a**, singular grain boundaries corresponds to $\Sigma 3(112)$ and $\Sigma 11(332)$. Stereographic representations (**Figure II- 7b**) are currently used to show the entire misorientation angle and identify the GB minimum energy.

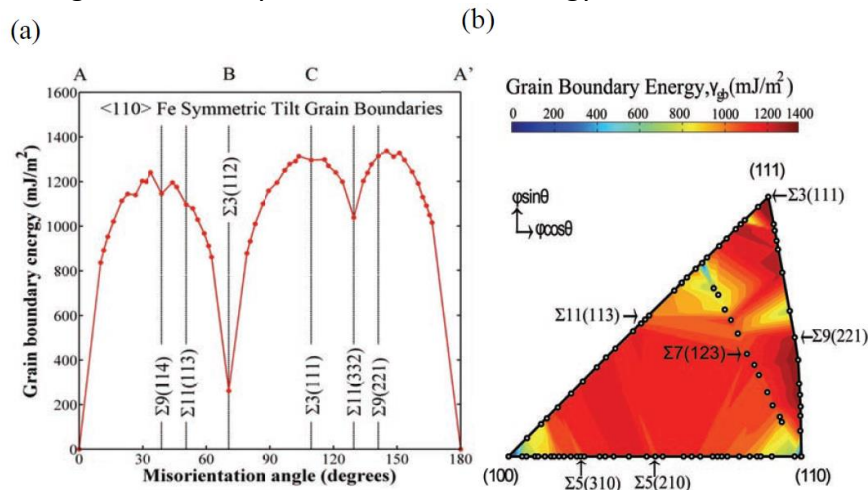


Figure II- 7: (a) GB energy for the [110] symmetric tilt GB system (b) contour plot of GB energies for the three symmetric tilt systems of Fe ([100], [110] and [111]) represented using polar and azimuthal angles [12].

The GB energy relationship with the misorientation angle of the neighbouring grain has been previously studied by Read-Shockley *et al* [17]. GBs are described as a disturbed region, associated to an **elastic deformation by the use of a dislocation model**.

II-2.1 Dislocation model and low angle GB description

Historically, the connection between two grains can be provided by an **array of dislocations** [16] (**Figure II- 8**). Since, at dislocation lines, little distortions of the atomic environment (called core dislocations) across the GB are observed, a low energy should be expected for these GBs.

Read and Shockley [17] proposed a model to calculate the formation energy of symmetric tilt low angle GB in simple cubic grains. Distances between etch pits can be compared with their theory knowing the misorientation angle. The dislocation separation D ($D = 2d$ in **Figure II- 8 B**) can be expressed as a function of the misorientation angle θ :

$$D = \frac{b}{2 \sin\left(\frac{\theta}{2}\right)} \approx \frac{b}{\theta} \text{ (eq II-11)}$$

Where b is the Burger's vector of the edge dislocations.

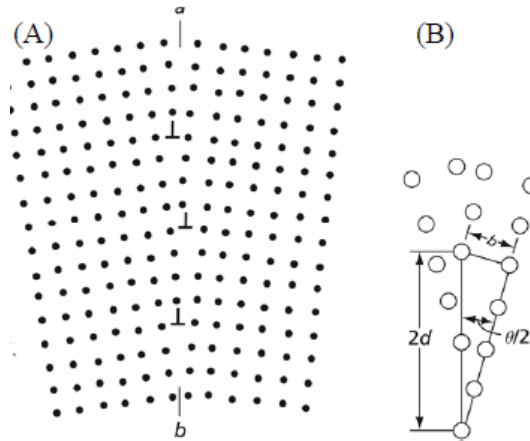


Figure II- 8: (A) Dislocation model of a small-angle GB, (B) The geometrical relationship between θ , the angle of tilt, and d , the spacing between the dislocations[16].

The integration of the elastic density leads to the GB energy which is expressed as:

$$E = \gamma_0 \theta (A - \ln(\theta)) \quad (\text{eq II-12})$$

$\gamma_0 = \frac{G_{\text{shear}} b}{4\pi(1-\nu)}$ is the stress field based on continuum model, as θ increases, the energy E increases.

where G_{shear} is the shear modulus, b is the Burger's vector, and ν is Poisson's ratio for an isotropic material.

$A = 1 + \ln\left(\frac{b}{2\pi r_{d0}}\right)$ is a constant, where r_{d0} is the dislocation core radius.

II-2.2 Limitations of the dislocation model for high angle GB

The dislocation model loses its significance if the corresponding dislocation spacing D is equal to or less than the dimension of the disturbed region of the individual dislocations [16]. A dislocation separation equals to $4b$, represents a reasonable lower limit and restricts the model to GB with low angles: according to **Brandon Criterion** [18] $\theta < 15^\circ$. Above this value, the dislocation model fails because of the too small spacing between lattice dislocations [19]. Dislocations lose their individuality and overlap leading to a rearrangement of dislocation cores that involves the formation of local atomic structures inside the GB.

Figure II- 9 shows that as θ increases, the energy E increases in the region of validity of the dislocation model. A sharply cusped minimum is observed for $\theta=0$ and a maximum energy is reached at $\theta=30^\circ$ which is out the validity domain. This breakdown is often described by a convenient expression which corresponds to a normalization of Read and Shockley formula:

$$E = E_m \frac{\theta}{\theta_m} \left(1 - \ln\left(\frac{\theta}{\theta_m}\right)\right) \quad (\text{eq II-13})$$

The energy E and θ are normalised by optimised constant values E_m and θ_m .

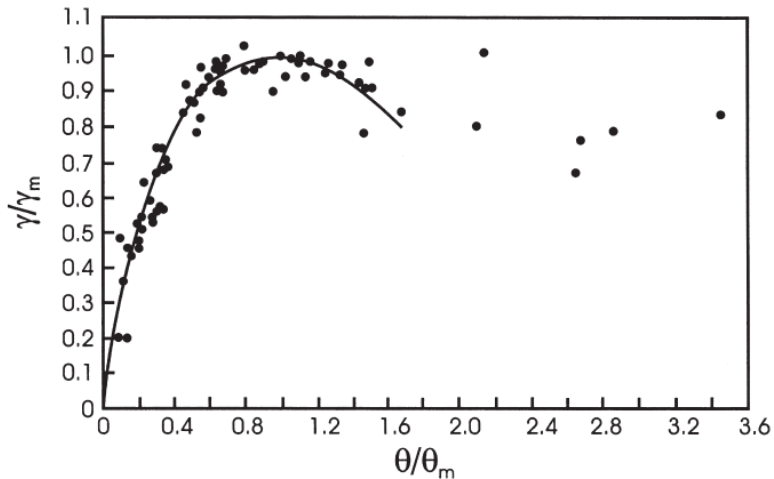


Figure II- 9: Experimental (symbols) and predictions of the Read-Shockley dislocation model for low angle tilt boundaries as a function of misorientation in metals (silicon iron, tin and lead) [20], [21]

There is a good agreement according to **Figure II- 9** between experimental and theoretical results. However, the agreement at large angle (i.e. above Brandon criterion) is probably due to a fortunate correlation of errors. The dislocation model provides an incomplete description of GB: it cannot take into account the atomic reconstructions within the core and the GB plane orientation which is foreseen to happen for large disorientation of the grain. Indeed, θ_m is generally chosen to fit the data at high angle. Finally, the dislocation model fails to predict the low-energy twin boundaries at high angle. Therefore, the **coincidence lattice site (CSL)** model has been used to describe energetic GB properties with an atomistic approach and to model high angle GB which cannot be represented by the dislocation model.

Energetic properties of GB can be described by the dislocation model for low angle GB, but the dislocation model is not adapted to high angle GB because of the overlapping dislocations. Thus, a more general energetic description using the coincidence lattice site (CSL) is usually used.

II-2.3 CSL meaning and relationship with GB energy

The density of the coincidence lattice site parameter is an important GB parameter which has a large influence on its **formation energy**. Indeed, it is assumed that the minimum energy of the system refers to the state of a perfect ordering of atoms in the lattice positions. The **GB energy is thus expected to be low when Σ is low** because the number of broken bonds across the boundary is small. If the interfacial energy is equal to 0 the GB is called a **“singular”** GB ($\Sigma=1$).

Each GB can be composed of a multiplicity of different atomic structures which are related to the arrangement of GB dislocations and can ultimately result in different GB energies and properties. A high angle high Σ GB can be decomposed by a sum of structural units (corresponding to lower Σ). GBs can thus be characterized by repeated **structural units with a small Σ that represents particular arrangements of a limited number of atoms.**

Once the local atomic structure is identified, the atomic structure of GBs can thus be predicted [5]. It gives rise to two classes of boundaries:

- **Favoured boundaries** are composed of a sequence of structural elements (called favoured boundary unit or structural unit) in their ideal undistorted state. The experiments and theoretical results show that low Σ values with a high misorientation angle are composed of favoured structural units [13].
- **Non-favoured boundaries** are composed of a mixture of two different structural units, which at least one distorted favourably boundary unit.

Liu [22] have reported the most relevant structural units present in STGB [100] and [110] in BCC α -iron GB (**Figure II- 10 and 11**).

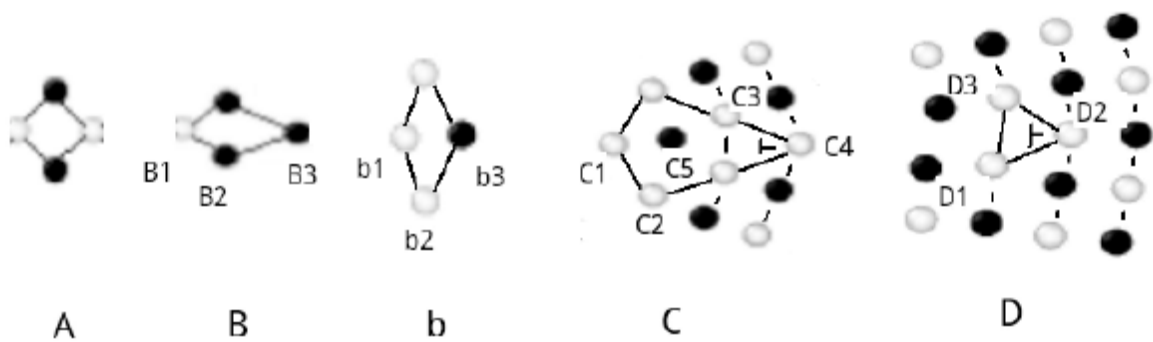


Figure II- 10: Structural units in the [100] STGBs, atomic sites are named by a letter with a number and the dislocations are indicated in Figure II- by Γ [22].

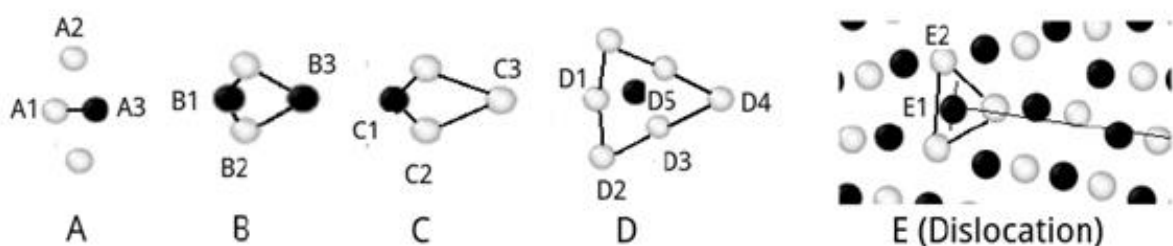


Figure II- 11: Structural units in the [110] STGBs, atomic sites are named and the dislocations are indicated in the Figure II-. The unit E shows the typical environment of dislocations in the high angle STGBs [22]

According to **Rittner and Seidman** [10] fcc STGB Σ 33 can be represented by a sum of Σ 3 (red, symbol D) and Σ 9 (yellow, symbol E) structural units (**Figure II- 12**).

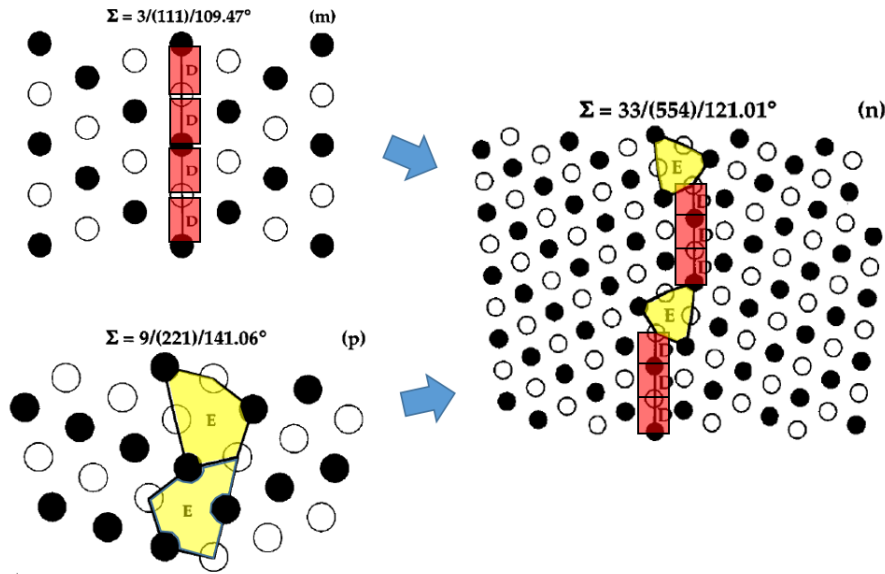


Figure II- 12: High angle GB decomposition into structural units in fcc metals [10]

In general this **structural unit model** is adapted for STGB systems, but may not accurately describe the structures where the dislocations dissociate. High degree of atomic-level coherency is maintained across the boundary but it is sometimes hard to distinguish the structural unit in high angle STGBs. As it is discussed in the previous part, high angle GB energy cannot be described by the **dislocation model**.

“Special” boundary reference structures have been proposed by **Sutton and Vitek** [23] to make a physically meaningful description of high angle GB. This new structure reference can be considered as an invariant plane of simple shear (dislocation free) and provides a more realistic description of the GB dislocation structure. “Special” GBs correspond to low- Σ values with the lowest GB energy. Low GB energy is expected for high density of coincide lattice sites. However, Wolf has defined the most physical parameters governing the energies of “special” (low energy) GB:

- **The spacing of lattice planes parallel to the boundary plane:** the interplanar spacing has to be sufficiently large because of the significant role of the local atomic coordination number in the relaxation process.
- **The area of the CSL unit cell** on the GB plane: this parameter has to be small enough to reach the largest planar atom density and thus the lowest GB energy as possible.

Low- Σ condition is necessary but not sufficient to identify “special” GBs [9].

According to Tschopp *et al* and Liu [13], [22], their experimental and simulation results showed that the evolution of the intergranular energy for symmetric bcc Fe GBs as a function of the misorientation angle is not monotonic (**Figure II- 13**). Since misorientation are directly linked to Σ value, Tschopp *et al* and Liu *et al* results are consistent with Wolf observations. The two strongest cusps in [100] GBs correspond to $36.87^\circ\Sigma(310)$ and $53.13^\circ\Sigma(210)$ GBs, and the strongest cusps in [110] GBs are represented by $70.53^\circ\Sigma(112)$ and $129.52^\circ\Sigma(11(332))$ GBs.

Thus, minimum energy is not only expected at low Σ values as $\Sigma 11(332)$ presents a significant cusp in energy, *i.e.* $\Sigma 3(111)$ is associated to a high GB formation energy in comparison to $\Sigma 11(332)$.

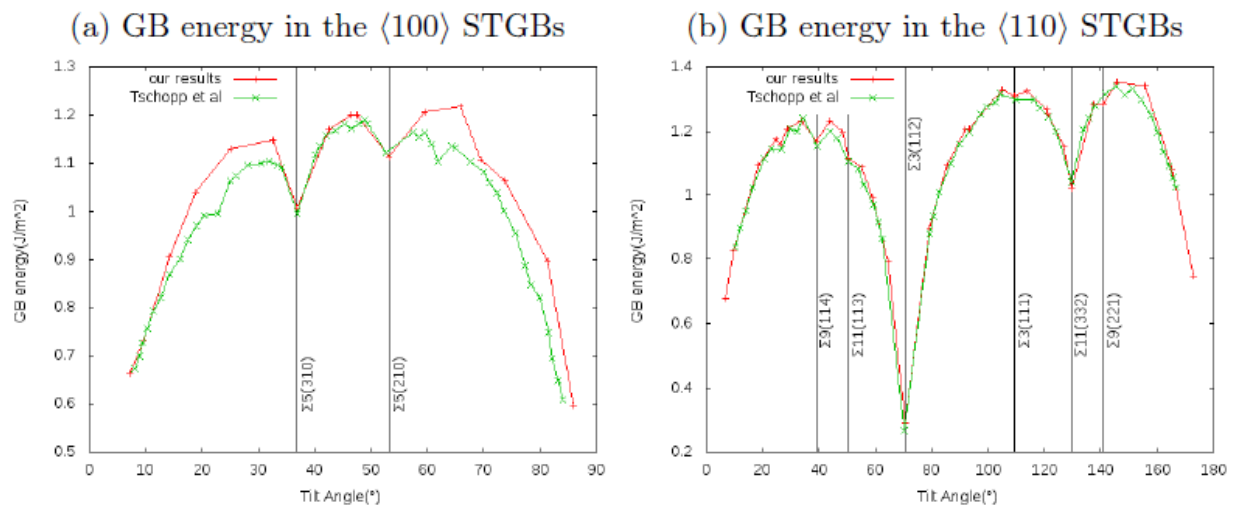


Figure II- 13: Relationship between the misorientation angle and GB energy for (a) [100] and (b) [110] systems. Liu’s results correspond to red line whereas Tschopp’s results refer to green line[22].

The orientation of GB plane has also a non-negligible influence [24]. Hasson *et al* [25] have demonstrated that the interfacial energy depends also on which **GB plane** is chosen. They have shown that $\Sigma 3 \{211\}$ has a higher GB energy than $\Sigma 3\{111\}$. Therefore, general GBs with higher Miller index planes have a higher GB energy. Based on these observations,

A good atomic representation with a structural unit model is expected for GBs that intersect a high density of coincident site lattice points [11]. A symmetric tilt boundary with a normal perpendicular to the misorientation axis should contain a high density of points. It suggests that STGB are energetically favoured over other types of GB [11].

Many studies focusing on STGB with CSL concept try to find a correlation between Σ and the energetic properties of the GB but the relation is not obvious. Structural unit models constitute another approach to describe a GB but its use becomes more and more difficult as Σ increases.

II-3. Atomistic description of GBs

While CSL is commonly used to construct high symmetry GBs, the use of computational methods may provide an **atomistic representation of GB**. Material science database calculations can be coupled to advanced structural descriptors as an alternative to predict and classify the models of target meaningful information and material properties.

II-3.1 Definition of physical descriptors

The crystal representation of GB can be made by **“physical descriptors”** [26] which are related to the elemental and structural atomistic description of the material. In order to represent the chemical environment correctly [27], a descriptor has to fulfil a certain number of criteria: invariant, unique, non-degenerate and continuous. For example, a compound c is represented by a collection of atomic representations N_x , the number of atoms in the unit cell compound is $N_a^{(c)}$ which is transformed into a set of descriptors, as illustrated in **Figure II- 14** [28].

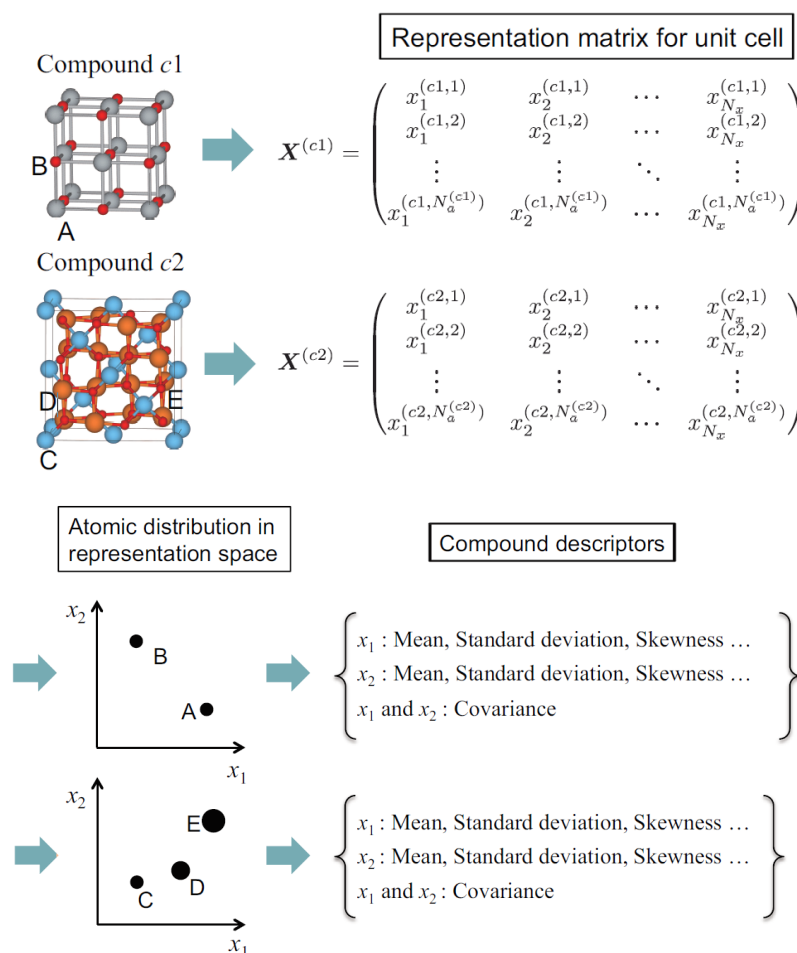


Figure II- 14: Typical generation of physical descriptors [28]

According to Priedemann *et al* [29], an ideal structural descriptor for a GB structure should be:

- easily interpretable
- easily visualized
- invariant with respect to symmetries, rotations and permutations
- able to accommodate structural perturbations
- applicable to GB 3D structure
- able to describe the correlation between interfacial atoms and the structural units
- able to be automated for the characterization of GB
- varying as well as the atomic positions varying

Two types of descriptors have to be distinguished, those leading to a local description of the atomic environment and those involving a more “global” (*i.e.* larger scale than only one atom) description.

The most known common local descriptors follow:

- **The atomic volume** represents a physical quantity easily calculable and permits a description of the GB atomic structure on an atom basis. This quantity is an obvious outcome of Voronoï tessellation. For a set of sites, Voronoï diagram partitions the space based on the minimal distance to each site. Thus, Voronoï polyhedron is determined for each central atom to quantify the volume deformation by the construction of all median plane around a centred atom (**Figure II- 15**) [28], [30].

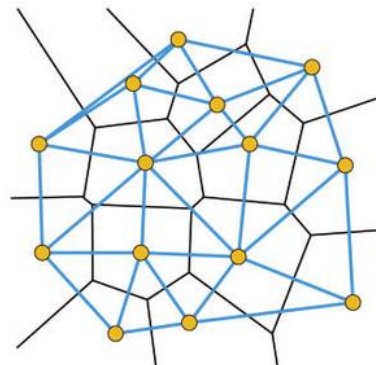


Figure II- 15: Delaunay tessellation is represented in blue lines and Voronoï diagram corresponds to black lines [31]

- **The radial distribution function** is a radial-dependent structural representation. The partial and general radial distribution functions (PRDF and GRDF)[28] describe the neighbour environment of an atom by an histogram pairwise structural representation. The number of counts in each bin for a given cut-off radius corresponds to the structural representation.
- **The bond-orientational order parameter (BOP)** is an angular-dependent structural representation that has been defined by Steindhardt *et al* [32] for liquids and metallic glasses. It relies on quadratic and third-order invariants formed from bond spherical harmonics providing an orientation correlation function. Thus, it is usually employed to determine correlations in the orientations of particle clusters [28].

- **Angular Fourier series (AFS)** [33] is another angular-dependent structural representation. The local environment is described by a system of orthogonal polynomials of the basis invariants, usually chosen as the Chebyshev-polynomials. But this method is limited by the truncated degree of its sum and the number of basis functions that have to be used in order to gain an accurate description of the system.
- **The Atom-Centred Symmetry Function (ACSF)** is a pairwise and angular-dependent structural representation. ACSF describes the local environment near an atom by using a fingerprint composed of the output of two or three body functions that can be adapted to detect structural characteristics of a system. This descriptor gives the chemical environment (distance and angular interactions with neighbour) for each atom in the material separately with symmetry functions. But, this type of descriptor needs a large training set and many symmetry functions, to fit the parameters to a system of interest with the desired sensitivity and accuracy.
- **The Smooth Overlap of Atomic Positions (SOAP)** refers to the **local environment around a central atom** obtained by a fit of Gaussian density distributions smeared around neighbour atoms by pairwise and angular-dependent. This descriptor resulted from an expansion of radial and angular bases including spherical harmonics [33], [34]. This descriptor gives rise to a SOAP vector, which is composed of fitted coefficients coming from Gaussian density fitting. A local atomic environment (LAE) is then defined for each atomic site by this numerical vector. The benefit of this representation is that this method is not specific to a given crystal structure and is invariant to translations, rotations and permutations of atoms. In practice, in order to use SOAP as a scalar descriptor and thus to construct a local representation of each GB site with respect to the one of the bulk, the difference between the SOAP vector characteristic of a site from the bulk \vec{b} and each atom from the GB is calculated \overrightarrow{gb} . This local quantity characterising each GB site, is called SOAP dissimilarity s and is given by:

$$s = \|\vec{b} - \overrightarrow{gb}\| = \sqrt{\vec{b} \cdot \vec{b} + \overrightarrow{gb} \cdot \overrightarrow{gb} - 2\vec{b} \cdot \overrightarrow{gb}} \quad (\text{eq II-14})$$

where \vec{b} corresponds to the SOAP bulk vector and \overrightarrow{gb} corresponds to the SOAP GB vector.

A matrix which contains all coefficients of each GB site can be defined and leads to a quantification of local environmental (elastic) deformations inside the GB.

Other approaches which use SOAP have been developed. Rosenbrock *et al.* [35] use a local average SOAP to form an Averaged SOAP representation (ASR) of Nickel GB. Then, the matrix descriptors are combined to create a representative matrix of the GB. Another method consists in looking for a subset of LAEs in the GB by its proportion of each LAE to get a local environment representation.

However, the use of SOAP descriptors is limited because of the huge computational cost and time consuming that are required to simulate all the GB sites. Indeed SOAP depends on a lot of parameters (local neighbourhood cutoff value and expansion limits for the radial and angular basis functions n_{\max} and l_{\max}) which are related to these computational time and cost limits. The higher the expansion limit for the radial and angular basis function, the higher the accuracy but the higher the computational cost.

“Global descriptors” have been proposed, which represent on a larger scale (usually a group of several atoms correlated by a structural periodicity or an electrostatic interaction) than the local previous descriptors the structural characteristics of a system. They thus give a more general description of the atomic environment:

- **The Coulomb Matrix descriptor (CM)** is a global descriptor, which is represented by a matrix where coefficients are calculated based on the pairwise coulomb repulsion of the nuclei.
- **The many body tensor representation (MBTR)** considers the group interactions by atomic type in a tensor. MBTR encodes the structures by a decomposition of the system in structural units.

GB local structures can be described from an atomistic point of view and can be characterized by physical quantities which are called “descriptors”. The easiest to calculate local atomic descriptor is the atomic volume which quantifies the dilation, or the compression of a given atomic site in a GB. However, many other physical descriptors have been recently proposed but for the most part there are hardly interpretable.

II-3.2 Towards specific iron bcc GB segregation descriptors

These descriptors presented in the previous section may help find correlations between information extracted from the descriptor analysis and segregation properties (binding energy) and thus permit an accurate prediction of GB segregation.

Very little literature about bcc iron descriptors of the segregation process is available [36]. Physical descriptors are often used to describe sets of clusters [26], [33] with different sizes, and the majority of studies test physical descriptors on GBs composed of other metals such as Mg [37], [38], Ni or Cu [39]. For example, Huber *et al* [38] expressed the binding energy and thus the segregation as a function of physical descriptors i.e. coordination number and atomic volume for Al GB, but their calculations have shown this approach does not work all the time and for instance it fails for Pb in Al.

The atomic volume is often used to characterize GB sites. In many studies only the first nearest neighbours are considered and the remaining local space is ignored. This description is, most of the time, too simple to characterize and discriminate local environments and distorted lattices. Indeed, in bcc metals, the distance between the first and second neighbour shell is small. Therefore, GB properties, such as the cohesive energy, elastic constants [28], the atomic density [39] and the centro-symmetry parameter [37] have been tested.

Tschopp *et al.* [37] suggested to use GB properties as descriptors such as the potential energy, the force and the stress-based metrics including hydrostatic stress in the case of the segregation of Al to Mg GBs. However, they found no obvious correlation between these descriptors and the segregation energy. Thus, they tried other GB properties to describe the GB such as the centrosymmetric parameter, coordination number etc. The correlation plot obtained by Tschopp *et al.* [37] descriptors for the segregation of Mg GB is represented in **(Figure II- 16)** :

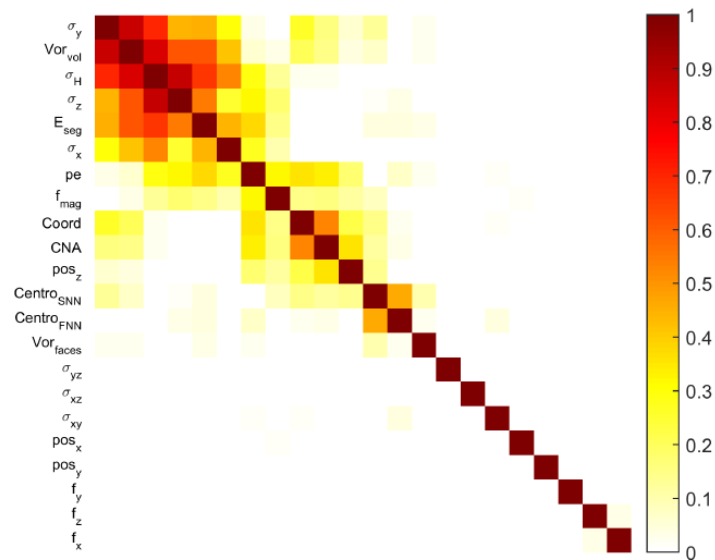


Figure II- 16: Correlation map between segregation energy and other common per atom variables: stress components, force components, atomic volume, centrosymmetric parameter, coordination number, atom coordinates and potential energy [37].

A lot of descriptors are available, and the main difficulty is to find the ones most adapted to the case of GB segregation in bcc iron. Very little literature is available in this specific case and the descriptors that have been tested so far do not display real obvious correlation with segregation energies. Physical descriptors used in machine learning like SOAP are appealing by their adaptability to any crystalline systems, but it must be borne in mind that these descriptors are often difficult to interpret and imply high computational costs.

The GB definition and description will permit to identify the best physical parameters and quantities that characterize GBs and GB segregation. Then the segregation energy can be written as a function of these physical descriptors. A combination of descriptors can be used to improve the accuracy of the prediction model. According to Jäger *et al* [26], learning simultaneously on a lot of different structures leads to a lower mean absolute error. Thus describing GBs and GB segregation with these methods requires a large experimental and computational database to extract macroscopic and atomistic information about GBs and GB segregation. Numerical tools that can be used are already presented in *Chapter I*.

In this work we have used as atomic descriptor:

- **The atomic volume** which represents an handy physical quantity to discriminate atomic configuration with respect to tension or compression atomic site. The bulk part of the GB is found to be constant (about 11.34 \AA^3); variations of atomic volume occur inside the GB therefore, the atomic volume is calculated for GB sites around the GB plane.
- **The centrosymetry parameter (CS)** corresponds to a measure of the local disorder around an atom, allows to distinguish a bulk atom (perfect structure $CS = 0$) from a defect ($CS > 1$ inside the GB). The vector corresponding to the perfect crystal is compared: $CS = \sum_{i=1,4} |R_i + R_{i+4}|^2$ (eq II-15) where R_i and R_{i+4} are the vectors or bonds corresponding to the eight pairs of opposite nearest neighbours in the bcc lattice.
- **The coordination number (CN)** : the number of first and second nearest neighbours.
- **The SOAP**
- **The atomic density**: in this PhD we define such quantity specifically for GB, we define an integration volume which is about one atomic layer (at each $a_0/2$) and is expressed in $\text{atoms}/\text{\AA}^3$. The atomic density is calculated perpendicular to the GB with a step of 0.05 \AA , that's why this atomic density is not null between two atomic layers. The GB density profiles are symmetric with the GB plane, it found to be constant in the bulk part of the GB; the variations of density around the GB plane constitute the signature of a given GB in comparison to the others.

More details about the description of twist GBs constructed during this PhD will be presented in *Chapter III*.

II-4. Conclusion

GBs are commonly described by the **misorientation angle** and the **orientation plane**. STGBs are the most studied GBs and are classified into two main types: LAGB and HAGB which require two different **descriptions**. The first one is the dislocation model for LAGB and the second one is the coincidence lattice site which is appropriate to describe HAGBs. Indeed, this geometrical construction corresponding to a **more general description** is the most used representation and describes the lattice formed by the positions where atoms are in coincidence after a given rotation. This concept gives rise, depending on the plane choice, to tilt and twist GBs. Sometimes **small displacements** of CSL occur. In that case, and to preserve the density of coincidence lattice sites, another representation is used: the DSC lattice. The **structure** of a GB can be also described by a set of repeated **structural units**. However, physical atomistic meaning has also to be introduced in the GB description. The structure can be characterized by physical quantities called "**descriptors**". The **atomic volume** corresponds to the easiest calculable local atomic descriptor, quantifying the dilatation or the compression of a given atomic site. **A lot of other descriptors exist (SOAP, ASF ...)**, the main difficulty being to find the one most adapted to the case of interest. Huber *et al* [30] calculations have shown that expressing the segregation process by the use of descriptors is difficult and does not work for some chemical species, such as Pb in Al. A large amount of data that can be obtained from experiments and simulations is needed to precisely describe GBs.

II-5. Bibliography

- [1] V. Randle, *The Measurement of Grain Boundary Geometry*. 1993.
- [2] H. Gleiter et B. Chalmers, « High-Angle Grain Boundaries », in *Progress in Materials Science*, Pergamon Press., vol. 16, Oxford, 1972, p. 1-272.
- [3] P. Lejcek, « Grain Boundaries: Description, Structure and Thermodynamics », in *Grain Boundary Segregation in Metals*, 2010.
- [4] M. Herbig *et al.*, « Grain boundary segregation in Fe-Mn-C twinning induced plasticity steels studied by correlative electron backscatter diffraction and atom probe tomography », *Acta Materialia*, vol. 83, p. 37-47, 2015.
- [5] R. C. Pond et V. Vitek, « Periodic grain boundary structures in aluminium I. A combined experimental and theoretical investigation of coincidence grain boundary structure in aluminium », *Proceedings of the Royal Society of London B*, vol. 357, p. 453-470, 1977.
- [6] J.-M. Zhang, Y.-H. Huang, X.-J. Wu, et K.-W. Xu, « Energy calculation for symmetrical tilt grain boundaries in iron », *Applied Surface Science*, vol. 252, p. 4936-4942, 2006.
- [7] A. D. Rollet, « Grain Boundary Engineering & Coincident Site Lattice (CSL) Theory », présenté à MSE, Texture, Microstructure & Anisotropy, 2016.
- [8] A. D. Rollett et S. R. Wilson, « Rodrigues vectors, unit Quaternions », présenté à MRSEC, 2015.
- [9] D. Wolf, « ON THE RELATIONSHIP BETWEEN SYMMETRICAL TILT, TWIST, "SPECIAL", AND "FAVORED" GRAIN BOUNDARIES », *Journal de Physique Colloques*, vol. 46, p. C4-197-C4-21, 1985.
- [10] J. D. Rittner et D. N. Seidman, « $\langle 110 \rangle$ symmetric tilt grain-boundary structures in fcc metals with low stacking-fault energies », *Physical Review B*, vol. 54, p. 7000-7015, 1996.
- [11] A. P. Sutton et R. W. Balluffi, « Overview no. 61 On geometric criteria for low interfacial energy », *Acta Metallurgica*, vol. 35, p. 2177, 1987.
- [12] M. Rajagopalan, M. A. Tschopp, et K. N. Solanki, « Grain boundary segregation of interstitial and substitutional impurity atoms in alpha-iron », *JOM*, vol. 66, p. 129, 2014.
- [13] M. A. Tschopp et K. N. Solanki, « Probing grain boundary sink strength at the nanoscale: Energetics and length scales of vacancy and interstitial absorption by grain boundaries in α -Fe », *Physical Review B*, vol. 85, p. 064108, 2012.
- [14] M. Yamaguchi, « First-Principles Study on the Grain Boundary Embrittlement of Metals by Solute Segregation: Part I. Iron (Fe)-Solute (B, C, P, and S) Systems », *Metallurgical and materials transactions A*, vol. 42A, p. 319-329, 2010.
- [15] V. Randle, « "Five-parameters" analysis of grain boundary networks by electron backscatter diffraction », *Journal of Microscopy*, vol. 22, p. 69-75, 2005.
- [16] N. H. Fletcher, « Crystal Interface Models - A Critical Survey », *Advanced Materials Research*, vol. 5, p. 281-314, 1971.
- [17] W. T. Read et W. Shockley, « Dislocation Models of Crystal Grain Boundaries », *Physical Review*, vol. 78, p. 275, 1950.
- [18] D. G. Brandon, « The structure of high-angle grain boundaries », *Acta Metallurgica*, vol. 14, p. 1479-1484, 1966.
- [19] S. Amelinckx et W. Dekeyser, « The Structure and Properties of Grain Boundaries », *Solid State Physics*, vol. 8, p. 325-499, 1955.
- [20] W. T. Read, *Dislocations in crystals*, McGraw Hill. G. P. Harnwell, 1953.
- [21] A. D. Rollet, F. J. Humphreys, G. S. Rohrer, et M. Hatherly, « Chapter 4: The structure and energy of grain boundaries », in *Recrystallization and Related Annealing Phenomena*, Australia, 2004.
- [22] Z. Liu, « Molecular Static Simulation: Grain Boundary Absorption of Point defects and Phosphorus solute in alpha-Fe », 2014.
- [23] A. P. Sutton et V. Vitek, « On the Structure of Tilt Grain Boundaries in Cubic Metals I. Symmetrical Tilt Boundaries », *Philosophical Transactions of the Royal Society of London. Series A*, vol. 309, p. 1-36, 1983.
- [24] L. Priestler, « Geometrical speciality and special properties of grain boundaries ». 1989.

- [25] G. C. Hasson, J. B. Guillot, B. Baroux, et C. Goux, « Structure and energy of Grain Boundaries: Application to symmetrical Tilt Boundaries around [100] in Aluminium and Copper », *Phys. stat. sol. (a)*, vol. 2, n° 3, p. 551, 1970.
- [26] M. O. J. Jäger, E. V. Morooka, F. F. Canova, L. Himanen, et A. S. Foster, « Machine learning hydrogen adsorption on nanoclusters through structural descriptors », *nature partner journals Computational Materials*, vol. 4, n° 1, p. 1-8, 2018.
- [27] A. P. Bartok, R. Kondor, et G. Csanyi, « On representing chemical environments », *Physical Review B*, p. 184115, 2013.
- [28] A. Seko, A. Togo, et I. Tanaka, « Chapter 1 Descriptors for Machine Learning of Materials Data », in *Nanoinformatics*, I. Tanaka., 2018.
- [29] J. L. Priedeman, C. W. Rosenbrock, O. K. Johnson, et E. R. Homer, « Quantifying and connecting atomic and crystallographic grain boundary structure using local environment representation and dimensionality reduction techniques », *Acta Materialia*, vol. 161, p. 431-443, 2018.
- [30] L. Huber, R. Hadian, B. Grabowski, et J. Neugebauer, « A machine learning approach to model solute grain boundary segregation », *nature partner journals Computational Materials*, vol. 64, p. 1-8, 2018.
- [31] W. Zhou et H. Yan, « Alpha shape and Delaunay triangulation in studies of protein-related interactions », *Briefings in Bioinformatics*, vol. 15, p. 54-64, 2012.
- [32] P. J. Steinhardt, D. R. Nelson, et M. Ronchetti, « Bond-orientational order in liquids and glasses », *Physical Review B*, vol. 28, p. 784, 1983.
- [33] A. P. Bartok, R. Kondor, et G. Csanyi, « On representing chemical environments », *Physical Review B*, vol. 87, p. 184115, 2013.
- [34] J. Schmidt, M. R. G. Marques, S. Botti, et M. A. L. Marques, « Recent advances and applications of machine learning in solid-state materials science », 2019.
- [35] C. W. Rosenbrock, E. R. Homer, G. Csanyi, et G. L. W. Hart, « Discovering the building blocks of atomic systems using machine learning: application to grain boundaries », *nature partner journals Computational Materials*, vol. 3, n° 29, p. 1-7, 2017.
- [36] F. Nielson, « Understanding Grain Boundaries Through Machine Learning in Regards to Hydrogen Embrittlement of Steel », 2018.
- [37] M. A. Tschopp, J. Kaushik, et S. Chaudhuri, « Coupling Molecular Dynamics and Machine Learning for Predicting Aluminium Segregation to Magnesium Grain Boundaries », 2018.
- [38] L. Huber, J. Rottler, et M. Militzer, « Atomistic simulations of the interaction of alloying elements with grain boundaries in Mg », *Acta Metallurgica*, vol. 80, p. 194-204, 2014.
- [39] S. Kiyohara, T. Miyata, et T. Mizoguchi, « Prediction of grain boundary structure and energy by machine learning », *arXiv*, 2015.

Chapter III: development of atomistic methods to construct twist GB

In complex materials containing more than one element, grain boundaries are usually decorated by solutes: solute segregation influences quite significantly the macroscopic properties; thus, it has been the subject of a large literature. Detrimental effects induced by this segregation process can reduce the toughness and ductility of a material. This type of embrittlement and the contributing role of certain alloying elements have been a subject of research for several decades [1] [2]. P remains the main impurity in ferritic low-alloy steels causing temper embrittlement resulting from segregation of phosphorus and other impurities. Its concentration in ferritic steels is strictly controlled [3], and intensive studies were conducted on its segregation process for a better understanding [4]–[6].

A detailed knowledge of the energy and microstructure in GBs is important for understanding phosphorus segregation. Tilt GBs have been extensively studied by simulation in α -iron [2], [3], [7]–[11] but very few are about twist (001) GBs [12], [13] in α -iron. Numerous investigations have been conducted in order to study twist GBs, in particular for face-centered cubic (fcc) metals [14]–[21] and a lot of studies [22]–[25] [26] for the body-centered cubic (bcc) metals but atomic researches are mainly focused on low-angle twist GB with an hexagonal dislocation network [23], [24]. McEniry *et al* [27] and Yang *et al* [22] developed atomic studies on (110) α -iron twist GB, however, literature on specific (001) GBs in α -bcc iron are relatively rare. Runnel *et al* [12] who developed an explicit model for the interfacial energy in crystals taking into account the geometric origin of the cusps in the energy profile have obtained some results about (001) twist GB in α -iron. It is the only study which focuses on (001) twist GB in α -iron with Wolf *et al* [13] simulations on twist GBs with Johnson *et al* [28] potential and Wang *et al* [29] DFT results on $\Sigma 5$ GB.

In this context, we will pay a particular attention on these twist GBs in this chapter. The main purpose of this section is to describe the methodology that we developed to construct bcc (100) twist GB in α -iron. The chapter is organized as follows: in Section 1, a brief literature overview of the approaches that have been developed over the past 30 years is presented. In Section 2, the methods we developed to construct ground state structures of twist GB is described. In Section 3, the generated GBs we obtained are analysed in terms of energy and microstructure in comparison with the literature. The study of P segregation on these generated GBs is developed in the next chapter.

III-1. Atomistic construction of GBs, literature overview

To investigate GB atomic properties, numbers of computational studies have been carried out over the past 30 years. In order to examine multiple starting configurations, most of them employed static relaxations, which are achieved by a conjugate-gradient minimization. This method is not the most sophisticated approach to find the best energy minimum, but it constitutes a low cost method in terms of computational time which permits to perform large number of GB calculations. The significance of analysing a high number of starting configurations has been identified by Tschopp and McDowell [30]. Furthermore, the majority of these studies represented the GB by a supercell with periodic boundary conditions (PBC), there are two possibilities:

- 2D PBC: parallel to the GB plane
- 3D PBC: perpendicular and parallel to the GB plane.

These representations are illustrated in the next subsection (**Figure III- 1**).

The search of relevant GB parameters that can be adjusted to find the best ground state structure has been examined in many studies. It turns out that the two main parameters that permit to approach the ground state structure are:

- The displacement of atoms through a translation of the upper part of the GB parallel to the GB plane.
- The density of atoms near the GB plane

III-1.1 GB representations

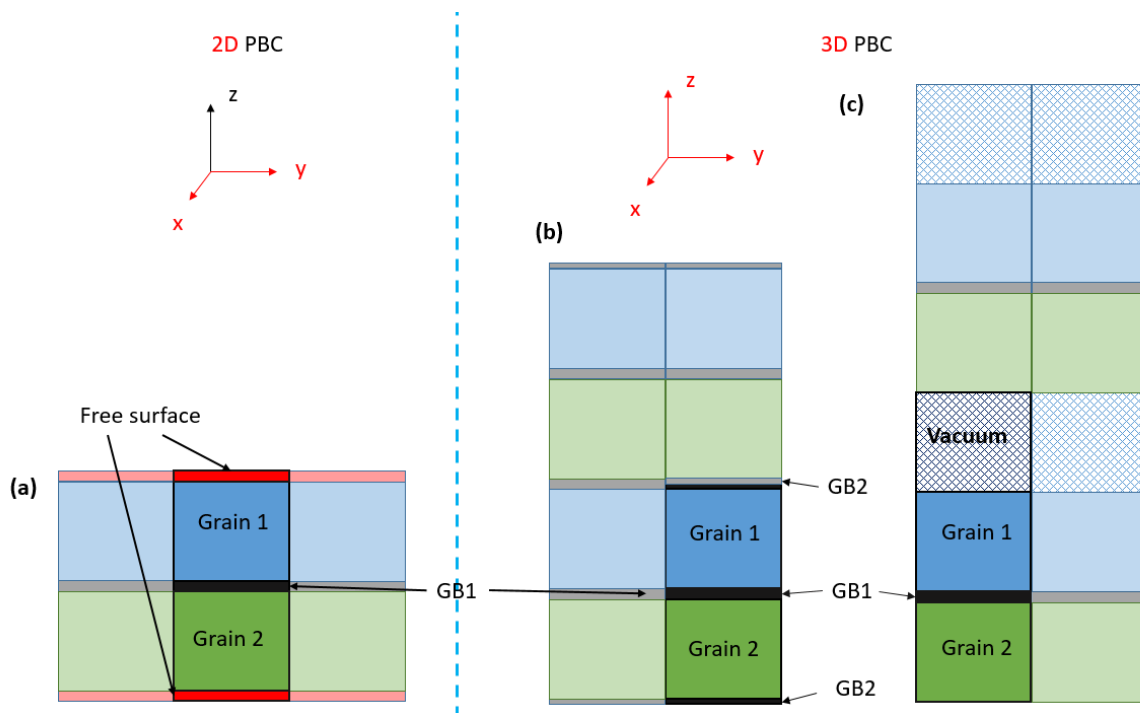


Figure III-1: Supercell that can be used to represent GBs in atomistic simulations. PBC are indicated by red axis. The periodicity is represented with transparent color.

III-1.1.1 2D PBC

2D PBC are often used [31]–[43](**Figure III- 1a**) : PBC are fixed in directions parallel to the GB plane and free to the direction perpendicular to the GB plane (no PBC were applied in the direction normal to the GB plane), resulting in the formation of two free surfaces on the top and the bottom of the simulation cell forming a bilayer.

The GB is sandwiched between two grains composed of two parts: a part contain free (dynamic) atoms adjacent to the GB, which are able to move under interatomic forces, and another part corresponding to the rest of the atoms which are fixed [31] in order to avoid surface relaxation. This latter region serves to represent lattice regions far away from the GB. The other regions (adjacent to the GB) can still move relative to each other in the direction parallel to the GB plane to accommodate the relative translation of the grains and in the direction perpendicular to the GB plane to accommodate the volume expansion. However, this type of GB representation can lead to elastic deformation in those regions adjacent to the GB and introduce stress parallel to the GB plane.

III-1.1.2 3D PBC

A majority of studies [9], [29], [44]–[51] used a cell containing a bi-crystal with three-dimensional periodic boundary conditions to represent tilt and twist GBs. A supercell with two GBs can be created using 3D PBC: GB bisects the bicrystal at its center, due to the PBC the supercell contained two GBs (**Figure III- 1b**). To perform correct simulations, the computational cells must be large enough to prevent interaction between the two parallel boundaries and other finite size effects. However, because of the fixed distance between the two GBs in the starting configurations, the grains may not be at the equilibrium distance and might introduce stress in the cell.

In order to avoid this problem, more recently other studies carried out by Scheiber *et al* [52], [53] has used and validated another 3D PBC representation for GBs. They used a simulation cell with only one GB at its center, two free surfaces on the top and the bottom of the two grains constituting the bi-crystal and vacuum on top of the supercell (**Figure III- 1c**). This type of representation refers to the “*slab mode*” [54], illustrated in **Figure III- 2**. This structural model is commonly used to determine the thermodynamic, kinetic and electronic properties of surfaces and interfaces.

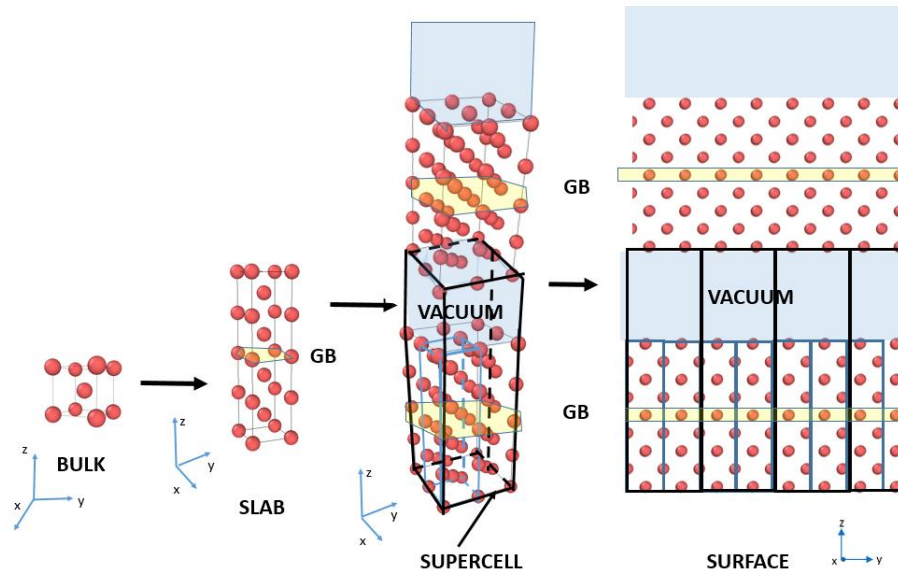


Figure III-2: “slab model” modelling GB. It consists of a thin film limited by two surface planes. The film is formed by a few atomic layers parallel to the (hkl) crystalline plane of interest with a finite thickness, large enough to minimize surface-surface interactions and recover a bulk-like interior. This film corresponding to a surface is constructed using a slab placed within a supercell separated from its periodic images by a vacuum layer thick enough to avoid interaction between two sides of the slab. For sufficiently thick slabs and thick vacuum layer, this kind of model can provide a faithful description of interfaces such as GBs.

The relaxation of the GB distance is absorbed by the vacuum. According to Scheiber *et al* study [52], the thickness necessary to converge the GB formation energy is lower (about 30 Å) than the other methods presented previously (between 40 to 80 Å), thus a least computational effort for a converged result is needed for this representation. Therefore, this setup with vacuum has been identified as the most convenient setup for GB simulations. In this work, this defines our reference configuration (more details are given in section III-2).

III-1.1.3 No PBC

Other methods not considering periodic boundary conditions can also allow modelling GBs. Li *et al* and Yang *et al* [55], [56] used a spherical cell with free surface composed of two hemispherical grains with the same size but different orientations to represent the GB. The advantage of this method is that it does not require adjustment of the sphere size to match periodic lattice lengths, thus it is applicable to arbitrary GBs. However, this representation suffers from surface GB-interaction on the computed GB energy. Despite these differences in terms of GB representation, their conclusions concerning the most influencing parameters on the GB energies which are developed in the next section, are close to studies using a cell with periodic boundary conditions.

III-1.2 Translations parallel to the GB plane and deletion of overlapping atoms

Number of authors have identified that making a translation parallel to the GB plane in tilt and twist GB can affect GB properties. Belov *et al* [33] have identified by MD simulations the significance of rigid body translations applied parallel to the GB plane in twist GB in silicon: alternative reconstructions involving conventional structural units can occur. Translations can change the stacking sequence present in FCC material.

Studies carried out by Wolf [13], [57], [58] in BCC GBs (tilt, twist and asymmetrical GBs in Fe and Mo) confirmed this tendency: they showed that the energy and other atomic physical descriptors (coordination and related volume expansion) are strongly sensitive to the potential translations parallel applied to the GB plane.

Zhang *et al* [18], [59] also reported the effect of translations applied along directions parallel to the GB plane in twist FCC GB in Cu, Ag and Al, on GB energy. They underlined that translation parallel to the GB plane causes a periodic energy variation. This variation of energy is usually minor and the choice of the translation vector along an edge or along the diagonal of the CSL seems to rarely influence this energy variation. However one exception concerns the $\Sigma 5$ (001) Ag GB with a significant variation of energy, about 0.15 J/m², for translations along an edge of the CSL compared to the variation of energy of all other GBs tested to the energy variation for diagonal translation (about 0.035 J/m²).

Olmsted *et al* [41], in order to represent all the possible non-equivalent configurations of tilt and twist GBs in FCC metals (Ni and Al), have developed a method based on these previous translation effect observations. GBs are constructed by translating one of the grain relative to the other by the vectors in a primitive cell of the DSC lattice and by removing from the system overlapping atoms i.e. if two atoms are within a critical distance, one of these atoms is deleted. The necessity of removing atoms is indicated in a number of studies concerning FCC metals: in Yin *et al* [47] FCC twist GB simulations, in Tschopp and McDowell [49], [50] Cu and Al FCC GB construction. Zheng *et al* [48] have used similar method more recently for BCC Mo and Nb tilt and twist GBs, however they observed only small contributions of the initial translation in the variation of the final formation energy of GBs. They observed variations below 0.05 J/m². The largest energy difference is noted for $\Sigma 5$ (013) twist GB of Mo.

This approach consisting in translating one of the grain relative to the other referred often to the γ surface method: the two misoriented perfect half crystals are joined together, while sampling relative translations of the grains. GB structures obtained are then statically relaxed, the atoms in the GB plane fall into a local minimum, which finishes the construction. This technique is relatively computationally inexpensive and often predicts the ground state structure. That's why it is the most common general approach to generate a large number of distinct grain boundary states with different energy that correspond to translation vectors. This technique has been extensively used in BCC materials (Mo, Fe and Ta) for tilt, twist and asymmetrical GBs [9], [13], [46], [52], [53], [57], [58], [60], [61].

The displacement of the atoms of the upper part of the GB along a direction perpendicular to the GB plane can also be done in addition to the parallel contribution usually used in the γ method. Indeed, Wang *et al* [29] added this displacement contribution along the perpendicular direction of the GB plane on the upper part of the GB to construct twist GB in α -Fe to perform DFT calculations.

III-1.3 GB density variation

Recently, several studies about the determination of phase transition of tilt GBs in FCC metals reported that the variation of atomic density in the GB, plane must be considered as an additional thermodynamic parameter which may involve structural transformations that can be described in terms of the structural unit model [62]. The addition or removal atoms from the GB can often involve lower GB formation energy. This variation of the GB energy as a function of the density of GB plane seems to be a general feature for tilt GBs. Number of studies in FCC Cu, Al and Ag, reported these trends and used these features to predict all possible GB structures [34], [36]–[40], [43], [63]. Only few studies concern BCC materials [35], [46], [60], [64] and they are focused on the study of tilt GBs.

Hicknam and Mishin [63] and Frolov *et al* [36]–[38], [40] have constructed a dataset of tilt GBs in FCC Cu using translations and variation of atomic density. In contrast to the γ method, the number of atoms in one plane of each adjacent crystals is not fixed, thus many potentially lower energy structures with different atomic density can be sampled with this grand-canonical approach. The reference GB is translated by random translation vectors of the upper grain relative to the lower, then N atoms are randomly deleted from the GB plane to explore an important number of GB phases from the GB phase space. More recently, Frolov *et al* [35], [39] used an evolutionary algorithm [35] on tilt BCC tungsten based on the USPEX crystal structure prediction code [65] to generate GBs structures. This code permits to perform an evolutionary grand canonical search of microstructural feature of a material i.e. GB. The search allows an automated exploration of GB structures with variable number of atoms and variable cell sizes. The tool generates a population of GB structures and improves them over several generations to predict low energy configurations. Phase transitions of the generated GB structures at high temperatures are then studied by performing MD simulations.

The significance of the density in the decrease of GB energy depends on the choice of the GB plane. Frolov *et al* observed that γ -method is sufficient for [001] tilt GB in Cu but not for [110] tilt GBs in which the addition of atoms leads to a prediction of many metastable states degenerated in energy corresponding to different interstitial positions.

Note that GB density variation methods have been applied according to the literature only to tilt GBs.

III-1.4 Melt and quench (MQ)

Alfthan *et al* [42] chose another approach to construct twist grain boundaries in Si by MD calculations. First, a certain number of atoms from the reference structure within the slab are removed and then the remaining atoms are melted at 3000 K during 100 ps and immediately quenched during at least 20 ns. The authors observed that the application of a melt and quench, which are orders of magnitude longer than methods have been performed before in the literature, allows sampling adequately the configurational phase space and seems to locate more easily than other studies the global energy minima.

From these studies, the γ method appears to be the only method efficient to construct tilt and twist GBs. Even if other methods have been developed that include varying the density around the GB plane, the reliability of these methods are confirmed only for tilt grain boundaries and most of the studies concern FCC materials (see Table III- 1 that summarizes all the influent parameters in atomistic studies). Twist GBs are composed of a network of screw dislocations and have thus a more complex energy landscape compared to the energy landscape created by edge dislocations in tilt GBs [66]. It is probably because of this complexity, that, apart from the γ method, no method has been developed to find the ground state of twist GB. In this context, a study of GB parameters that influence GB energy have been carried out in the specific case of twist GBs in order to then, based on these observations, develop a more efficient method than the γ method.

Authors	Material	Type of GB	Simulation method	γ -method	Remove overlapping atoms	Atomic density	MQ
Rittner <i>et al</i> [44]	FCC	Tilt	MS (EAM)	X			
Belov <i>et al</i> [33]	FCC Si	Twist	MS (EP)	X			
Wolf <i>et al</i> [13], [57], [58]	BCC Fe and Mo	Tilt, twist and asymmetric	MS (EAM and LJ)	X			
Zhang <i>et al</i> [18], [59]	FCC Cu, Ag and Al	Twist	MS (EAM)	X			
Scheiber <i>et al</i> [52]	BCC Mo, Fe and W	Tilt, twist $\Sigma 5$ (001)	MS (2NN-EAM), DFT	X			
Scheiber <i>et al</i> [53]	BCC Mo	Tilt	DFT	X			
Wang <i>et al</i> [29]	BCC Fe	Tilt and twist	DFT	X + Translation normal to the GB plane			
Zheng <i>et al</i> [48]	FCC and BCC materials	Tilt and twist	DFT	X + Translation normal to the GB plane			
Olmsted <i>et al</i> [41]	FCC Ni and Al	Twist	MS (EAM)	X (DSC lattice)	X		
Yin <i>et al</i> [47]	FCC Al	Twist	MS (EAM)	X	X		
Rajagopalan <i>et al</i> [9]	BCC Fe	Tilt	MS (EAM), DFT	X	X		
Tschopp <i>et al</i> [46]	BCC Fe	Tilt	MS (EAM Mendeleev [67] <i>et al</i>), DFT	X	X		
Tschopp <i>et al</i> [50]	FCC Cu and Al	Tilt	MS (EAM)	X	X		
Tschopp <i>et al</i> [49]	FCC Cu and Al	Tilt	MS (EAM)	X	X		
Hahn <i>et al</i> [61]	BCC Ta	Tilt	MS (EAM)	X	X		
Yu <i>et al</i> [43]	FCC Cu	Tilt	MS (EAM)			X	
Yesiltepe <i>et al</i> [60]	BCC Mo	Tilt	MS (MGPT [68])	X (DSC lattice)		X	
Hickman and Mishin [63]	FCC Cu	Tilt	MS (EAM)	X		X	
Frolov <i>et al</i> [40]	FCC Cu	Tilt	MS (EAM)	X		X	
Frolov <i>et al</i> [37]	FCC Cu	Tilt	MS (EAM)	X		X	
Frolov <i>et al</i> [36]	FCC Cu Ag	Tilt	MS (EAM)	X		X	
Frolov <i>et al</i> [35]	BCC W	Tilt	MS (EAM)	X		X	
Meiners <i>et al</i> [39]	FCC Cu	Tilt	MS (EAM)	X		X	
Zhu <i>et al</i> [34]	FCC Cu	Tilt	MS (EAM)	X		X	
Von Alphan <i>et al</i> [42]	FCC Si	Twist	MS (TS)	X	X		X

Table III- 1: Summary of the influent parameters that have been used in atomistic studies from literature. Studies which used the same potential as this thesis are coloured in blue.

III-2. Development of effective methodologies to construct twist GBs in α -iron

III-2.1 Computational details

The atomic configurations of GBs presented in this work have been obtained using molecular statics (MS) and empirical potentials as well as first principles techniques. In a first step, MS is used to construct and approach rapidly the lowest energy of the GB i.e. due to its low computational time cost, the use of EAM potentials allows to make rapidly a large number of calculations and thus, browse a large configuration space.

As described in *Chapter I* in *section I-1.3.1*, in this thesis, the DYMOKA code [69] has been used to relax on GB structures with EAM potentials. In this work, GBs are constructed with Fe-P Ackland *et al.* [70] empirical many-body potential which is adapted to study GBs and its P segregation in low alloy α -iron steels. This potential which has been produced by fitting to first-principles calculations has been used in many studies concerning P-Fe interaction and diffusion in alpha Fe matrix and GB [71]–[76]. It is considered as the best EAM for dilute Fe-P system [77]: this single potential takes into account Fe and P atoms together, in contrast to the older Fe-Fe potential and Fe-P Morse pairwise potential used in other studies [78], [79]. Nevertheless, Ackland *et al* [70] did not consider covalent bonds between phosphorus. This potential can be used to the study of point defects in bcc iron and their interactions with phosphorus atoms. With this potential, pure phosphorus compounds and phosphorus compounds cannot be treated [3].

GBs generated with Ackland *et al* potential [70] are then compared with GBs relaxed with Marinica *et al* potential [80], [81] for α -iron in order to make a first validation of one of the two twist GB construction methodology we have developed.

All these results obtained with empirical potentials will be only meaningful if the potentials are “good” [71]. That’s why in a second step, the configurations obtained are relaxed using DFT as implemented in the Vienna ab initio simulation package (VASP).

III-2.2 Grain boundary construction methodologies

III-2.2.1 Simulation box settings

III-2.2.1.1 Validation of the supercell model

As introduced in section III-1., different setups of supercells can be used to study GB properties. Usually, supercells with 3D PBC, containing two GBs are used. However, in this work, we use a simulation cell with 3D PBC with one GB, two free surfaces and vacuum on top [52]. We also checked that these two approaches led to equivalent properties. DFT calculation were performed on tilt GBs in α -iron contained one GB and two GBs. The binding energy of P with different GBs remains the same whatever the setting used, within the DFT accuracy limit as shown on **Figure III- 3**.

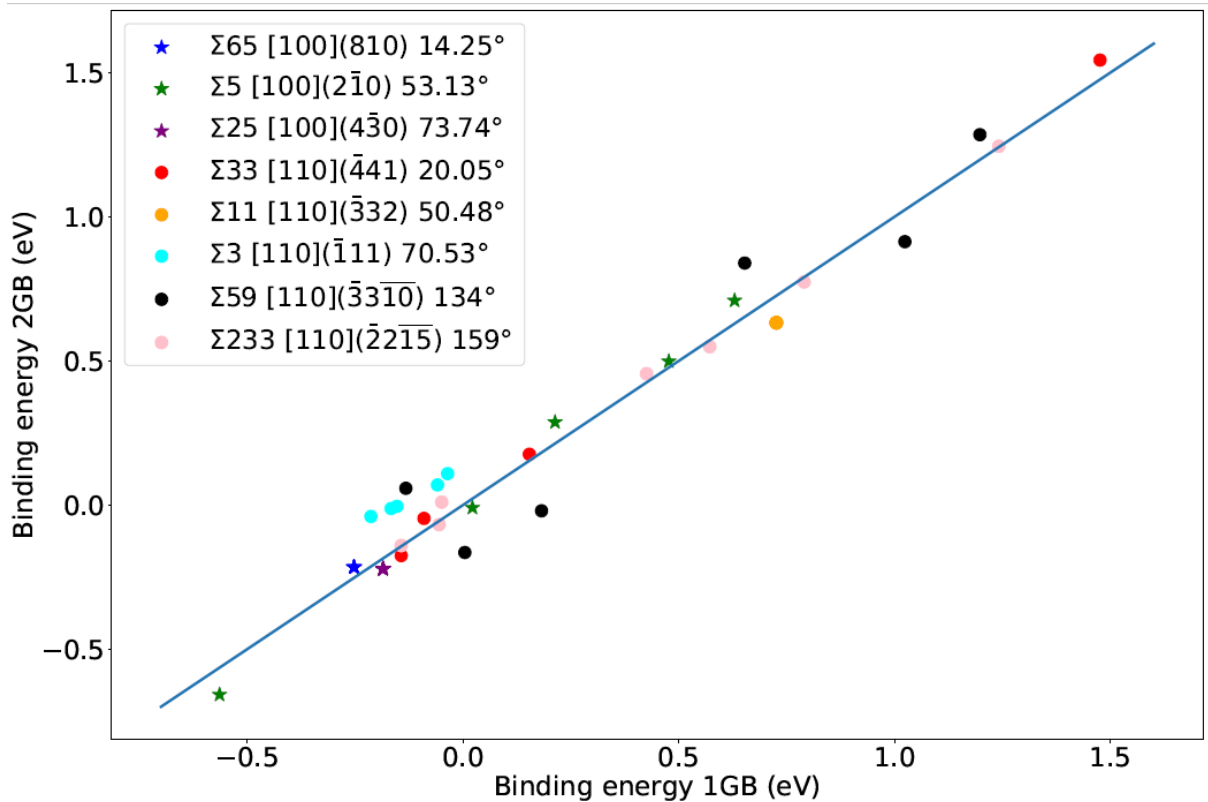


Figure III-3: Comparison of phosphorus binding energy with GB, between supercells containing one and two tilt GBs.

The microstructures represented as a function of the atomic volumes are also equivalent, as shown on **Figure III- 4**.

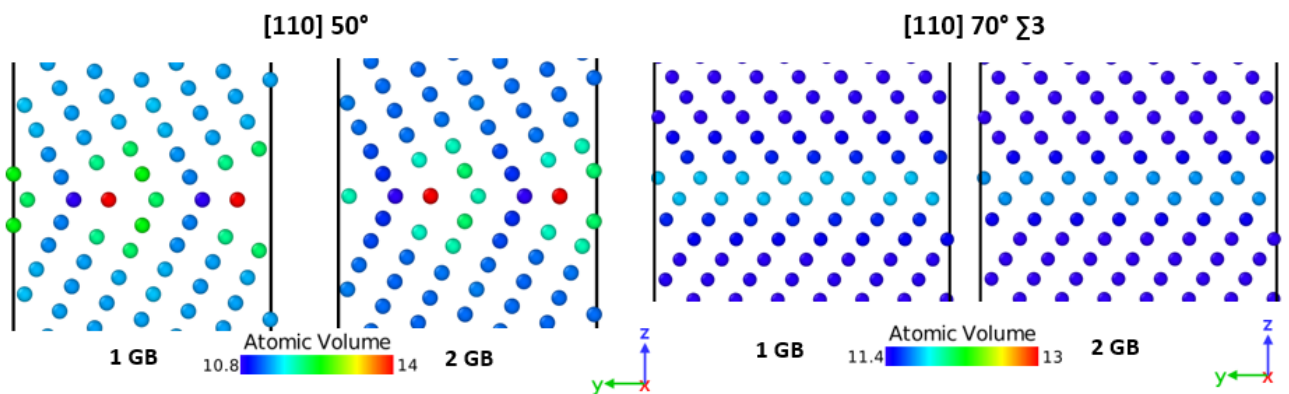


Figure III-4: Microstructure comparison between supercells containing one and two tilt GBs. The color indicates the atomic volume.

III-2.2.1.2 Construction of twist GBs

The GBs were constructed considering mirror symmetry for bi-crystals and using the standard Coincidence Site Lattice method (CSL) illustrated on **Figure III- 5** [82]. One grain of bcc Fe is rotated against the other grain around the common [100] axis by angles determined as follows to preserve the translation invariance along X and Y:

$$\theta = 2 \arctan \left(\frac{n}{\sqrt{2}m} \right) \text{ (eq III-1)}$$

where (m,n) are the coordinates of the superimposed points considering that a coincident site is located at (0,0), m is measured parallel to the mirror plane and n perpendicular to the mirror plane.

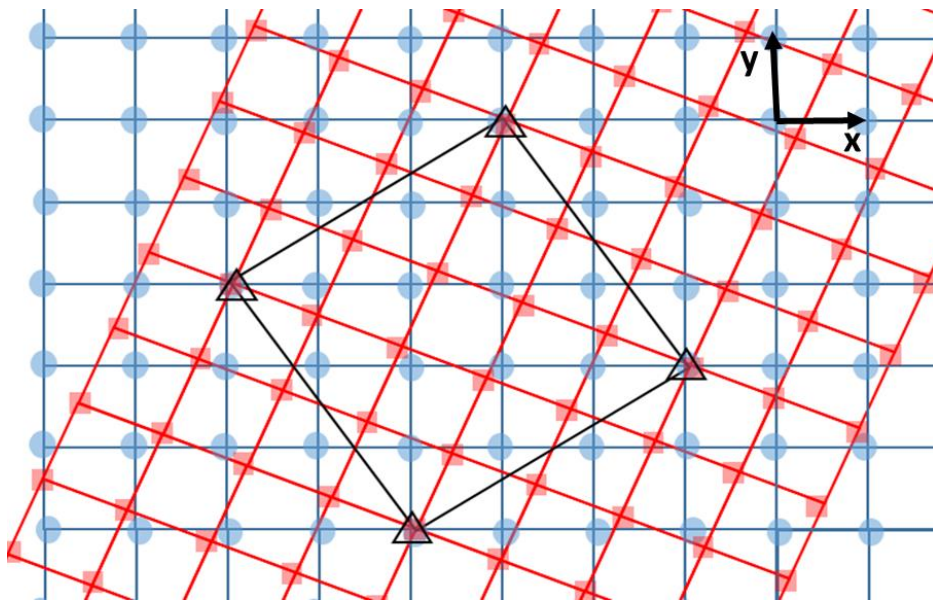


Figure III-5: Illustration of $\Sigma 13$ twist CSL projected along the [001] direction. The blue and red colors correspond to the two crystals and the coincidence sites are indicated in black.

The twist GB characteristics used in this paper are summarized in **Table III- 2**.

Grain boundary	θ°	Box dimensions (nm ³)
$\Sigma 37100$	18.92	1.722 x 1.722 x 5.096
$\Sigma 13100$	22.62	1.444 x 1.444 x 5.096
$\Sigma 17100$	28.07	1.167 x 1.167 x 5.096
$\Sigma 5100$	53.13	1.266 x 1.266 x 5.096
$\Sigma 29100$	43.60	1.525 x 1.525 x 5.096
$\Sigma 25100$	73.74	1.456 x 1.456 x 5.096

Table III- 2: Characteristics of the twist GBs that have been characterized in this study: misorientation angle θ° and box size.

The thickness of the GB must be sufficiently large to avoid interactions between the surface and the GB plane. In this work, the thickness of the box is 5.096 nm which corresponds to about 24 atomic layers occupying the 2/3 of the box and a vacuum part corresponding to the remaining 1/3 (about 1.7 nm).

The width of the vacuum of the supercell is in good agreement with the literature which recommends a minimum vacuum thickness about 8 Å [52] on the top of the supercell.

For each GB supercell, the atomic geometry was optimized so as to minimize its formation energy. The three main techniques including translations, as in the γ -method, addition of defects and melt and quench atomic treatment presented in the first part of this chapter that allow exploring GB phase space, are tested on the twist GBs described in **Table III- 2** using MS calculations. Based on these results, two methods permitting to access ground state structures have been developed. These methodologies are presented in *section III-2.3*.

III-2.2.2 Test on twist α -iron GBs of the main techniques used to find the GS GB structures

III-2.2.2.1 Translation

The γ -method has been applied on the CSL: the CSL is sampled by different translations (**Figure III- 6**) along X and Y applied to the upper grain.

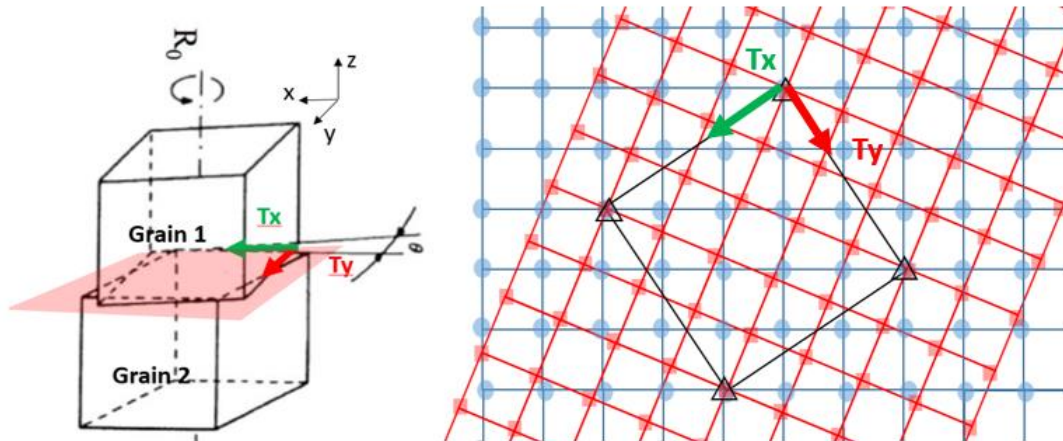


Figure III- 6: Representation of translations along the X and Y directions of the CSL lattice: 3D picture on the left and projection on the CSL lattice on the right. The red and green arrows correspond to the Y and X translations vectors respectively. The blue and red lattices correspond to the two crystals and the coincidence sites are indicated in black.

The formation energy varies as a function of the GB misorientation angle (**Figure III- 7**). The couple of translations X and Y of the CSL corresponding to the lowest formation energy for each misorientation angle is presented in **Table III- 3**.

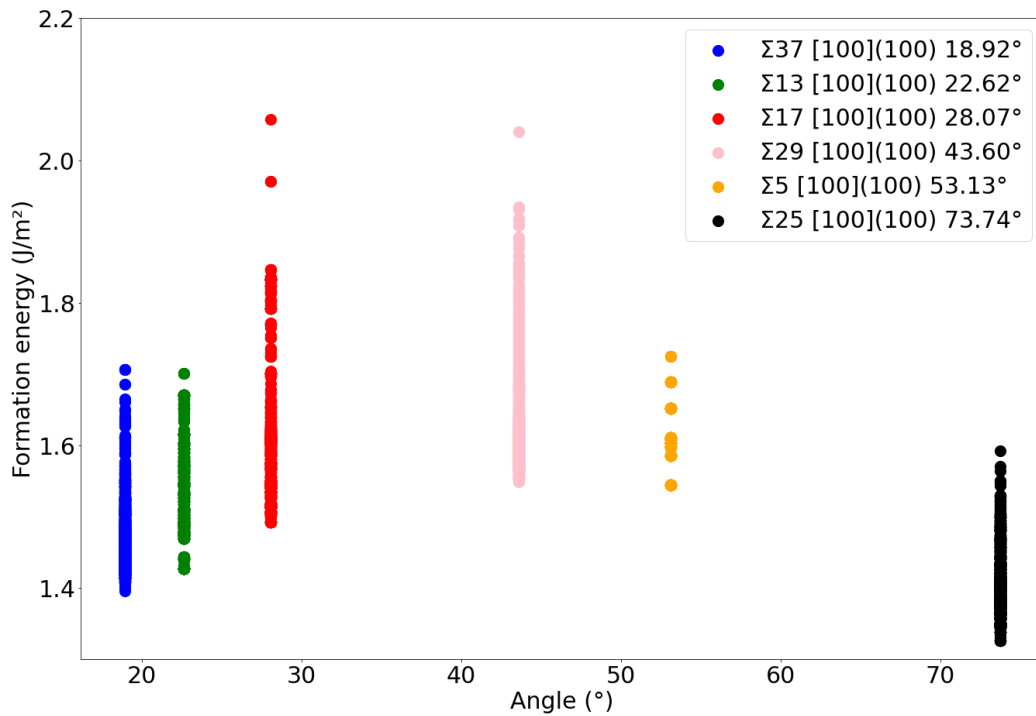


Figure III-7: Formation energy (in J/m^2) as a function of twist misorientation angle (in degrees), for GBs that have been translated by vectors constructed by a sampling of the CSL lattice along X and Y.

As in Wang *et al* [29] study, at the beginning of this thesis, we tried to reduce the number of translations that we have to explore to find the ground state by sampling the DSC lattice along X, Y and Z directions applied to the upper grain (**Figure III- 7**).

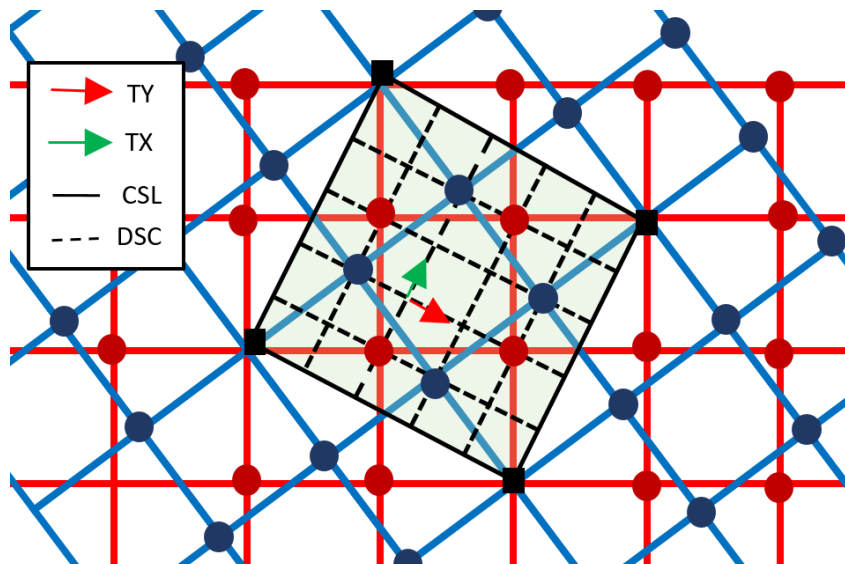


Figure III-8: Representation of translations along the X and Y directions of the $\Sigma 5$ DSC lattice projected along [001]. The red and green arrows correspond to the Y and X translations vectors respectively. Black lines indicate the projection of CSL lattice and black dotted lines highlight the DSC lattice. The blue and red lattices correspond to the two crystals.

This technique does not permit to browse a sufficient number of translations to access an equivalent GB ground state in comparison to the CSL sampling: according to **Figure III- 9** and **Table III- 3**, the GBs obtained have a higher formation energy than the ones obtained with the CSL sampling; the maximum energy difference is about 0.05 J/m² and the associated GB microstructures are different. The addition of a Z contribution in the translation of the DSC lattice was tested but the value that optimizes the translations is close to 0. This observation is consistent with the way we construct our supercells. Due to the presence of vacuum in the upper part of the supercell, relaxations along Z can occur naturally. Thus, sampling CSL or DSC along Z is not necessary. Hence, CSL sampling along X and Y has been chosen as a first step of the methodologies we developed to find twist GB ground state configurations, which are described in *section III-2.3*.

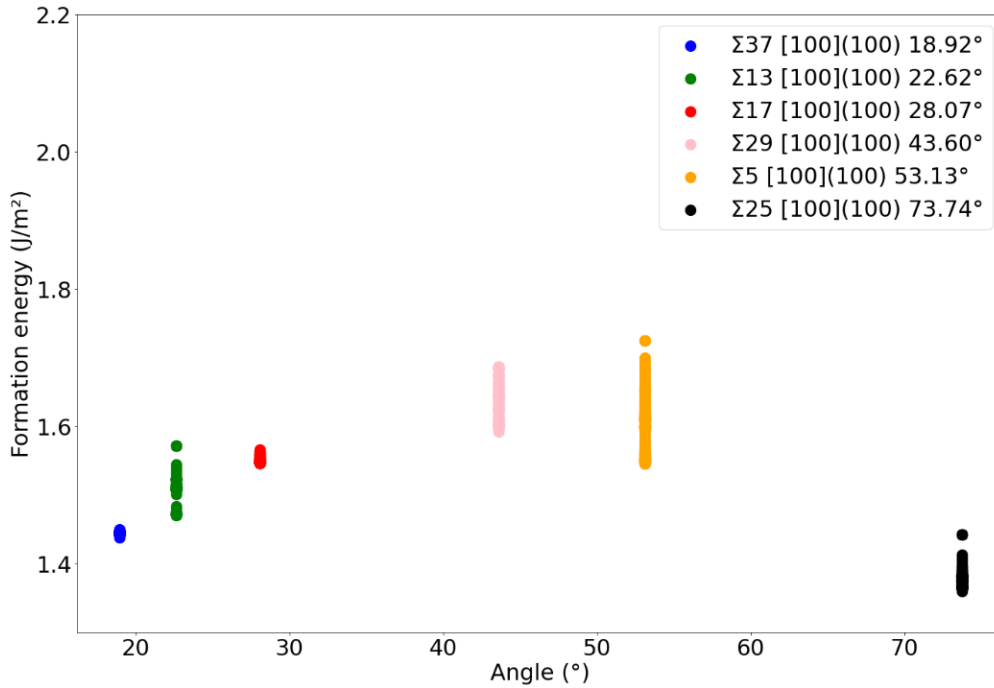


Figure III-9: Formation energy (in J/m²) as a function of twist misorientation angle (in degrees), for GBs that have been translated by vectors constructed by a sampling of the DSC lattice along X and Y.

GB	Σ37	Σ13	Σ17	Σ29	Σ5	Σ25
Ef _{min} CSL (J/m ²)	1.396	1.426	1.493	1.548	1.544	1.326
Ef _{min} DSC (J/m ²)	1.438	1.470	1.547	1.592	1.545	1.360

Table III- 3: Comparison of the lowest formation energies obtained with DSC and CSL sampling.

In the same manner as in Zhang *et al* study [59], we find that translating the GB plane along CSL X and Y-axis gives a periodic rise of energy, function of the translation torque. **Figure III- 10** highlights the periodicity of the GB energy as a function of translation vector coordinates X and Y. Central symmetry can be clearly identified. Therefore, for the methodologies we developed in *section III-2.3*, and in order to reduce the computational time, we restrict our calculations to translations concerning one pattern only for each GB misorientation angle (**Figure III- 11**).

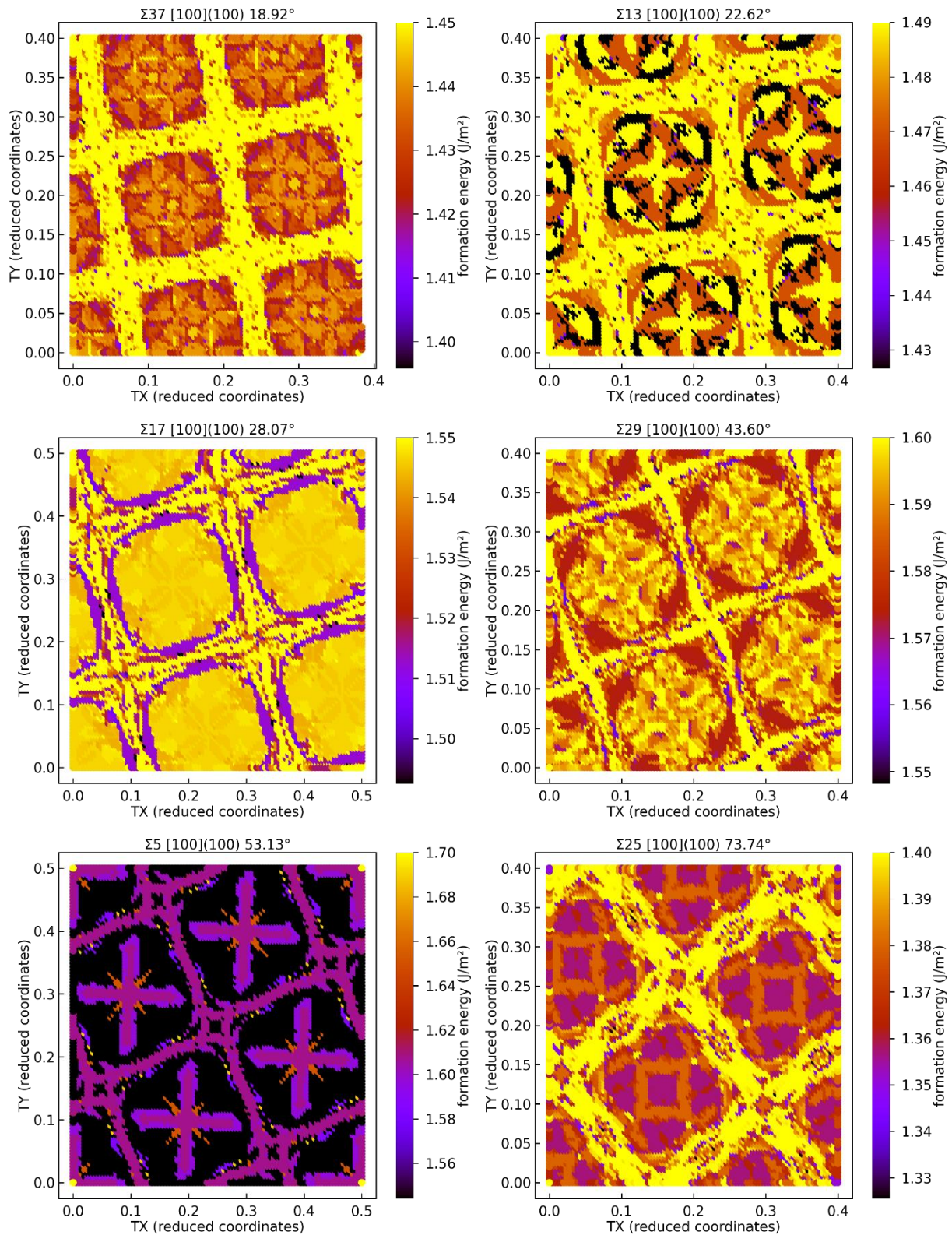


Figure III-10: Color maps of the GB formation energy (J/m^2) as a function of the translation X and Y applied, expressed in reduced coordinates.

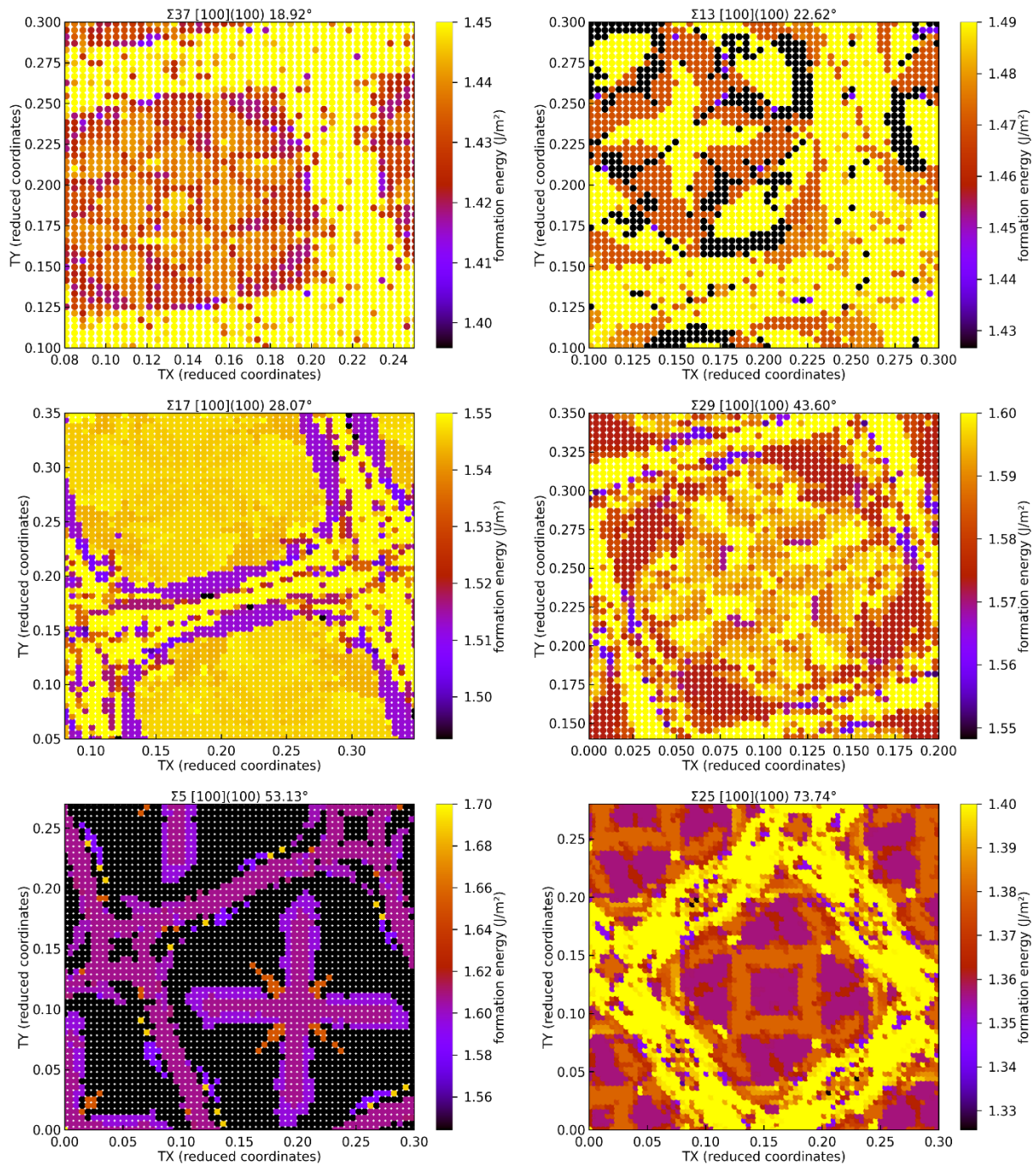


Figure III-11: Reduced color maps of the GB formation energy (J/m^2) as a function of the translation X and Y applied, expressed in reduced coordinates.

The microstructures associated to the lowest formation energy are represented on **Figure III-12**. Since several initial translations can lead to the same GB structure (**Figure III-13**), we chose arbitrarily one couple of translation TX and TY to represent the GB microstructure corresponding to the lowest energy state.

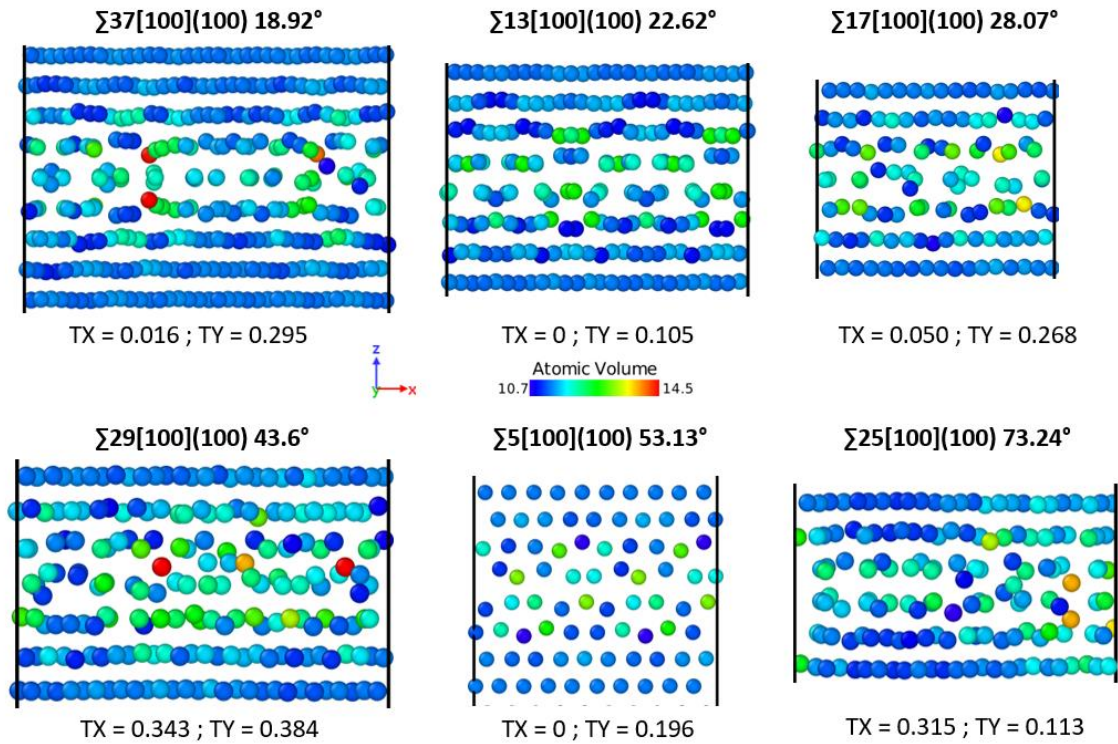


Figure III-12: Representation of the lowest translated GB microstructures as a function of atomic volume. The initial translations are indicated in reduced coordinates.

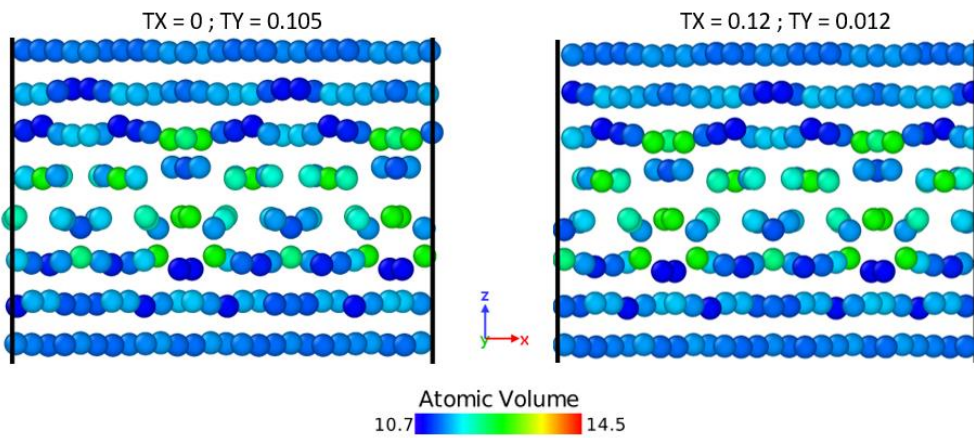


Figure III-13: Representation of different translations for $\Sigma 13100$ 22.62° with the same final formation energy.

According to the literature [57], the energies predicted for $\Sigma 5$ should correspond to a minimum in comparison to other misorientation angles. However, according to **Figure III- 7 and 9**, the γ -method does not lead to this conclusion for $\Sigma 5$. Therefore, in a second step, we tested another atomic treatment: we added on these translated GB structures some point defects. Furthermore, the lowest translated energy configurations are composed of sites with high atomic volume (higher than the atomic volume in the bulk part of the GB about 12 Å³ to 14.5 Å³). Therefore, adding interstitials could stabilize the GB structure and then lead to lower GB energy states. This will be investigated in the next section (III-2.2.2.2 Addition of defects).

III-2.2.2.2 Addition of defects

The introduction of defects like self-interstitial atoms (SIA) and vacancies in the translated GBs which conduct to the lowest energy state has been tested for each misorientation angle in order to find more favourable energetic states. **Table III- 4** summarizes the translations that have been chosen to perform these tests.

GB	TX	TY	Ef (J/m ²)
$\Sigma 37100 18.92^\circ$	0.016	0.295	1.396
$\Sigma 13100 22.62^\circ$	0	0.105	1.426
$\Sigma 17100 28.07^\circ$	0.050	0.268	1.493
$\Sigma 29100 43.60^\circ$	0.343	0.384	1.548
$\Sigma 5100 53.13^\circ$	0	0.196	1.544
$\Sigma 25100 73.24^\circ$	0.315	0.113	1.326

Table III- 4: GB used to perform tests with PD introduction. TX and TY indicate the initial translations applied to the upper part of the GB; they are expressed in reduced coordinates.

Introduction of interstitials

Since twist GBs have complex GB plane microstructure, introducing interstitials in them is difficult. For a perfect bcc lattice, several possibilities can be considered:

- the introduction of a $\langle 110 \rangle$ dumbbell which is the most stable SIA configuration in α -Fe [83], [84]. However the motion of two atoms is necessary: one needs to add one atom and reposition the atom already present in the lattice;
- the introduction of a $\langle 100 \rangle$ dumbbell but it is not the most stable dumbbell in α -Fe, and it also requires the motion of two atoms;
- the introduction of interstitials in octahedral sites. It is not the most stable configuration for interstitials in bcc lattices [84]–[86] however, only one atom has to be positioned and it is more simple to determine where to introduce the supplementary atom. In GBs it is difficult to find the direction of the GB. Moreover, octahedral sites can easily relax in dumbbell as much in an GB environment which is not a symmetrical octahedral site.

Among all these possibilities, we chose to introduce interstitials in the GB in octahedral positions. An octahedral site, near the GB, is selected, if the distance d between atom A and atom B (the two blue atoms in **Figure III- 14**) ranges from 2.6 to 3 Å. The atomic positions of A and B are then shifted manually by ± 0.05 Å along Z.

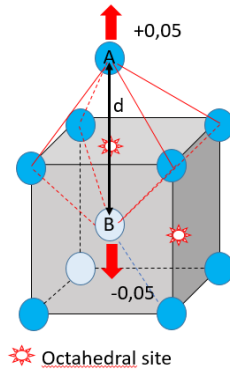


Figure III-14: Introduction of a SIA on octahedral sites. Atoms are represented in blue; red arrows correspond to the atomic relaxations made manually.

Adding interstitials in octahedral sites permits to be initially in a high energetic state and therefore not to be blocked in a local energetic minimum corresponding to metastable GB states and allows exploring easier the phase space.

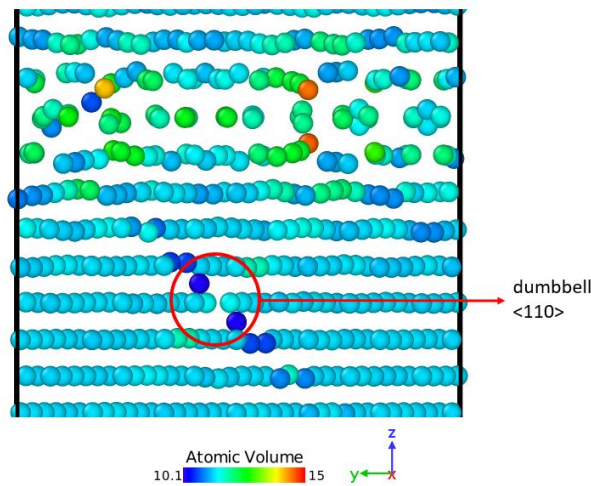


Figure III-15: Formation of a dumbbell in $\Sigma 37100$ 18.92°

Even if octahedral positions are not the most favourable energetically, it should be born in mind that these positions are only initial positions and that relaxation to more favourable energetic position can take place. Since, with the Ackland potential [70] the most stable interstitial configuration is the dumbbell $\langle 110 \rangle$ [79], the introduction of an interstitial in an octahedral position in the bulk part in the GB can easily lead, after proper relaxation, to the formation of a more stable structure: the $\langle 110 \rangle$ dumbbell (**Figure III- 15**).

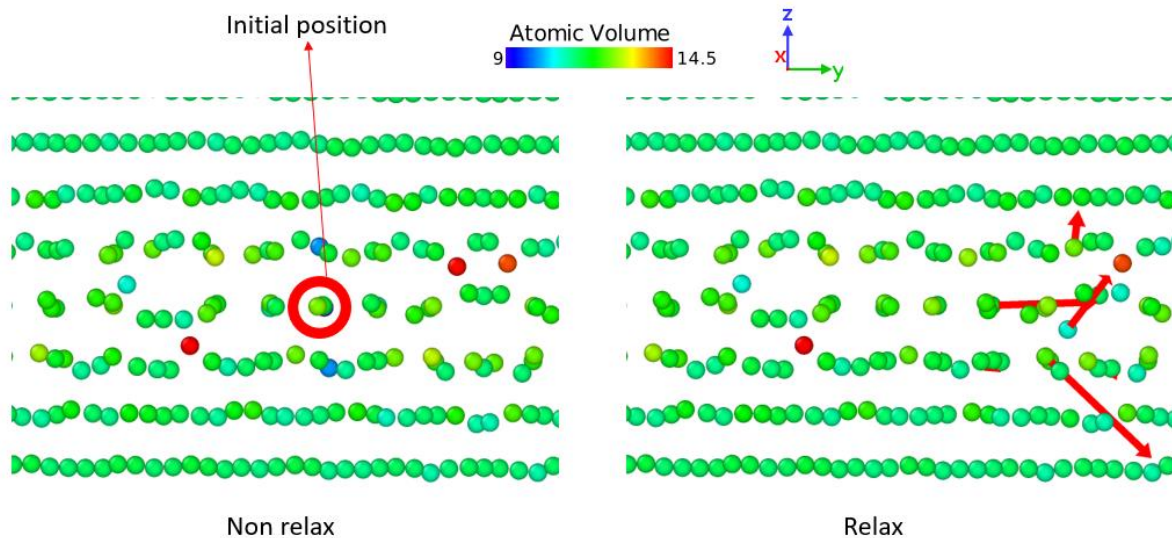


Figure III-16: Illustration of the difficulties in finding suitable interstitial positions inside the GB ($\Sigma 13100 22.62^\circ$). The relaxations are represented by red arrows in the right-hand side of the **Figure III-16** (the scaling factor is about 2, the distance between two atomic layers is to 1.42 Å).

It is difficult to determine the final position of the interstitial after relaxation since significant relaxations can occur (**Figure III- 16**) and the final position of the SIA can be very different from its initial, in particular for interstitials associated to a binding energy higher than the formation energy of this interstitial in the bulk.

According to **Figure III- 17**, the binding energy converges with the distance to the GB plane: the binding energy converges to 0 for a distance from 6 Å to the GB plane. This value is of the same order of magnitude as Tschopp *et al* [46] study which finds a convergence of the binding energy of an interstitial with the GB from a distance to the GB about 10 Å using the same potential. Due to the placement of interstitials on octahedral positions, interstitials are not in the most stable positions; negative binding energies about -0.60 eV corresponds to the energy necessary for an interstitial placed on an octahedral position compared to form the dumbbell $\langle 110 \rangle$.

According to **Figure III- 17**, some interstitials present a binding energy with the GB higher than their formation energy in the bulk which is about 3.56 eV, therefore the addition of interstitials in the GB could lead to lower GB energy state. This observation is different from the conclusions established by Tschopp *et al* [46]: they predicted that the maximum mean binding energy of an interstitial with a twist GB does not exceed 2.5 eV around the GB plane. The binding energy of the interstitial with the GB decreases from 2.5 eV to 1 eV over a distance of 5 Å to the GB plane (which is used as the 0-distance reference). However, we must bear in mind that they considered a binding energy average of all sites of all GBs, therefore a direct comparison seems difficult.

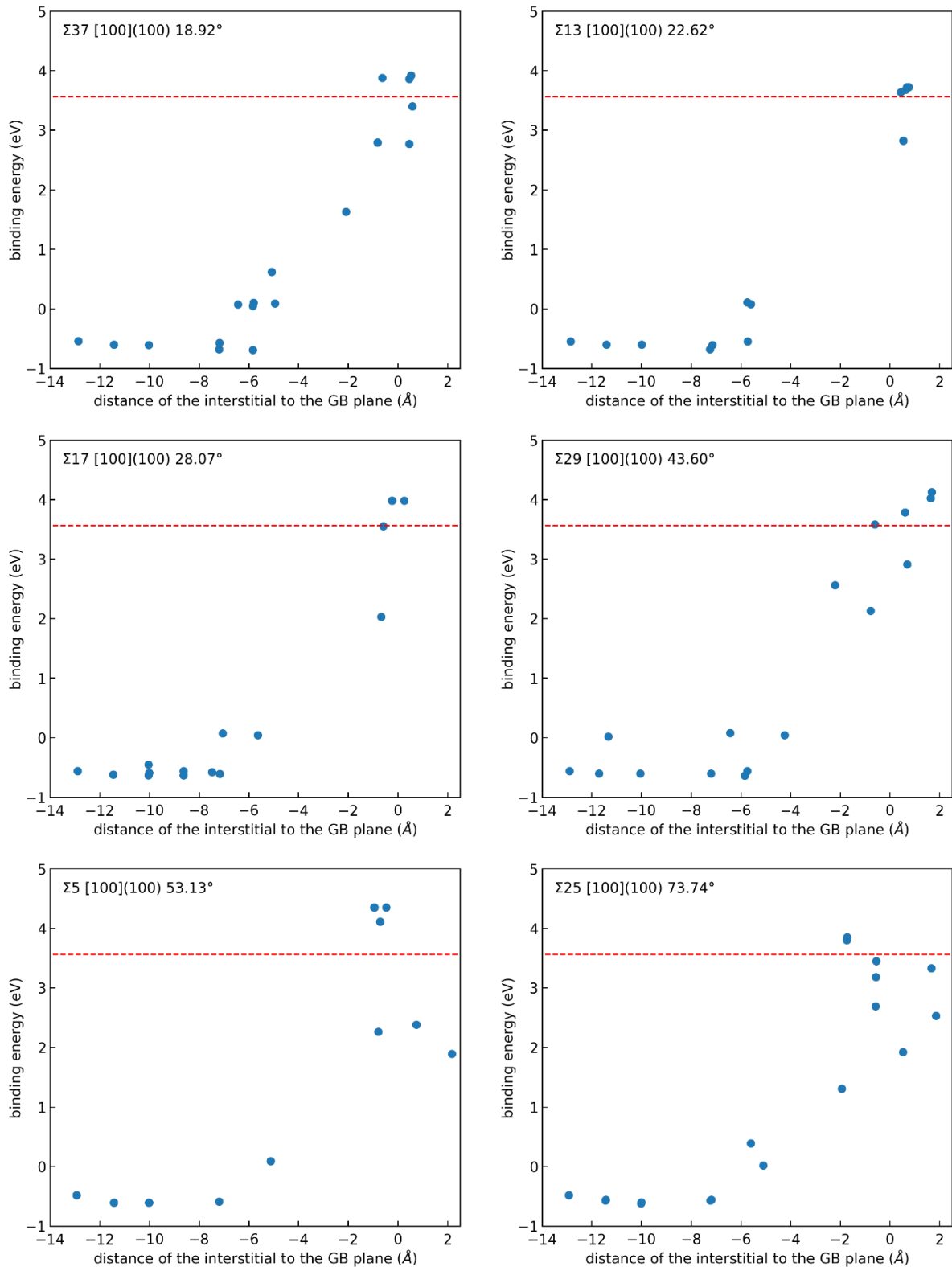


Figure III- 17: Binding energy (eV) of an interstitial placed on an octahedral position as a function of its final distance to the GB plane. Only few points have been plotted on each figure because despite a lot of results and many attempts, it is difficult to find in the ovito representation, the final position of the interstitial inside the GB. The red dotted line corresponds to the formation energy for the <110> dumbbell in the bulk (thus our reference) calculated with Ackland [70] EP. Since the GB is symmetric with respect to the GB, the introduction of interstitial is studied only in the lower part of the GB

Figure III- 18 shows that for all GBs, interstitials corresponding to a high binding energy (>3.56 eV) have undergone significant relaxation (in comparison to an interstitial placed in the bulk part of the GB) which leads to a change of the atom GB layer position (a “migration” to the GB plane). These relaxations along the z axis are between 0.5 \AA to 4 \AA . They occur if an interstitial is placed between -4 \AA and the GB plane.

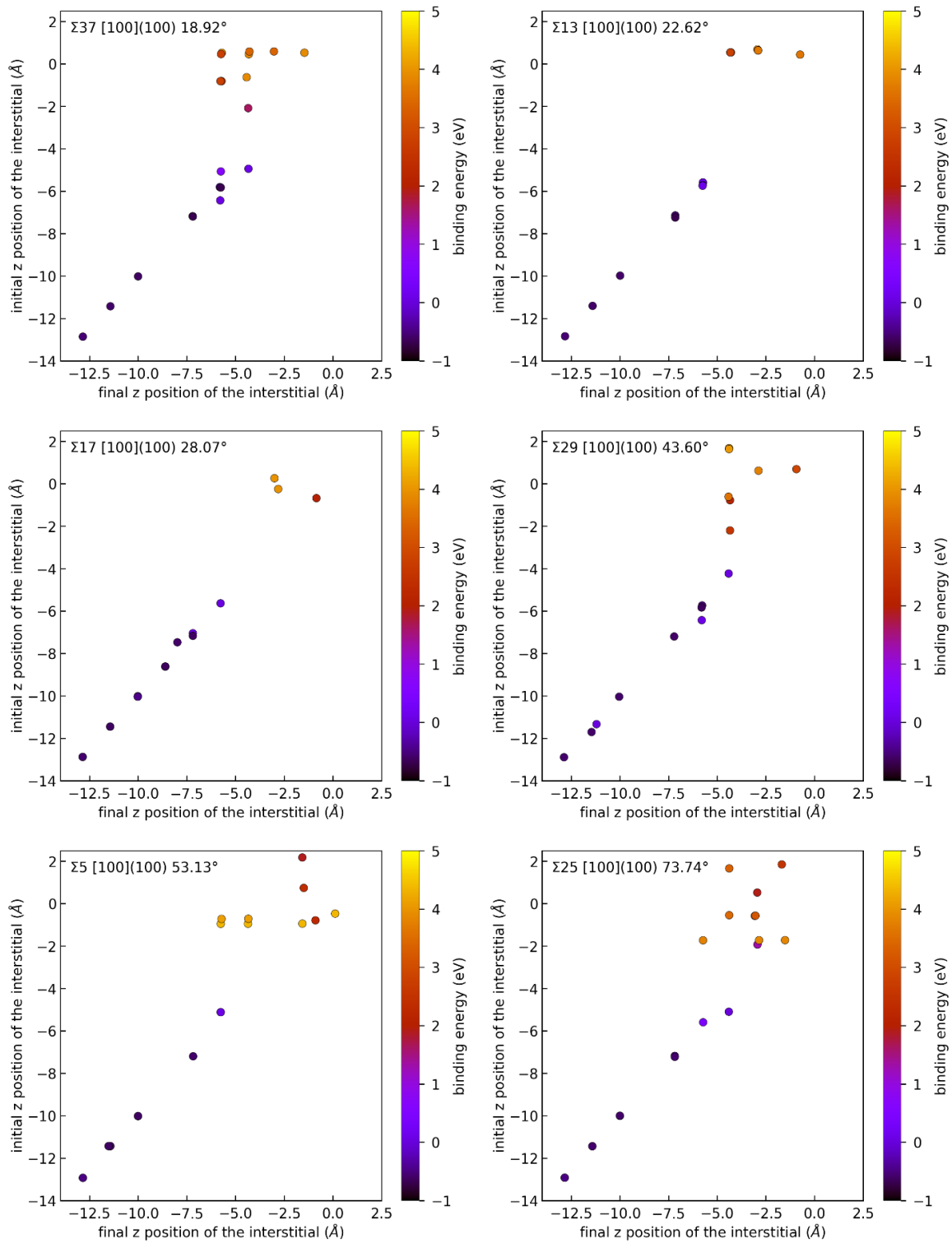


Figure III- 18: Binding energy of an interstitial as a function of the initial and final distance to the GB. The colour indicates the binding energy.

To be more thorough, we calculated the binding energy for an interstitial placed in all possible octahedral sites located at a distance from -8 \AA to 8 \AA of the GB plane. The number of octahedral sites that have been considered for each GB and the number of octahedral sites that are associated to a higher binding energy with the GB than their formation energy with the bulk is presented in **Table III- 5**.

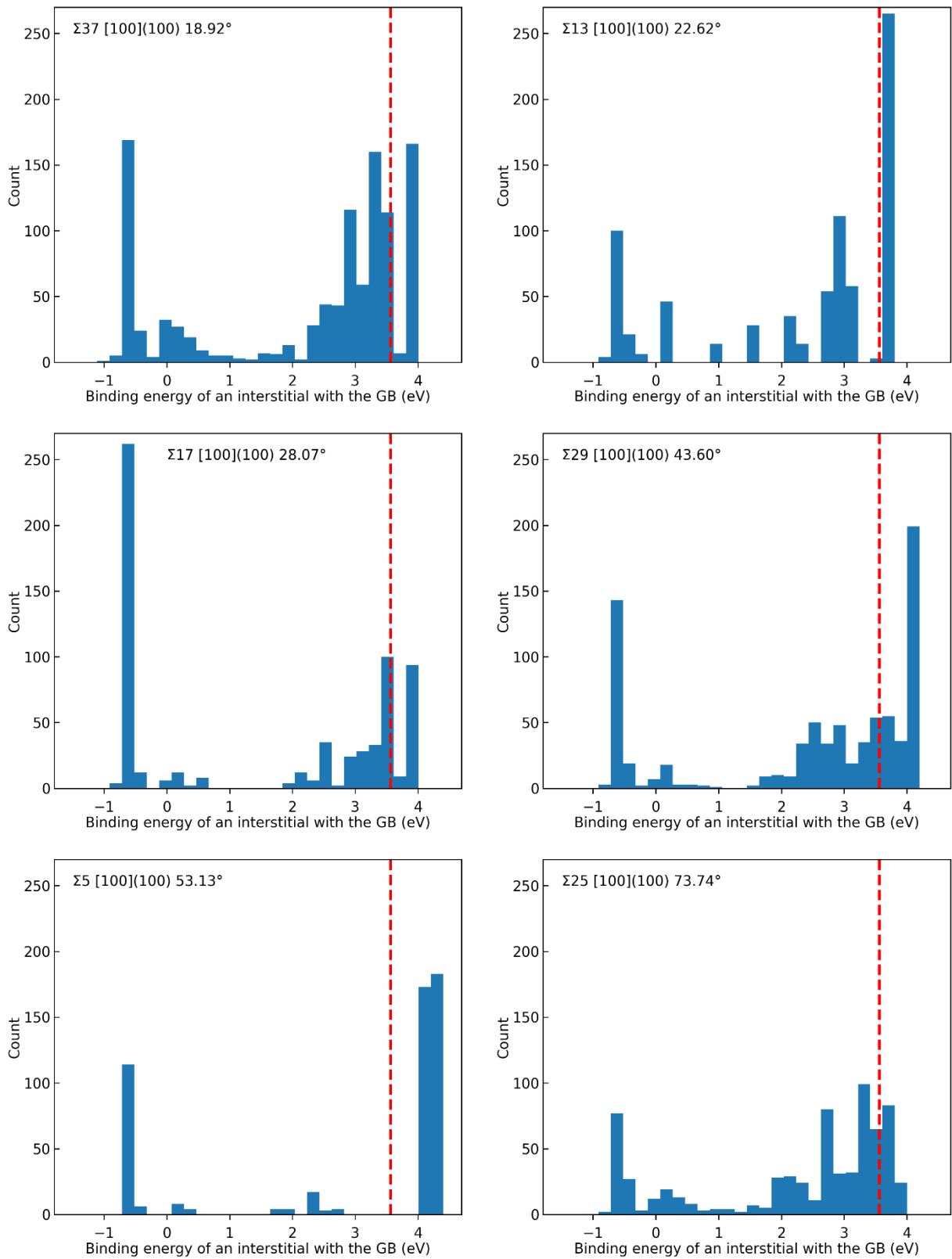


Figure III- 19: Distributions of binding energy of an interstitial in the GB. The red dotted line corresponds to the formation energy of the <110> dumbbell in the bulk (thus our reference) calculated with Ackland [70] EP.

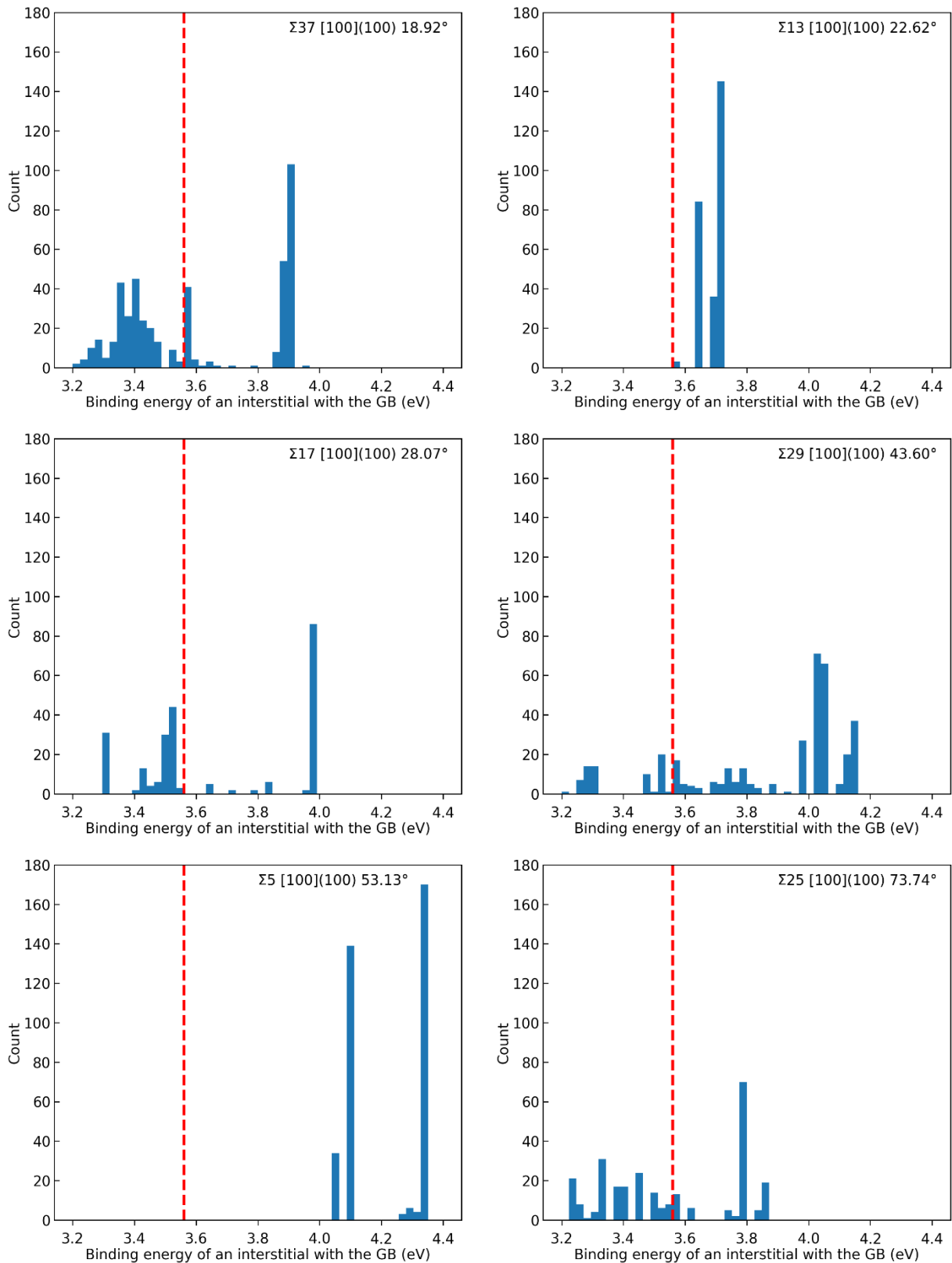


Figure III- 20: The tail of the distributions of binding energy of an interstitial in the GB corresponding the **Figure III- 19**. The red dotted line corresponds to the formation energy of the <110> dumbbell in the bulk (thus our reference) calculated with Ackland [70] EP.

GB	$\Sigma 37$	$\Sigma 13$	$\Sigma 17$	$\Sigma 29$	$\Sigma 5$	$\Sigma 25$
Number of sites with $E_b > 3.56$ eV	218	268	103	312	356	119
Total number of sites that have been tested	1070	759	653	795	520	692
% of sites with $E_b > 3.56$ eV	20	35	16	39	68	17

Table III- 5: Number of octahedral sites that have been considered for each GB and the number of octahedral sites and its percentage that are associated to a higher binding energy with the GB than their formation energy with the bulk.

According to **Figure III- 19**, for all GBs, the addition of interstitials around the GB plane allows to find more stable GB states: all GBs present interstitial sites associated to an interstitial energy superior to the formation energy of a dumbbell $\langle 110 \rangle$ in the bulk. The number of GB sites that could lead to a more stable state in proportion to the total GB sites that have been tested is superior to 16% for all GBs. $\Sigma 5$ GB presents the highest number of interstitials corresponding to a binding energy superior to 3.56 eV; it is about 68%. In contrast, $\Sigma 17$, $\Sigma 25$ and $\Sigma 37$ possess a lower percentage which is between 16 to 20%. $\Sigma 13$ and $\Sigma 29$ have a percentage about 35-36% of the tested octahedral positions. It should be noticed that $\Sigma 5$ and $\Sigma 29$ integrate easier interstitials i.e. higher binding energies than other GBs. **Figure III- 20** focuses on the repartition of the binding energies of the interstitials with the GB for binding energies higher than 3.56 eV. The tail of these distributions shows that except for the $\Sigma 29$ the repartition of binding energies is restricted to only few values i.e the tail of the distribution is pitted around one or more values. Indeed, $\Sigma 29$ presents a *skewed distribution*.

The lowest energetic GB microstructure obtained are represented in **Figure III- 21** as a function of the atomic volume. The variation of GB formation energy is accompanied by changes in terms microstructure: in particular, small variations of atomic volume occur. A detailed comparison of the atomic volume distributions between the different possible minimized path is given at the end of this section.

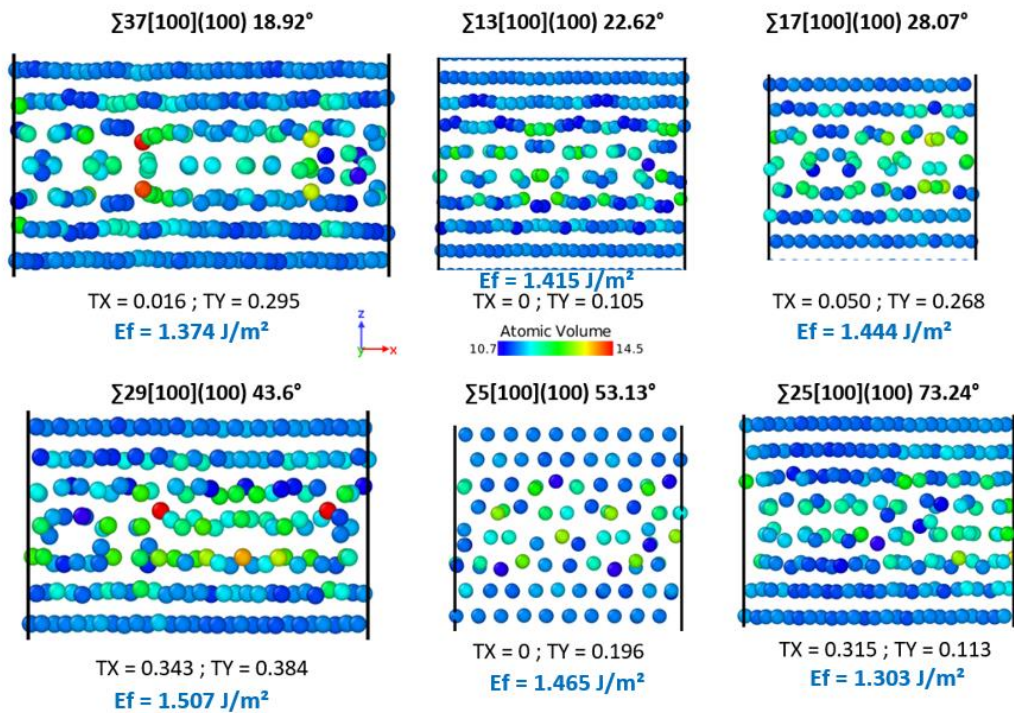


Figure III- 21: Lowest energetic GBs obtained after a translation step and the addition of an interstitial. The initial translation in reduced coordinates is indicated on the bottom of each figure as the final formation energy of the GB in blue.

We tested **another method to introduce SIA**: we looked for free volumes (**Figure III- 22**) in the simulation box and tested all the positions associated to these free volumes. We thus determined isosurfaces in the lattice and detected minimum energy cups in the energetic landscape by a screening of the atomic environment. This method is based on a smeared-out representation of the finite-sized particle spheres in terms of overlapping Gaussian distribution functions centered at each particle. The resulting density field, computed on a discrete grid, has local maximums at each particle site and decays to zero far away from any particles (**Figure III- 23**). Next, the surface boundary is constructed as an isosurface of the Gaussian density field (**Figure III- 22**), with the threshold chosen such that the resulting isosurface roughly matches the finite diameters of the spherical input particles. In the case of **Figure III- 22** a threshold in [1.23,1.25] has been chosen

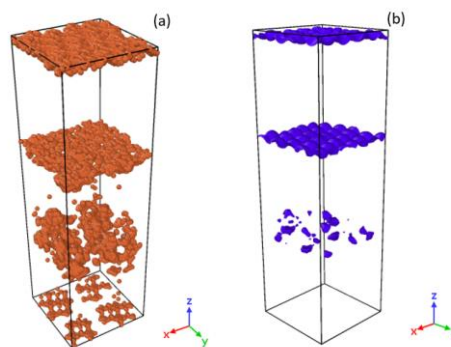


Figure III- 22: (a) representation of the sites determined by the isosurface method, (b) representation of isosurfaces associated with a diameter of spherical input particle threshold in [1.23,1.25]

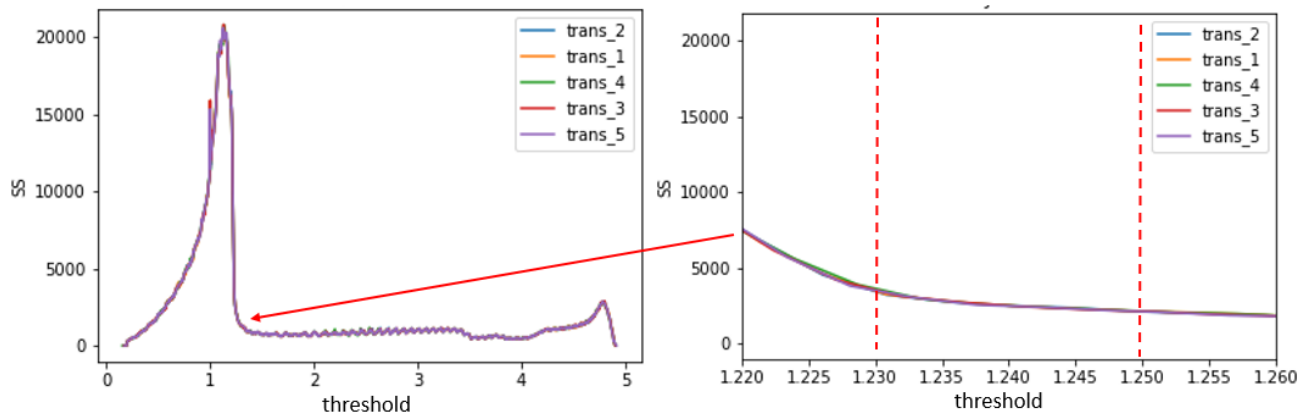


Figure III- 23: Illustration of the choice of the diameter of spherical input particle threshold interval for $\Sigma 29$. The Gaussian density field is given on the ordinates. Five different random translations have been tested.

To determine the appropriate isosurface threshold, we performed tests on the translated GBs containing one interstitial introduced in an octahedral position. For each translated GBs, we tested 20 different positions (i.e. 20 different octahedral interstitial positions) situated at a distance ranging from 0 to 8.5 Å to the GB plane and chose the lowest energetic GB state. Five random translations have been tested for each misorientation angle and a common threshold of the isosurface has been determined (**Figure III- 23**), it is given by the interval [1.23,1.25].

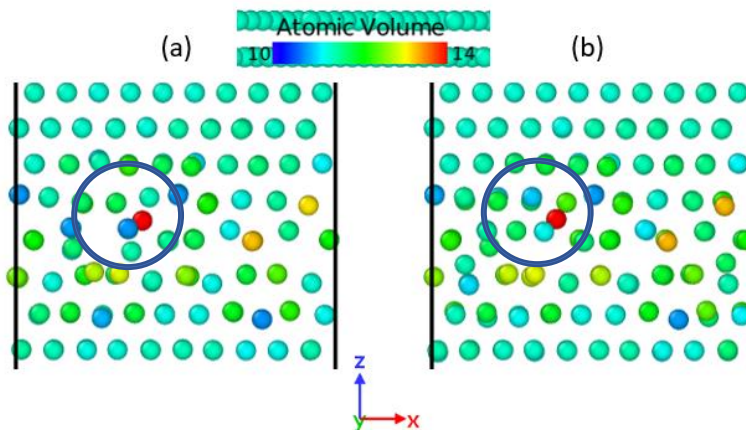


Figure III- 24: Final $\Sigma 5$ GBs obtained after translation and addition of an interstitial (a) in an octahedral position, (b) in a site determined by the isosurface method.

In contrast to the previous method, more physics is integrated in this method as interactions between atoms are taken into account. The previous method captures less physics as it relies only on the estimate of the distance between atoms to determine the octahedral positions. However, because of the high energy that is added to the GB by adding an interstitial in an octahedral position, this previous method permits to avoid local minima and thus explores more easily the GB phase space.

The formation energies of the GBs obtained with this new method are higher than or equal to the energies obtained by introducing the SIA in octahedral positions. The differences in terms of formation energy are about 0.1 J/m² for $\Sigma 29$, 0.18 J/m² for $\Sigma 37$ and 0.26 J/m² for $\Sigma 5$. The microstructures associated are also different (an example for the $\Sigma 5$ GB is shown **Figure III-24**). Hence, introducing interstitials on octahedral positions around the GB plane appear to be an efficient method to lower the GB energy.

- ➔ **A strong interaction between all twist GB considered and interstitials placed on an octahedral position is observed: a number of interstitial positioned on octahedral position near the GB plane (0 to 4 Å near the GB plane) have a binding energy with a twist GB higher than the formation energy of the most stable <110> dumbbell [83] in bcc Fe which is about 3.56 eV with EP Ackland [70]. Therefore, introducing interstitials on octahedral positions around the GB plane allows to find more favorable energetic states. Hence, this atomic treatment will be used to construct more stable GBs.**
- ➔ **$\Sigma 5$ possesses in comparison to other GB tested the more available GB interstitial sites that could lead to a more stable state. In terms of microstructure changes of the GB plane, this atomic treatment allows to significant relaxations about 0.5 – 2 Å along Z axis which lead to a change of some atom GB layer position (Figure III- 18).**

Introduction of vacancies

In contrast to SIAs, adding a vacancy in the GB is not favourable: according to **Figure III- 25**, the vacancy binding energy with GB is always lower than the vacancy formation energy in the bulk which is about 1.73 eV with EP Ackland [70]. Therefore, introducing vacancies inside the GB plane does not permit to find more stable GB state.

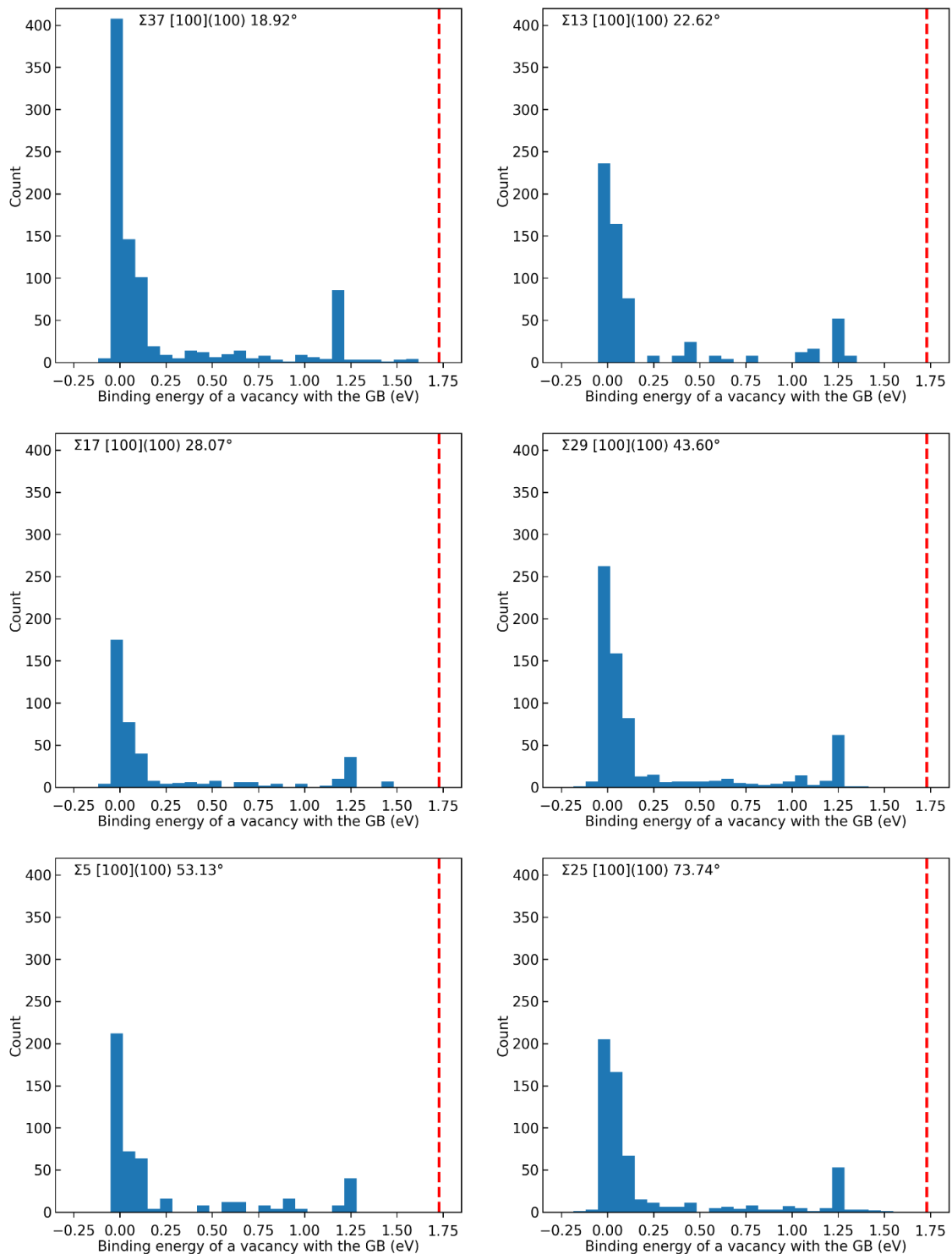


Figure III- 25: Binding energy (eV) distribution of a vacancy in the GB. The red dotted line corresponds to the formation energy of the vacancy in the bulk (thus our reference) calculated with Ackland [70] EP.

According to **Figure III- 26**, the binding energy of a vacancy with the GB converges toward 0 eV for a distance about 7 Å from the GB plane, which is in good agreement with Tschopp *et al* [46] results. However the maximum of binding energy observed, in our case, is higher than the mean value predicted by Tschopp *et al* [46]: we identified a maximum vacancy - GB binding energy of about 1.55 eV for $\Sigma 37$ and Tschopp *et al* predicted a mean of vacancy binding energy for vacancies for a large set of twist GBs (about 170 GBs) about 0.55 eV. Note that the potential used in the study of Tschopp *et al* is the same as the potential used in this thesis.

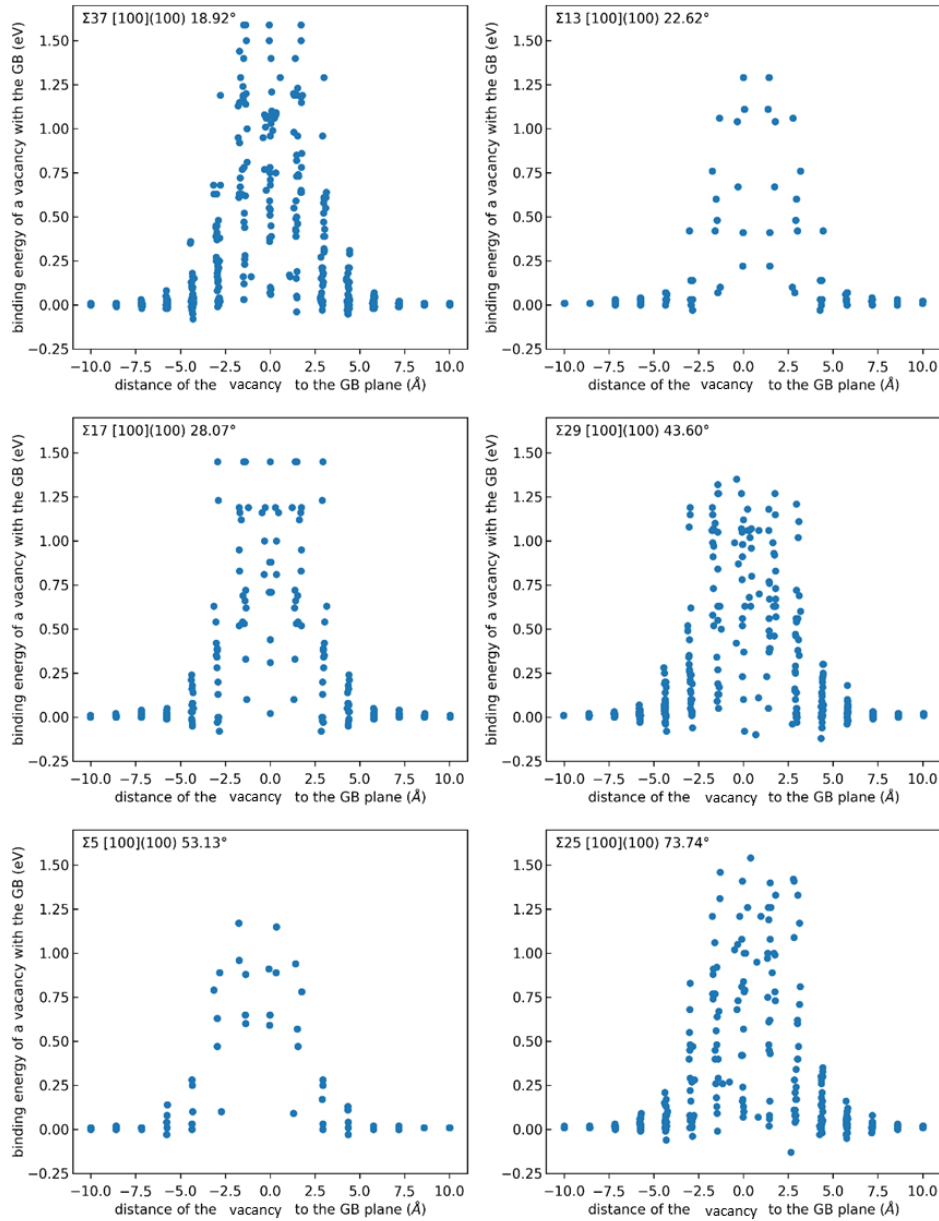


Figure III- 26: Binding energy of a vacancy with the GB as a function of distance to the GB. Similar to what we observed with the interstitials, it is difficult to determine the final position of the vacancy after relaxation. Therefore, the binding energies are represented as a function of the initial distance of the vacancy to the GB (before relaxation).

→ Introducing vacancies around the GB plane is not favorable: the binding energies of vacancies with the GB plane are always lower than the formation energy of a vacancy in the bulk. As in Tschopp *et al* [46] study, in addition to quantifying the binding energetics and the absorption length scale of point defects, we identified that there is an energetic preference for self-interstitial atoms to preferentially bind to grain boundaries over vacancies.

→ Introducing SIAs in octahedral positions allows to reach lower formation energies than only applying translations for twist GB in α -Fe. Hence, a second step after translating the GB (i.e. after applying the γ -method) will be the introduction of an SIA.

III-2.2.2.3 Melt and quench (MQ)

The MQ procedure has then been investigated. The advantage of this method is that the kinetic energy added by the heating allows the system to leave local minima. The procedure is as follows: the supercell is heated at 1000 K and quenched for 50 ps. As the GB final energy depends on the cooling rate, we have optimised it by trial and error and found an optimum cooling rate of 20 K/ps. Taking a lower cooling rate does not give better results than the cooling rate we have chosen. For instance, a cooling rate of about 6.25 K/ps, leads the $\Sigma 29$ GB to converge towards a higher energetic state than the state reached using a cooling rate of about 20 K/ps: the mean energy difference between the two states is about 0.3 eV

The number of annealing sequences has also been optimised: for each GB, 100 MQ have been done (i.e., 100 heating sequences at 1000 K followed by cooling sequences are performed with different seeds). The lowest energetic GB structures found after a translation step and this MQ step are presented on **Figure III- 27**.

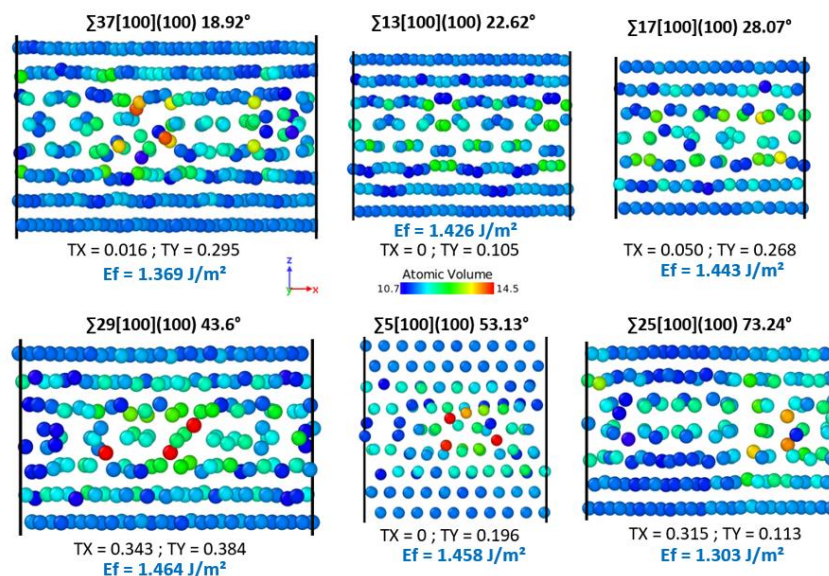


Figure III- 27: Lowest energetic GBs obtained after a translation step and a MQ step. The initial translation in reduced coordinates is indicated on the bottom of each figure as the final formation energy of the GB in blue.

The GB microstructure generated using this MQ procedure is often characterized by the presence of a lot of atoms with a high atomic volume, about 13-14 Å³, in comparison with the microstructures that have been generated with the two techniques presented before. However, no surface reconstruction was observed, and only small atomic restructuring phenomena corresponding to a small shift of the GB plane about one layer (1.4155 Å) towards the upper or the lower part of the supercell occurred. We observed however, in the rest of the study that this GB shift disappeared in the DFT calculations. This phenomenon related to the motion of GB plane caused by heating is commonly observed [24], [87]. The form of screw dislocation junction like twist GBs is predicted to enhance the dislocation mobility and the cooperative motion of GB atoms during the boundary relaxation has been found to play a role in low temperature deformation in BCC metals [24].

Figure III- 28 indicates that the formation energy obtained with this method is always lower than the one obtained by translation of the GB. However, it is not necessarily lower than the formation energy obtained by adding SIAs. For example, adding SIAs in the $\Sigma 13100$ GB leads to lower GB formation energy than using only the MQ method.

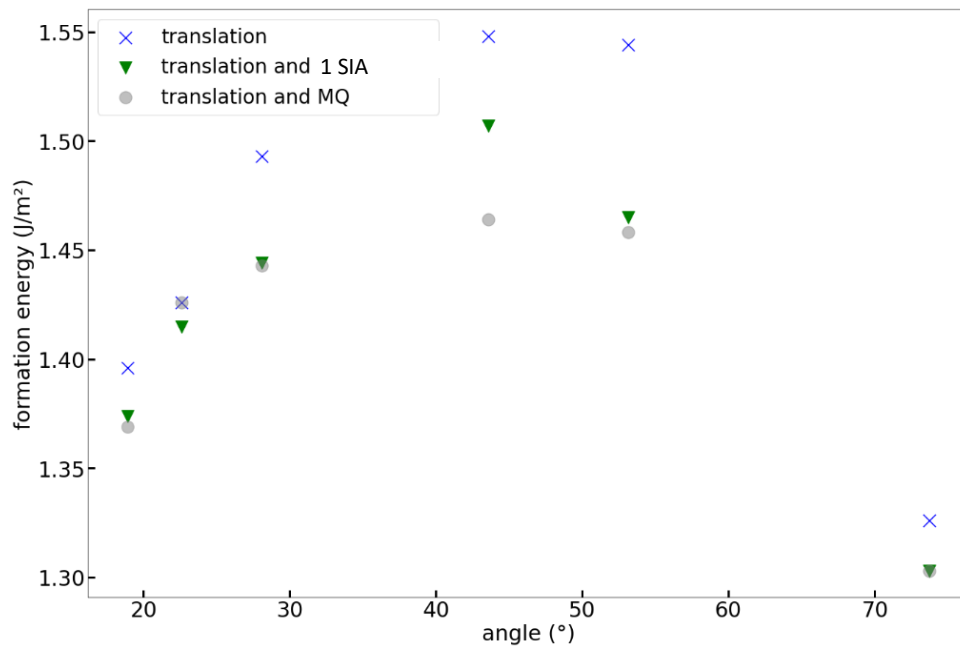


Figure III- 28: GB formation energy (J/m²) as a function of misorientation angle and atomic treatment; blue crosses indicate translation steps, grey circles correspond to melt and quench (MQ) steps after a translation step and green triangle indicates the addition of SIA on an octahedral site after translation step.

The application of a MQ treatment allows to decrease the energy of translated GB generated by the γ -method. However, adding SIA on octahedral positions sometimes leads to lower energetic state. Hence, a methodology composed of sequential MQ treatment and addition of SIAs on octahedral positions has been developed and is presented in *section III-2.3*.

III-2.2.2.4 Comparison of the microstructures obtained with these different techniques

Variation of formation energy is accompanied by changes in terms of microstructure [46]. Indeed, according to **Figure III- 12, 21 and 27**, translation, addition of defects and MQ treatment lead to the formation of tension sites. The presence of this type of sites is not due to any residual pressure of the supercell, as the construction of the simulation box (and in particular the supercell thickness) has been optimized as described in the next section (III-2.2.3 Supercell thickness);

In **Figure III- 29 and 30**, the variation of the atomic volume of atoms in the GB plane has been investigated. We chose to focus the study only to the GB layers which are the closest to the GB plane center: the width investigated from each part of the GB plane is about 4 Å. **Figure III- 29** indicates that all GBs present atomic sites with an atomic volume higher than 12 Å³. $\Sigma 5$ presents the highest maximum atomic volume whatever the treatment performed. **Figure III- 30** shows that these sites which present the maximum atomic volume are often located on the two layers near the GB plane center and are symmetric.

The γ -method does not lead to the lowest energetic state. In order to explore more efficiently the GB phase space and find more stable states, we applied different atomic treatments after the initial translation step. We find that adding SIA on octahedral positions and making MQ treatments allow reaching lower energetic states. Hence methodologies based on these atomic treatments have been developed and are described in section III-2.3.

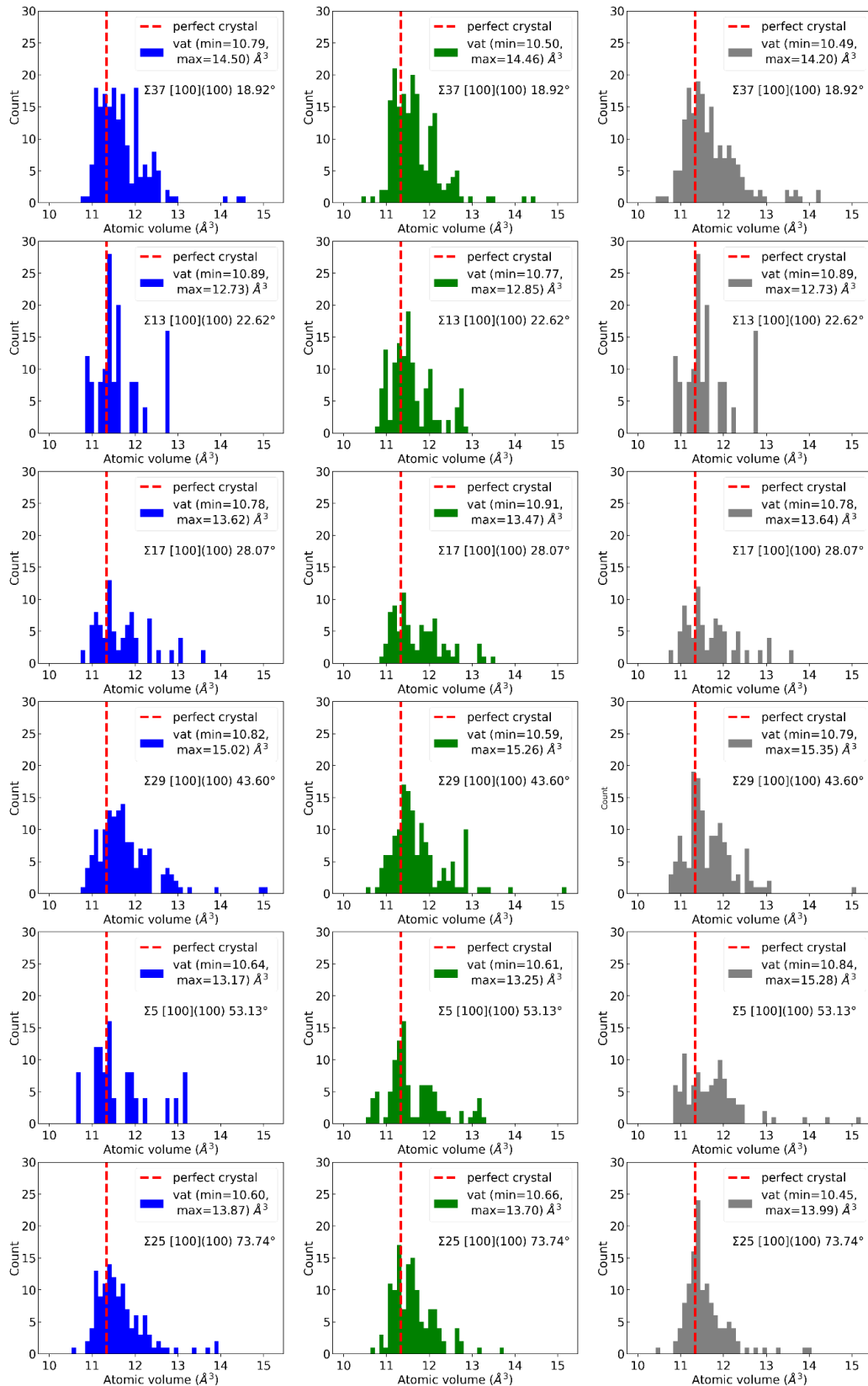


Figure III-29: Atomic volume distributions of GBs obtained by making translations (blue histograms), adding on a translated GB a SIA on an octahedral position (green histograms) and by performing a MQ on a translated GB (grey histograms). The theoretical atomic volume of the bulk is indicated by the red dotted line.

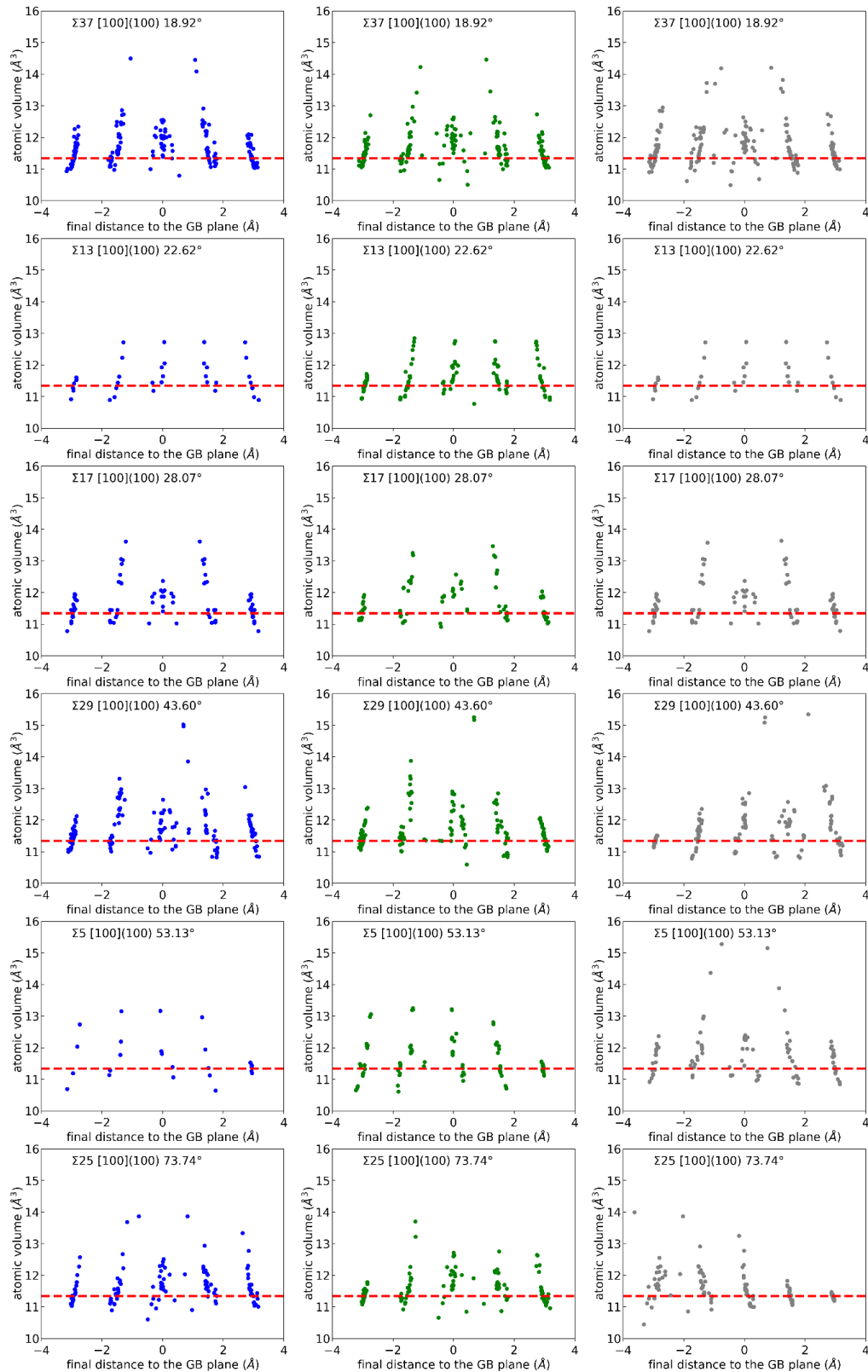


Figure III- 30: Atomic volume as a function of final atomic distance (after relaxation) of GBs obtained by making translations (blue histograms), adding on a translated GB a SIA on octahedral position (green histograms) and by performing a MQ on a translated GB (grey histograms). The theoretical atomic volume of the bulk is indicated by the red dotted line.

III-2.2.3 Supercell thickness

The thickness of the supercell must be sufficiently large to avoid interaction between the surface and the GB plane. The initial translated structure presented in **Table III- 4 section III- 2.2.2** has been used to determine the supercell thickness necessary. The choice of the supercell thickness has been validated according to several criteria which are presented in what follows:

- The GB formation energy: **Figure III- 31** shows that the formation energy is the same regardless of the supercell thicknesses.

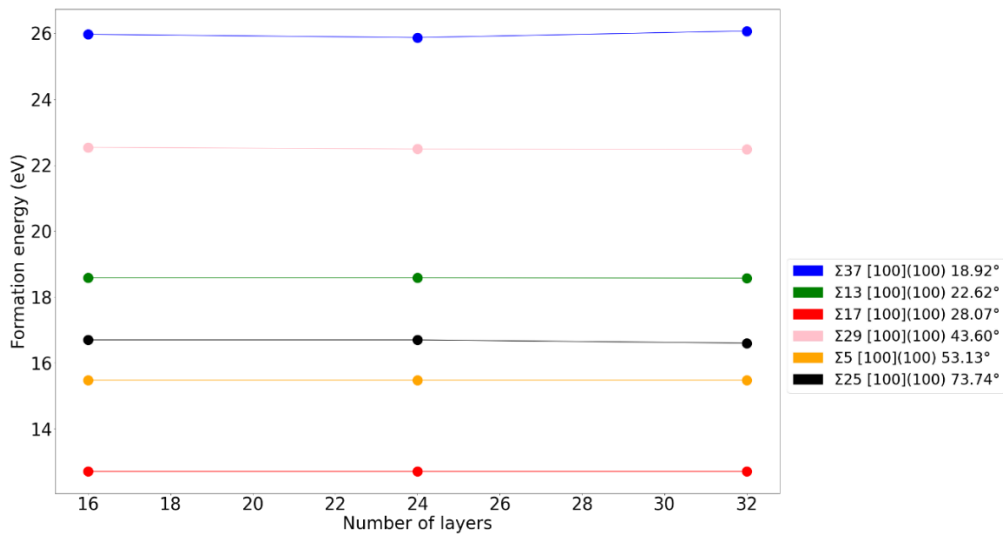


Figure III- 31: Formation energy (J/m^2) for different twist GB translated only as a function of GB thickness.

- The atomic microstructures: **Figure III- 32** shows that the atomic volumes are the same whatever the cell thickness: the atomic volume patterns are identical for $\Sigma 5100$.

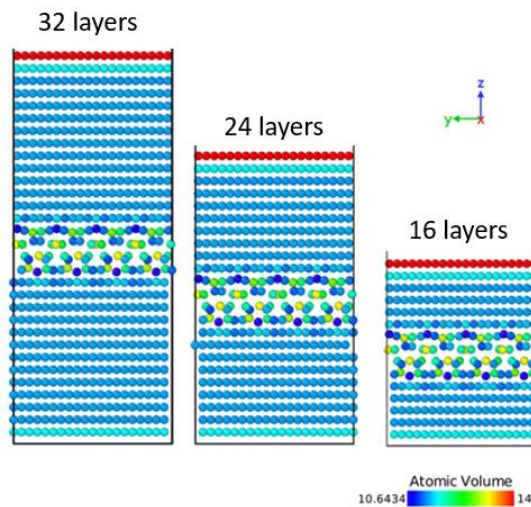


Figure III- 32: Sigma 5 GB translated only microstructure for different cell thicknesses. The color indicates the atomic volume (in \AA^3).

- The binding energy between phosphorus and GB: the P-GB binding energy decreases when the distance between an atomic site and the GB plane increases. It must be equal to 0 eV in the bulk part of the supercell, here close to 0.7 nm away from the GB plane as found by EDF simulation team and Rajadopalan *et al* [9] for tilt GBs. **Figure III- 33** shows the phosphorus binding energy with the GB as a function of the GB distance and the GB thickness. The MS calculations have been done using Ackland potential [70]. Phosphorus has been placed on substitutional sites. A detailed analysis of the phosphorus behavior in the GB presented here is given in the chapter concerning segregation.

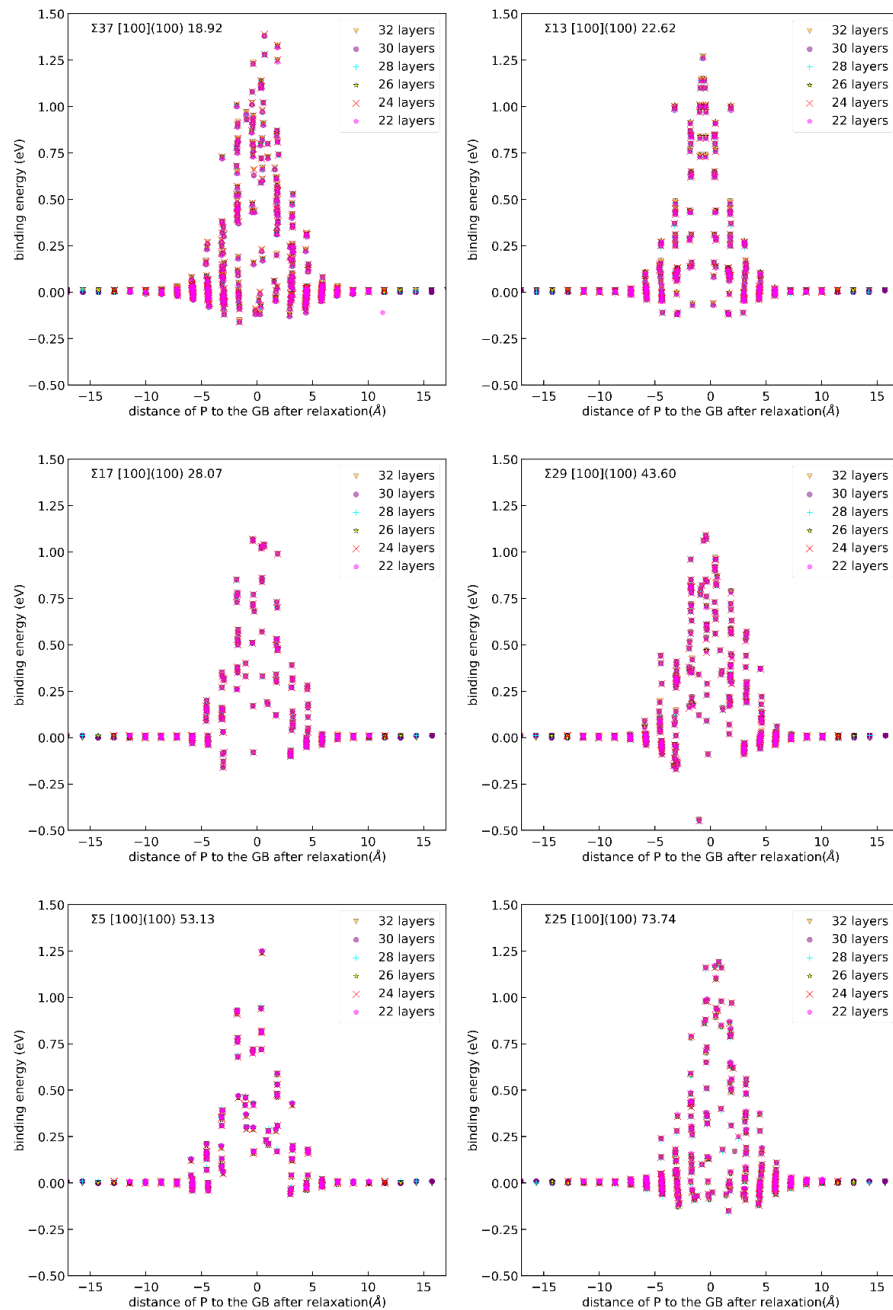


Figure III- 33: Binding energy as a function of distance to the GB plane for GBs initially translated only. Phosphorus is placed on substitutional sites

III-2.3 Iterative GB construction processes developed

In this part, the **two GB construction processes** that have been developed in this thesis to reach the lowest energetic GB configurations are presented: both of them used the concepts previously described in *section III-2.2*. We will use three different atomic events, that we will refer to as steps:

- the **TRANS step** consists in translating the upper part of the grain boundary along the X and Y direction (moving thus on the γ surface). This step is done only once, right after the GB has been constructed using the CSL method.
- the **INT step** consists in relaxing 20 GB configurations by trying 20 different octahedral positions near the GB plane (i.e between 0 to 7 Å from the GB plane **Figure III- 17**) to insert an interstitial and selecting the position for which the SIA has the highest binding energy with the GB (thus leading to the lowest GB formation energy).
- the **MQ step** consists in 100 trials of heating the supercell at 1000 K and quenching it at the rate of 20 K/ps. The configuration that has the lowest GB formation energy among the 100 configurations thus generated is selected for the next step.

Both methodologies consist in a succession of stages, the first one being always a **TRANS step**.

The first methodology considers the sequential addition of interstitials on octahedral positions, for all the possible translations found with the γ surface method. Each stage consists thus in an **INT step** and the methodology will be call the **All_trans method**. **Figure III- 34** provides a schematic view of this methodology.

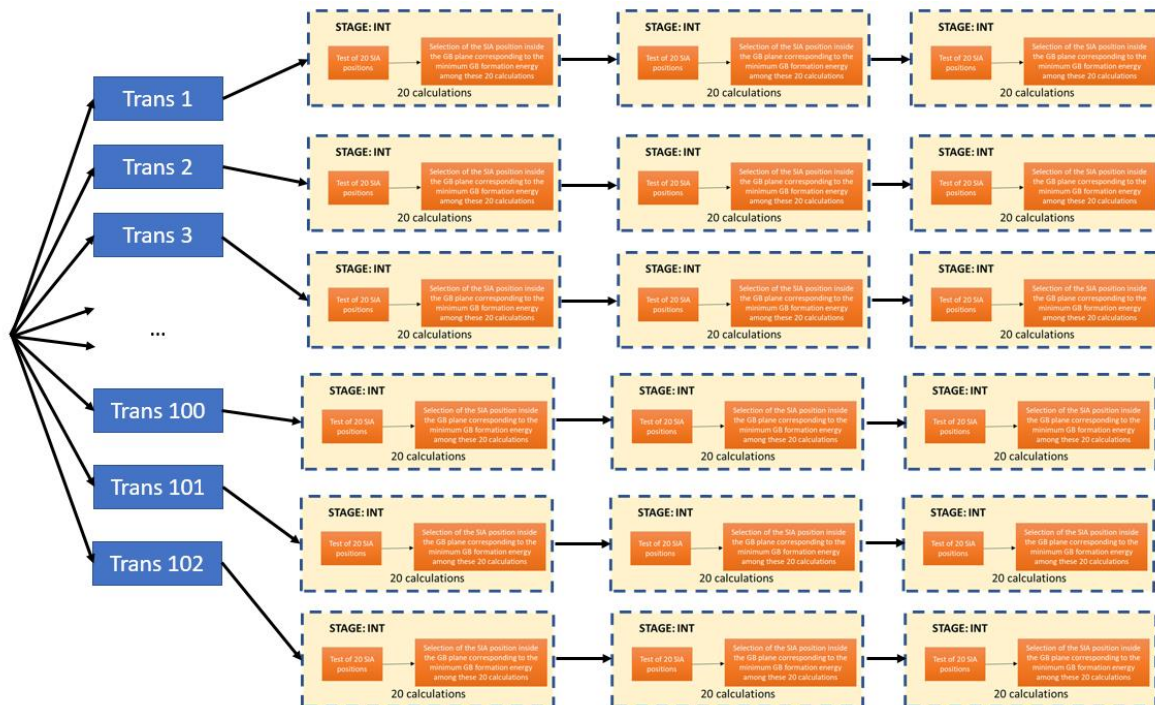


Figure III- 34: Schematic view of the **All-trans methodology**. The sequential addition of 3 SIAs is represented here, however more interstitials can be introduced.

The **second method**, that will be referred to as the **MQ_method**, consists, at each iteration, to do two possible actions (**Figure III- 35**). One corresponds to the addition of a SIA (i.e. an **INT step**) and the other one corresponding to a two-step action: a **MQ step** followed by an **INT step** (i.e. a MQ treatment is performed first and is then followed by the introduction of a SIA). At each iteration of this process, two branches are thus formed, corresponding to the two possible actions (**Figure III- 35**). At the end of each stage (INT or MQ+INT), we select the lowest energy configuration and start two new branches by repeating these two actions, thus adding one SIA per iteration. Ultimately, **for a given translation**, a tree of configurations is formed (**Figure III- 36**), having 2^N branches, where N is the number of SIA introduced. This method is really time consuming: this is why it was applied only to a few translations chosen among all the possible translations issued from the γ surface method.

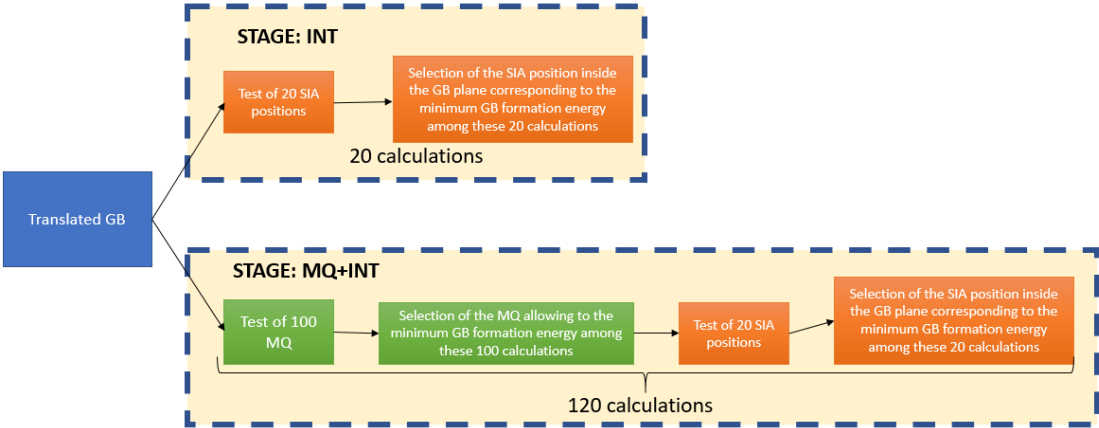


Figure III- 35: Description of the first step of the MQ methodology developed. The two possible stages are framed in blue.

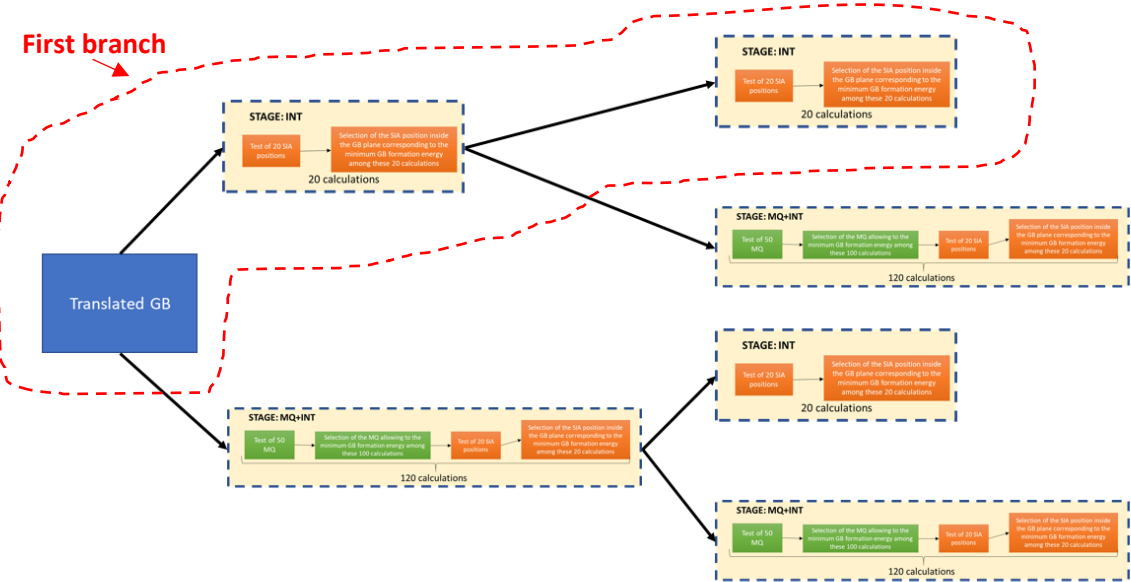


Figure III- 36: Schematic view of the MQ methodology after two iterations and the four corresponding branches. The stages repeated to explore the GB space phase are framed in blue. The first branch represented here which is framed in red is similar to branches obtained with the **All_trans method**.

The results obtained with the **All-trans methodology** are presented first. The second part is dedicated to the **MQ_method**. Finally, in a third part we compare the two methods.

III-2.3.1 The All_trans method

As mentioned previously, in this method, for each GB, we find, for all the possible translations of the γ -surface method, how many SIAs need to be introduced to minimize the formation energy. We obtain this way a distribution of formation energies, the minimum of which, gives us, we hope, the GB ground state. **Table III- 6** presents the results obtained by this method.

In order to better understand the physical mechanisms that occur during the relaxation, we quantify the relaxations by a vector at each step of the methodology. This vector represents the mean atomic translations that take place between the two grains, it corresponds to the sum of two vectors, one related to the bulk-like part of the upper grain and the other to the bulk-like part of the lower grain; in that case one has to define a region in each grain. We can then define the “**global translation**” vector for each minimum energy GB state by summing up all the translation vectors evaluated at each step of the building process.

GB	$\theta(^{\circ})$	$E_{f_{ini}}$ (J/m ²)	E_f (J/m ²)	TX_{ini} (Å)	TY_{ini} (Å)	TZ_{ini} (Å)	TXG (Å)	TYG (Å)	TZG (Å)	Number of SIA
$\Sigma 37$	18.92	1.444	1.299	1.3915	4.7312	0	1.2628	4.0484	0.0740	11
$\Sigma 13$	22.62	1.427	1.288	3.0912	3.3828	0	2.8879	1.807	0.0748	8
$\Sigma 17$	28.07	1.544	1.281	1.2969	2.9476	0	1.1296	2.5662	0.0474	4
$\Sigma 29$	43.60	1.596	1.271	0.4928	3.4495	0	0.0653	3.2528	0.0502	7 ¹³
$\Sigma 5$	53.13	1.608	1.142	2.9414	1.2789	0	2.9191	0.7686	0.0455	4
$\Sigma 25$	73.74	1.403	1.252	4.0034	2.0589	0	3.5499	1.927	0.05	4

Table III- 6: formation energy, initial translations applied (i.e. after the γ -surface method) (TX_{ini} , TY_{ini} and TZ_{ini}), global translations (TXG , TYG and TZG) and the number of interstitials that have to be added to reach the lowest energetic configuration. Only one minimum per misorientation angle is indicated because of the high number of GB configurations corresponding to the same energy minimum that have been found as it can be seen in the next figures.

As expected, the introduction of SIAs results in the minimization of the GB formation energies. **Figure III- 37** represents typical evolutions of the formation energy during the process for the $\Sigma 5$ and $\Sigma 37$ GB. Increases in formation energy before reaching the local minimum can occur but do not exceed 0.07 J/m² when 20 positions of SIA are tested. Due to this observation, we have tested for $\Sigma 37$ and $\Sigma 13$ to increase the number of positions tested during these types of events. According to **Table III- 7**, when the number of SIA positions tested is larger, there is a decrease of these increases of formation energy. However, the energy rises before going back down to a lower energy is classic and encountered in minimization techniques.

In order to stop the simulations after the GS has been found, one needs to establish a stopping criterion.

¹³ For some other initial translations generated with the γ -method, the minimum can occur also for the addition of 6 SIA instead of 7. For a given translation it is often observed that the final formation energies with 6 SIA and 7 SIA are very close ($\Delta E_f = 0.0001$ J/m²) which is in good agreement with III-Annex 2.

Our analysis which is detailed for **MQ_method (III-Annex 5)** shows that the energy increase is not greater than 0.07 J/m² in all the cases. Therefore, we can set a stopping criterion for the method by saying that when the energy increase is more than 0.1 J/m², we passed the minimum. In the next section, we will verify the applicability of this criterion on **MQ_method**.

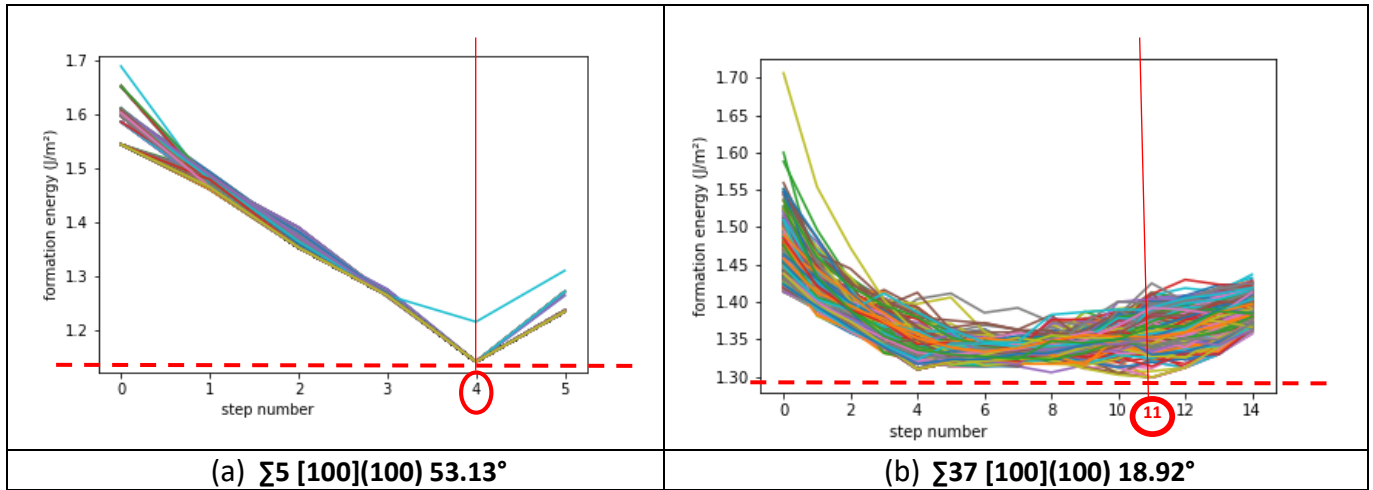


Figure III- 37: Evolution of the grain boundary formation energy versus the number of SIA introduced corresponding here to the step number (a) $\Sigma 5$ 100 53.13° b) $\Sigma 37$ 100 18.92°. The evolution of the formation energies for the other GBs are represented in **III-Annex 2**. The minimum formation energy obtained and its associated number of SIA is indicated by red lines.

GB	θ (°)	INT step	Ef (J/m ²)			
			Before 20 tests	After 20 tests	After 40 tests	After 60 tests
$\Sigma 37$	18.92	9	1.368	1.376	1.361	1.361
$\Sigma 37$	18.92	10	1.341	1.364	1.36	1.36
$\Sigma 37$	18.92	8	1.34	1.36	1.36	1.347
$\Sigma 13$	22.62	7	1.319	1.386	1.354	1.331
$\Sigma 13$	22.62	7	1.341	1.374	1.349	1.349
$\Sigma 13$	22.62	6	1.331	1.352	1.319	1.319

Table III- 7: formation energy obtained for a given **INT step** during the GB construction, for different number of SIA positions tested. Each line in this table corresponds to a different initial translation applied.

In order to assess the exploration of the phase space with our method, we represent, in **Figure III- 38 and 40**, for two GBs ($\Sigma 37$ and $\Sigma 5$) which corresponds to the two extreme cases; the minimum formation energies selected at each step in the plane of the global translation. The other figures corresponding to other GB misorientation angles are shown in **III-Annex 3**. In the same manner only two cases ($\Sigma 37$ and $\Sigma 5$), for the distributions of the minimum formation energies selected at each stage (associated to the same formation energies as **Figure III- 38 and 40**) are represented in **Figure III- 39 and 41**. The other GB misorientation angle distributions are presented in **III-Annex 4**.

The introduction of SIAs results in the minimization of the GB formation energies, however, differences can be noted: according to **Figure III- 39 and 41**, all configurations tested for $\Sigma 5$ seem to converge to a single state of low formation energy.

However, for other GBs (**Figure III- 38 and 40, III-Annex 3 and 4**), not all initial configurations converge to the GB configuration corresponding to the minimum formation energy. Indeed, $\Sigma 17$ has many initial configurations that lead to the minimum of energy, but they do not all lead to it and the $\Sigma 13$ has only a few translations that lead to a minimum of energy. The extreme case was observed for $\Sigma 37$: according to **Figure III- 38 and 40**, only few cases are associated to the minimum formation energy. Similarly to $\Sigma 37$, the $\Sigma 29$ and $\Sigma 25$ have very few cases that lead to the minimum GB formation energy.

The number of initial translations that conducted to the lowest formation energy are summarized in **Table III- 8**. As observed in **Figure III- 38 and 40 and III-Annex 3 and 4**, $\Sigma 37$, $\Sigma 29$ and $\Sigma 25$ the lowest percentage of initial translation that conducts to the GS whereas $\Sigma 5$ leads to 100% of success. Note that for $\Sigma 37$, $\Sigma 29$ and $\Sigma 25$ this percentage is inferior or equal to 5%, which is really low.

In addition, for all GBs tested the minima obtained are associated with different global translations. It is therefore difficult to link global translation value and final energy/microstructure of lower energy. The final microstructures are given in **Figure III- 48**.

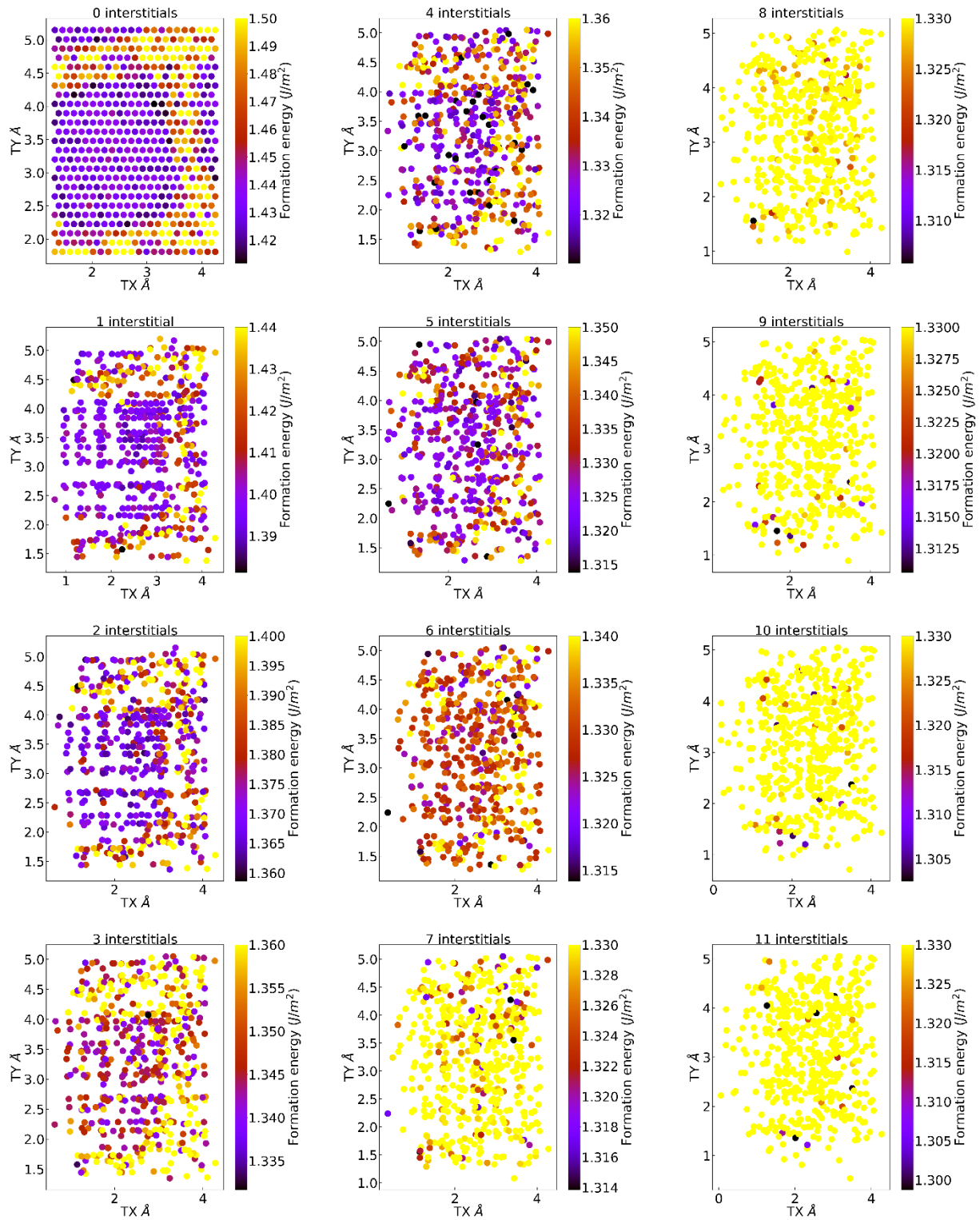


Figure III-38: $\Sigma 37$ formation energies (J/m²) selected at each step of `All_trans_method` as a function of TX and TY coordinates of the corresponding global translation expressed in Å.

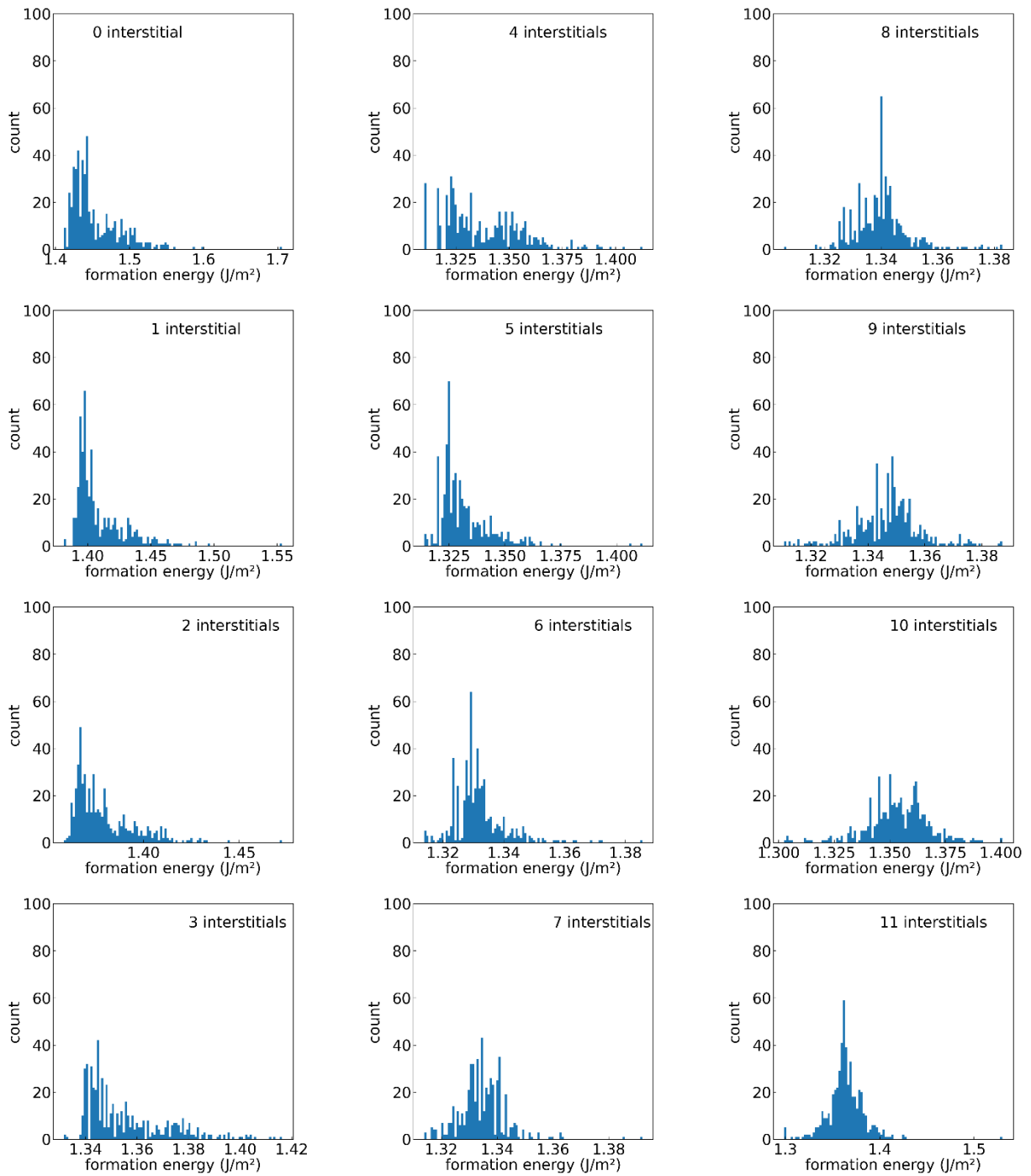


Figure III- 39: $\Sigma 37$ distributions of the formation energies selected at each step of the **All_trans** method with the same formation energy data displayed in **Figure III- 38**.

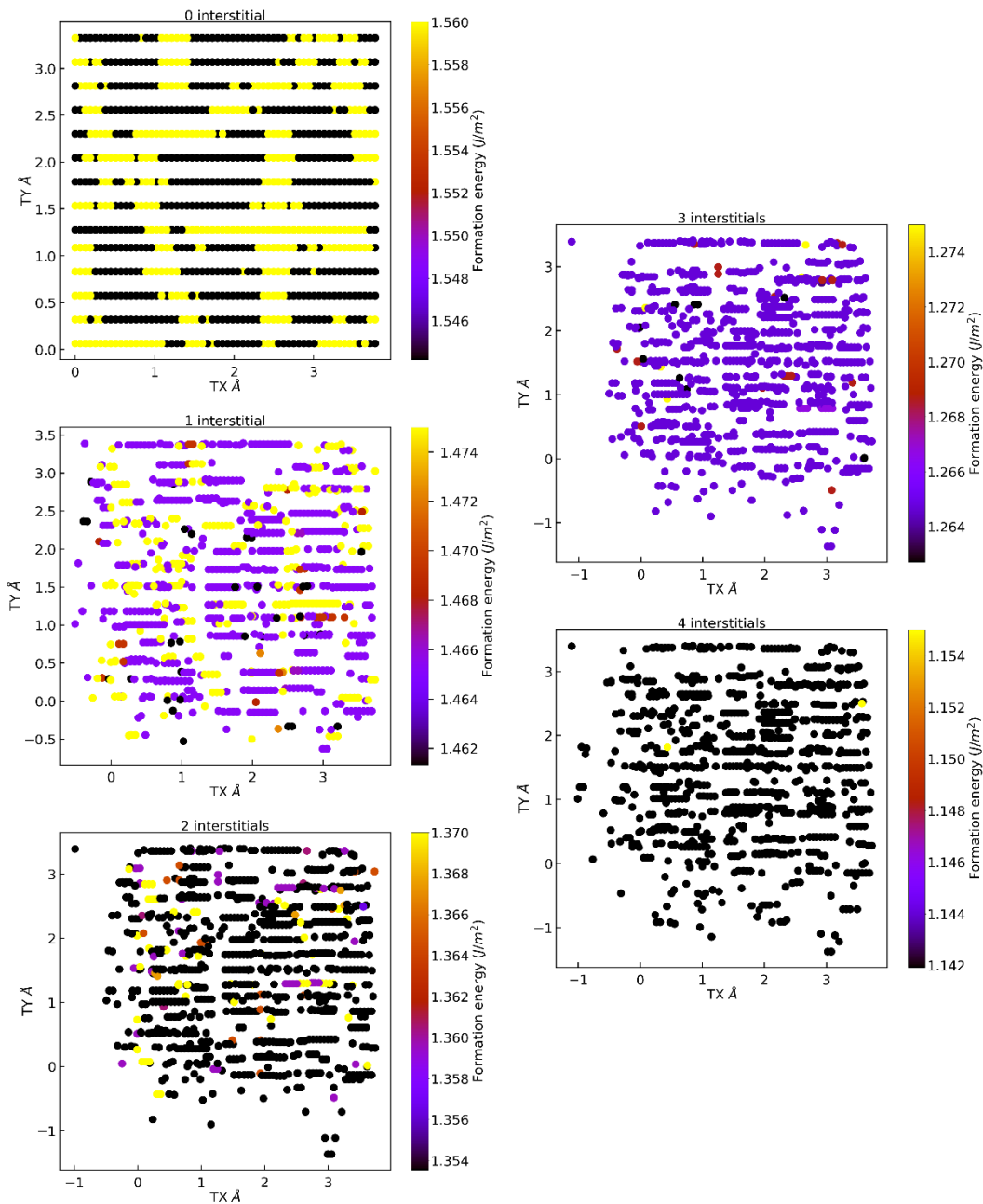


Figure III- 40: $\Sigma 5$ formation energies (J/m^2) selected at each step of `All_trans_method` as a function of TX and TY coordinates of the corresponding global translation expressed in \AA .

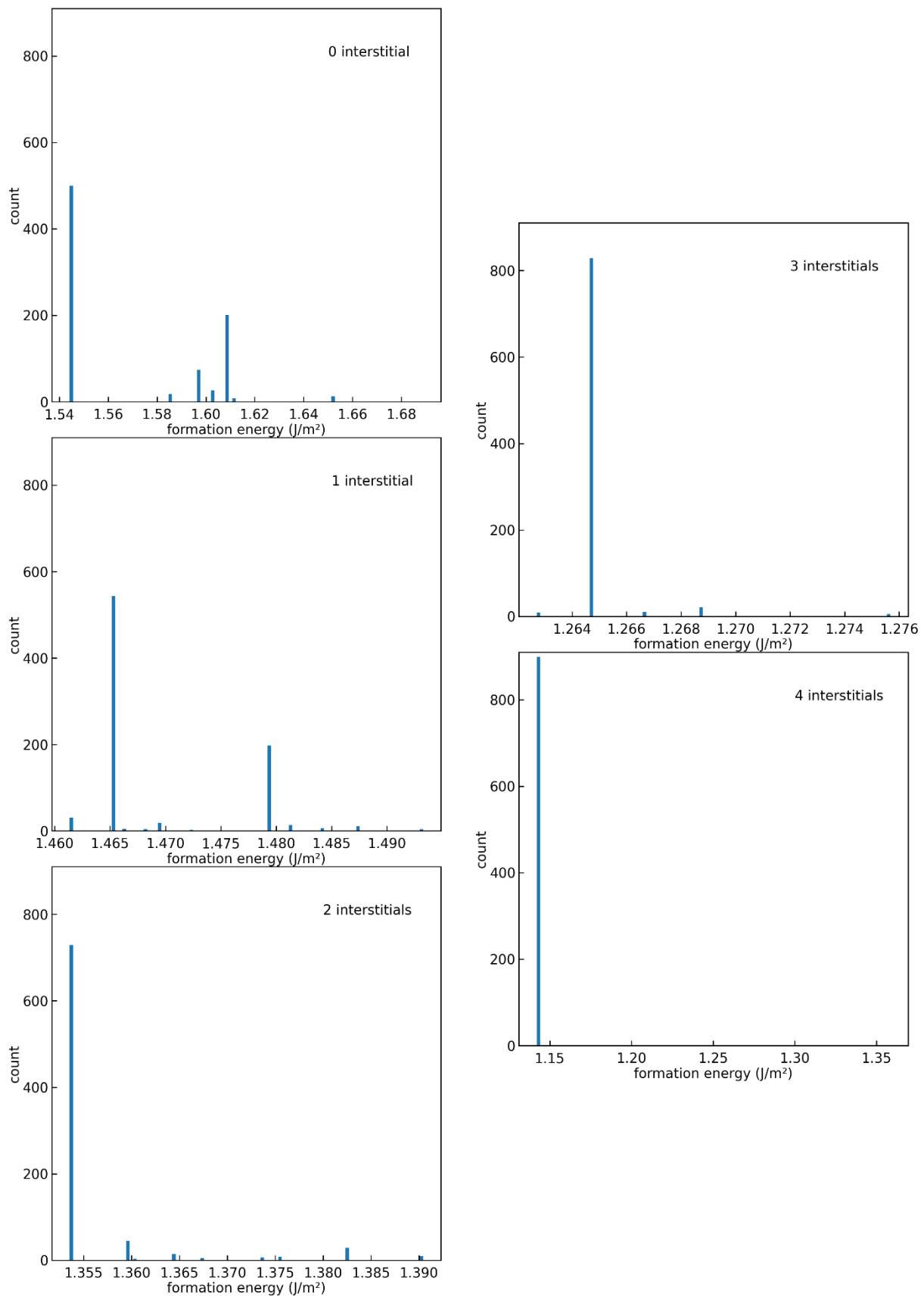


Figure III- 41: Σ distributions of the formation energies selected at each step of the **All_trans** method with the same formation energy data displayed in **Figure III- 40**.

GB	$\theta(^{\circ})$	All_trans_method		
		number of times the GS is reached	number of translations tested	% GS
$\Sigma 37$	18.92	5	538	1
$\Sigma 13$	22.62	189	625	30
$\Sigma 17$	28.07	408	675	60
$\Sigma 29$	43.6	36	675	5
$\Sigma 5$	53.13	838	840	100
$\Sigma 25$	73.74	11	657	2

Table III- 8: Percentage of GS found with **All_trans_method** relative to the total number of initial translations generated by γ -method that have been taken into account.

III-2.3.2 The MQ_method

As mentioned above, in the **MQ_method**, rather than trying all possible translations of the γ **surface**, we explore, for one initial translation, the GB phase space using a combination of interstitial addition (**INT stage**) and melt and quench followed by the introduction of interstitials (**MQ + INT stage**).

Adding SIAs on octahedral positions and performing MQ sequentially allows to converge to the GB ground state as seen **Figure III- 42** which shows the evolution of the formation energy as several iterations of the two-stage process are applied. The figure also displays at each iteration, which stage produces the lowest energy configuration. Overall, it can be seen that the formation energy of the GB decreases with the number of iterations, ultimately increasing again upon adding new iterations. The initial translations for this figure are the ones leading to the lowest (initial) formation energy for γ -method except for $\Sigma 29$ where another initial translation close in terms of formation energy to the lowest initial formation energy for γ -method ($E_f = 1.553 \text{ J/m}^2$). Only one branch conducts to the lowest formation energy is displayed. The other branches are not represented in this figure.

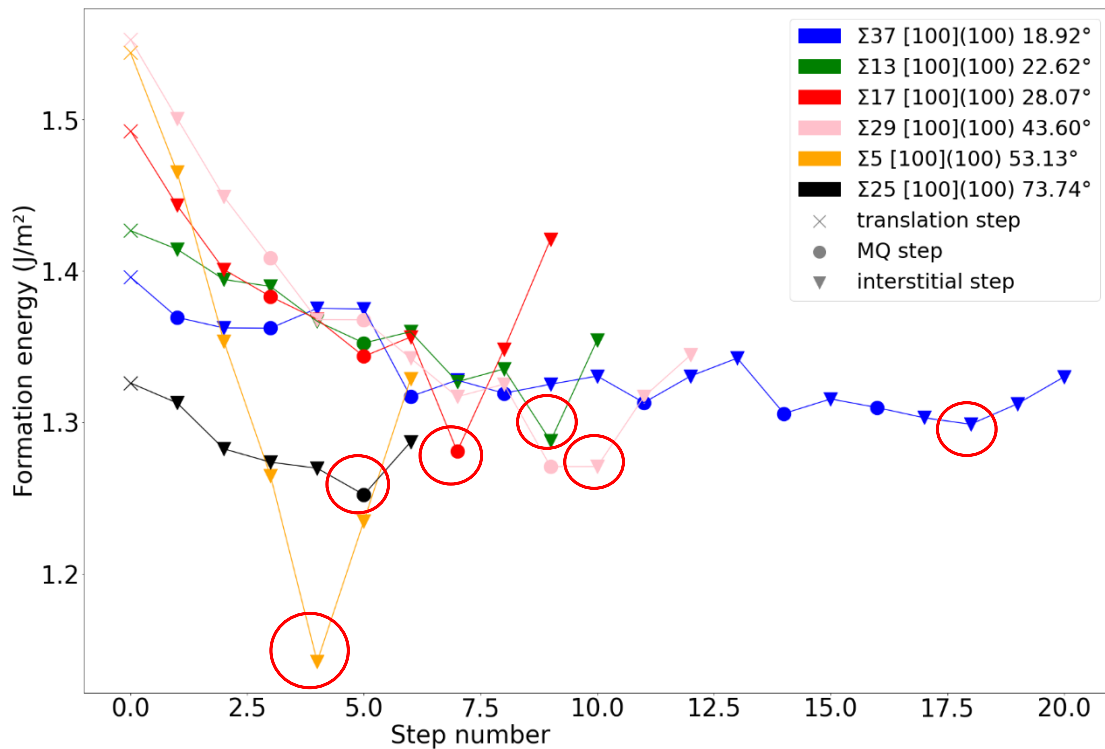


Figure III- 42: Formation energy as a function of step number. A translation step is indicated by a cross, a MQ step by a circle and an interstitial step by a triangle. The color indicates the corresponding misorientation angle. The initial translations for this figure are the ones leading to the lowest (initial) formation energy for γ -method. GS obtained are indicated by red circles.

The changes in formation energy between two steps (of **Figure III- 42** but also for the other branches not represented **Figure III- 42**) are presented on **III-Annex 5**. For the sake of clarity, energetic results are represented by two histograms:

- Left hand side: all ΔE between two steps
- Right hand side: positive ΔE before reaching the GS

According to **Figure III- 42**, the **MQ_method** allows to reduce the formation energy by at least 0.1 J/m^2 for all twist $\langle 100 \rangle$ GBs considered here. However, some differences can be observed depending on the GBs. The most significant reduction is found for $\Sigma 5$ with 0.4 J/m^2 and $\Sigma 29$ with almost 0.3 J/m^2 of decay. The number of iterations required to reach the lowest energy configuration depends also on the nature of the grain boundary. $\Sigma 37$, $\Sigma 13$ and $\Sigma 29$ require more iterations than $\Sigma 5$ and $\Sigma 25$. For $\Sigma 25$ and $\Sigma 5$ no MQ steps are even necessary. The decrease in formation energy occurs more or less quickly: the number of steps required to reach the GS is more or less important depending on the GB considered. Indeed, the variations in formation energy between each stage are more or less important: $\Sigma 5$ has formation energy decreases of the order of 0.05 J/m^2 at each stage unlike $\Sigma 37$ which, on average, has energy differences between each stage of the order of 0.01 J/m^2 . The stages MQ+INT and INT seem to lead to formation energy variations of the same order of magnitude.

According to **III-Annex 5 and 42**, in the same manner as **All_trans_method**, increases of formation energy can occur before reaching a local minimum. In that case, a stop condition of 0.14 J/m^2 can be used to determine the lowest energetic state. These increases of formation energy are characteristic for $\Sigma 37$ and $\Sigma 29$. An example for $\Sigma 37$ is presented **Figure III- 43**.

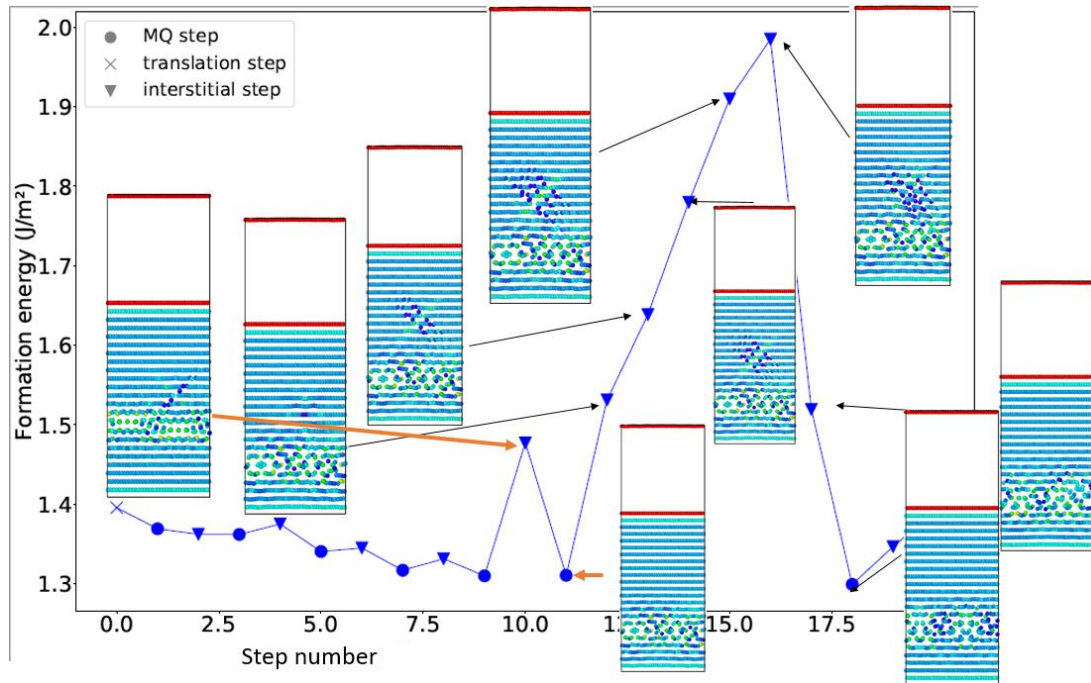


Figure III-43: Increases of formation energy before reaching the lowest formation energy for $\Sigma 37$, with the initial translation corresponding to the initial translation using in **Figure III- 42**

Increases of formation energy seem to be linked to a migration of the SIA inside the bulk part from the GB. Moreover, it should be noted that even when the minimum formation energy is reached, the GB plane can have migrated inside the bulk. It is the case of the example presented **Figure III- 43**. However, the microstructure obtained is the same as a centered GB. Furthermore, we have conducted a study of the impact of GB shifts. Details about the study are given in **III-Annex 6**. We have observed that migration of the GB is often associated to **MQ_steps** but it is not always the case.

The decrease in formation energy is accompanied by a decrease in the number of tension sites present in the GB compared to the initial translated microstructure. The same conclusion has been observed for **All_trans_method**. This evolution of the microstructure for **MQ_method** is illustrated for $\Sigma 5$ and $\Sigma 29$ in **Figure III- 44 and 45**. GB atomic volume distributions are represented in **III-Annex 1**; we observe that the atomic volume distribution of GBs generated shifts to lower atomic volume than GBs generated only with the γ -surface method, i.e. after the initial translation. The number of atoms with an atomic volume higher than 13 \AA^3 is null for GBs constructed with the **MQ_method**.

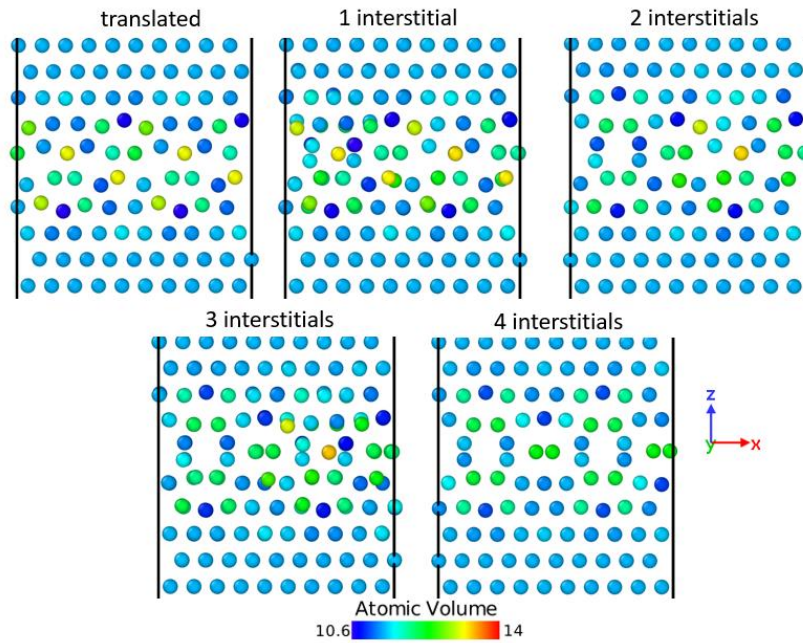


Figure III- 44: Evolution of $\Sigma 5$ microstructure as a function of the construction steps. The initial translation was the one leading to the lowest initial formation energy (lines in red in **Table III- 18** of **III- Annex 7**). The corresponding formation energy evolution is shown in **Figure III- 42**.

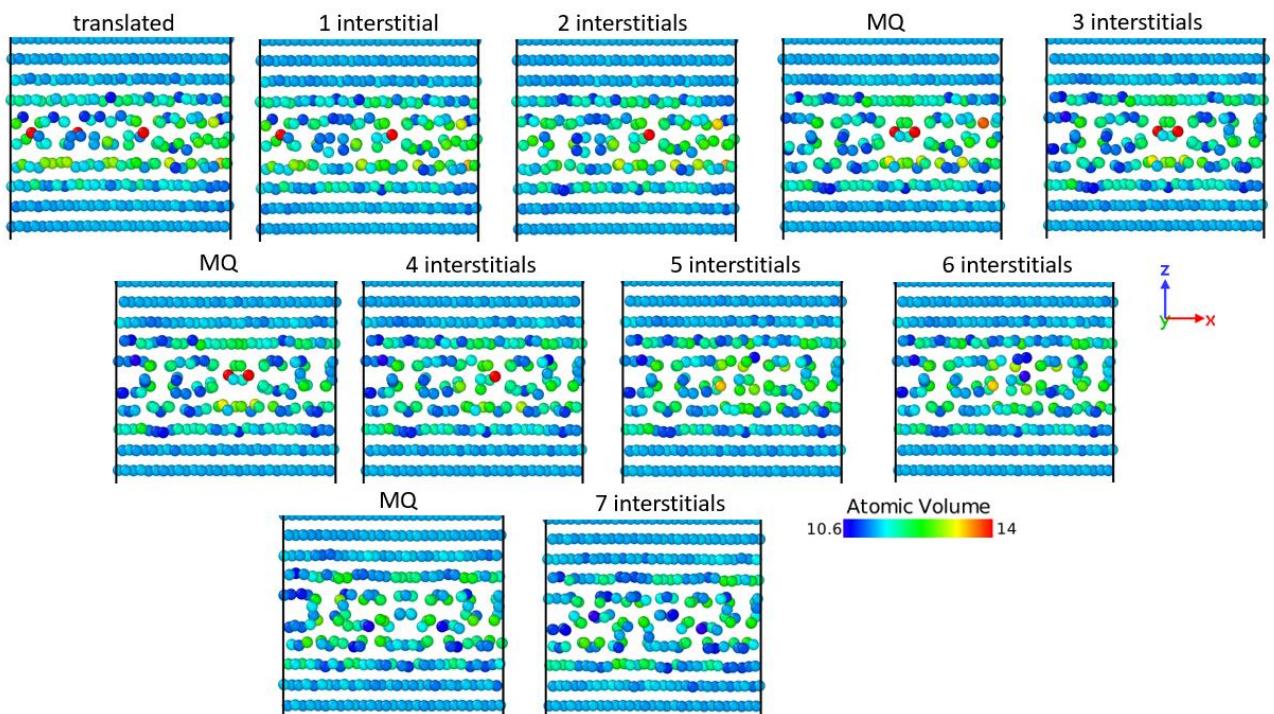


Figure III- 45: Evolution of $\Sigma 29$ microstructure as a function of the construction steps. The initial translation was the one leading to the lowest initial formation energy (lines in red in **Table III- 18** of **III- Annex 7**). The corresponding formation energy evolution is shown in **Figure III- 42**.

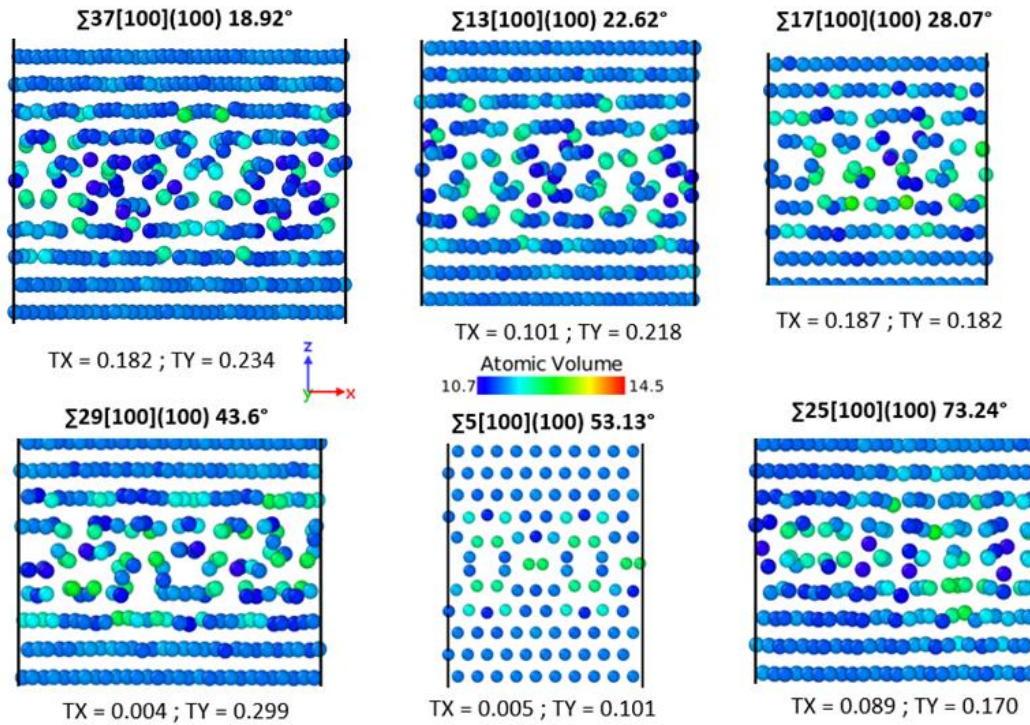


Figure III- 46: Final microstructure of GBs whose initial translation (in reduced coordinates) was the one leading to the lowest initial formation energy (lines in red in **Table III- 18** of **III-Annex 7**). The corresponding formation energy evolution is shown in **Figure III- 42**.

To check on the efficiency of **MQ_method**, we applied it to a few translations chosen so as to sample the **γ -surface** space (or the initial formation energy space). Due to the high computational cost of this method, only a limited set of translations corresponding to different initial energetic states have been tested. **Table III- 18** in **III-Annex 7** summarizes the different initial translations chosen for each GB as well as the results obtained with the **MQ_method**. **Figure III- 47** shows the evolution of the formation energy for each GB given in **III-Annex 7**. The initial translations have been chosen as a function of the formation energy: the aim is to compare GBs with different formation energy. After applied **MQ_method** only one GB which conducted to the GS has been selected because of the high number of GS structures that can be found. Because of the shift (part **2.2.2.3.**) of the GB during the GB construction only branches conducted to center GB have been selected. **III-Annex 8** shows the microstructures obtained. For each GB tested, the final minimum formation energy obtained is the same whatever the initial translation that has been applied. Even if the initial configurations have high initial formation energies, the GB formation energy quickly reaches values that are comparable within the set of translations considered here. A corollary to this observation is that initial configurations with high formation energy tend to see their formation energy decrease faster within the first steps of the building process. We can observe this fact on **Figure III- 47**, where different initial translations have been tested, the decrease of the first step of minimization is proportional to the initial formation energy of the translated GB constructed with the γ -method.

Interestingly, the number of interstitials (see **Table III- 18 in III-Annex 7**) that must be added is also the same whatever the initial translation. The number of necessary **MQ steps** (see **Table III- 18 in III-Annex 7**) on the other hand depends on the minimization series. Global translations obtained for each translated GBs for $\Sigma 37$, $\Sigma 13$, $\Sigma 17$, $\Sigma 29$, $\Sigma 5$ and $\Sigma 25$ represented on **Figure III- 48** are given in **Table III- 18 in III-Annex 7**. The final microstructures obtained are exactly the same regardless of the initial translation applied (**III-Annex 8**). On the other hand, the global translations, calculated for final minimized GB structures with different initial translations and the same final energy are always different. The same conclusion is observed for relative translation (Global – initial). Perhaps, these differences come from the symmetry of the GB pattern or the periodicity of the cell which is not considered in the calculation of the global translation.

According to **Table III- 9**, as with **All_trans_method** (**Table III- 8**), the percentage of branches that lead to a GS configuration is the lowest for $\Sigma 37$ and $\Sigma 25$. However, these percentages remain higher than the ones obtained with **All_trans_method**. Thus **MQ_method** seems to be more efficient to find the lowest energetic state than **All_trans_method** even if migration phenomena of the GB plane can take place during the construction of GBs especially during a **MQ_step** (more details part **2.2.2.3.**) and have to be taken into account.

GB	$\theta(^{\circ})$	MQ_method		
		mean number of GS obtained (mean of GS obtained for all translations tested Table III- 18 III-Annex 7)	total number of branches	% GS
$\Sigma 37$	18.92	3185	8192	39
$\Sigma 13$	22.62	579	1024	57
$\Sigma 17$	28.07	31	64	48
$\Sigma 29$	43.6	78	128	61
$\Sigma 5$	53.13	62	64	97
$\Sigma 25$	73.74	22	64	34

Table III- 9: Percentage of GS found with **MQ_method** relative to the total number of branches that have been taken into account.

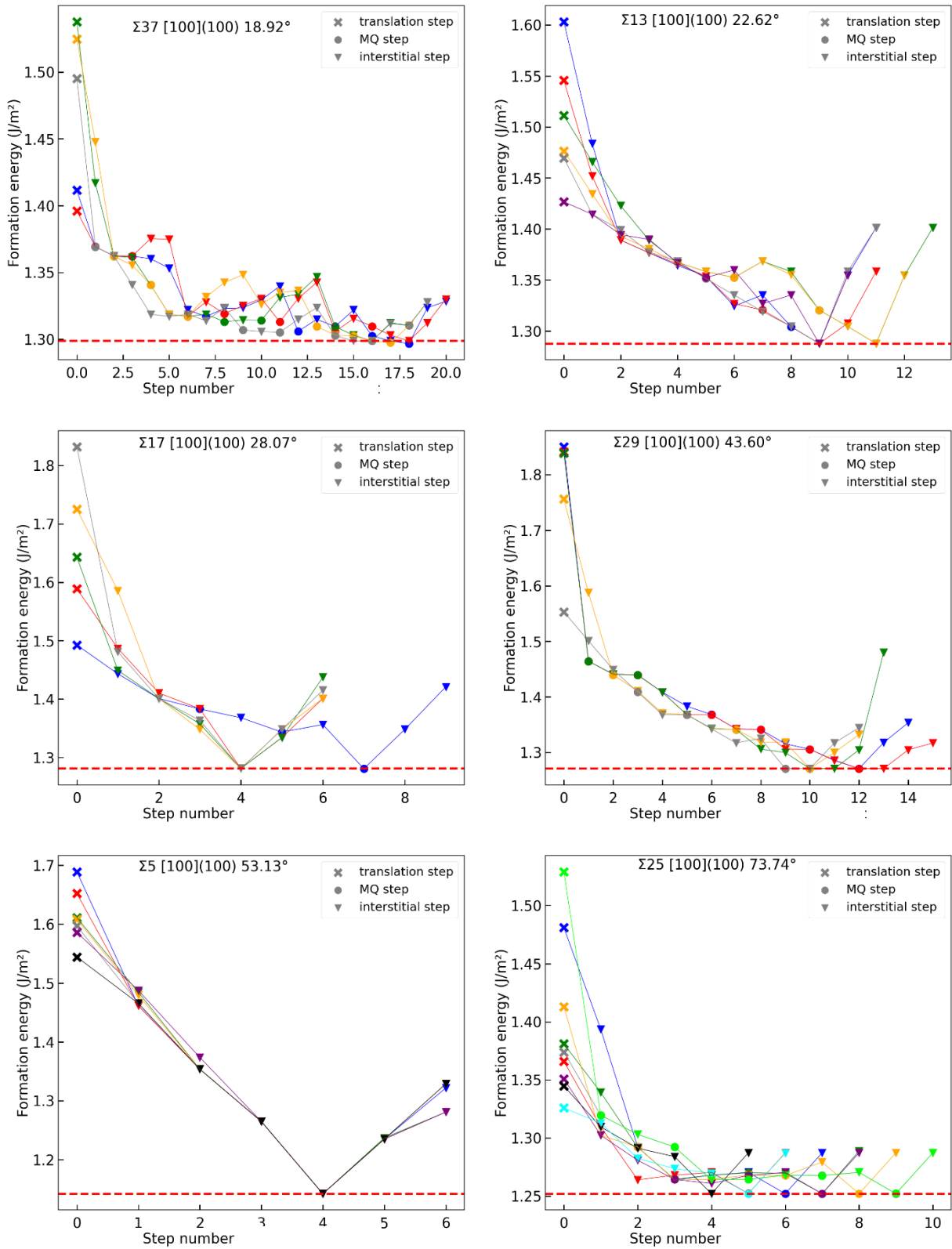


Figure III- 47: Formation energies of twist GB as a function step number obtained with **MQ method**. A translation step is indicated by a cross, a MQ step by a circle and an interstitial step by a triangle. Different colour indicates a different initial translation. The red-dotted line indicates the minimum GB formation energy obtained with this method.

GENERAL CONCLUSIONS FOR MQ_METHOD AND ALL_TRANS_METHOD

- The application of MQ INT and INT stages on a given translated GB seems to systematically lower the formation energy of the GB. Regardless of the initial formation energy of the translated GB, this methodology permits to approach the GS configuration rapidly: first steps of minimization are associated to a significant decrease of the formation energy.
- The number of interstitials that must be added can be large (4, 6, 7, 8 and 11 interstitials). $\Sigma 5$, $\Sigma 25$ and $\Sigma 17$ need only 4 interstitials to lower their GS energy. Thus, these GBs converge faster to the lowest energetic state.
- The percentage of GS structures is always lower for $\Sigma 37$ and $\Sigma 25$ whatever the method.
- MQ_method allows to construct low energy GB configurations without any translation step other than the initial one, however we observe that the introduction of SIAs followed by MQ steps could lead to a global translation (shift) of the GB. Furthermore, we observed that MQ steps can lead to a migration of the GB plane.
- We showed that the final GS when MQ_method is applied does not depend on the initial translation, this remains to be confirmed and a future work would be to study a larger set of initial translations.

III-2.3.4 Comparison of the two methods

III-2.3.4.1 Comparison of GB microstructures and formation energies.

The final formation energies, the number of SIA introduced, as well as the associated microstructure of the optimized GBs obtained with **All_trans_method** are the same as those obtained with **MQ_method**. **Table III- 10** and **Figure III- 48** illustrate these two points. According to **Figure III- 48**, as it is already explained in the previous part, the minimization of the GB formation energy is accompanied by a decrease of the number of tension sites around the GB plane, whatever the construction method has been chosen. However, the global translations and the relative translations associated with the minimum energy obtained for each GB for are always different between the two methods.

Method	GB	θ (°)	$E_{f_{ini}}$ (J/m ²)	E_f (J/m ²)	TX_{ini} (Å)	TY_{ini} (Å)	TZ_{ini} (Å)	TXG (Å)	TYG (Å)	TZG (Å)	TX (Å)	TY (Å)	TZ (Å)	Nb SIA	Nb MQ
MQ	$\Sigma 37$	18.92	1.396	1.299	0.278	5.079	0	2.397	2.300	0.063	2.119	-2.779	0.063	11	7
All_trans	$\Sigma 37$	18.92	1.444	1.299	1.392	4.731	0	1.263	4.048	0.074	-0.129	-0.683	0.074	11	0
MQ	$\Sigma 13$	22.62	1.426	1.288	1.458	3.150	0	2.261	5.735	0.081	0.803	2.586	0.081	8	1
All_trans	$\Sigma 13$	22.62	1.427	1.288	3.091	3.383	0	2.888	1.807	0.075	-0.203	-1.576	0.075	8	0
MQ	$\Sigma 17$	28.07	1.493	1.281	2.181	2.122	0	2.735	3.345	0.049	0.554	1.223	0.049	4	3
All_trans	$\Sigma 17$	28.07	1.544	1.281	1.297	2.948	0	1.130	2.566	0.047	-0.167	-0.381	0.047	4	0
MQ	$\Sigma 29$	43.6	1.553	1.271	0.062	4.558	0	-0.856	8.215	0.070	-0.917	3.657	0.070	6	3
All_trans	$\Sigma 29$	43.6	1.596	1.271	0.493	3.450	0	0.065	3.253	0.050	-0.428	-0.197	0.050	7	0
MQ	$\Sigma 5$	53.13	1.544	1.142	0.064	1.279	0	-0.920	1.877	0.044	-0.984	0.598	0.044	4	0
All_trans	$\Sigma 5$	53.13	1.608	1.142	2.941	1.279	0	2.919	0.769	0.046	-0.022	-0.510	0.046	4	0
MQ	$\Sigma 25$	73.74	1.326	1.252	3.260	0.629	0	6.007	1.131	0.039	2.747	0.502	0.039	4	1
All_trans	$\Sigma 25$	73.74	1.403	1.252	4.003	2.059	0	3.550	1.927	0.050	-0.454	-0.132	0.050	4	0

Table III- 10: Comparison of **All_trans_method** and **MQ_method**: formation energy, initial translations applied (after the γ -surface method) (TX_{ini} , TY_{ini} and TZ_{ini}), global translations (TXG , TYG and TZG), the relative translation between initial and global translation and the number of interstitials that have to be added to reach the lowest energetic configuration. **MQ_method** characteristics are indicated in blue colour and **All_trans_method** characteristics in orange colour.

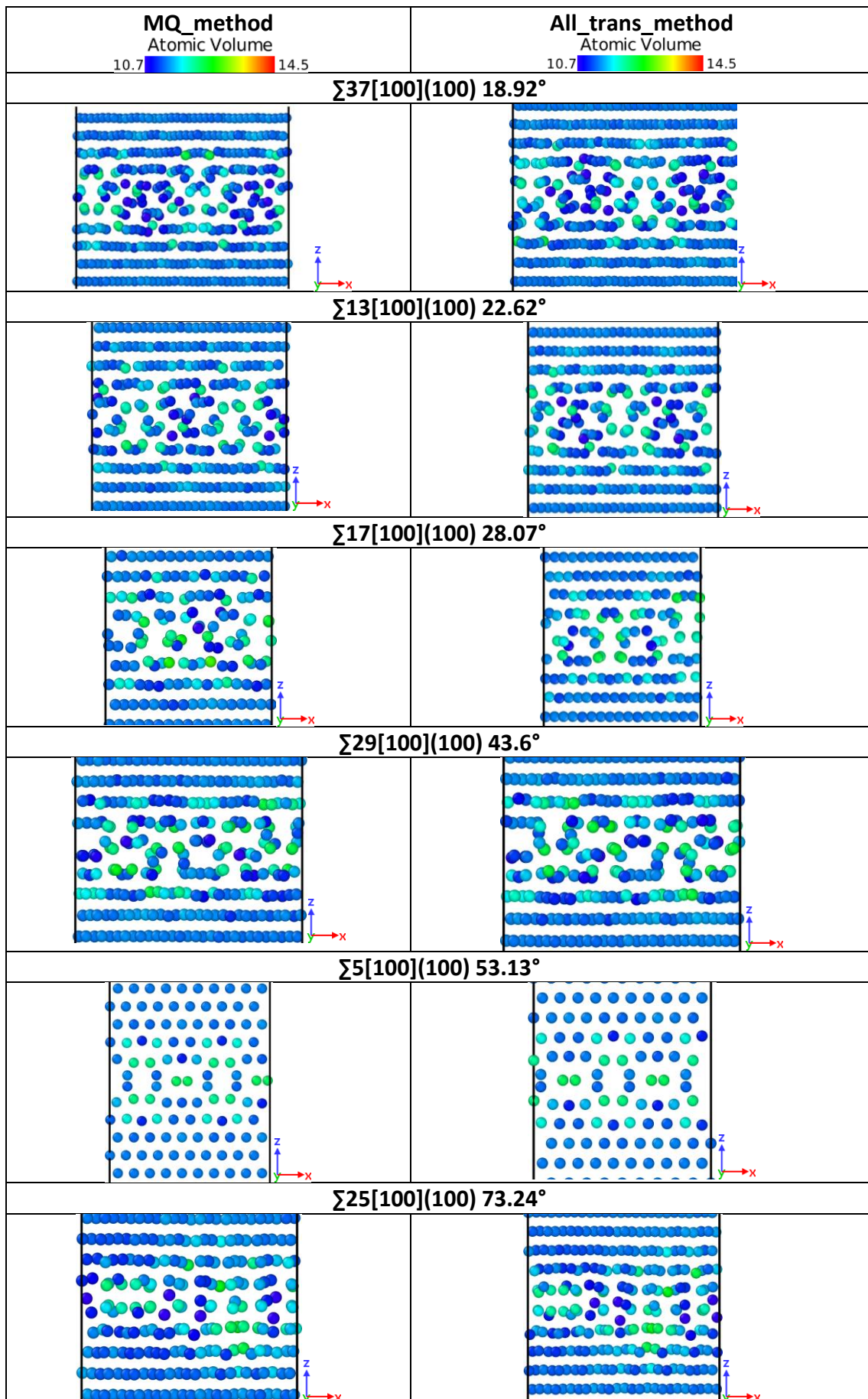


Figure III- 48: Microstructure comparison (atomic volumes) between the two methods

III-2.3.4.2 Comparison of computation time

Table III- 11 summarizes the number of calculations, the number of translations and the computational time for each method.

GB		$\Sigma 37$	$\Sigma 13$	$\Sigma 17$	$\Sigma 29$	$\Sigma 5$	$\Sigma 25$
Time 1 MQ (s)		82	91	39	101	71	56
Time INT (s)		30	20	14	22	16	20
All_trans method	Number of translations	538	625	675	675	840	657
	Number of calculations	139880	125000	81000	108000	100800	78840
	CPU time (h)	1166	694	315	660	448	438
	Real time (h)	2.18	1.11	0.46	0.98	0.53	0.67
	MQ_method	Number of translations	1	1	1	1	1
	Number of calculations	1146460	143220	8820	35700	8820	8820
	CPU time (h)	21390	2816	79	780	137	114
	Real time (h)	255	32	1.35	8.75	1.35	1.35

Table III- 11: Computational time characteristics of calculations performed with EP Ackland [70] and number of calculations and translations that have been performed for the two methods. The real time corresponds to parallelized calculations.

According to **Table III- 11**, the CPU time is always lower for **All_trans_method** than **MQ_method**, **MQ_method** is difficult to parallelize, thus the physical time needed for the calculation to finish is lower for **All_trans_method** which is easier to parallelize than **MQ_method**. For instance, for $\Sigma 37$ $\Sigma 13$ and $\Sigma 29$ the computational time is divided by 120, 32 and 9 respectively.

III-2.3.4.3 Comparison of GS percentage and CPU time for each method relative to the number of translations tested

GB	Angle (°)	All_trans_method				MQ_method	
		%GS 20 positions	%GS 60 positions	CPU time (h) 20 positions	CPU time (h) 60 positions	%GS 20 positions	CPU time (h) 20 positions
$\Sigma 37$	18.92	1		1166		39	21390
$\Sigma 13$	22.62	30		694		57	2816
$\Sigma 17$	28.07	60		315		48	79
$\Sigma 29$	43.6	5	30	660	1980	61	780
$\Sigma 5$	53.13	100		448		97	137
$\Sigma 25$	73.74	2	2	438	1314	34	114

Table III- 12: Computational time characteristics and GS percentage of calculations performed with **All_trans_method**, for 20 and 60 positions tested at each INT step and **MQ_method** for 20 positions tested at each INT step.

MQ_method seems more efficient than **All_trans_method** to generate low energy GB configurations. For some GBs ($\Sigma 37$, $\Sigma 29$ and $\Sigma 25$), **All_trans_method** leads to obtain a minimal energy poorly represented relative to the number of initial translations tested. Due to these observations, we have increased the number of positions of SIA tested (**Table III- 12**), nevertheless the percentage of GS obtain not always increases ($\Sigma 25$).

III-2.3.4.4 Comparison of the phase space explored by each method

We have compared the formation energy distributions of all minima (all minima obtained at each step of the construction are considering) obtained for each method. It is illustrated on **Figure III- 49**; the distribution is zoomed in **Figure III- 50** on the tail of the distribution for the sake of clarity.

By considering all possible translations, **All_trans_method** allows to explore extensively the configuration space; the configurations explored are more distributed over higher formation energy intervals than those explored by **MQ_method**. For example, for $\Sigma 17$, $\Sigma 29$ and $\Sigma 5$ the configurations with formation energies between 1.6 and 2 J/m² are more represented in percentage than with **MQ_method**. In contrast, **MQ_method** has sharper distributions of formation energies which are centered close to the minimum formation energy.

MQ_method permits to reach higher percentages of minimized GBs or configurations very close to the minimum energy than **All_trans_method**; the lowest energetic configurations do not represent more than 5% and often approach 0% of the configuration database for **All_trans_method** whereas GS GB configurations are more represented in the **MQ_method** method in terms of percentage: minimum energy configuration represents about 22% for $\Sigma 29$, 11% for $\Sigma 5$, 10% for $\Sigma 17$, 7% for $\Sigma 37$ of the configuration database for **All_trans_method** and the lowest percentages are attributed for $\Sigma 13$ and $\Sigma 25$ which are about 2%.

The percentages calculated for each method are different from those presented in **Table III- 8, 9 and 12** because we compared the number of GS obtained with all minimum formation energy obtained during the construction and not with the number of branches tested as it has been done in **Table III- 8, 9 and 12**. In this way, we can compare the configuration space explored by each method.

Finally using only one translation with MQ_method seems to be more adapted to find lowest energetic GB structures. However, we should bear in mind that the number of calculations that are performed for each method are different as explained in Figure III- 35 and 36 and Table III- 11, thus this conclusion must be taken with care.

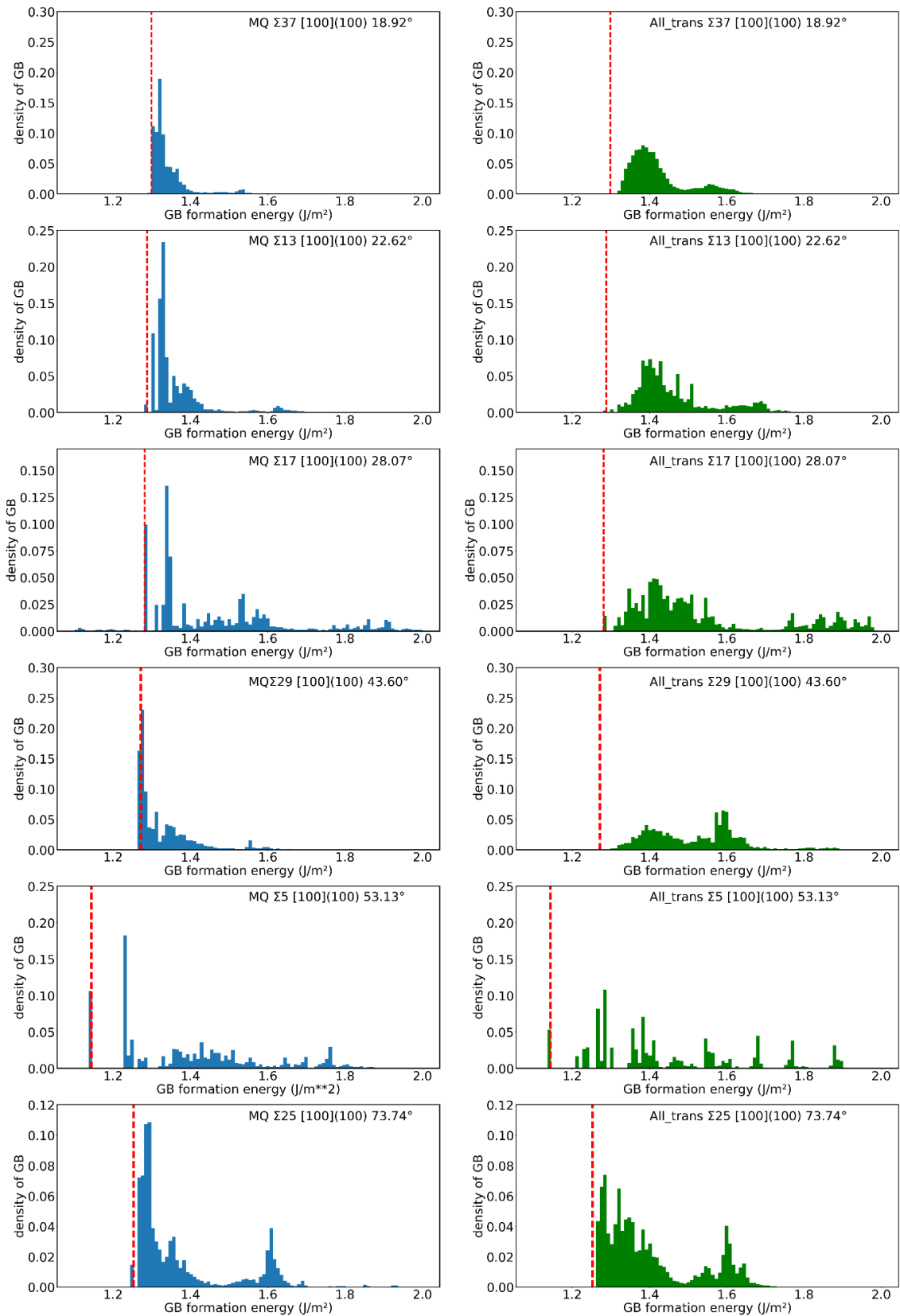


Figure III- 49: formation energy distributions of all the calculations made for **MQ_method** and **All_trans_method**. **MQ_method** is indicated by blue histograms and **All_trans_method** by green histograms. The red dotted line represents the minimum formation energy obtained for each construction method, for each misorientation angle.

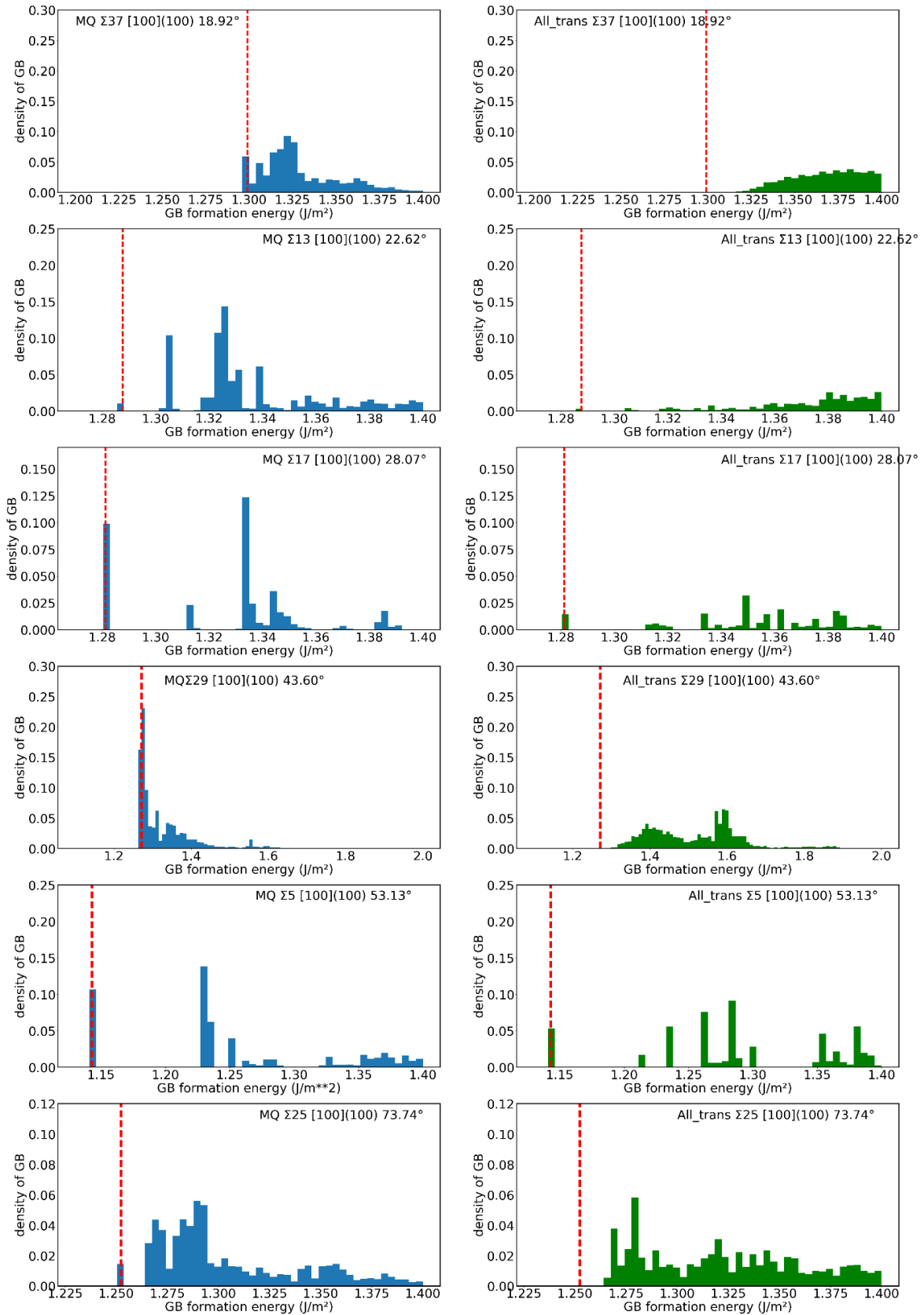


Figure III- 50: Tail of formation energy distributions of all the calculations made for **MQ_method** and **All_trans_method**. **MQ_method** is indicated by blue histograms and **All_trans_method** by green histograms. The red dotted line represents the minimum formation energy obtained for each construction method, for each misorientation angle.

- **MQ_method** seems more efficient than **All_trans_method** to generate low energy GB configurations. The formation energies, the number of interstitials to be added and the associated microstructures are very similar. The process of building the minimum GB formation energy with **All_trans_method** is dependent (not invariant) on the initial translation except for $\Sigma 5$ where all translations generated with the γ -method lead to the GS. The use of the γ -surface method in **All_trans_method**, which allows to generate all the possible translations, is therefore essential to find low GB energy configurations with this method unlike in the **MQ_method** in which the MQ steps help screen the translation space.
- For both methods, the global translations and the relative translations are not correlated with the variation of formation energy: for several GBs with the same formation energy and the same microstructure the global translation and the relative translation are both different. The global translation and the relative translation are therefore not good descriptors of the physical mechanisms, i.e. the relaxations taking place to reach the minimum energy final configuration.
- Energy decreases for both of methods. In some cases, there are energy rises before going back down to a lower energy, which is classic and encountered in minimization techniques.
- For some GBs ($\Sigma 37$, $\Sigma 29$ and $\Sigma 25$), **All_trans_method** leads to obtain a minimal energy poorly represented relative to the number of initial translations tested. Due to these observations, we have increased the number of position of SIA tested (Table III- 12), nevertheless the percentage of GS obtain not always increases ($\Sigma 25$).

III-3. Comparison of EP results with other potentials and DFT

So far the **MQ** and the **All_Trans** methods have been applied using EP only. DFT calculations have then been performed in order to confirm our conclusions and in particular the capability of this type of grain boundary to accommodate such a high number of interstitial atoms. As the two methods exposed before cannot be applied directly with DFT, only DFT calculations of relaxed EP configurations at each atomic treatment of the construction of a given branch have been performed.

In order to further validate our GB construction methodology, we calculated using another EP or DFT the following properties: (i) the formation energy of the GB, (ii) the binding energy of a point defect (self interstitial and vacancy) with the GB, (iii) the atomic volume and (iv) the atomic density of the GB per unit surface. The first two energetic properties have been described in *Chaper I*. The other properties related to the GB microstructure are described in *Chapter II*.

III-3.1 Comparison between EP and DFT

In this section, only DFT relaxation **Figure III- 51** calculations of relaxed EP configurations at each atomic treatment of the construction corresponding to the lowest intermediate energetic state of a given branch have been performed. We pay a particular attention on **MQ_method**, which seems to be more efficient than **All_trans_method** to find the lowest energetic state for twist GBs.

III-3.1.1 GB formation energy

To validate our methodologies, we have relaxed, **using DFT**, configurations obtained using the **MQ_method** and **All_trans_method**. For each GB we relaxed, using DFT, all the configurations leading to the most stable one (including the most stable one), i.e. all the configurations represented by crosses, circles and inverse triangles on **Figure III- 51a** (which is identical to **Figure III- 42**, except for $\Sigma 25$ for which another initial translation has been tested). All the resulting relaxed DFT formation energies are represented **Figure III- 51b**

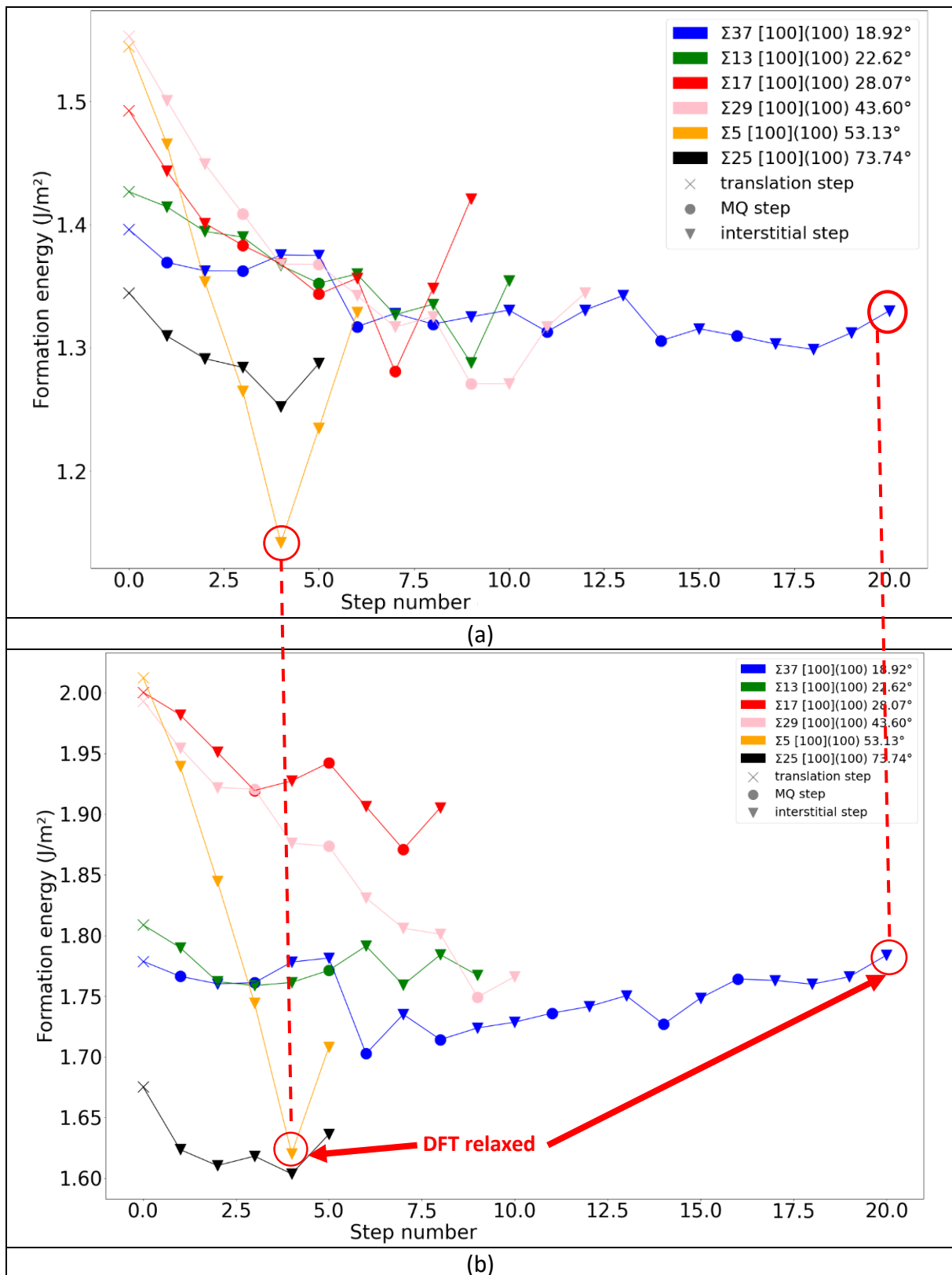


Figure III- 51: evolution of the formation energy vs the number of steps (a) using the **MQ_method** and as initial translation the one leading to the lowest initial formation energy same as in **Figure III- 42**, except for $\Sigma 25$ ($E_{f_{ini}} = 1.345$), (b) using as input for the DFT calculations, the configurations obtained using the **MQ_method**, i.e. using the data from (a). A translation event step is indicated by a cross, a MQ event by a circle and an interstitial event by a triangle. The color indicates the corresponding misorientation angle.

Figure III- 51b shows similar trends in the energy variations as for the EP calculations. The overall reduction in the formation energy obtained with the DFT is of the same order of magnitude as the reductions in formation energy obtained with the EP. It is at least for these tests 0.1 J/m^2 . The reduction is the most significant for $\Sigma 5$: 0.45 J/m^2 and for $\Sigma 29$: almost 0.25 J/m^2 .

To check if the conclusions drawn above apply whatever the method, we relaxed, using DFT, the configurations obtained for another set of **MQ_method** minimisation and with the set of configurations obtained with the **All_trans_method**, which led to the lowest GB formation energy. All these configurations, were, here also, relaxed using DFT calculations. The results are shown in **III-Annex 9**; we thus have, on **Figure III- 69**, for each GB, three series of calculations that have been minimized using DFT. The results are presented in **Table III- 13** where the first **MQ_method** case is referred to as a **MQ lowest initial energy** and the second **MQ_method** case is referred to as a **high MQ initial energy**.

Figure III- 69 shows similar trends in the energy variations as for the EP calculations whatever the input method for the DFT calculation (**MQ_method** or **All_trans_method**) except for $\Sigma 37$ and $\Sigma 13$ which present, as was the case during the EP calculations, a particular behavior: at some steps of the minimization the energy increases by about 0.01 J/m^2 then decreases to reach a more stable structure.

The decrease in the formation energy occurs quickly for $\Sigma 5$ in comparison to $\Sigma 37$, $\Sigma 13$ and $\Sigma 29$ which require more intermediate steps and therefore more interstitials. The variations in formation energy between each stage are more or less important depending on the GB. For $\Sigma 5$, the energy decrease is of the order of 0.1 J/m^2 at each stage whereas for $\Sigma 37$ the energy differences between each stage are of the order of 0.015 J/m^2 on average.

However, the GB created with the **MQ_method** can have final formation energies not exactly the same in comparison to those created with **All_trans_method** when they are relaxed by DFT while when they are relaxed with EP Ackland [70] they have the same final formation energy and the same microstructure. For example, $\Sigma 25$ created with **MQ_method** leads to a DFT formation energy close to 1.61 J/m^2 lower whereas when it is created with **All_trans_method**, the DFT formation energy is 1.627 J/m^2 . The same is observed for $\Sigma 37$ and $\Sigma 13$. The number of interstitials that have to be added seems to be the same, whatever the EP calculation (**MQ_method** or **All_trans_method**) investigated, for all GBs, except for $\Sigma 37$ and $\Sigma 13$:

- For $\Sigma 37$, for the GBs created with the **MQ_method**, the number of interstitials that must be added is about 3 for the lowest energy DFT configuration, in contrast to 5 interstitials with **All_trans_method**. In addition, the minimum DFT formation energy obtained is also a little bit different: 1.7 J/m^2 for **MQ_method** and 1.72 J/m^2 for **All_trans_method**.
- For $\Sigma 13$, for the GBs created with the **MQ_method**, the number of interstitials that must be added is 6 for the lowest energy DFT configuration and 4 for **All_trans_method**. In addition, the minimum DFT formation energy obtained is also a little bit different: 1.76 J/m^2 for **MQ_method** and 1.75 J/m^2 for **All_trans_method**.

It should be noted for $\Sigma 25$, that the minimum DFT formation energy is reached in two different steps corresponding to different numbers of interstitials (2 and 4 interstitials). The number of atomic treatments that have to be performed to obtain a ground state GB, is summarized in **Table III- 13**.

For each GB tested, the final minimum formation energy obtained is the same whatever the initial translation applied for **MQ_method**. The formation energy decreases and the decrease corresponding to the first steps of the minimization is as large as the GB formation is high.

- $\Sigma 17$, $\Sigma 29$ and $\Sigma 5$ created using either the **MQ_method** or the **All_trans_method** have similar energetic trends when they are relaxed using DFT calculations. The addition of the same number of interstitials as for the EP only minimizations leads to the same minimum DFT formation energy.

-For $\Sigma 37$ and $\Sigma 13$, the results obtained are different: the number of interstitials in the minimum energy DFT configurations is different from the number of SIAs in minimum energy for the EP only minimizations. Perhaps, it can be explained by the fact that DFT seems to relax at a shorter range than EP. In addition, we observed different energetic trends between **MQ_method** and **All_trans_method** for these two GBs: the number of interstitials and the minimum formation energy predicted by both these methods are different.

- Differences between DFT and EP can be explained by the fact that Ackland EP [70] is close to Mendeleev EP [67] which underestimates energies in comparison to DFT.

Method	GB	θ (°)	E_{EPini} (J/m ²)	E_{EP} (J/m ²)	E_{DFT} (J/m ²)	TX_{ini} (Å)	TY_{ini} (Å)	TZ_{ini} (Å)	TXG (Å)	TYG (Å)	TZG (Å)	TX (Å)	TY (Å)	TZ (Å)	Nb SIA EP	Nb MQ EP	Nb SIA DFT	Nb MQ DFT
MQ	$\Sigma 37$	18.92	1.396	1.299	1.703	0.278	5.079	0	2.397	2.300	0.063	2.119	-2.779	0.063	11	7	3	3
	$\Sigma 37$	18.92	1.525	1.299	1.698	3.618	1.948	0	2.625	0.689	0.119	-0.993	-1.259	0.119	11	6	3	3
All_trans	$\Sigma 37$	18.92	1.444	1.299	1.719	1.392	4.731	0	1.263	4.048	0.074	-0.129	-0.683	0.074	11	0	5	0
MQ	$\Sigma 13$	22.62	1.426	1.288	1.759	1.458	3.150	0	2.261	5.735	0.081	0.803	2.586	0.081	8	1	3	0
	$\Sigma 13$	22.62	1.546	1.288	1.757	3.674	4.083	0	6.757	7.598	0.070	3.083	3.515	0.070	8	1	6	0
All_trans	$\Sigma 13$	22.62	1.427	1.288	1.745	3.091	3.383	0	2.888	1.807	0.075	-0.203	-1.576	0.075	8	0	4	0
MQ	$\Sigma 17$	28.07	1.493	1.281	1.871	2.181	2.122	0	2.735	3.345	0.049	0.554	1.223	0.049	4	3	4	3
	$\Sigma 17$	28.07	1.643	1.281	1.876	3.478	2.358	0	6.668	3.589	0.059	3.190	1.231	0.059	4	0	4	0
All_trans	$\Sigma 17$	28.07	1.544	1.281	1.872	1.297	2.948	0	1.130	2.566	0.047	-0.167	-0.381	0.047	4	0	4	0
MQ	$\Sigma 29$	43.6	1.553	1.271	1.749	0.062	4.558	0	-0.856	8.215	0.070	-0.917	3.657	0.070	7	3	6	3
	$\Sigma 29$	43.6	1.839	1.271	1.749	1.971	2.341	0	2.499	3.490	0.071	0.528	1.150	0.071	7	4	6	4
All_trans	$\Sigma 29$	43.6	1.596	1.271	1.751	0.493	3.450	0	0.065	3.253	0.050	-0.428	-0.197	0.050	7	0	6	0
MQ	$\Sigma 5$	53.13	1.544	1.142	1.620	0.064	1.279	0	-0.920	1.877	0.044	-0.984	0.598	0.044	4	0	4	0
	$\Sigma 5$	53.13	1.689	1.142	1.622	1.726	0.064	0	2.751	-0.482	0.075	1.025	-0.546	0.075	4	0	4	0
All_trans	$\Sigma 5$	53.13	1.608	1.142	1.620	2.941	1.279	0	2.919	0.769	0.046	-0.022	-0.510	0.046	4	0	4	0
MQ	$\Sigma 25$	73.74	1.326	1.252	1.604	3.260	0.629	0	6.007	1.131	0.039	2.747	0.502	0.039	4	1	4	0
	$\Sigma 25$	73.74	1.529	1.252	1.607	2.230	3.546	0	2.613	6.820	0.036	0.383	3.274	0.036	4	5	2	2
All_trans	$\Sigma 25$	73.74	1.403	1.252	1.627	4.003	2.059	0	3.550	1.927	0.050	-0.454	-0.132	0.050	4	0	4	0

Table III- 13: Initial translations (TX_{ini} , TY_{ini} and TZ_{ini}) applied during the γ -method, global translations (TXG , TYG and TZG) and the relative translation (TX , TY , TZ) between initial and global translation obtained for each translated GB after the application of **MQ_method** or **All_trans_method**. E_{EPini} is the initial formation energy obtained after the γ -surface method, E_{EP} the formation energy corresponding to the lowest energetic state after the application of each method and E_{DFT} the formation energy for the lowest energetic state configuration after the application of each method used as an Input for DFT calculation. The number of interstitials and MQ that have to be added to reach the lowest energetic configuration are indicated in the four last columns.

III-3.1.2 GB microstructures

In complement to the energetic study, a comparison of the microstructures obtained has been carried out. Relaxed microstructures of GBs generated with **MQ_method** and **All_trans_method** by EP Ackland [70] calculations have been compared with the same structures relaxed in DFT: the microstructures are represented as a function of atomic volume in **Figure III- 53**, the atomic volume distributions are presented on **Figure III- 52** and finally atomic density repartition are showed in **Figure III- 54**. As in the previous section, two initial translations have been studied for **MQ_method**: one translation corresponding to a low energetic state generated by using an initial translation close or equal to the lowest energetic GB structure obtained by γ -method and the other one to a low energetic state generated by using a high energetic GB initial translated state close or equal to the highest energetic GB structure obtained by γ -method. For **All_trans_method** we considered only one configuration corresponding to the lowest energetic structure among all initial translations tested. It corresponds for each misorientation angle to the three microstructures presented in **Table III- 13**.

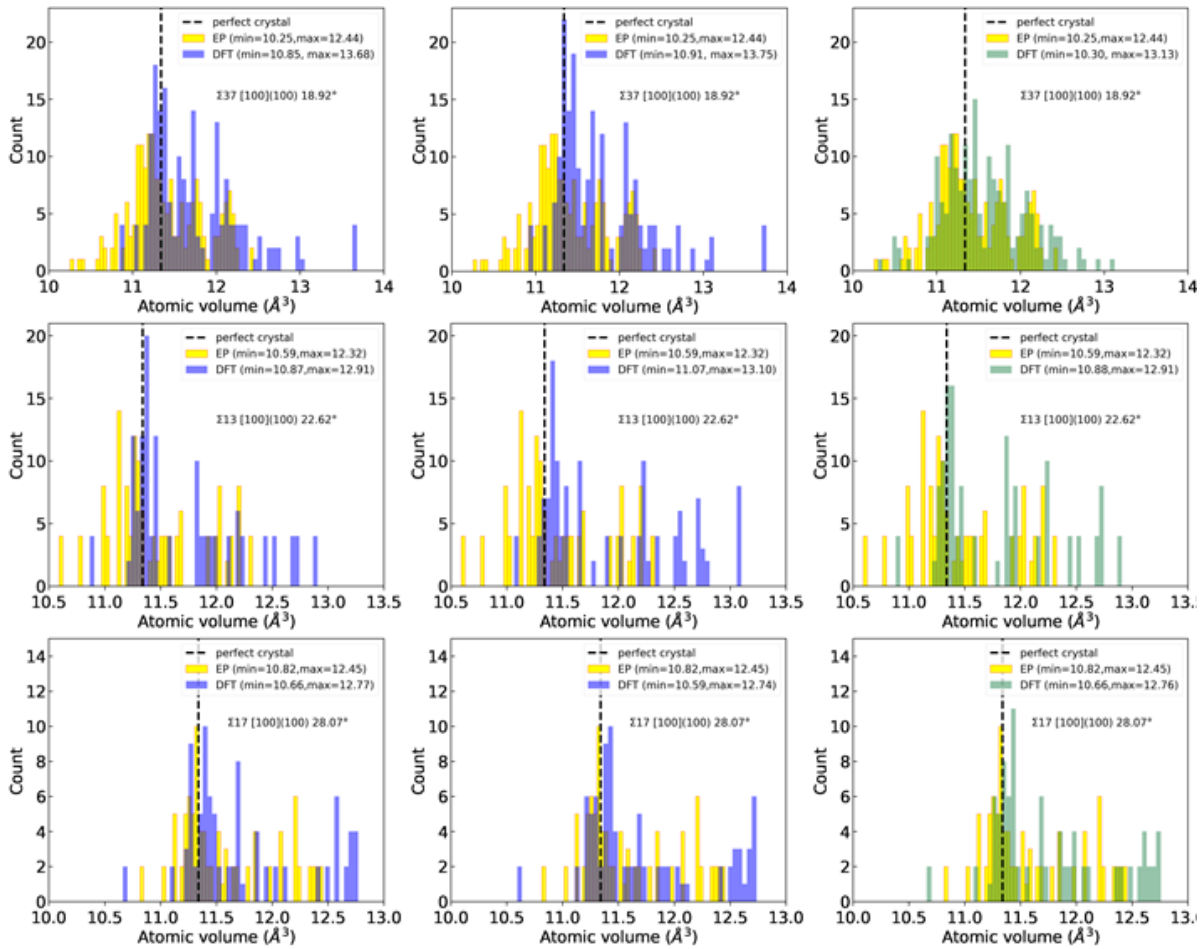


Figure III- 52 part 1: Atomic volume DFT distributions obtained with **MQ_method** results as input are plotted in blue; two different translations are considered the first column corresponds to low energetic initial translated GB (close to the minimum found with the γ -method) and the second column corresponds to higher energetic initial translated GB (close to the maximum formation energy found with the γ -method). The third corresponds to DFT distributions corresponding to **All_trans_method** Input are plotted in green. All these atomic volume distributions are compared to **MQ_method** and **All_trans_method** results (using Ackland *et al* EP [70]) coloured in yellow with both of these methods. The atomic volume of the bulk is indicated by black dotted lines.

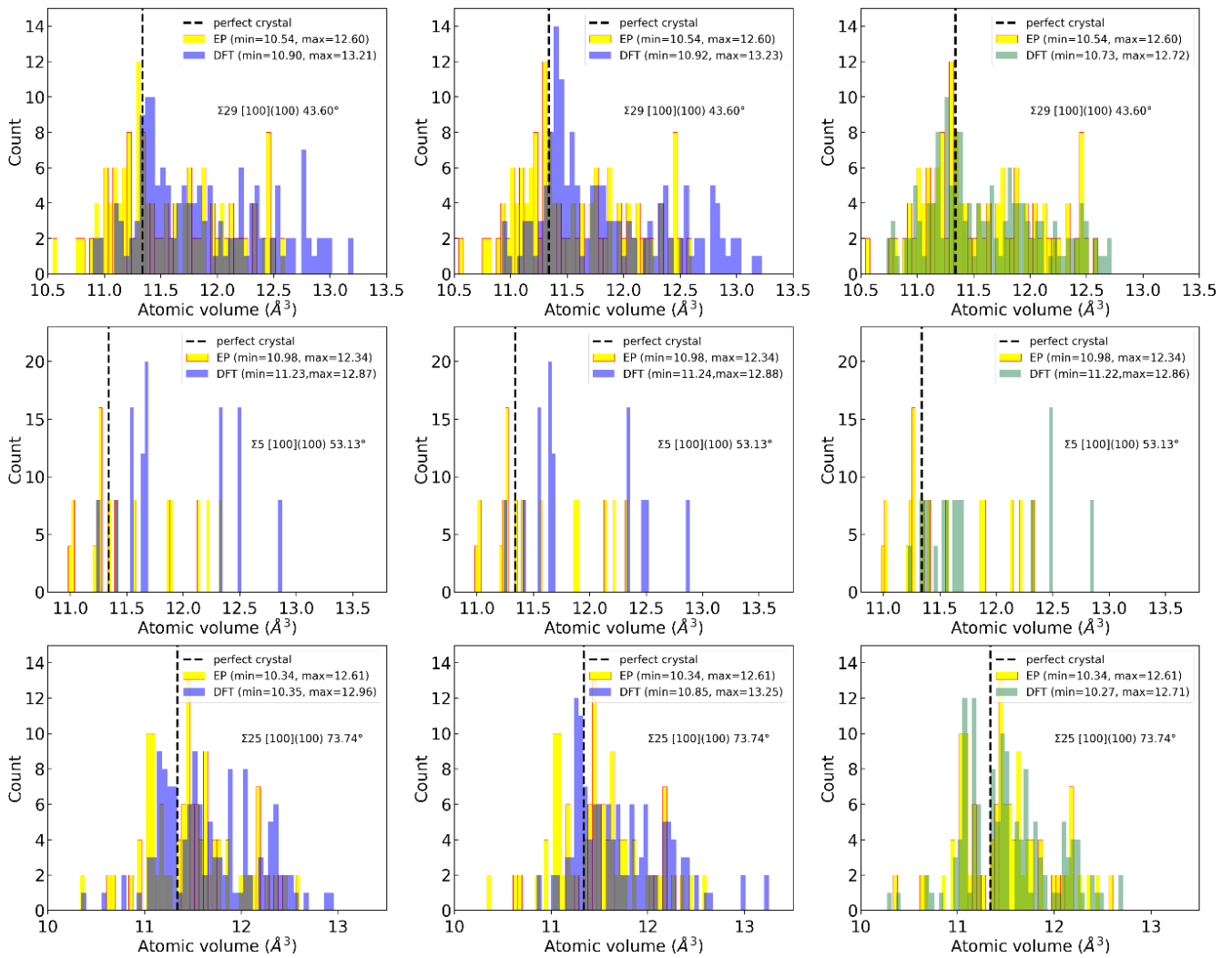


Figure III- 52 part 2: Atomic volume DFT distributions obtained with **MQ_method** results as input are plotted in blue; two different translations are considered the first column corresponds to low energetic initial translated GB (close to the minimum found with the γ -method) and the second column corresponds to higher energetic initial translated GB (close to the maximum formation energy found with the γ -method). The third corresponds to DFT distributions corresponding to **All_trans_method** Input are plotted in green. All these atomic volume distributions are compared to **MQ_method** and **All_trans_method** results (using Ackland *et al* EP [70]) coloured in yellow with both of these methods. The atomic volume of the bulk is indicated by black dotted lines.

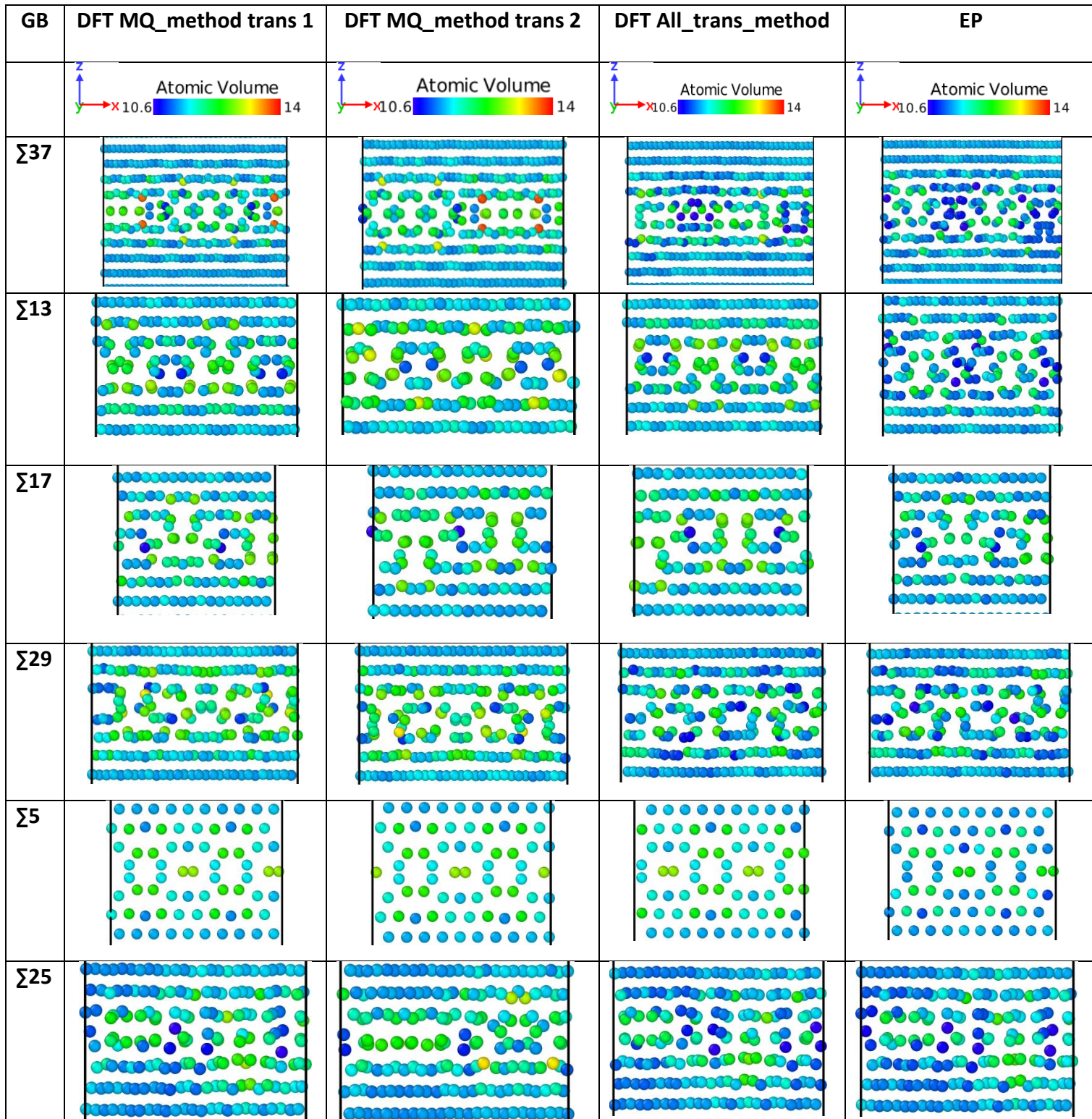


Figure III- 53: GB microstructures obtained with **MQ_method** and **All_trans_method**, relaxed using DFT are plotted as a function of misorientation angle and compared to results of **MQ_method** and **All_trans_method** (obtained by EP Ackland [70] calculation); two different translations are considered for **MQ_method**, trans 1 corresponds to an initial low energetic initial translated GB and trans 2 corresponds to an initial higher energetic initial translated GB.

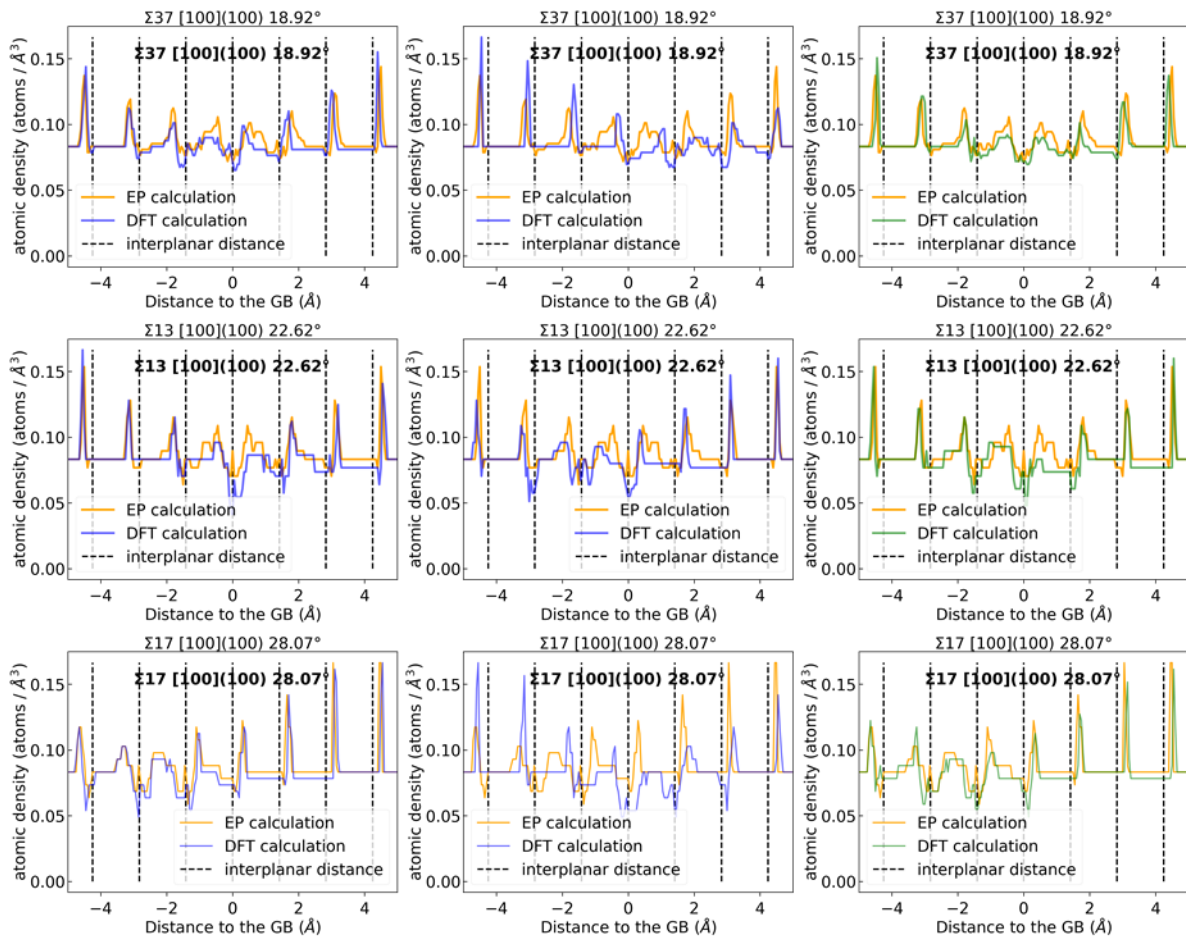


Figure III- 54 part 1: Atomic density distributions centred on the GB plane obtained with **MQ_method** relaxed using DFT are plotted in blue; two different translations are considered the first column corresponds to a low energetic initial translated and the second column corresponds to a higher energetic initial translated GB. Distributions centred on the GB corresponding to **All_trans_method** relaxed using DFT are plotted in green. All these atomic density distributions are compared to **MQ_method** and **All_trans_method** (i.e. to EP results obtained with Ackland *et al* EP [70]) coloured in yellow with both of these methods. The interatomic distance is indicated by black dotted lines.

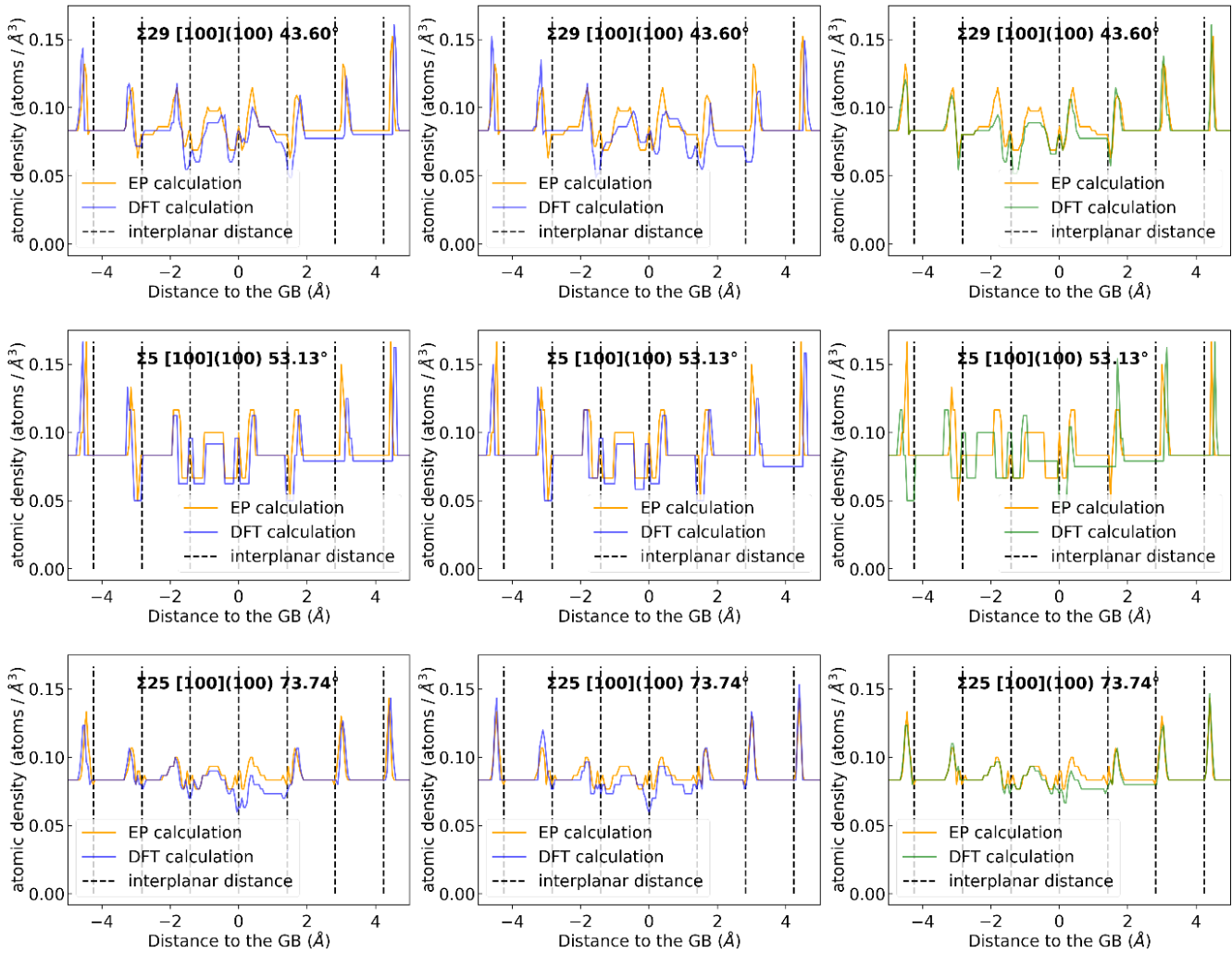


Figure III- 54 part 2: Atomic density distributions centred on the GB plane obtained with **MQ_method** relaxed using DFT are plotted in blue; two different translations are considered the first column corresponds to a low energetic initial translated and the second column corresponds to a higher energetic initial translated GB. Distributions centred on the GB corresponding to **All_trans_method** relaxed using DFT are plotted in green. All these atomic density distributions are compared to **MQ_method** and **All_trans_method** (i.e. to EP results obtained with Ackland *et al* EP [70]) coloured in yellow with both of these methods. The interatomic distance is indicated by black dotted lines.

Microstructures produced with **MQ_method** and **All_trans_method**, using as an Input for DFT calculations are very close in comparison to EP simulation for $\Sigma 17$, $\Sigma 5$, $\Sigma 29$ and $\Sigma 25$ with similar atomic volume patterns observed (**Figure III- 54**). The associated atomic volume distribution seems to overlap, in particular for $\Sigma 29$ and $\Sigma 25$. However, all atomic volume distributions seem to shift to high atomic volume values for the case of DFT calculations; the atomic density distributions are very close except for $\Sigma 17$ trans 2. It should be noted that $\Sigma 25$ trans 2 microstructure is different from other microstructures obtained with **MQ_method** and **All_trans_method** but the corresponding atomic volume distribution is similar to other DFT GB tested

In contrast $\Sigma 37$ and $\Sigma 13$ DFT configurations present different microstructures from GBs obtained with EP Ackland [70]. For example, $\Sigma 37$ contains more tension sites in its DFT structure and its microstructural pattern is different from the EP structure. $\Sigma 13$ have also a very different atomic volume microstructural pattern compared to GBs obtained with EP. The atomic volume distribution is similar for $\Sigma 37$, in particular for DFT **All_trans_method** GB. A high proportion of atoms with atomic volume close to the bulk is observed for these two GBs. A shift to high atomic volume values is also clearly identified for both of these two GBs.

MQ_method and All_trans_method allow to for $\Sigma 17$, $\Sigma 5$, and $\Sigma 29$ whatever the type of calculation to similar atomic construction which lead to similar GB microstructure. For those three GBs, the number of interstitials that must be added in the GB are exactly the same and the resulting microstructures are very close to DFT calculations.

For $\Sigma 37$ and $\Sigma 13$, DFT calculations showed a different behavior: the number of interstitials that have to be added can be smaller and the final DFT microstructures obtained are different i.e. apparition of tension sites.

In addition, MQ_method and All_trans_method can predict different final DFT microstructures which correspond to different formation energies ($\Sigma 25$).

III-3.2 Impact of the choice of EP

III-3.2.1 GB formation energy

In complement to the DFT study, the **MQ_method** has also been tested using Marinica potential [80], [81]. We observe that whatever the potential used (EP Ackland [70] and EP Marinica [80], [81]), the number of SIAs that have to be added around the GB plane, is the same for a given misorientation angle (**Figure III- 55 and Table III- 14**) except for $\Sigma 29$. The number of MQ is less predictable.

GB	Θ°	EP Marinica			EP Ackland		
		Nb SIA	Nb MQ	Ef (J/m ²)	Nb SIA	Nb MQ	Ef (J/m ²)
$\Sigma 13$	22.62	8	0	1.356	8	1	1.288
$\Sigma 17$	28.07	4	0	1.359	4	3	1.281
$\Sigma 29$	43.60	8	1	1.285	7	3	1.271
$\Sigma 5$	53.13	4	0	1.141	4	0	1.142
$\Sigma 25$	73.74	4	1	1.330	4	1	1.252

Table III- 14: Number of **MQ_steps** microstructures obtained with **MQ_method** using EP Marinica and EP Ackland, number of SIA, for microstructures obtained with **MQ_method** using EP Marinica and EP Ackland and their associated formation energy.

Note that the initial translations using to make the comparisons in **Table III- 14-16**, are different between Marinica and Ackland calculations.

As it has been done in section III-3.1.1, DFT calculations using as Input GS GBs and the lowest energetic GB intermediate state, of **MQ_method** construction have been performed. According to **Table III- 15**, the number of interstitials and formation energies predicted in DFT for Input GBs relaxed with EP Marinica [80], [81] are the same as DFT Input GBs relaxed with EP Ackland [70] except for $\Sigma 17$.

GB	Θ°	DFT Input "Marinica"			DFT Input "Ackland"		
		Nb SIA	Nb MQ	Ef (J/m ²)	Nb SIA	Nb MQ	Ef (J/m ²)
$\Sigma 13$	22.62	3	0	1.754	3	0	1.759
$\Sigma 17$	28.07	4	0	1.912	4	3	1.871
$\Sigma 29$	43.60	6	1	1.746	6	3	1.749
$\Sigma 5$	53.13	4	0	1.622	4	0	1.620
$\Sigma 25$	73.74	4	1	1.605	4	0	1.604

Table III- 15: Number of **MQ_steps** microstructures obtained with **MQ_method** using Input GBs relaxed with EP Marinica [80], [81] and EP Ackland [70] for DFT calculation, number of SIA, for microstructures obtained with **MQ_method** using Input GBs relaxed with EP Marinica and EP Ackland for DFT calculation and their associated formation energy.

The number of atomic treatments that has to be performed to obtain a ground state GB, is summarized in **Table III- 16**.

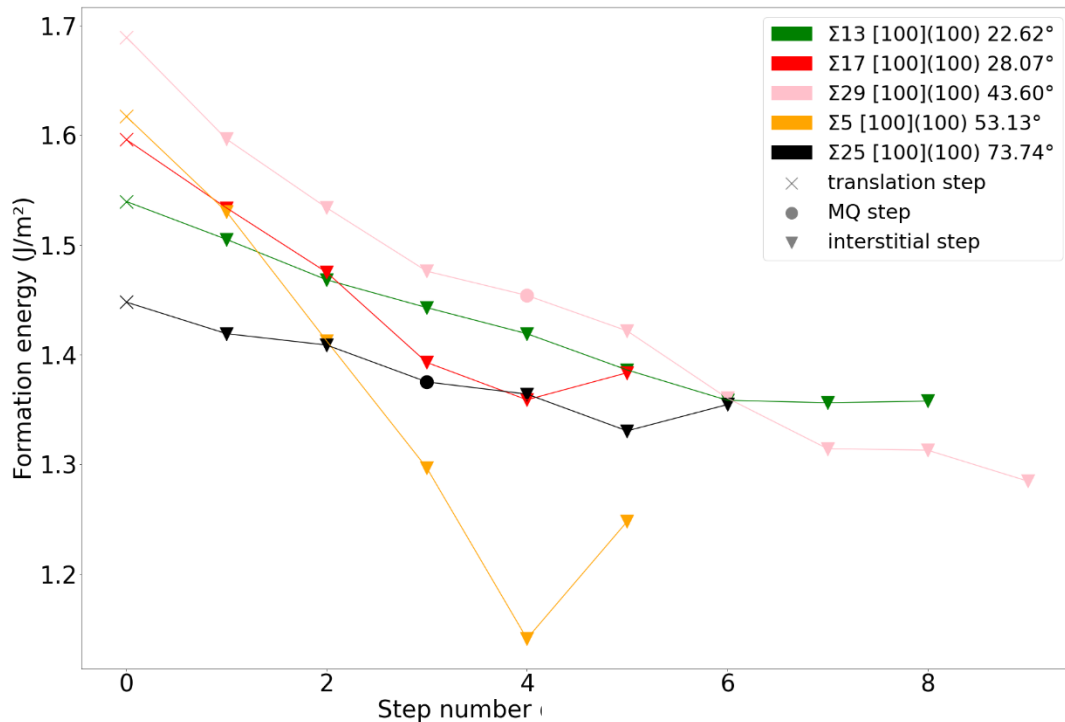


Figure III- 55: Formation energy (**MQ_method**) calculated with EP Marinica [80], [81] of twist GBs as a function of step number. A translation step is indicated by a cross, a MQ step by a circle and an interstitial step by a triangle.

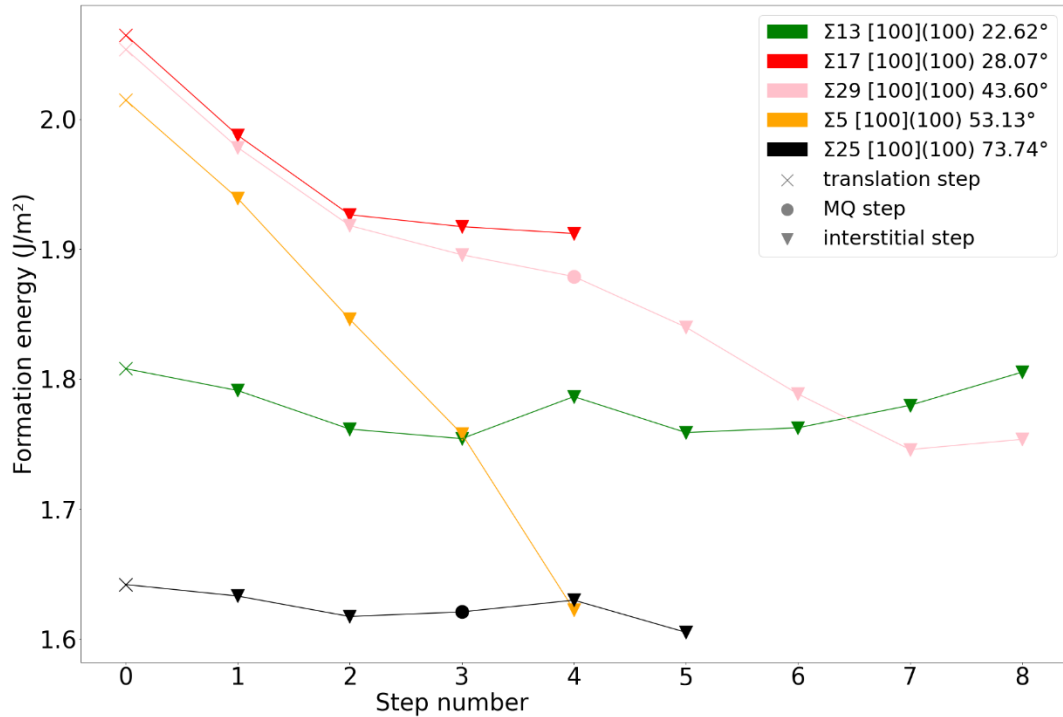


Figure III- 56: Evolution of the formation energy vs the number of steps using as input for the DFT calculations, the configurations obtained using the **MQ_method**, i.e. using the data from **Figure III- 55**. A translation event step is indicated by a cross, a MQ event by a circle and an interstitial event by a triangle. The color indicates the corresponding misorientation angle.

GB	Θ°	Nb of SIA EP Marinica	Nb of SIA DFT	Nb of MQ EP Marinica	TX_{ini}	TY_{ini}	TZ_{ini}
Σ_{13}	22.62	8	3	0	0.101	0.121	0.0
Σ_{17}	28.07	4	4	0	0.081	0.152	0.0
Σ_{29}	43.60	6	6	1	0.101	0.218	0.0
Σ_5	53.13	4	4	0	0.005	0.025	0.0
Σ_{25}	73.74	4	4	1	0.012	0.178	0.0

Table III- 16: Initial translations TX_{ini} , TY_{ini} and TZ_{ini} (correspond to the initial translation in reduced coordinates which conducted to the minimum formation energy with γ -method with EP Marinica potential), number of **MQ_steps** microstructures obtained with **MQ_method** using EP Marinica, number of SIA, for microstructures obtained with **MQ_method** using EP Marinica and for the microstructures associated relaxed with DFT.

III-3.2.2 GB microstructures

The microstructures obtained are given in **III-Annex 10**. The atomic distributions of EP Ackland [70] and EP Marinica [80], [81] are similar for all GBs. The microstructural atomic volume pattern is also analogous except for Σ_{29} which leads to a different atomic density.

DFT relaxed GBs obtained with **MQ_method** with EP Ackland [70] and with EP Marinica [80], [81] are also compared in **III-Annex 12**. They present similar atomic volume distribution. Σ_{13} and Σ_{29} obtained with “Marinica input”, have a wider atomic volume distribution to higher atomic volume sites, however their microstructural atomic patterns are similar.

Microstructural atomic patterns of GBs obtained with Marinica and Ackland input are the same.

The comparison between, GBs relaxed with EP Marinica [80], [81] and those GBs relaxed with DFT leads to the same conclusion as GBs initially relaxed with EP Ackland [70] which are then relaxed with DFT (**III-Annex 11**): the microstructures and the atomic distributions are similar for all GBs except for $\Sigma 13$. The atomic distributions obtained for GBs relaxed with DFT are shifted to high atomic volume values.

Whether with EP calculations or with DFT calculation with GBs obtained with MQ_method, the atomic volume distribution, the microstructure atomic volume pattern and the atomic density are similar whatever the potential initially used. It suggests that the MQ_method is independent of the EP used.

III-3.3 Comparison with literature

As introduced in *section III-1* tilt GBs have been extensively studied by simulation in α -iron but very few are about twist (001) GBs [12], [13] in α -iron. McEniry *et al* [27] and Yang *et al* [22] investigated (110) α -iron twist GB, however, literature on specific (001) GBs in α -bcc iron are relatively rare. Runnel *et al* [12] who developed an explicit model for the interfacial energy in crystals taking into account the geometric origin of the cusps in the energy profile have obtained some results about (001) twist GB in α -iron. It is the only study which focuses on (001) twist GB in α -iron with Wolf *et al* [13] simulations on twist GBs with Johnson *et al* [28] potential and Wang *et al* [29] DFT results on $\Sigma 5$ GB.

Energetic properties of the GBs obtained with **MQ_method** and **All_trans_method** are compared to the literature [12], [13], [26] (**Figure III- 57**). Wolf *et al* [13] have made MS simulations with Johnson *et al* [28] potential on twist GBs in α -iron and Wang *et al* [29] performed some DFT calculations on twist (001) GB $\Sigma 5$. Runnel *et al* [12] developed an explicit model for the interfacial energy in crystals taking into account the geometric origin of the cusps in the energy profile and have obtained some results about (001) twist GB in α -iron. Schober *et al* [26] developed a general model to predict the energetic variations as a function of misorientation angle for any GB with a bcc structure. In order to complete this comparison, twist GBs (001) from Imeall [88] database generated by J. Kermode *et al* have been relaxed during this PhD using Ackland's potential [70].

Figure III- 57 indicates the variation of formation energy as a function of GB misorientation angle. The results shows besides zero energy in a perfect crystal (corresponding to a misorientation angle 0° and $\Sigma 1$), a highest cusp occurring at 53° corresponding to $\Sigma 5$ (indicated by a green solid line on **Figure III- 57**) which is coherent with Runnels *et al* [12] and Wolf *et al* [13] results. Our results are also in good agreement with the general knowledge of GB energetic properties: a low GB energy is expected for high density of coincide lattice sites corresponding to a low Σ value.

The methodology we used, whatever the EP chosen, leads to lower energy GB than other studies and thus to more stable GBs. Runnels model [12] presents a difference about 0.2 J/m² higher than our results and Wolf *et al* [13] calculations lead to a formation energy 0.42 J/m² higher than our results. A comparison with the generalized energetic curve for bcc twist materials obtained by Schober *et al* [26] allows us to confirm our results: the energy curve is similar to our results.

Twist GBs from Imcell database [88] constructed by only atom deletion method, relaxed with Ackland *et al* [70] potential give different results (Kermode *et al* GBs relaxed with Ackland EP in **Figure III- 57**): $\Sigma 5$ GB corresponds to a maxima in contrast to Runnels *et al* [12] and Wolf *et al* [13] results.

When comparing DFT calculations, the GB grain boundaries constructed in this work leads to DFT calculated formation energy lower than the one obtained in Wang *et al* [29].

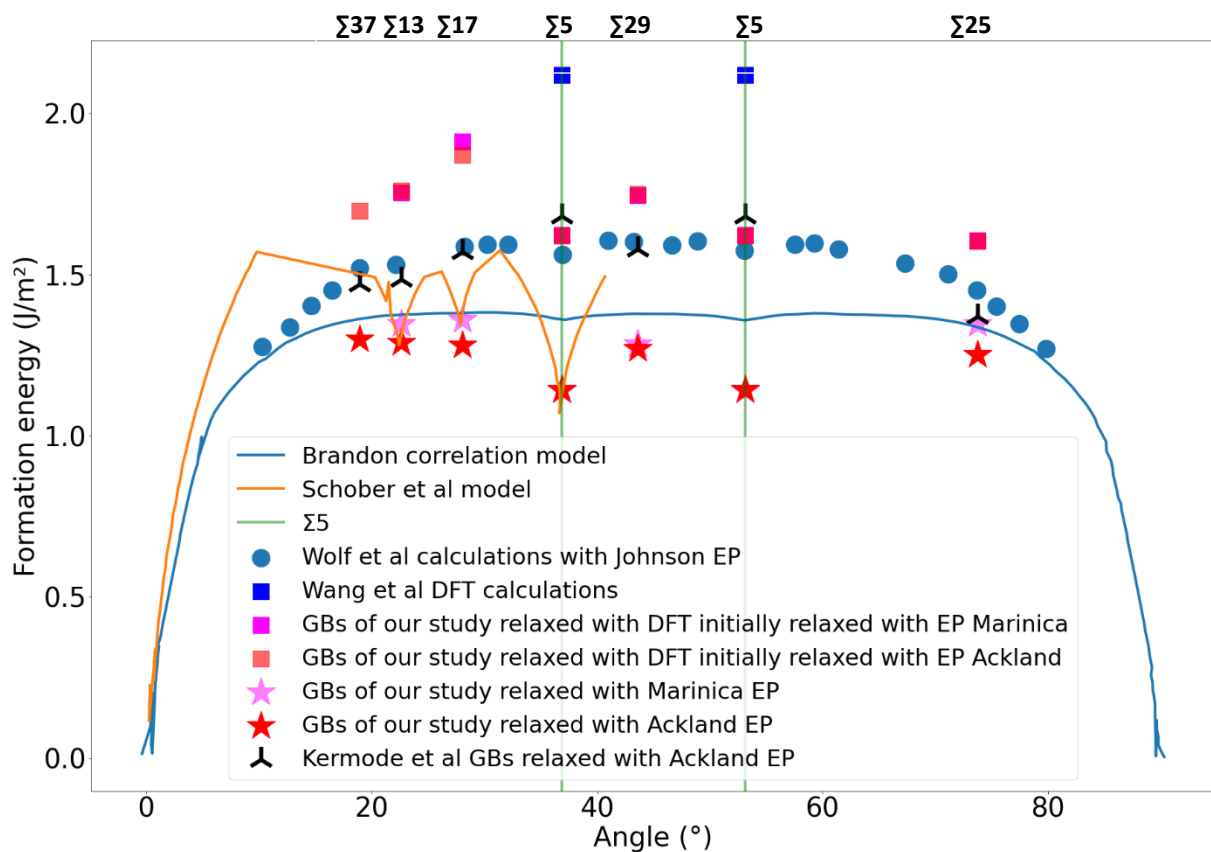


Figure III- 57: Formation energy as a function of GB misorientation angle. Since the results obtained with EP Ackland are the same whatever the method chosen, the method used is not precise. For DFT results, the lowest energetic state has been chosen within **All_trans_method** and **MQ_method** results. For Marinica results with DFT or EP, only **MQ_method** energetic results have been plotted as Marinica EP has been used only with **MQ_method**.

III-4. Conclusion

- EP calculations permit to highlight that **MQ_method** seems to be more efficient to find minimum GB energetic states than **All_trans_method**. The addition of SIA on octahedral positions and the application of MQ treatments permits to explore to some extent the potential energy surface in order to find lower GB energetic states. The application of a translation as it is performed in γ -method is thus not necessary: whatever the initial state chosen; all translated GBs seem to converge to the same minimized GB state.
- DFT relaxation of GB structures generated with **MQ_method** and **All_trans_method** leads to the same GB construction scheme (the same number of interstitials) for $\Sigma 17$, $\Sigma 29$ and $\Sigma 5$. However, for more complex microstructures where no clear geometric visual pattern as a function of atomic volume could be found, such as $\Sigma 37$ and $\Sigma 13$ GBs the number of steps is different from EP results. In addition, even if **MQ_method** and **All_trans_method** lead to the same formation energy at the end, for such GB with DFT calculations, **MQ_method** and **All_trans_method** converges to different GB formation energy for these two complex GBs.
- EP and DFT energetic results are in a good agreement with the literature and their predicted formation energy are always lower than values reported in the literature.
- It is found that for $\langle 100 \rangle$ twist grain boundaries in α iron, with EP it is necessary to add interstitials in the vicinity of the GB grain boundary plane: from 4 to 11 SIAs.
- These two methods developed during this thesis permit to reach more stable twist GBs than twist GBs produced already in the literature.

III-5. Bibliography

- [1] P. Lejcek, P. Sandrera, J. Hornikova, P. Rehak, et J. Pokluda, « Grain boundary segregation of elements of 14 and 15 and its consequences for intergranular cohesion of ferritic iron », *Journal of Materials Science*, vol. 52, p. 5822-5834, 2017.
- [2] K. Masuda-Jindo, « On the grain boundary segregation of sp-Valence Impurities in b.c.c. transition metal », *phy. stat. sol. (b)*, vol. 134, p. 545-550, 1986.
- [3] W.-S. Ko, « Atomistic modeling of an impurity element and a metal-impurity system: pure P and Fe-P system », *J. Phys. : Condens. Matter*, vol. 24, p. 225002, 2012.
- [4] S. H. Song, H. Zhuang, J. Wu, L. Q. Weng, Z. X. Yuan, et T. H. Xi, « Dependence of ductile-to-brittle transition temperature on phosphorus grain boundary segregation for a 2.25Cr1Mo steel », *Material Science and Engineering A*, vol. 486, p. 433-438, 2008.
- [5] D. Kalderon, « Steam Turbine Failure at Hinkley Point "A" », *Proceedings of Institution of Mechanical Engineers*, vol. 186, p. 341, 1972.
- [6] E. D. Hondros, « Grain boundary segregation assessment of investigative techniques », in *Grain Boundary Structure and Properties*, London: G.A. Chadwick, D.A. Smith, 1976, p. 265-298.
- [7] M. Hashimoto, Y. Ishida, R. Yamamoto, et M. Doyama, « Atomistic studies of grain boundary segregation in Fe-P and Fe-B alloys-I atomic structure and stress distribution », *Acta Metallurgica*, vol. 1, p. 1-11, 1984.
- [8] W.-S. Ko, J. B. Jeon, C.-H. Lee, J.-K. Lee, et B.-J. Lee, « Intergranular embrittlement of iron by phosphorus segregation: an atomistic simulation », *Modelling and Simulation in Materials Science and Engineering*, vol. 21, p. 025012-025028, 2013.
- [9] M. Rajagopalan, M. A. Tschopp, et K. N. Solanki, « Grain boundary segregation of interstitial and substitutional impurity atoms in alpha-iron », *JOM*, vol. 66, p. 129, 2014.
- [10] M. Yamaguchi, « First-Principles Study on the Grain Boundary Embrittlement of Metals by Solute Segregation: Part I. Iron (Fe)-Solute (B, C, P, and S) Systems », *Metallurgical and materials transactions A*, vol. 42A, p. 319-329, 2010.
- [11] E. Wachowicz, T. Ossowski, et A. Kiejna, « Cohesive and magnetic properties of grain boundaries in bcc Fe with Cr additions », *Physical Review B*, vol. 81, n° 9, Art. n° 9, mars 2010.
- [12] B. Runnels, I. J. Beyerlein, S. Conti, et M. Ortiz, « A relaxation method for the energy and morphology of grainboundaries and interfaces », *Journal of the Mechanics and Physics of Solids*, vol. 94, p. 388-408, 2016.
- [13] D. Wolf, « Correlation between the energy and structure of grain boundaries in b.c.c. metals I. Symmetrical boundaries on the (110) and (100) planes. », *Philosophical Magazine B*, vol. 59, p. 667-680, 1989.
- [14] E. E. Badiyan et O. V. Shekhovtsov, « On the Nature of the Low Energy of Special Twist Grain Boundaries », *The Physics of Metals and Metallography*, vol. 102, p. 181-185, 2006.
- [15] X. M. Wei, J. M. Zhang, et K. W. Xu, « The energy and structure of (001) twist grainboundary in noble metals », *Applied Surface Science*, vol. 253, p. 854-858, 2006.
- [16] X. M. Wei, J. M. Zhang, et K. W. Xu, « Energy calculation of (011) twist grainboundary in noble metals. », *Applied Surface Science*, vol. 252, p. 7331-7336, 2006.
- [17] X. M. Wei, J. M. Zhang, et K. W. Xu, « The periodicity in translation of Ag (001) and(110) twist grain boundary », *Applied Surface Science*, vol. 253, p. 4307-4310, 2007.
- [18] J. M. Zhang, X. M. Wei, et H. Xin, « Energy analysis for (111) twist grain boundary innoble metals », *Applied Surface Science*, vol. 243, p. 1-6, 2005.
- [19] S. Dai, Y. Xiang, et D. J. Srolovitz, « Atomistic, generalized Peierls-Nabarro and analytical models for (111) twist boundaries in Al, Cu and Ni for all twist angles. », *Acta Materialia*, vol. 69, p. 162-174, 2014.
- [20] S. Dai, Y. Xiang, et D. J. Srolovitz, « Structure and energy of (111) low-angle twistboundaries in Al, Cu and Ni. », *Acta Materialia*, vol. 61, n° 4, p. 1327-1337, 2013.

- [21] Z. H. Liu, Y. X. Feng, et J. X. Shang, « Characterizing twist grain boundaries in BCC Nb by molecular simulation: Structure and shear deformation », *Applied Surface Science*, vol. 370, p. 19-24, 2016.
- [22] J. B. Yang, Y. Nagai, M. Hasegawa, et Y. N. Osetsky, « Atomic scale modeling of 110 twist grain boundaries in α -iron: structure and energy properties », *Philosophical Magazine*, vol. 90, n° 7-8, p. 991-1000, 2010.
- [23] J. B. Yang, Y. N. Osetsky, R. E. Stoller, Y. Nagai, et M. Hasegawa, « The effect of twist angle on anisotropic mobility of 110 hexagonal dislocation networks in α -iron. », *Scripta Materialia*, vol. 66, n° 10, p. 761-764, 2012.
- [24] V. Bulatov et W. Cai, « Nodal effects in dislocation mobility », *Physical Review Letters*, vol. 89, n° 11, p. 115501, 2002.
- [25] Y. X. Feng, J. X. Shang, Z. H. Liu, et G. H. Lu, « The energy and structure of (110) twist grain boundary in tungsten. », *Applied Surface Science*, vol. 357, p. 262-267, 2015.
- [26] T. Schober et R. W. Balluffi, « Quantitative Observation of Misfit Dislocation Arrays in Low and High Angle Twist Grain Boundaries », *Philosophical Magazine*, vol. 21, p. 109-123, 1970.
- [27] E. J. McEniry, T. Hickel, et J. Neugebauer, « Hydrogen behaviour at twist {110} grain boundaries in α -Fe. », *Philosophical Transactions of the Royal Society of London. Series A*, vol. 375, p. 20160402, 2017.
- [28] R. A. Johnson, « Interstitials and vacancies in α -iron », *Physical Review A*, vol. 134, p. 1329, 1964.
- [29] J. Wang, « Grain boundaries in bcc-Fe: a density-functional theory and tight-binding study », *Modelling and Simulation in Materials Science and Engineering*, vol. 26, p. 025008, 2018.
- [30] M. A. Tschopp et D. L. McDowell, « Microrotation-augmented energy-minimization for 3D nanocrystalline Cu structures », présenté à European Conference on Fatigue, Atlanta, 2006.
- [31] A. Suzuki et Y. Mishin, « Atomistic Modeling of Point Defects and Diffusion in Copper Grain Boundaries », *Interface Science*, vol. 11, p. 131-148, 2003.
- [32] X. Yan et H. Zhang, « On the atomistic mechanisms of grain boundary migration in [001] twist boundaries: Molecular dynamics simulations. », *Computational Materials Science*, vol. 48, p. 773-782, 2010.
- [33] A. Y. Belov, D. Conrad, K. Scheerschmidt, et U. Gösele, « Atomistic study of the (001), 90° twist boundary in silicon. », *Philosophical Magazine A*, vol. 77, p. 55-65, 1998.
- [34] Q. Zhu, A. Samanta, B. Li, R. E. Rudd, et T. Frolov, « Predicting phase behavior of grain boundaries with evolutionary search and machine learning. », *nature communications*, vol. 9, p. 467, 2018.
- [35] T. Frolov, Q. Zhu, T. Ooppelstrup, J. Marian, et R. E. Rudd, « Structures and transitions in bcc tungsten grain boundaries and their role in the absorption of point defects », *Acta Materialia*, vol. 159, p. 123-134, 2018.
- [36] T. Frolov, M. Asta, et Y. Mishin, « Segregation-induced phase transformations in grain boundaries », *Physical Review B*, vol. 92, p. 020103, 2015.
- [37] T. Frolov, D. L. Olmsted, M. Asta, et Y. Mishin, « Structural phase transformations in metallic grain boundaries », *nature communications*, vol. 4, p. 1899, 2013.
- [38] T. Frolov, M. Asta, et Y. Mishin, « Phase transformations at interfaces: Observations from atomistic modeling. », *Current Opinion in Solid State and Material Science*, vol. 20, p. 308-315, 2016.
- [39] T. Meiners, T. Frolov, R. E. Rudd, G. Dehm, et C. H. Liebscher, « Observations of grain-boundary phase transformations in elemental metal », *Nature*, vol. 579, p. 375-378, 2020.
- [40] T. Frolov, S. V. Divinski, M. Asta, et Y. Mishin, « Effect of Interface Phase Transformations on Diffusion and Segregation in High-Angle Grain Boundaries. », *Physical Review Letters*, vol. 110, p. 255502, 2013.
- [41] D. L. Olmsted, S. M. Foiles, et E. A. Holm, « Survey of computed grain boundary properties in face-centered cubic metals: I. Grain boundary energy. », *Acta Materialia*, vol. 57, p. 3694-3703, 2009.

- [42] S. von Alfthan, P. D. Haynes, K. Kaski, et A. P. Sutton, « Are the Structures of Twist Grain Boundaries in Silicon Ordered at 0 K ? », *Physical Review Letters*, vol. 96, p. 055505, 2006.
- [43] W. S. Yu et M. J. Demkowicz, « Non-coherent Cu grain boundaries driven by continuous vacancy loading. », *Journal of Materials Science*, vol. 50, p. 4047-4065, 2015.
- [44] J. D. Rittner et D. N. Seidman, « $\langle 110 \rangle$ symmetric tilt grain-boundary structures in fcc metals with low stacking-fault energies », *Physical Review B*, vol. 54, p. 7000-7015, 1996.
- [45] B. Schönfelder, G. Gottstein, et L. S. Shvindlerman, « Comparative study of grain-boundary migration and grain boundary self-diffusion of [001] twist-grain boundaries in copper by atomistic simulations. », *Acta Materialia*, vol. 53, p. 1597-1609, 2005.
- [46] M. A. Tschopp, K. N. Solanki, F. Gao, X. Sun, M. A. Khaleel, et M. F. Horstemeyer, « Probing grain boundary sink strength at the nanoscale: Energetics and length scales of vacancy and interstitial absorption by grain boundaries in α -Fe », *Physical Review B*, vol. 85, p. 064108, 2012.
- [47] Q. Yin, Z. Wang, R. Mishra, et Z. Xia, « Atomistic simulations of twist grain boundary structures and deformation behaviors in aluminium », *AIP Advances*, vol. 7, p. 015040, 2017.
- [48] H. Zheng et al., « Grain boundary properties of elemental metals », *Acta Materialia*, vol. 186, p. 40-49, 2020.
- [49] M. A. Tschopp et D. L. McDowell, « Asymmetric tilt grain boundary structure and energy in copper and aluminium », *Philosophical Magazine*, vol. 87, p. 3871-3892, 2007.
- [50] M. A. Tschopp, S. P. Coleman, et D. L. McDowell, « Symmetric and asymmetric tilt grain boundary structure and energy in Cu and Al (and transferability to other fcc metals) », *Integrating Materials and Manufacturing Innovation*, vol. 4, n° 1, p. 1-14, 2015.
- [51] D. Zhao et Y. Li, « Revealing the factors influencing grain boundary segregation of P, As in Si: Insights from first-principles. », *Acta Materialia*, vol. 168, p. 52-62, 2019.
- [52] D. Scheiber, R. Pippan, P. Puschnig, et L. Romaner, « Ab initio calculations of grain boundaries in bcc metals », *Modelling and Simulation in Materials Science and Engineering*, vol. 24, n° 3, Art. n° 3, 2016.
- [53] D. Scheiber, L. Romaner, R. Pippan, et P. Puschnig, « Impact of solute-solute interactions on grain boundary segregation and cohesion in molybdenum », *Physical Review Materials*, vol. 2, p. 093609, 2018.
- [54] D. S. Sholl et J. A. Steckel, « Chapter 4: DFT Calculations for surfaces of solids », in *Density Functional Theory: A practical Introduction*, 2009, p. 83-112.
- [55] S. Li, L. Yang, et C. Lai, « Atomistic simulations of energies for arbitrary grain boundaries. Part I: Model and validation », *Computational Materials Science*, vol. 161, p. 330-338, 2019.
- [56] L. Yang, C. Lai, et S. Li, « Atomistic simulations of energies for arbitrary grain boundaries. Part II: Statistical analysis of energies for tilt and twist grain boundaries. », *Computational Materials Science*, vol. 162, p. 268-276, 2019.
- [57] D. Wolf, « Correlation between the energy and structure of grain boundaries in b.c.c. metals II. Symmetrical tilt boundaries », *Philosophical Magazine A*, vol. 62, p. 447-464, 1990.
- [58] D. Wolf, « Structure and energy of general grain boundaries in bcc metals », *Journal of Applied Physics*, vol. 69, p. 185-196, 1991.
- [59] J. M. Zhang, X. M. Wei, et H. Xin, « Calculating the energies for Ag (001) twist boundaries utilizing the modified analytical embedded atom method. », *Surface and Interface Analysis*, vol. 36, p. 1500-1504, 2004.
- [60] T. A. Yesiltepe et T. A. Arias, « Atomic-level physics of grain boundaries in bcc molybdenum », *Physical Review B*, vol. 64, p. 174101, 2001.
- [61] E. N. Hahn, S. J. Fensin, T. C. Germann, et M. A. Meyers, « Symmetric tilt boundaries in body-centered cubic tantalum », *Scripta Materialia*, vol. 116, p. 108-111, 2016.
- [62] A. P. Sutton et V. Vitek, « On the Structure of Tilt Grain Boundaries in Cubic Metals I. Symmetrical Tilt Boundaries », *Philosophical Transactions of the Royal Society of London. Series A*, vol. 309, p. 1-36, 1983.
- [63] J. Hickman et Y. Mishin, « Extra variable in grain boundary description », *Physical Review Letters*, vol. 1, p. 010601, 2017.

- [64] I. Novoselov et A. Yanilkin, « Impact of segregated interstitials on structures and energies of tilt grain boundaries in Mo », *Computational Materials Science*, vol. 112, p. 276-281, 2016.
- [65] A. R. Organov et C. W. Glass, « Crystal structure prediction using ab initio evolutionary techniques: Principles and applications », *Journal of Chemical Physics*, vol. 124, p. 244704, 2006.
- [66] H. Jiang et I. Szlufarska, « Small-Angle Twist Grain Boundaries as Sinks for Point Defects », *nature scientific reports*, vol. 8, n° 1, p. 1-13, 2018.
- [67] M. I. Mendeleev, « Development of new interatomic potentials appropriate for crystalline and liquid iron », *Philosophical Magazine*, vol. 83, p. 3977, 2003.
- [68] J. A. Moriarty et R. Phillips, « First-Principles Interatomic Potentials for Transition-Metal Surfaces », *Physical Review Letters*, vol. 66, p. 3036, 1991.
- [69] C. S. Becquart, C. Domain, A. Legris, et J. C. Van Duysen, « Influence of the interatomic potentials on molecular dynamicssimulations of displacement cascades », *Journal of Nuclear Materials*, vol. 280, p. 73-85, 2000.
- [70] G. J. Ackland, M. I. Mendeleev, D. J. Srolovitz, S. Han, et A. V. Barashev, « Development of an interatomic potential for phosphorus impurities in alpha-iron », *Journal of Physics: Condensed Matter*, vol. 16, n° 27, p. 1-14, 2004.
- [71] C. Domain et C. S. Becquart, « Solute - $\langle 111 \rangle$ interstitial loop interaction in Fe: A DFT study », *Journal of Nuclear Materials*, vol. 499, p. 582-594, 2018.
- [72] C. Domain et C. S. Becquart, « Diffusion of phosphorus in α -Fe: An ab initio study », *Physical Review B*, vol. 71, p. 214109, 2005.
- [73] E. Meslin, C.-C. Fu, A. Barbu, F. Gao, et F. Willaime, « Theoretical study of atomic transport via interstitials in dilute Fe-P alloys. », *Physical Review B*, vol. 75, p. 094303, 2007.
- [74] M. I. Pascuet, E. Martínez, et L. Malerba, « Solute effects on edge dislocation pinning in complex alpha-Fe alloys. », *Journal of Nuclear Materials*, vol. 494, p. 311-321, 2017.
- [75] K. Ebihara et T. Suzudo, « Atomistic Simulation of Phosphorus Segregation to sigma 3 (111) Symmetrical Tilt Grain Boundary in alpha-iron », *Modelling and Simulation in Materials Science and Engineering*, vol. 103122.R1, p. 1-16, 2018.
- [76] S. M. J. Gordon, S. D. Kenny, et R. Smith, « Diffusion dynamics of defects in Fe and Fe-P systems. », *Physical Review B*, vol. 72, p. 214104, 2005.
- [77] L. Malerba *et al.*, « Ab initio calculations and interatomic potentials for iron and iron alloys: Achievements within the Perfect Project. », *Journal of Nuclear Materials*, vol. 406, p. 19-38, 2010.
- [78] S. M. J. Gordon, H. Hurchand, S. D. Kenny, et R. Smith, « Diffusion of radiation damage in Fe-P systems », *Nuclear Instruments and Methods in Physics Research Section B: Beam Interactions with Materials and Atoms*, vol. 228, n° 1-4, p. 131-136, 2005.
- [79] H. Hurchand, S. D. Kenny, C. F. Sanz-Navarro, R. Smith, et P. E. J. Flewitt, « The influence of P solutes on an irradiated alpha-Fe matrix », *Nuclear Instruments and Methods in Physics Research B*, vol. 229, p. 92-102, 2005.
- [80] L. Malerba *et al.*, « Comparison of empirical interatomic potentials for iron applied to radiation damage studies », *Journal of Nuclear Materials*, vol. 406, n° 1, p. 19, 2010.
- [81] M.-C. Marinica, F. Willaime, et J.-P. Crocombette, « Irradiation-induced formation of nanocrystallites with c15 laves phase structure in bcc iron », *Physical Review Letters*, vol. 108, p. 025501, 2012.
- [82] M. L. Kronberg et F. H. Wilson, « Secondary recrystallization in copper », *Metals Transactions*, vol. 185, p. 501-502, 1949.
- [83] C. Domain et C. S. Becquart, « Ab initio calculations of defects in Fe and dilute Fe-Cu alloys », *Physical Review B*, vol. 65, p. 024103, 2001.
- [84] G. Simonelli, R. Pasianot, et E. J. Savino, « Self-Interstitial Configuration in B.C.C. Metals. An Analysis Based on Many-Body Potentials for Fe and Mo », *Phys. stat. sol. (b)*, vol. 217, p. 747, 2000.
- [85] C.-C. Fu, F. Willaime, et P. Ordejón, « Stability and Mobility of Mono- and Di-Interstitials in alpha-Fe », *Physical Review Letters*, vol. 92, p. 175503, 2004.

- [86] D. Nguyen-Manh, A. P. Horsfield, et S. L. Dudarev, « Self-interstitial atom defects in bcc transition metals: Group-specific trends », *Physical Review B*, vol. 73, p. 020101, 2006.
- [87] W. B. Jiang, Q. P. Kong, P. Cui, Q. F. Fang, D. A. Molodov, et G. Gottstein, « Internal friction in Al bicrystals with $\langle 111 \rangle$ tilt and twist grain boundaries. », *Philosophical Magazine*, vol. 90, p. 753-764, 2010.
- [88] H. Lambert, A. Fekete, J. R. Kermode, et A. D. Vita, « Imcell: A Computational Framework for the Calculation of the Atomistic Properties of Grain Boundaries », *Computer Physics Communications*, vol. 232, p. 256-263, 2018.

Chapter IV: Segregation of P on twist GBs

Solute segregation influences quite significantly the macroscopic properties; thus, it has been the subject of a many studies and research work and extensively reported in the literature. Detrimental effects induced by this segregation process can reduce the toughness and ductility of a material. In this context, in order to highlight the contribution of microstructural non-hardening mechanisms in the irradiation embrittlement and thus in DBTT, it is necessary to assess and quantify the potential embrittlement caused by solute segregation and to model GB segregation. The chapter is organized as follows. A bibliographic review is carried out in *Section 1*. In *Section 2*, thermodynamic models necessary to allow a quantification of GB segregation are presented. In the last Section, segregation results for the twist GBs constructed in *Chapter III* are presented. The experimental approach are presented in *IV-Annex 1*.

IV-1. Phosphorus GB segregation

Figure IV- 3This form of embrittlement and the contributing role of certain alloying elements has been a subject of research for several decades. The great diversity of possible solutes and combination of chemical species that could be introduced in a material explain the large number of studies that have been made. 14th and 15th groups of the periodic table are among the most frequently studied segregants. It is now well accepted that segregation of P, S, Sn, Sb is implicated in the **embrittlement of steels** [1]. C and N, on the other hand, enhance the GB cohesion. Sulphur has been shown to enhance surface diffusion in iron at high temperature, and compete with other segregants such as C, Si, P. Most of the impurities and solutes which promote an intergranular fracture are **sp valence atoms** and have tendency to form covalent bonds with host iron atoms. According to **Masuda-Jindo** [2], Mg, Al, Si, P, S and Cl always present an attractive interaction with the matrix atoms.

Phosphorus is currently used in industry for its **beneficial** effects. It is one of the most potent solid solution strengtheners of ferrite. The addition of low phosphorus content (0.17%) increases both the yield and tensile strength of low-carbon sheet steel by about 62 MPa and also improving the bake hardening response and deep drawability [3]. This is the reason why rephosphorized high-strength steels is a method widely used for cold-forming applications. Phosphorus is also used as an additive in steels to improve machining characteristics and atmospheric corrosion resistance.

Detrimental effects of phosphorus in steels include various forms of embrittlement which reduce the toughness and ductility. P remains the main impurity in ferritic low-alloy steels causing temper embrittlement (**Figure IV- 1**) resulting from segregation of phosphorus and other impurities. Its concentration in ferritic steels is strictly controlled [4], and its segregation process has to be better understood.

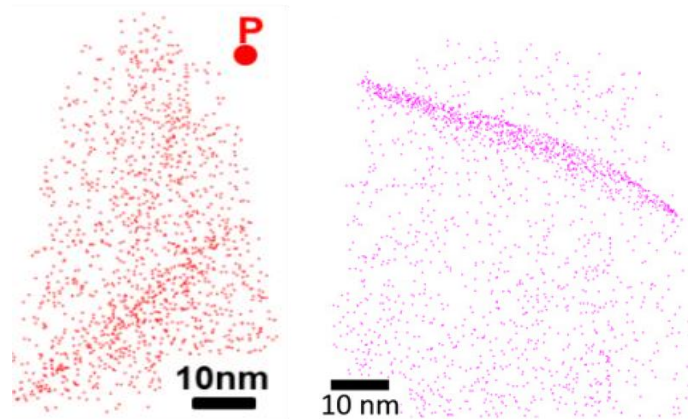


Figure IV- 1: Atom maps showing GB phosphorus segregation. The left picture corresponds to Zhang’s results and the right one to Styman’s observations [5], [6].

According to Song *et al* [7], phosphorus is a strong embrittling element in α -Fe and ferritic steels, and its segregation at GB has a considerable effect on the DBTT. The analysis of the temper embrittled steam turbine disc involved in the failure at Hinkley Point NPP in 1969 showed that the effect of P was significant [8]. A linear relationship exists between P segregation and DBTT shift and the average shift is around 300°C per monolayer of P segregated [7]. Moreover, studies carried out by Hondros *et al* [9] show that intergranular failure in many commercial alloys is dominated by segregation of P. In what follows we will provide key elements of the vast literature on phosphorous segregation.

IV-1.1 Macroscopic and microstructural results

IV-1.1.1 Macroscopic experimental results

Phosphorus segregation at GBs introduces structural changes by a lattice distortion in the neighbourhood of GBs and induces a drop of the free segregation energy which usually varies, for this element, in the range of 33 to 56 kJ/mol in a temperature range 350-600 degrees in Fe-based alloys [10] [1], [11]. The augmentation of the phosphorus content in the bulk (**Figure IV- 2**) enhances the phosphorus segregation at GB and leads in case of high concentration (1 %at) to larger structural changes with a formation of facets and clusters of Fe_3P near GB.

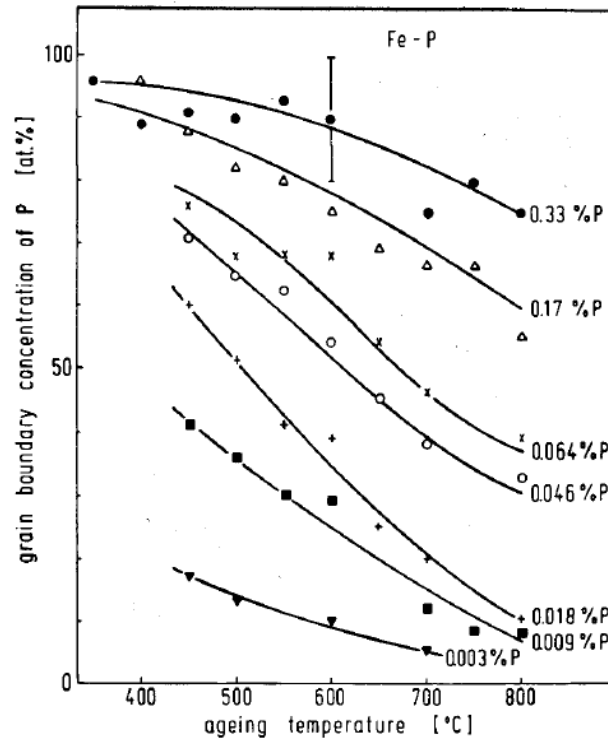


Figure IV- 2: Dependence of GB concentration of phosphorus in Fe-P alloys with bulk concentration and annealing temperatures [12]

In agreement with thermodynamic theory, AES experiments [12] have demonstrated that lower ageing temperatures lead to slower phosphorus GB segregation. Furthermore, the higher the temperature, the higher the equilibrium value.

ATP experiments made by Sakurai in Fe-0.04 %at P steels [13] confirm these trends: phosphorus was found to segregate to GB below 600°C. More recently APT maps made by Styman *et al* [5] and Zhang [6] reveal also significant GB segregation in ferritic low alloy steels. Styman *et al*. [5] investigated high copper and nickel ferritic alloy (0.44 % at Cu, 1.66 %at Ni, 1.38 %at Mn, 0.75 %at Si, 0.19 %at C, 0.24%at Mo, 0.018 %at P and 0.054 %at Cr), while Zhang [6] looked at 16MND5 classical French iron steel (0.04 %at Cu, 0.72 %at Ni, 1.60 %at Mn, 0.84 %at Si, 0.34 %at C, 0.34 %at Mo, 0.014 %at P and 0.18 %at Cr) for different misorientation angles (LAGB, HAGB and Σ 3 HAGB) (**Figure IV- 3**).

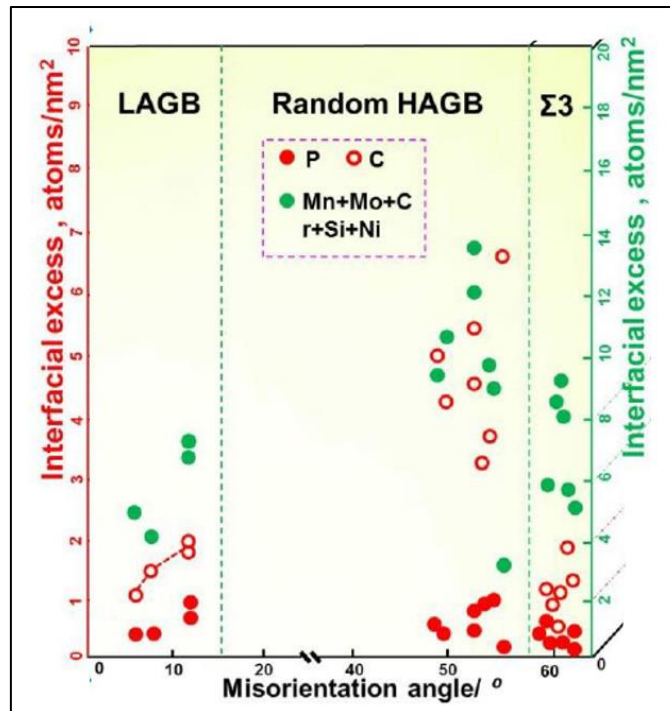


Figure IV- 3: Variation of interfacial excess value with misorientation angle. The segregated values of C, P and (Mn +Mo +C +Si +Ni) are plotted with different marks [6].

AES experiments in 2.25Cr-1Mo steels, with different grain sizes produced through austenitization by different heat treatments, have demonstrated that phosphorus segregation at GB **increases when the grain size increases**, as the Auger peak height of phosphorus increases with increasing grain size. Note that low extra Auger peaks were also observed for Cr Mo and C [14].

Recent APT analysis [15] in Fe -0.034 at.% P-0.01 at.% C after ion irradiation up to 0.75 dpa at 450°C has shown that the mean phosphorus segregation at HAGBs increases with the irradiation dose (**Figure IV- 4**). The phosphorus segregation at high-angle GBs in all irradiated samples is larger than the equilibrium GB segregation of phosphorus at the same temperature. A radiation induced segregation mechanism seems to occur: the authors explain their results by a flux coupling effect between the irradiation point defects and phosphorus atoms

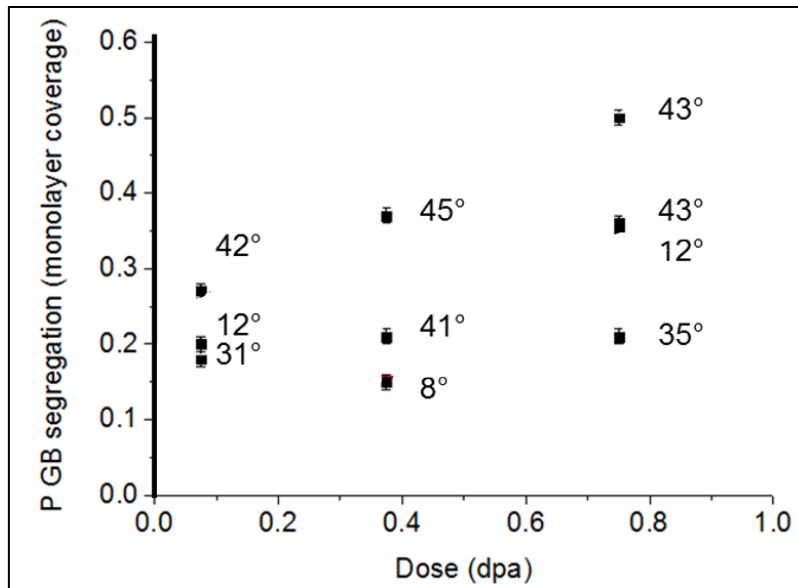


Figure IV- 4: Dose dependence of phosphorus GB segregation in the Fe-0.034 at% P-0.01 at% C (dose rate = $3 \cdot 10^{-5}$ dpa/s) with APT data at 450°C [15]

Detailed examinations of the neutron dose dependence have not been reported to our knowledge.

Thermodynamic equilibrium for phosphorus segregation at GB is reached at 600°C in Fe. The augmentation of phosphorus content, the grain size and the irradiation dose seem to enhance the segregation at GBs.

IV-1.1.2 Microstructural results from computational and APT studies

Ko *et al* [4] compared the segregation of phosphorus on different types of GBs: LAGB, HAGB and special GB. They considered two classes of regions: incoherent and coherent HAGB contain only **incoherent** regions, LAGB are constituted of both coherent and incoherent regions and special GBs, which correspond to a GB plane with a high symmetry and ordered atoms, are fully coherent (**Figure IV- 5**). They find that phosphorus is concentrated in the incoherent regions, where the ability of a solute atom to bind is favourable.

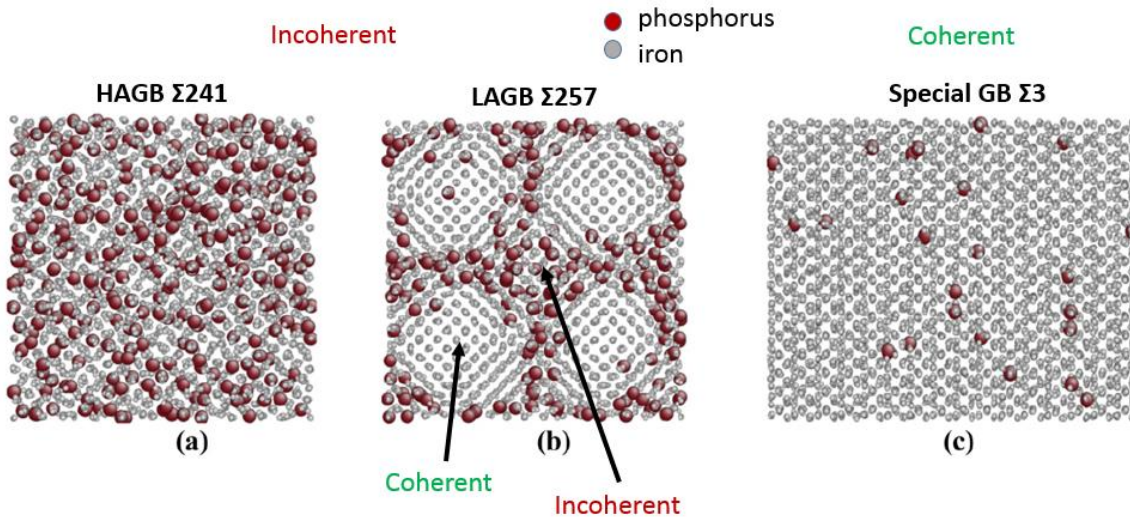


Figure IV- 5: coherent and incoherent regions in the three kinds of GB investigated by Ko *et al.* [16]

Table IV- 1 summarizes the different GB investigated so far both using calculations experimental means.

L. Zhang [6] APT results on reference 16MND5 welds have shown a high segregation of P at LAGBs $(5^\circ[6\bar{5}2](\bar{5}0\bar{3})/(3\bar{2}0)$, $7^\circ[0\bar{1}1](\bar{4}34)/(\bar{6}56)$, $12^\circ[104](54\bar{6})/(53\bar{5})$, $13^\circ[\bar{3}10](\bar{6}3\bar{1})/(\bar{6}3\bar{1})$) and general HAGBs $(52^\circ[\bar{1}01](6\bar{1}5)/(25\bar{3})$, $49^\circ[403](010)/(35\bar{5})$, $49.5^\circ[\bar{1}10](\bar{4}2\bar{5})/(5\bar{4}2)$, $54^\circ[2\bar{4}3](1\bar{1}0)/(1\bar{5}0)$, $52^\circ[\bar{3}3\bar{1}](\bar{5}43)/(6\bar{5}5)$, $54^\circ[\bar{5}25](\bar{1}1\bar{2})/(0\bar{3}1)$, $54^\circ[433](5\bar{5}2)/(3\bar{3}1)$).

Yamaguchi *et al.* [17] DFT calculations on $\Sigma 3(111)$ GB have shown the same trends for HAGB. Usually, HAGB lead to a higher segregated phosphorus concentration compared to LAGB.

He *et al.* [18] molecular static simulations with EP derived from Ackland, have shown that P is strongly attracted to symmetric GB $[110]$ tilt axis: $\Sigma 19[110](331)$, $\Sigma 9[110](221)$, $\Sigma 3[110](111)$, $\Sigma 3[110](112)$, $\Sigma 11[110](113)$, $\Sigma 9[110](114)$ and $[100]$ tilt axis $\Sigma 13[100](510)$, $\Sigma 17[100](410)$, $\Sigma 5[100](310)$ and $\Sigma 5[100](210)$ in α -Fe.

Molecular dynamic results using Morse EP, of Hashimoto *et al.* [19] on symmetric GB $\Sigma 5(013)$ and $\Sigma 9(114)$, tight binding calculation of Masuda [20] on $\Sigma 5$ and $\Sigma 9$ GB, Monte-Carlo calculation of Ko *et al.* [4], [21] on HAGB $\Sigma 241$, LAGB $\Sigma 257$ and $\Sigma 3$ in α -Fe predicts a segregation of phosphorus. Yamaguchi *et al.* [17], [22] DFT calculations on $\Sigma 3(111)$ STGB revealed also preferential atomic sites for the phosphorus segregation, corresponding to a segregation energy around -1eV/atom.

Table IV- 1: Summary of the different GB investigated with regards to P segregation in bcc-Fe. For the computational and experimental investigations, they are ranged from the most appropriate technique to the most accurate. The P coverage has been estimated with classical McClean’s Model introduced in **section 3.1**, this coverage has been expressed in atoms/nm² in order to be compared with results obtained in **section 4**.

COMPUTATIONAL INVESTIGATIONS ¹⁴					
Reference	Method	Material	GB	Segregation energy (eV/atom)	Coverage (McClean’s Model) (atoms/nm ²)
Hashimoto <i>et al</i> [19]	DM with an EP Morse Potential derived by the authors.	Fe with P impurities	$\Sigma 5[100](013)$	-2.25	
			$\Sigma 9[110](1\bar{1}4)$	-2.14	
Ko <i>et al</i> [4], [21]	MC with a EP 2NN MEAM developed by Baskes <i>et al</i> [23] improved by Ko <i>et al</i> for the Fe-P case.	BCC Fe P Impurities	Twist HAGB $\Sigma 241$, LAGB $\Sigma 257$ and special GB $\Sigma 3$	(-1.1) – (-0.8)	
He <i>et al</i> [18]	MS with the EP derived by Ackland in 2004 (potential A04) [24]	BCC Fe subs	$\Sigma 19[110](331)$	-0.32	
			$\Sigma 9[110](221)$	-1.2	
			$\Sigma 3[110](111)$	-1.2	
			$\Sigma 3[110](112)$	-0.10	
			$\Sigma 11[110](113)$	-1.25	
			$\Sigma 9[110](114)$	-1.2	
			$\Sigma 13[100](510)$	-1.8	
			$\Sigma 17[100](410)$	-0.65	
			$\Sigma 5[100](310)$	-0.5	
			$\Sigma 5[100](210)$	-0.28	
Masuda-Jindo [2]	TB Method of moments and the self-consistent Hartree approximation for defect perturbing potential	BCC Fe with P impurities	$\Sigma 5[001](310)$	-0.15141 with Masuda’s model (if all the system is considered) -0.7 eV for the contribution of only P in segregation	

¹⁴ Only one P is placed in the GB therefore no coverage value can be determined and its calculation supposed that P doesn’t interact with its periodic images.

Rajagopalan <i>et al</i> [25]	MS with EAM Ackland 2004 Potential (A04) [24]	BCC Fe Subs	$\Sigma 5[100](210)$	-0.8			
			$\Sigma 13[100](320)$	-0.8			
			$\Sigma 3[110](111)$	-1.06			
			$\Sigma 3[110](112)$	-0.1			
			$\Sigma 11[110](332)$	-0.7			
Yamaguchi <i>et al</i> [17], [22]	DFT PAW VASP	BCC Fe subs	$\Sigma 3 [110](111)$	-1.35			
				Subs	Int	Subs	Int
Wachowicz <i>et al</i> [26]	DFT PAW GGA PW91	BCC Fe subs and int	$\Sigma 5[100](210)$	0	-5		
			$\Sigma 3[110](111)$	0.05	-5.5		
EXPERIMENTAL INVESTIGATIONS							
Reference	Method	Material	GB	Segregation energy (eV)	Coverage (McClean's Model) (atoms/nm ²)		
Akhatova [15]	AES	Fe-0.034 at% P- 0.01 at% C model alloy. As received*	HAGBs		1.4±0.5		
Grabke <i>et al</i> [27]	AES	Fe-P(0.003- 0.33%wt)	Polycrystalline	-34.8kJ/mol thus -0.36 eV			
Wu <i>et al</i> [11]	AES	Fe-2.25Cr1Mo steel. Quench from 980 °C and tempering at 650 °C, followed by ageing for different times at 560 °C, 520 °C and 480 °C.	Polycrystalline	-38.0kJ/mol thus -0.395 eV			
Chen <i>et al</i> [28]	AES	Fe-Ti stabilized interstitial steel. "Specimens aged for adequate time at different temperatures between 600 and 850°C." [29]	Polycrystalline	-44.8 kJ/mol thus 0.465 eV			

Zhang [6]	APT	16MND5 reference welds: H80 steel. The black data correspond to the steel "as received"**. The blue ones correspond to measures done after 80000 h of thermal ageing at 400°C .		Subs	Int	Subs	Int		
			LAGB				0.5±0.2	1.7±0.4	
			5° $[\bar{6}52](\bar{5}03)/(\bar{3}20)$			0.3	1.45		
			7° $[0\bar{1}1](\bar{4}34)/(\bar{6}56)$			0.3	1.9		
			12° $[104](\bar{5}46)/(\bar{5}35)$			0.9	2.7		
			13° $[\bar{3}10](\bar{6}31)/(\bar{6}31)$			0.3	2.5		
			HAGB				0.6±0.1	1.8±0.7	
			52° $[\bar{1}01](\bar{6}15)/(\bar{2}53)$			0.4	7		
			49° $[403](010)/(\bar{3}55)$			0.6	4.7		
			49.5° $[\bar{1}10](\bar{4}25)/(\bar{5}42)$			0.3	5.65		
			54° $[243](\bar{1}10)/(\bar{1}50)$			1	4.5		
			52° $[\bar{3}31](\bar{5}43)/(\bar{6}55)$			0.8	4.5		
			54° $[\bar{5}25](\bar{1}12)/(\bar{0}31)$			0.1	5		
			54° $[433](\bar{5}52)/(\bar{3}31)$			0.8			
			59° $[111](\bar{6}52)/(\bar{5}03)$			0.2	0.8		
			60° $[\bar{1}11](\bar{1}12)/(\bar{3}10)$			0.2	1.15		
			60° $[343](\bar{4}41)/(\bar{4}15)$			0.3	1.4		
			59.5° $[\bar{1}11](\bar{4}11)/(\bar{5}22)$			0.3	1.5		
60° $[111](101)/(\bar{0}11)$			0.1	1.6					
60° $[554](101)/(\bar{0}11)$			0.4	2.2					
Akhatova [15]	APT	Fe-0.034 at% P- 0.01 at% C model alloy	HAGB				1.6±0.7		
			35° $[014](\bar{1}61)/(\bar{3}31)$				2.0		
			35° $[143](\bar{5}41)/(\bar{3}21)$				1.7		
			41° $[010](\bar{1}30)/(\bar{1}20)$				2.2		
			42° $[\bar{3}11](\bar{1}01)/(\bar{1}51)$				2.2		
			6° $[412](\bar{1}24)/(\bar{1}34)$				0.6		
			8° $[033](\bar{2}52)/(\bar{5}23)$				0.6		
Hsu <i>et al</i> [30]	STEM-EDX	Fe-0.034 at% P- 0.01 at% C model alloy	35° $[143](\bar{5}41)/(\bar{3}21)$				2.06±0.38		
			42° $[\bar{3}11](\bar{1}01)/(\bar{1}51)$				2.63±0.24		
Styman <i>et al</i> [5]	APT	RPV steels, 50000 h of thermal ageing at 365°C	Polycrystalline				0.664		

* 110 x 100 x 80 mm³ ingot, cast in vacuum, reheated at 1200°C, hot rolled in 6 passes to 20 mm thickness and air-cooled down to room temperature.

** see Figure IV-

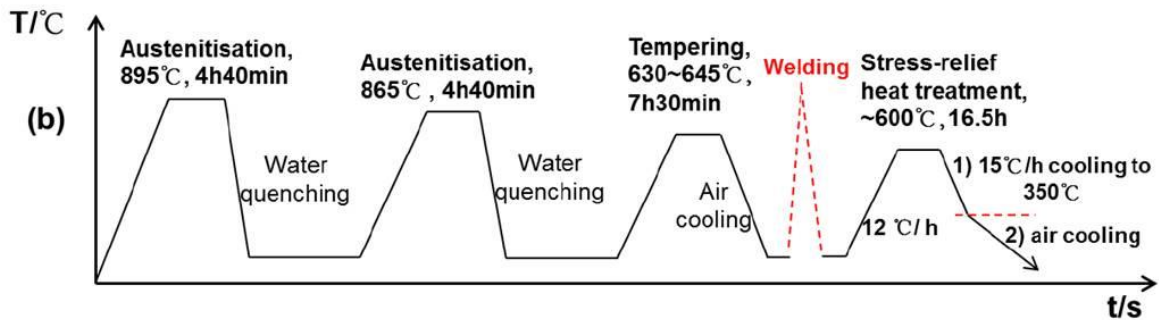


Figure IV- 6: Preparation of « as received » state for Zhang [6]

Computational and experimental results both predict and show a preferential segregation of phosphorus at GBs. A higher segregated concentration is observed in HAGB compared to LAGB.

[IV-1.1.2.1 Preferential sites for segregation of phosphorus](#)

The atomistic modeling approach reveals the presence of preferential sites for the segregation of phosphorus. Indeed, sites with a large volume excess present a high binding energy and correspond to a favourable site for the segregation. The GB interaction energy is **non-uniform** and depends significantly on the specific lattice site into which a phosphorus is inserted. As the adatom produces a local distortion of the lattice, the adatomic size plays an important role in this mechanism. According to He *et al.* [18], the difference in the interaction energy for two neighbouring sites can go up to 1.5 eV in $\Sigma 3$ (111) GB, depending on the GB structure. According to Hashimoto *et al.* [19], hydrostatic tension and the compressive stress spread out on the region around the boundary and enhance the phosphorus atoms segregation not only on the GB plane but also on the nearest layers.

The segregation energy is not homogenous in the GB. Segregation is an anisotropic process which depends significantly on the GB structure and on the characteristics of the segregant (the size, the chemical species...). Certain sites in or near GB, such as compressive sites filled with undersized segregants are more favourable than others.

[IV-1.1.2.2 Substitutional and interstitial site dependence](#)

Phosphorus, is in most of computational studies accepted as a **substitutional segregant** [31]–[34]. Lecjek and al [35] predicted, using DFT, that substitutional phosphorus is energetically more favourable than interstitial phosphorus at the $\Sigma 5(210)$. However, they have shown that the total energy of a $\Sigma 3(111)$ GB containing a P in an interstitial site with the total energy of the same system but the P is in a substitutional position lead to the same segregation energy.

Indeed, phosphorus is also sometimes considered as **an interstitial segregant**, [4], [19], [36]. Braithwaite and Rez [37] have reported the interstitial position to be more stable at the

$\Sigma 5(210)$ GB than a substitution site near GB (2nd layer). Wachowicz and Kiejna [26] find a lower segregation for phosphorus in interstitial position for both $\Sigma 3(111)$ and $\Sigma 5(210)$ GB.

These results can be understood with the enthalpy-entropy compensation effect described in the following section (*Section 2*) and more detailed in *IV-Annex 4*. Phosphorus can both segregate in substitutional and interstitial sites and can be considered as a substitutional segregant at lower temperature $T = 0$ K in DFT studies and an interstitial segregant in temperatures of practical interest (700 K) [38] (**Figure IV- 7**). A change of the temperature leads to a change of the segregant behaviour in the GB corresponding to a variation of the entropy (**Figure IV- 7**).

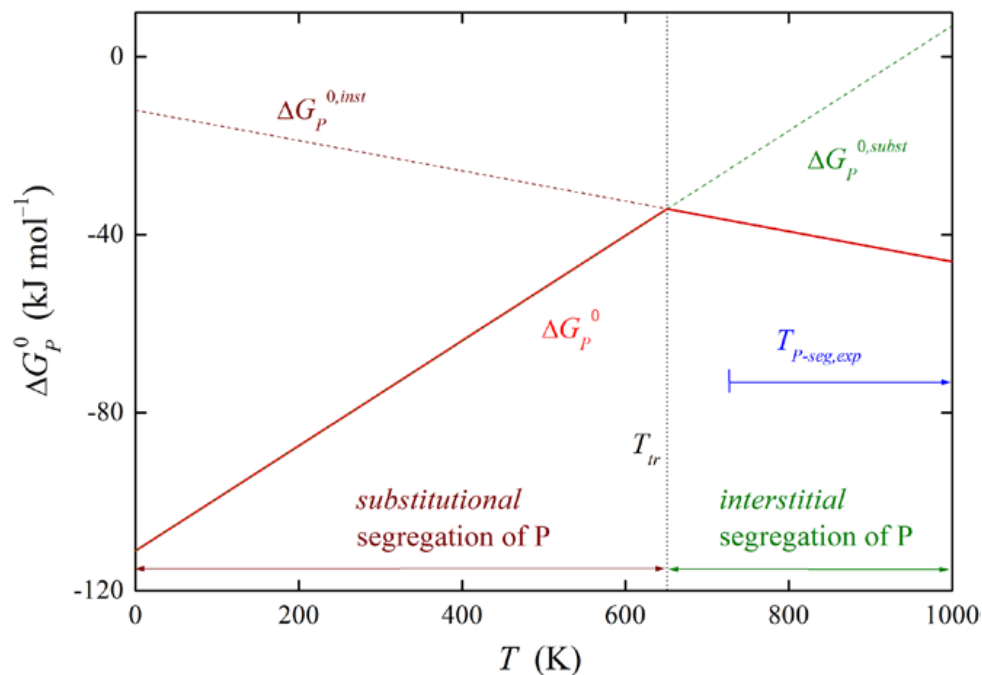


Figure IV- 7: Temperature dependence of the phosphorus's segregation enthalpy ΔG_p^0 in α -Fe [35]

Phosphorus is expected to be a substitutional segregant in alpha iron up to about 650 - 700°C and an interstitial segregant at higher temperatures. This underlines the need to take into account the entropy contribution, which is often omitted in computational studies and needs to be considered to evaluate the preferential sites for GB segregation. Lejcek developed a model which takes into account this entropy contribution (*IV-Annex 4* and *Section 3.2*), however due to the complexity of his model to be applied on atomistic studies, this model has not be used to estimate P segregation in *Section 3*.

[IV-1.1.2.3 Site distance from GB](#)

The concentration is maximum close to the GB plane, as represented **Figure IV- 8**.

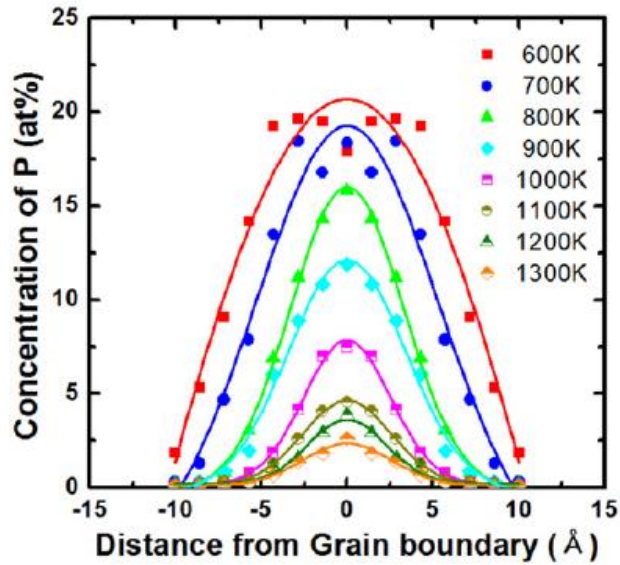


Figure IV- 8: Concentration profiles of P atoms on tilt HAGBs for 0.1 at% bulk concentration of P in Fe at temperatures ranging from 600 to 1300 K. The lines are Gaussian fitting.[4]

Molecular static simulations with the EAM Ackland potential [39] of He *et al.* [18] and Rajagopalan *et al* [25] have shown that the segregation energy of P approaches zero at a distance about 7 Å from the GB plane. This agrees with the data presented in **Figure IV- 8**. The same trends have been identified, **using DFT**, by our EDF team for substitutional phosphorus segregant (**Figure IV- 9**). Note that this seems to be a general feature for the segregants that were investigated.

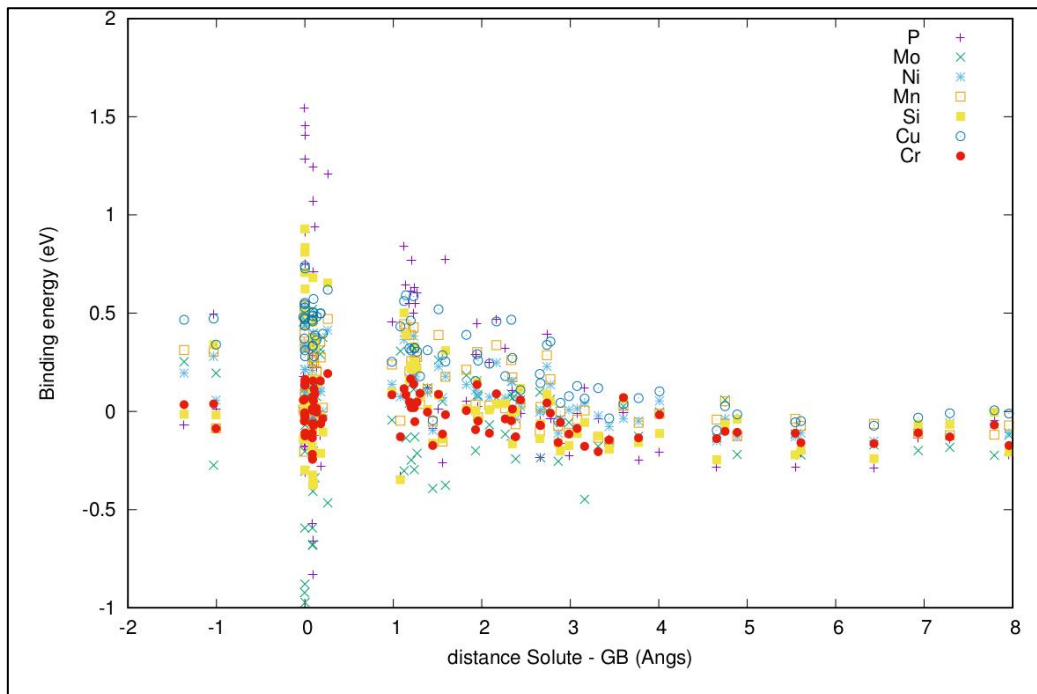


Figure IV- 9: Variation of binding energy as a function of distance from tilt grain boundary for different solutes [40]

The segregation process occurs mainly at segregation sites distributed in the direct vicinity of the GB. The binding energy between phosphorus and a given segregation site decreases when the distance from the GB increases. Segregation can be considered to be null above a distance about 7 Å.

The addition of other chemical species can lead to synergetic solute segregation mechanisms. This is the topic of the next section.

IV-1.2 Synergetic segregation

Synergetic relations often exist between solute atoms. Some solutes are considered (P, S, Sn, Sb) to be implicated in the **embrittlement of steels** [1] whereas C and N, on the other hand, enhance the GB cohesion. The addition of other solute atoms leads to **co-segregation and in some cases to site competition**, which has an impact on segregation.

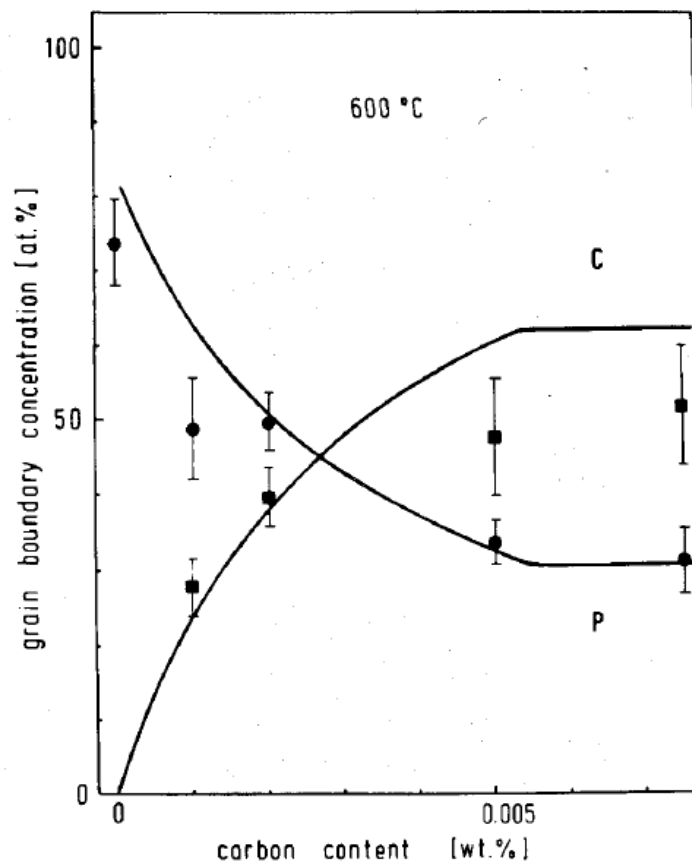
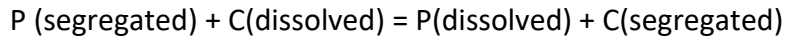


Figure IV- 10: GB concentrations of phosphorus and carbon in Fe-0.17%P. Dependence on the bulk concentration of carbon after equilibration at 600°C [41]

According to Erhart *et al.*, R.Möller *et al.* and Grabke [10] [42] [12] AES experiments, there is a synergetic segregation between carbon and phosphorus which leads to higher grain-boundary cohesion. Indeed, phosphorus segregates where the concentration of carbon is really low (as for instance in a 7 ppm C, 310 ppm P and 0.36 %at Mn steel) and leads to the

formation of an intergranular surface of P, whereas a higher concentration of carbon (as for instance in a 14 ppm C, 80 ppm P and 0.38%Mn steel) does not lead to such an embrittlement.

This is due to a site competition between phosphorus and carbon, which displaces equilibrium as follows:



Another property which can explain this phenomenon is the existence of a repulsive interaction between carbon and phosphorus, *i.e.*: carbon is able to segregate in the GBs and repel the phosphorus. The more powerful segregant carbon repel the less surface-active phosphorus in the boundaries. This is illustrated in **Figure IV - 10**, where AES analysis of ferritic steels shows that phosphorus concentration decreases when carbon concentration increases. Zhang [6] observed a similar competition site mechanism between carbon and phosphorus: a thermal ageing with a low cooling rate leads to a high phosphorus segregation, leaving less sites for carbon segregation during cooling and thus to a decrease of carbon segregation at the GB.

Chromium, on the other hand, enhances the segregation of phosphorus in the case of Fe-Cr-C-P alloy (**Figure IV- 11**): the strong affinity between carbon and chromium permits the creation of an attractive interaction between them and in the same time leads to the formation of carbides and a decrease of carbon activity (the effective concentration of carbon in the solution) [10].

The carbon activity will not be sufficient to repel the phosphorus away from the GB and an increase of P GB segregation is observed. However, the segregation of phosphorus in Fe-Cr-C-P alloy is not enhanced by a co-segregation effect between chromium and phosphorus, *i.e.*: chromium in Fe-Cr-P alloys does not increase phosphorus segregation. Other elements such as manganese and vanadium [43] also decrease the activity of carbon because of their strong affinity with it and can thus enhance phosphorus segregation in the same way as chromium. In contrast, nickel is supposed to increase the activity of carbon and decrease phosphorus segregation.

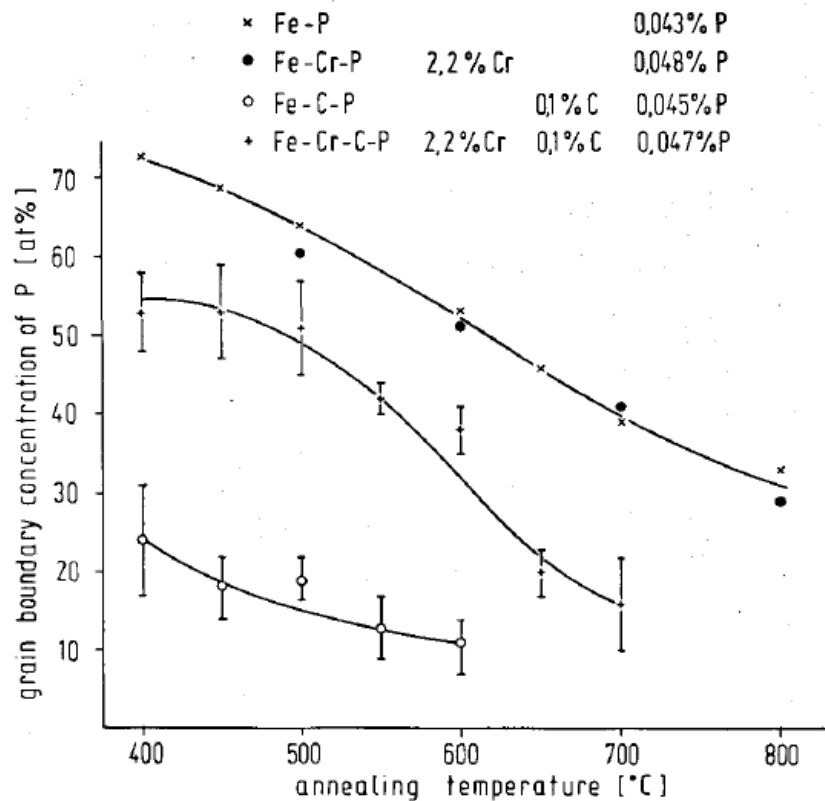


Figure IV- 11: Effects of carbon and chromium on the GB segregation in Fe-P, Fe-Cr-P, Fe-C-P and Fe-Cr-C-P alloys with about the same P concentration [12]

Erhart *et al.* [10] attribute to Mo a special role leading to the formation of Mo-P compound and a decrease of phosphorus segregation. In 2.25Cr1Mo steels thermal aged analysed with electrical resistivity measurement, Song *et al* [7] highlighted that, similar to the behaviour of Cr, the addition of Mo leads to the formation of carbides and an increase of phosphorus segregation. According to Zhang [6], Mo-enriched carbides can create massive sites for phosphorus segregation (in the transitioning region from the interface to the adjacent GB). In a more general case, they find that carbide-matrix interfaces can provide effective sites for phosphorus segregation.

Other studies, however, show that the co-segregation effect of phosphorus and Mo is not strong enough to cause an increase of P segregation. Indeed, Mo has a strengthening effect which over compensates the segregation of phosphorus [44]. According to Möller [45] AES experiments in Fe-P-Nb alloys, Nb leads to a decrease of phosphorus segregation by the formation of NbP precipitates. Adding carbon enhances P segregation by the formation of strong bonds between Nb and C, and favours the dissociation of P from P-Nb-C carbides

To conclude this section, the segregation mechanism in low alloy steels containing carbon, is mainly determined by the influence of the alloying element on carbon activity which often counteracts the embrittlement in low alloy steels. Experiments on industrial ferritic steels lead to the same conclusion [43], [46].

Phosphorus segregation at GB can be enhanced or reduced by the addition of other chemical species. Carbon tends to decrease phosphorus segregation at GB, but the addition of other elements such as chromium and vanadium reduces the activity of carbon or leads to the formation of carbides and promotes an increase of phosphorus content at GBs. **Mo** seems to reduce phosphorus segregation by the formation of complexes Mo-P, but the results are controversial as some studies have shown the opposite.

IV-2. Equilibrium GB segregation models

The elastic energy induced by segregation can be explained by thermodynamics models. The influence of the GB characteristics (structure and orientation) defined in *Chapter II* on the segregation process leads to the development of atomistic models. A summary of these different segregation models is presented at the end of this section.

In a system containing a GB, at equilibrium, a partitioning of solutes is often observed that results in an enrichment of the GB. The levels of this enrichment are defined only by the system parameters at equilibrium and not by the history of the material. This phenomenon corresponds to a reversible adsorption usually described by Gibbs adsorption theory. Langmuir-McLean models which are usually called “McLean models” have been derived from this approach. More accurate models which consider the solubility limit and the interaction between atoms, have been developed later on. The next sections describe briefly (some of) the models existing so far, starting from McLean model.

IV-2.1 McLean models

IV-2.1.1 Gibbs theory and the development of McLean approach

McLean models a matrix containing a GB as a solid dilute binary solution where solute atoms are distributed at random amongst bulk sites and grain boundary sites. The GB is represented as an interface between two grains (the matrix), and McLean applies Gibbs principles to determine **the equilibrium segregation at GB interfaces** using one single parameter: the interfacial energy E_ϕ . This quantity is defined as the excess energy at the surface of a material compared to the bulk or as the work required to build an area of a particular surface and refers to the energy cost associated to the introduction of that interface, due to the breaking of bonds necessary to produce the surface. Following Gibbs approach, the decrease of the surface or interface energy is caused by the redistribution of solutes at the interface [47]:

$$\frac{dE_\phi}{d\mu_S} = -\Gamma_S \quad \frac{dE_\phi}{d \ln a_S} = -RT\Gamma_S \quad (\text{eq IV-1})$$

where E_ϕ is the interfacial energy, Γ_S the excess concentration of the dissolved solute species S, a_S its thermodynamic activity and μ_S its chemical potential.

Gibbs expression is not directly usable because it is difficult to measure the intergranular energy as a function of the solute concentration and temperature. Thus, several approaches, based on this theory, like McLean model, have been developed to overcome these problems and link directly the GB composition, volume and temperature.

In MacLean's model, the GB is considered as a particular surface, i.e. an interface between two grains where Gibbs approach can be used to develop models which quantify GB segregation.

IV-2.1.2 Langmuir-McLean approach for binary solutions with ideal random mixing atoms

According to McLean [48], a distortion energy is needed to introduce solute atoms in the crystalline network and the equilibrium segregation can be explained in terms of lattice distortion around solute atoms, where the GB structure consists of a number of finite distorted sites. Moreover, Gibbs considers that the driving forces for segregation correspond to the saturation of free bonds at the surface or interface and a release of strain energy which lead to a decrease of interfacial energy [49]. Since the energy of a GB is different from the one in the bulk, **the segregation energy or Gibbs free energy can be defined** as the difference between these two energies.

A regular¹⁵ binary solid solution is considered everywhere: N solute atoms are distributed randomly among M lattice sites and n solute atoms are also randomly distributed among m independent distorted GB substitution sites; the total free enthalpy (Gibbs free energy) G of this binary system is given by:

$$G = nU_S^{gb} + NU_S^B - k_B T [\ln m! M! - \ln(m-n)! n! (M-N)! N!] \quad (\text{eq IV-2})$$

This equation can be divided into two main parts: a first part which refers to the **internal energy of solute atoms S** at the GB and in the lattice U_S^{gb} and U_S^B respectively, and a second part corresponding to the **configurational entropy** of solute atoms positioned in the matrix and at the GB, which can be obtained using Boltzmann equation.

If the total Gibbs free energy G of a solution goes through a minimum value as the composition changes, then all net changes will increase and the reaction system will be in a state of *chemical equilibrium*: **equilibrium** is reached. The free enthalpy G is minimum and its differentiation with respect to n (the number of solute atoms in the bulk) is equal to 0. Noting that the sum of n and N is constant: $N = A + n$ with A a constant.

$$\frac{dG}{dn} = 0 \quad (\text{eq IV-3})$$

Using Stirling formula, G is given by:

$$G = nU_S^{gb} + (A-n)U_S^B - k_B T [m \ln(m) + M \ln(M) - (m-n) \ln(m-n) - n \ln(n) - (A-n) \ln(A-n) - (M-A+n) \ln(M-A+n)] \quad (\text{eq IV-4})$$

¹⁵ A **regular solid solution** is a solution defined by an entropy of mixing equal to that of an ideal solution with the same composition, but is non-ideal due to a nonzero enthalpy of mixing.

The segregation energy or Gibbs free segregation energy can be expressed as:

$$U_S^{gb} - U_S^B = k_B T \ln \left(\frac{m-n}{n} \times \frac{N}{M-N} \right) \quad (\text{eq IV-5})$$

The concentration (atomic fraction) of solute S in the distorted region (corresponding to the GB solute concentration) is given by $X_S^{gb} = \frac{N}{M}$ and the concentration (atomic fraction) of solute S in the undistorted region (corresponding to the grain/bulk solute concentration) is given by $X_S = \frac{n}{m}$

Standard Gibbs energy of segregation for an ideal entropy of mixing solid solution is given as:

$$\Delta G_S^0 = U_S^{gb} - U_S^B \quad (\text{eq IV-6})$$

Therefore, equation (eq IV-2) can be written for a binary ideal solution as [48]:

$$\frac{X_S^{gb}}{1-X_S^{gb}} = \frac{X_S^B}{1-X_S^B} \exp(-\Delta G_S^0/RT) \quad (\text{eq IV-7})$$

Langmuir-McLean model describes in a first approach the GB segregation for ideal GB random mixing regular binary solid solution on substitutional sites. The concentration ratio balance between matrix $\frac{X_S^B}{1-X_S^B}$ and GB $\frac{X_S^{gb}}{1-X_S^{gb}}$ is expressed as a function of the standard free energy ΔG_S^0 . Thus equation (eq IV-7) permits to estimate the solute segregation on the GB.

IV-2.1.3 General Langmuir-McLean for regular binary solutions

However, in the general case of regular solid solutions, an “**interfacial excess energy**” is created. **There are some deviations between ideal random mixing atoms and real behaviour of any thermodynamic system.** The entropy changes and thus the Gibbs energy changes above and below the ideal entropy of mixing.

McLean derived a more general relationship of equilibrium segregation for a binary **regular** solution M-S. The general Langmuir-McLean isotherm can be expressed as:

$$\frac{X_S^{gb}}{X_S^{0,gb} - X_S^{gb}} = \frac{X_S^B}{1-X_S^B} \exp(-\Delta G_S/RT) \quad (\text{eq IV-8})$$

where $X_S^{0,gb}$ is the GB concentration of S **at saturation**, which is often accepted to be equal to 1. More details are given in *IV-Annex 2*.

In the approach above the interfacial segregation is defined **independently of the system nature** (not only ideal random mixing atom solution). Moreover, the Langmuir-McLean equation is only valid for a **constant free energy of segregation**: for one type of segregation site and for the case of no interaction between the solute atoms either at the interface or in the bulk. Thus, the McLean-Langmuir absorption isotherm is only an approximation for real cases.

In the same way as for an ideal random mixing regular solution, Langmuir-McLean general theory models the GB segregation for a regular GB binary solid solution on substitutional sites. The concentration of solute at saturation is not always equal to 1, and can be replaced by $X_S^{0,gb}$. All substitution sites are not necessarily occupied, the concentration ratio balance between matrix $\frac{X_S^B}{1-X_S^B}$ and GB $\frac{X_S^{gb}}{X_S^{0,gb}-X_S^{gb}}$ is expressed as a function of the free energy which incorporates the extra contribution of interfaces, *i.e.* the excess free energy ΔG_S^E , which is the difference between the ideal free segregation ΔG_S^0 and the free segregation ΔG_S .

Extensions and modifications on Langmuir-McLean model have been made to account for solute interactions and competition between the different sites available. Solid solubility in a material is strongly correlated to the effective concentration of solutes (activity of solutes) in the bulk, thus this aspect has to be taken into account in thermodynamic segregation models. They are described in the following sections.

IV-2.2 Improvement of McLean model

IV-2.2.1 Seah and Hondros models

Seah and Hondros [9] extended McLean approach for **regular solutions** to **interstitial elements**. The fraction of atomic sites at saturation including interstitial and substitutional sites is given by:

$$X_S^{0,gb} = \frac{n_S^{gb\ int}}{n_S^{gb\ int} + n_S^{gb\ subs}} \quad (\text{eq IV-9})$$

As solute atoms at saturation do not necessary occupy all the sites available, a coverage rate can be estimated as:

$$\theta_S^{gb} = \frac{X_S^{gb}}{X_S^{0,gb}} \quad (\text{eq IV-10})$$

The Langmuir-McLean isotherm equation [48] can be rewritten:

$$\frac{\theta_S^{gb}}{1-\theta_S^{gb}} = \frac{X_S^B}{1-X_S^B} \exp(-\Delta G_S^0/RT) \quad (\text{eq IV-11})$$

By application of the **truncated Brunauer, Emmett and Teller (truncated BET isotherm) gas adsorption theory**, Seah and Hondros [9] describe the GB enrichment in a binary alloy using the solute solubility limit because this quantity is directly correlated to the solute activity and thus to the concentration of solute atom in the GB.

The enrichment factor of a segregant/solute S, for the dilute case is given by: $\beta_S^{gb} = \frac{X_S^{gb}}{X_S^B}$ where X_S^B is, as usual, the bulk concentration of the segregated element S and X_S^{gb} the concentration of S in the distorted region, *i.e* the GB.

According to Seah and Hondros, X_S^{gb} depends on the **solubility limit** X_S^* in the matrix and the associated free energy ΔG_{sol} can be obtained from the considerations described on IV-Annex 3. The Langmuir-McLean equation is then transformed as:

$$\frac{X_S^{gb}}{1-X_S^{gb}} = \frac{X_S^B}{X_S^*} \exp(-(\Delta G_S - \Delta G_{S sol})/RT) \quad (\text{eq IV-12})$$

where ΔG_S is the segregation free energy.

Experimental investigations have shown that this model applies for numerous binary systems. **Figure IV- 12** shows the dependence of the GB enrichment ratio β_S with the solute solubility limit in Fe, Cu or Ni. The lower the solubility, the larger the segregation level, and the enrichment factor.

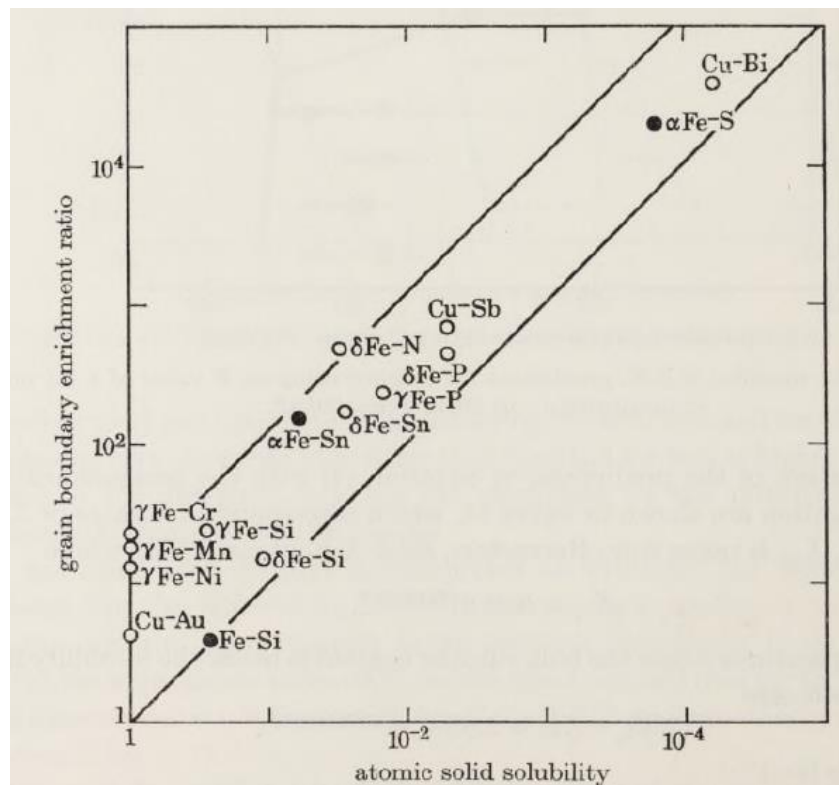


Figure IV- 12: Correlation of the enrichment ratio, with the inverse solubility, white circles correspond to GB energy values and black circles to AES values [9]

Seah and Hondros include in the general McLean model, interstitial segregation sites in a first approach, and the precipitation of solute at GB in a second model by the introduction of matrix solute solubility in McLean's formula.

IV-2.2.2 Fowler and Guggenheim theory

McLean model does not take into account any solute-solute interactions. However, in many cases, solute-solute interactions cause significant deviations from the ideal Langmuir-McLean behaviour specially at high segregation levels.

Fowler and Guggenheim [50] thus introduced in McLean model, an interaction term (per molar unit) between two nearest solute neighbours inside the GB; this term is defined as a pair interaction energy:

$$w_{ij}^{gb} = A_{avogadro} [\varepsilon_{ij}^{gb} - 1/2 (\varepsilon_{ii}^{gb} + \varepsilon_{jj}^{gb})] \quad (\text{eq IV-13})$$

where A is Avogadro number, ε_{ij}^{gb} , ε_{ii}^{gb} and ε_{jj}^{gb} are interaction pair potentials between atoms on sites i and j.

The additional energy term for the GB segregation free energy is proportional to the fractional amount of segregation $X_S^{gb}/X_S^{0,gb}$. Hence, the free GB segregation energy ΔG_S is obtained by:

$$\Delta G_S = \Delta G_S^0 + 2Zw_{ij}^{gb} \frac{X_S^{gb}}{X_S^{0,gb}} \quad (\text{eq IV-14})$$

Where Z is the coordination number of nearest neighbours in the GB. Finally, the Langmuir-McLean equation can be rewritten as:

$$\frac{X_S^{gb}}{1-X_S^{gb}} = \frac{X_S^B}{1-X_S^B} \exp\left(-\left(\Delta G_S^0 + 2Zw_{ij}^{gb} \frac{X_S^{gb}}{X_S^{0,gb}}\right)/RT\right) \quad (\text{eq IV-15})$$

If $w_{ij}^{gb} = 0$, there is no mutual interaction, and the ideal Langmuir-McLean model is obtained.

In this model, negative values of the pair interaction energy w_{ij}^{gb} correspond to attractive interactions between segregants and an increase of the free energy of segregation, whereas positive values of w_{ij}^{gb} lead to a segregation decrease.

Fowler and Guggenheim include solute-solute interaction occurring inside the GB, by the introduction of a pair-interaction term in McLean's formula.

IV-2.2.3 Guttman theory for multicomponent systems

In Fowler and Guggenheim model, the solute and solvent atoms are supposed to be distributed randomly on equivalent sites, either in the grain or at the GB. However, it is well known that, on the one hand all sites are not equivalent, and on the other hand that segregation of one **solute depends on the segregation of others**. A wide range of possible synergistic/competing segregation behaviors between solute elements are thus possible. These include effects such as site competition between segregating species, reduced segregation due to formation of competing bulk phase and co-segregation. Guttman

proposed an approach to model co-segregation in multicomponent alloys, first for a dilute solid solution composed of substitution sites competing against each other. In a second step, interstitial sites were added to the model.

IV-2.2.3.1 Regular solid solution model composed of substitution sites competing

To go deeper into the Fowler and Guggenheim theory, Guttman has developed a model that takes into account the interactions between co-segregation substitutional species in a ternary or higher order alloy. The expression for the intergranular segregation of solutes S in a multicomponent system is given by:

$$\frac{X_S^{gb}}{X_S^{0gb} - \sum_j^{m-1} X_j^{gb}} = \frac{X_S^B}{1 - \sum_j^{m-1} X_j^B} \exp\left(-\frac{\Delta G_S}{RT}\right) \quad (\text{eq IV-16})$$

where X_S^{gb} is the concentration of solute S at the GB, X_j^{gb} and X_j^B are the concentration of a chemical species different from the solute S in the GB and in the bulk, respectively.

ΔG_S is the free segregation energy which can be expressed as a function of the solute-matrix and solute-solute interaction coefficient respectively α_{SM} and $\alpha'_{SS'}$, as:

$$\Delta G_S = \Delta G_S^0 - 2\alpha_{SM}(X_S^{gb} - X_S^B) + \sum_{S'} \alpha'_{SS'}(X_{S'}^{gb} - X_{S'}^B) \quad (\text{eq IV-17})$$

with $S' \neq \{S, M\}$ and where ΔG_S^0 is the standard Gibbs free segregation energy.

$\alpha'_{SS'}$ is the net molar interaction energy between solutes in the matrix. It is obtained as the difference between the solute-solute interactions $\alpha_{SS'}$ and the solute-matrix interactions ($\alpha_{SM}, \alpha_{S'M}$):

$$\alpha'_{SS'} = \alpha_{SS'} - \alpha_{SM} - \alpha_{S'M} \quad (\text{eq IV-18})$$

One limitation of the model is that the interaction coefficients in the matrix and in the GB are supposed to be the same, while these coefficients are different in general.

IV-2.2.3.2 Regular solid solution with substitution and interstitial without site competition

In the case of both substitution and interstitial sites, the site network is divided in two subsets: a first one fully filled by solvent atoms with some solute atoms S on substitution sites; another one, made of interstitial sites, partly filled by the solute atoms S'.

The proportion of these two types of sites is given by a and b respectively, satisfying $a + b = 1$. Three interaction coefficients need to be defined: Φ_{SM} and $\Phi_{VS'}$ corresponding to the interaction between solute atom S and matrix atom in the substitutional network and interactions between solute atom S' with non-occupied sites in the sub-set interstitial network, the last term $\Phi'_{SS'}$ refers to the interaction between these two solute segregated atoms in a substitutional network and in an interstitial network respectively. If the interactions

between solute and solvent atoms Φ_{SM} or vacancies Φ_{VS} , are neglected, the free segregation energy can be rewritten as shown:

$$\Delta G_S = \Delta G_S^0 + \frac{\phi'_{SS'}}{b} (Y_{S'}^{gb} - Y_{S'}) \quad \text{and} \quad \Delta G_{S'} = \Delta G_{S'}^0 + \frac{\phi'_{SS'}}{a} (Y_S^{gb} - Y_S) \quad (\text{eq IV-19})$$

where Y_S^{gb} and $Y_{S'}^{gb}$ are the atomic fraction of solute S and S' in the sub-network of substitution and interstitial sites respectively, and ΔG_S^0 and $\Delta G_{S'}^0$ are the corresponding standard free segregation energies.

If $\phi'_{SS'} < 0$, the interaction is attractive and the segregation energy of both S and S' decreases by the presence at the same time of S' and S.

IV-2.2.3.3 General approach for any complex system

The approach described above can be generalised for regular multicomponent solid solutions [51]. In the case of a dilute bulk solid solution and neglecting Fowler interaction terms, segregation can be described by:

$$\frac{X_S^{gb}}{X_M^{gb}} \approx X_S \exp\left(-\frac{\Delta G_S}{RT}\right) \quad (\text{eq IV-20})$$

$\Delta G_S = \Delta G_S^0 + \sum Q_S X_J^{gb}$ where X_J^{gb} and Q_S are the generalized terms for the interfacial concentrations and the solute interactions respectively.

Numerous models of GB segregation relying on the **Guttman multicomponent model** [52], [53] have been fitted to experimental values. A typical example is the model developed by Seah [54] based on AES experiments made on a sample of the SAE 340 steel (Fe-0.79 Mn, 1.26Ni, 0.77Cr and P steels) used in isothermal temper embrittlement experiments made by Carr *et al* [55].

Guttman model further developed McLean and Folwer and Guggenheim models by taking into account the co-segregation of a multi-component system, in the case of a regular solid multi-component solution composed of substitution sites competing, and for the case of regular solid solution with substitution and interstitial site without competition. A general formula close to McLean formula can be extracted from Fowler and Guggenheim theory and Guttman approaches which expresses the GB concentration in terms of interaction terms

Although the method presented above seems to be sufficiently well elaborated to account for experimental results, it must be kept in mind that these theories suppose that segregation is independent of the segregation site. The segregation obtained remains an “average” quantification of the segregation and thus does not correspond to the real enrichment at the GB. The next section will present more realistic segregation models.

IV-2.3 Towards more realistic segregation models

It is commonly accepted that the free segregation energy varies from one GB to another and to one site to another for a given GB. Despite the usefulness of McLean models that are often

employed to determine the average concentration of solute atom at the GB, it is often necessary to consider the relationship between the GB geometry/structure and segregation on specific GB sites.

Indeed, according to **Sutton and Balluffi** [56], any understanding of the variations of the interfacial energy must account for the atomic structure and the details of the sites in the GB. A particular useful data is the **solute binding energy to the GB**, which represents how much a solute prefers being located within the GB than being in the bulk. Simulation studies at the atomistic levels are the more suitable methods to extract results in this direction, as obtaining data at the atomic level from experimental results is more difficult.

IV-2.3.1 Comparing experimental and simulation segregation

Most of experimental studies estimate the GB enrichment using McLean model and thus consider an average free segregation energy or an average binding energy: the GB details altogether are ignored and the interaction is described by a single value per solute. However, the binding energy, as other energetic properties at the atomistic level is directly correlated to the GB structure and varies from one site to another. **Figure IV- 13** compares the prediction of McLean model using as input experimental data with an atomistic model that takes into account the different sites in a $\Sigma 5/(310)$ GB in Ni-Pt. The discrepancy is obvious.

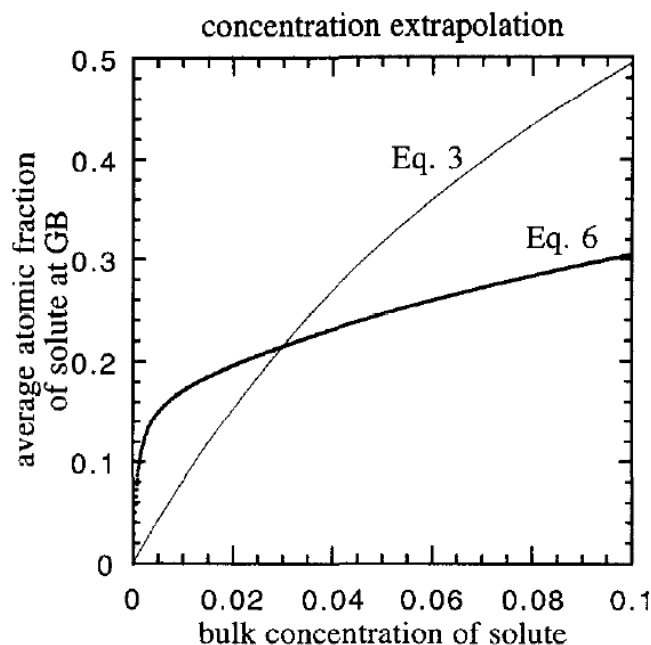


Figure IV- 13: Solute concentration calculated by classical McLean model (Eq. 3) and by atomistic extrapolation (Eq. 6) as a function of solute bulk concentration at the $\Sigma 5/(310)$ GB in Ni-Pt [57]

In order to model more properly segregation, the GB type and orientation, the influence of configurational entropy and solubility limit and the site of segregation have to be taken into account. Indeed, as mentioned previously, the solute GB binding energy depends on the GB

structure. For instance, HAGBs are usually more “porous” (irregular) and thus the elastic strain energy induced by a solute atom when staying at this GB type is often lower [14], and the solute segregation energy often higher. In contrast, LAGBs are usually less “porous” and lead to a lower segregation energy.

Furthermore, electronic microscopic investigations have revealed that certain positions at the GB are energetically preferential. They correspond to compressive sites according to microscopic STEM (high resolution imaging scanning transmission electron microscopy) investigations in Mg, Zn and Gd alloys [58]. The presence of substitutional and interstitial sites depends on the GB structure.

Lejcek *et al* [59], [60] plot (**Figure IV- 14**) the segregation energy as a function of the solubility limit in Fe obtained both experimentally and using DFT and empirical potentials. They show that for elements with a low solubility limit ($X_i^* < 0.01$), the agreement between the theoretically calculated segregation energy ΔE_I and the experimental values of the standard segregation enthalpy ΔH_I^0 is poor. For elements with high solute solubility ($X_i^* > 0.01$), the agreement is much better.

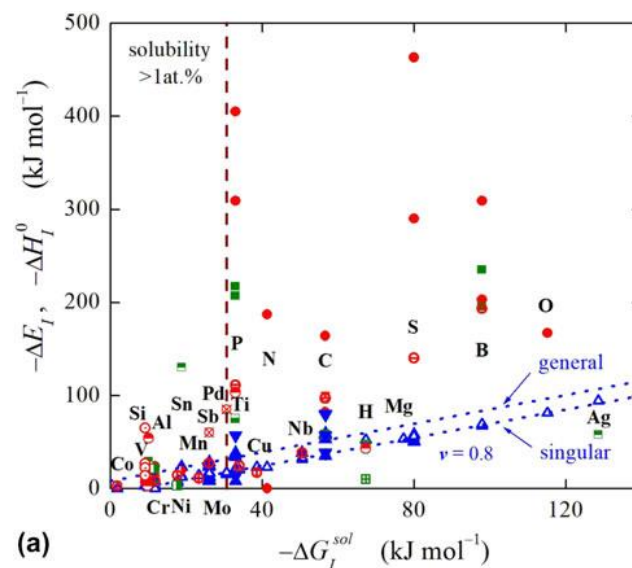


Figure IV- 14: Plot of the segregation energy and/or the enthalpy of GB segregation, ΔE_I and ΔH_I^0 , versus Gibbs energy of solution $\Delta G_I^{sol} = RT \ln X_i^*$, in α -Fe. Solid triangles correspond to experimental data, empty triangles and/or dashed lines correspond to experimental prediction, solid circles represent DFT values and solid squares show other theoretical values (MS, TB) [60]

Erhart and Grabke [10] analysis of phosphorus segregation evolution with temperature at GB in ferritic iron, has shown that the segregation entropy ($\Delta S_s^0 = 22 - 21.5 J/(mol K)$) cannot be omitted if one wants to precisely reproduce the experimental results at high temperature (**Figure IV- 15**).

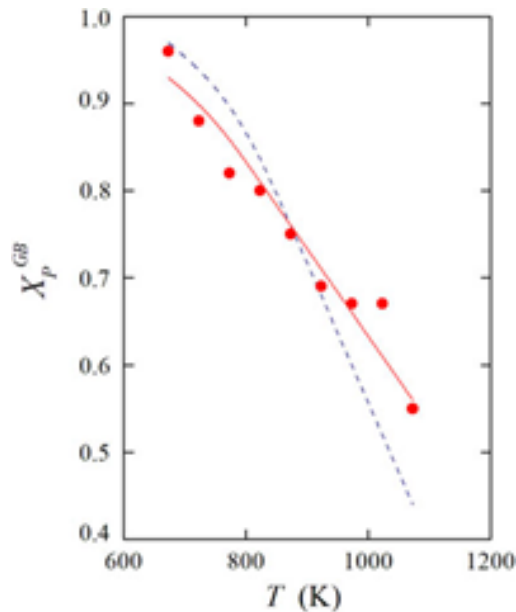


Figure IV- 15: Temperature dependence of phosphorus GB segregation in α -iron. $X_p = 0.0017$. Red circles are the experimental GB concentrations and solid red line correspond to data with $\Delta H_I^0 = -36 \text{ kJ/mol}$ and $\Delta S_I^0 = 22 \text{ J/(mol K)}$ fits with the entropy and the blue dashed line represents effective enthalpy segregation $\Delta H_I^{eff} = -36 \text{ kJ/mol}$ without considering the segregation entropy [38]

Therefore, temperature dependent terms should be included in the free energy models as already proposed by Seah [54]. Note that, similar to the binding energy, the entropy depends on the GB structure: for HAGB, the segregation entropy is less negative whereas for LAGB, the segregation entropy is more positive because of the more irregular structure of HAGBs [14]. Indeed, according to **White and Coghlan** [61], as the tilt angle increases, the average solute segregation at the GB increases due to a higher stress in the vicinity of the boundary.

Experimental and simulations studies provide two different points of view on GB segregation. Experimental techniques permit to obtain an average quantification of GB segregation and thus an average free energy. Segregation process is difficult to predict, and its quantification difficult to estimate, it depends on a lot of parameters such as GB atomic structure (site of segregation and GB orientation), and on temperature and composition effects (entropy and solubility limit). Thus, it is necessary to use computational techniques in complement to experiments in order to provide more accurate predictions about segregation and non-hardening-embrittlement.

IV-2.3.2 Lejcek *et al.* model

As discussed in the previous sections, the segregation at the GB is directly linked to the **free segregation enthalpy or Gibbs free energy**, however, the orientation and geometric characteristics of the GB play a crucial role in the GB segregation. In order to show that one binding energy is not sufficient to characterize GB segregation, Lejcek *et al* [62] developed a thermodynamic model fitting experimental data of free segregation energy (enthalpy and entropy terms) in order to take into account the GB structure.

Lejcek *et al.* [62] model takes into account the solute solubility with respect to the GB structure. This model constitutes an extension of Seah and Hondros [9] model by the introduction of:

- the anisotropy of the GB segregation
- the consideration of a non-ideal behaviour of the solid solutions at the solubility limit and its dependence on temperature

To tackle the entropy issue, Lejcek *et al* [62] have developed a concept to estimate the standard segregation entropy ΔS_s^0 from experimental data. One of the significant result is that they have highlighted a linear relationship between segregation entropy and enthalpy as well as the impact of the nature of the segregation sites (substitutional or interstitial) as shown by the split into two branches, one for substitutional segregating solutes and the other for interstitial segregating solutes. One needs thus to be careful when using this compensation effect that only one single segregation mechanism is active.

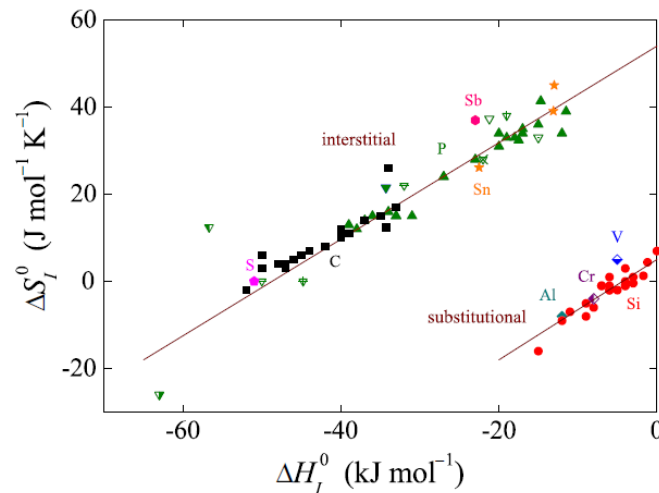


Figure IV- 16: Enthalpy-entropy compensation effect for GB segregation in alpha-Fe. Full symbols the segregation at individual GB, other symbols are literature data for polycrystalline alpha-Fe [35]

More details about the derivation of Lejcek model are given in *IV-Annex 4*.

Lejcek improves Seah and Hondros model and Guttmann model by taking into account the GB orientation, the solid solubility and the type of segregation site (substitutional or interstitial site). Entropy effects are estimated by the concept of the enthalpy-entropy compensation effect.

IV-2.3.3 Towards atomistic models

IV-2.3.3.1 White and Stein GB site segregation model

Several studies try to develop models taking into account the binding energy of each atomic site at the GB. White *et al* [61], [63] were the first ones to treat the segregation to each site individually. In contrast to the earlier McLean model, White model considers the segregation

process as a variation of the elastic strain of a substitutional solute moving to the GB. The segregation energy is expressed as a function of the fraction of the total sites F_i at the GB having a binding energy E_{bi} which is supposed to follow a normal probability distribution. It is given by:

$$X_{S,i}^{gb} = \frac{X_S^B \exp\left(\frac{E_{b,i}^{gb,S}}{k_B T}\right)}{1 - X_S^B + X_S^B \exp\left(\frac{E_{b,i}^{gb,S}}{k_B T}\right)} \quad (\text{eq IV-21})$$

where X_i^{GB} is the fraction of the solute filled GB sites i , X_S is the solute concentration in the bulk, and E_{bi} is the binding energy for each site.

A weighted average of the concentration of the solute at the GB X_S^{gb} can be then calculated:

$$X_S^{gb} = \frac{\sum_i F_i X_{S,i}^{gb}}{\sum_i F_i} \quad (\text{eq IV-22})$$

where F_i is the fraction of the sites i at the GB corresponding to a concentration of the solute filled GB sites $X_{S,i}^{gb}$.

Since the total GB segregation is a sum over all segregation sites, White *et al* [61], [63] model permits to make a quantification of solute GB segregation from **a distribution of the binding energies (each site at the GB corresponds to a binding energy)**. Note that the calculation does not require the knowledge of the saturation limit. The normalized distribution function for a certain number of sites with a given energy is given by:

$$N(E_{b,i}^{gb,S}) = \frac{2n_i}{n_t(E_{b,i+1}^{gb,S} - E_{b,i-1}^{gb,S})} \quad (\text{eq IV-23})$$

where n_t is the total number of sites and n_i is the number of sites that have energy less than $(E_{b,i+1}^{gb,S} - E_{b,i}^{gb,S})/2$ and greater than or equal to $(E_{b,i}^{gb,S} - E_{b,i-1}^{gb,S})/2$

According to White and Coghlan, this new model permits an improved correspondence of theoretical values with the experimental data for δ -iron (alloys FeCrNi and CuNi steels) [64]. However, some problems remain: very little area near the boundary can be investigated, the distance of the solute site to the GB has to be defined and the solute-solute interaction is not taken into account. Recent studies conducted by Huber *et al.* [65] [66] have made use of this atomistic approach to GB segregation. They replaced White *et al* model's free energies by the binding energies of the solutes at specific sites:

$$X_S^{gb} = \frac{1}{N} \sum_i \frac{1}{1 + \frac{1 - X_S^B}{X_S^B} \exp(-E_{b,i}^{gb,S}/k_B T)} \quad (\text{eq IV-24})$$

where N is the number of the sites at GB, X_S^B is the solute concentration in the bulk and $E_{b,i}^{gb,S}$ is the binding energy of the solute at site i of the GB.

White *et al* model constitutes an extension of McLean model by giving an atomistic point of view of GB segregation: each GB segregation site behaviour is taken into account

Recent developments tend to by the use of physical descriptors, capture the pertinent information for each possible segregation and to define a relation between the data and segregation energy. This will be the topic of the next sections.

IV-2.3.3.2 Application of White model with binding energy explained by physical descriptor model

Huber *et al* [66] [65] expressed the segregation energy for a given site as a function of two descriptors: the atomic volume and the coordination number, within White's model.

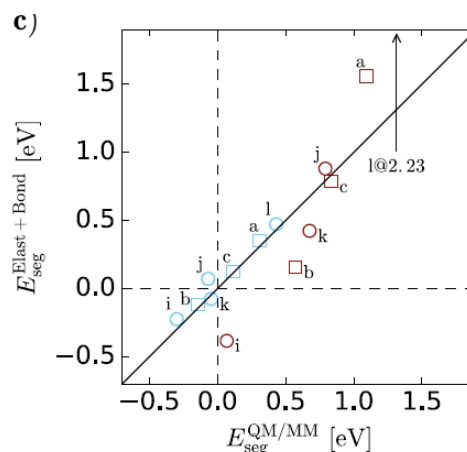


Figure IV- 17: Segregation energies for Mg (blue) and Pb (brown) at sites along the Σ 5 GB (squares) and general tilt GB (circles) calculated by the full elastic plus bonding model compared to quantum mechanical/ molecular mechanical results. The letters correspond to different sites of the GB [65]

Huber *et al* [66] present a fully atomistic model taking into account GB properties. The strength of this model lies in the use of only few physical parameters (atomic volume and coordination number) to calculate free energy and to quantify GB segregation. However, this estimation at each GB site by only two local physical descriptors leads to a loss of accuracy. In some cases, this description may **not capture all the physics** which drives the segregation process. For example, the model performs well for Mg segregation at GB in Al, but not in the case of Pb in Al (**Figure IV- 17**) [65]. Moreover, no assumption is made about the shape/size of the GB site and the bulk modulus is not differentiated for each solute species. Increasing the accuracy of these models can be done by using descriptors complementary to the coordination number.

Huber *et al* used White *et al* model and expressed the free energy as a function of physical descriptors in order to simplify the GB analysis. However, using only few descriptors is sometimes not sufficient to describe all the physics that explain GB segregation.

IV-3. Study of P segregation on twist GBs in α -iron

IV-3.1 Methodology adopted

Phosphorus is expected to be a substitutional segregant in alpha iron at $T = 0$ K and an interstitial segregant at higher temperatures [38]. Thus, our study of phosphorus segregation has been done with phosphorus placed on a substitutional site. We used twist GS GB microstructures constructed in *Chapter III* and Ackland EP [39] to make the relaxations and energetic calculations.

The volume of the supercell we consider to ensure the convergence of the GB coverage is close to distance of -6 and 6 Å from the GB plane (**Figure IV- 18 and 19**), i.e, one phosphorus atom is placed on each substitutional sites at a distance of -6 and 6 Å from the GB plane. No P-P interactions are taken into account.

Figure IV- 18 and 19 shows the convergence of P coverage as a function of the thickness of the volume of the supercell on both sides of the GB plane considered for the estimation of the phosphorus GB segregation. The P coverage has been calculated with White-Coghlan model.

The coverage of phosphorus is calculated with White *et al* model described in *Section 2.3*:

$$X_S^{gb} = \frac{1}{N} \sum_i \frac{1}{1 + \frac{1-X_S^B}{X_S^B} \exp(-E_{b,i}^{gb,S}/k_B T)} \quad (\text{eq IV-25})$$

where N is the number of the sites at GB, X_S^B is the solute concentration in the bulk and $E_{b,i}^{gb,S}$ is the binding energy of the solute at site i of the GB. The binding energy of phosphorus at a site i of the GB is given by:

$$E_{b,i}^{gb,P} = E^{gb} - E_i^{gb,P} + E^{bulk} - E^{bulk+P} \quad (\text{eq IV-26})$$

where E^{gb} is the total energy of the GB, $E_i^{gb,P}$ the total energy of the GB with a phosphorus at a site i of the GB, E^{bulk} the total energy of the perfect crystal and E^{bulk+P} the total energy of the perfect crystal with a phosphorus on substitutional site on its center.

The percentage of phosphorus in the initial solid solution has been chosen to be 0.008 at% corresponding to the average concentration of phosphorus present in RPV steels.

The “coverage” or “intergranular segregation amount” can be expressed in different units, like fraction of a monolayer [67], atomic percentage [68], [69], and surface concentration (atom/unit surface) [70]. It is practically impossible to compare intergranular segregation quantification results from different sources: some units require hypothesis that are rarely verified. For instance, assumptions about the crystallography (Miller indices) of the segregated plane is necessary to define a fraction of a monolayer. In this study, we will estimate P coverage expressed in atoms/nm². This definition is clear and permits to compare the results with quantifications from other methods.

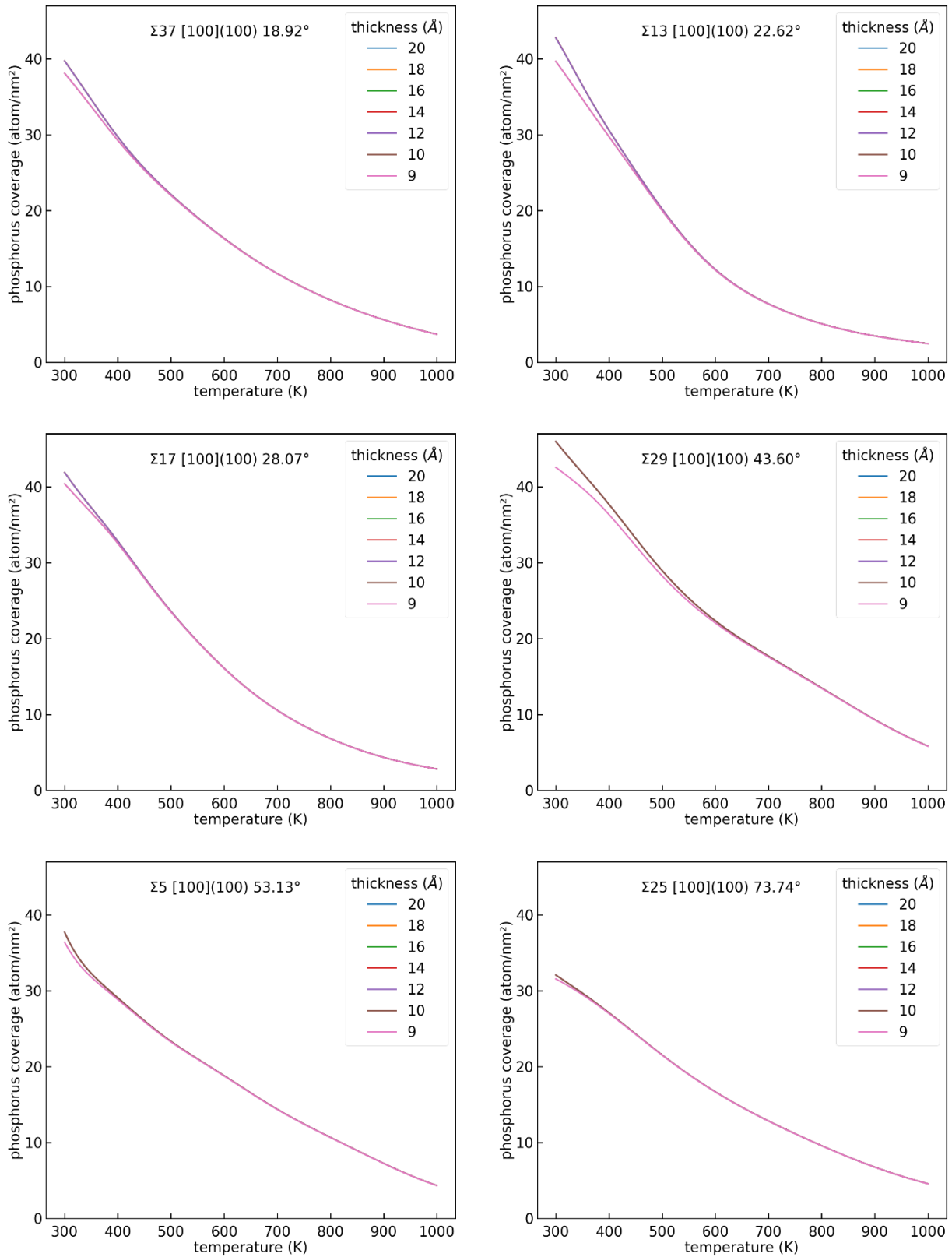


Figure IV- 18: phosphorus coverage calculated with White Coghlan model in atomic percent per nm² as a function of temperature in K and the thickness considered for the calculation of the coverage.

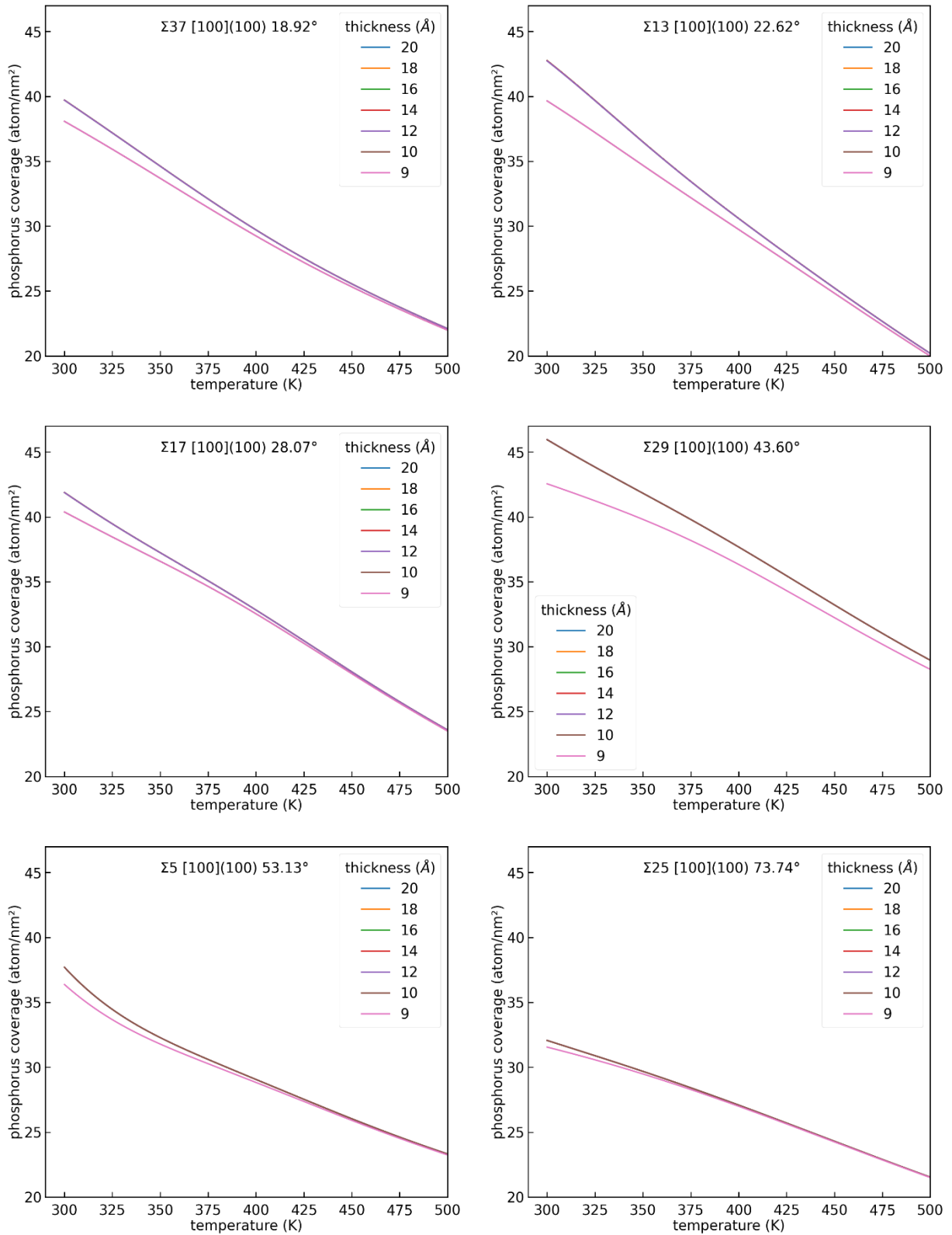


Figure IV- 19: Low temperature zoom of phosphorus coverage calculated with White Coghlan model in atomic percent per nm² as a function of temperature in K and the thickness considered for the calculation of the coverage.

IV-3.2 Phosphorus segregation results

IV-3.2.1 Phosphorus coverage on twist GBs

Phosphorus coverage has been estimated for the (001) twist GBs generated in *Chapter III*. A comparison of segregation levels between **MQ_method** and **All_trans_method** is first done; the final segregation levels of GS structures obtained with our two methodologies are then compared.

IV-3.2.1.1 Comparison of segregation levels between **MQ_method** and **All_trans_method** for different GB configurations.

Figure IV- 20 presents a comparison of phosphorus coverage obtained with White Coghlan model (methodology *section 3.1.*) for different misorientation angle at different steps of the GB construction for **MQ_method** and **All_trans_method**. The part of GB simulation box considered for the phosphorus coverage calculations is an atomic box with a thickness range from -6 to 6 Å on either side of the GB plane. For **MQ_method** the GBs that have been chosen to make the calculations corresponds to the branches leading to the GS, indicated by red color in **III-Annex 7** except for $\Sigma 25$ which another translation corresponding to the second minimum has been tested. For **All_trans_method**, GB branches leading to the GS considered are summarized in the **Table III- 6** of *Chapter III*. All of these final GS GBs considered, for both of these two methodologies have the same final microstructure and formation energy.

This figure permits a comparison of phosphorus coverage obtained for GS GBs constructed with our two different methodologies. In addition, **Figure IV- 20** compared the phosphorus coverage of different GB microstructures with different formation energy generated at different steps of the GB construction.

We observe that for all the misorientations, as one would expect, whatever the method used to construct the GS structure, the phosphorus coverage obtained for the final lowest energetic structure for a given misorientation angle is the same. **This result is consistent with the fact that GS GBs tested have the same microstructure and formation energy whatever the construction method that has been chosen.**

The phosphorus coverage associated to the GS structure at the segregation equilibrium temperature (between 600°C (873 K) and 650°C (923 K)) is the lowest in comparison to other GB configurations tested corresponding to other steps of GS GB construction, whatever the misorientation angle chosen. The relation between the formation energy of the GB structure and phosphorus coverage at 873 K seems to be linear for a given misorientation angle. However, there are some cases where it is not the case, for example, $\Sigma 25$ has a translated GB with a phosphorus coverage lower than a lower energetic GB configuration with 2INT.

For the final GS structure, for each misorientation angle (except $\Sigma 5$) GS structure coverage has been compared with the phosphorus coverage of another GB configuration with the same

number of interstitials added during the GB construction. The coverage profiles associated to different formation energies and thus different microstructures are different from those obtained with the GS GBs.

Whatever the method used to obtain the GS structure, the phosphorus coverage profile is the same and it is associated to the lowest coverage at 873 K in comparison to other GB configurations generated. The relation between initial formation energy of the GB used as an input for the estimation of phosphorus coverage and phosphorus coverage at 873 K seems to be linear, in most of the cases tested, for a given misorientation angle.

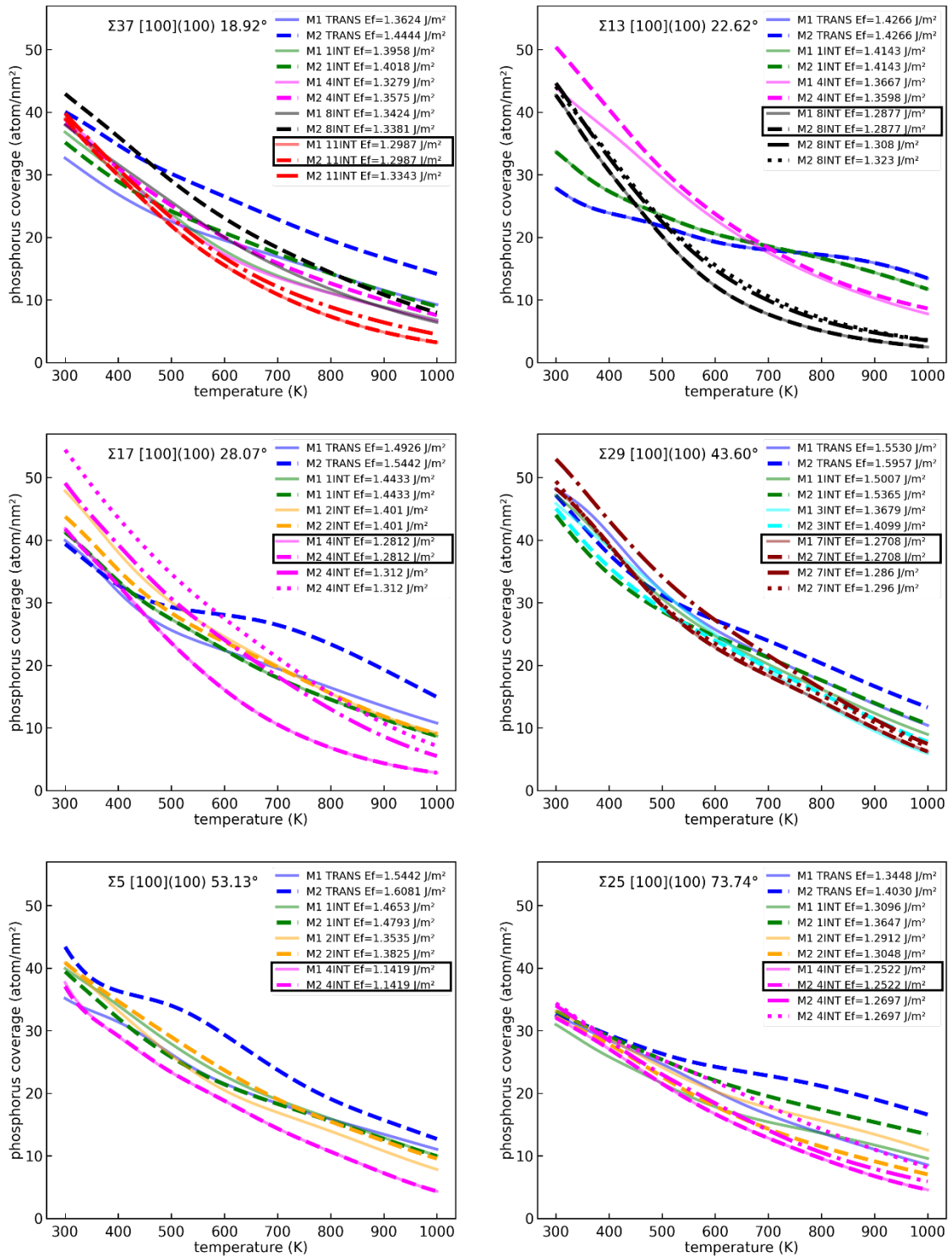


Figure IV- 20: Comparison of GB phosphorus coverage (atoms/nm²) as a function of temperature (K) for GB configurations obtained during the GB construction with **MQ_method** (named M1 in this figure) and with **All_trans_method** (named M2 in this figure). Final GS structures are framed in black in the legend. For the final GS structure, for each misorientation angle (except $\Sigma 5$), the GS structure coverage has been compared with the phosphorus coverage of another GB configuration with the same number of interstitials added. A Translated GB used as an Input for the calculation of phosphorus coverage is indicated by a blue color. For a GB with 1INT added is represented by green color, 2INT by orange color, 3INT by cyan color, 4INT by magenta color, 7INT by brown color, 8INT by black color, and 11INT by red color. The part of GB simulation box considered for the phosphorus coverage calculations is an atomic box with a thickness range from -6 to 6 Å on either side of the GB plane.

IV-3.2.1.2 Segregation levels

Segregation levels associated to the lowest energy GB (i.e. the GS of **Figure IV- 20**) are presented in **Figure IV- 21**. We show only the GS structures obtained with **All_trans_method**, because as shown **Figure IV- 20**, both methods lead to the same coverage. **Table IV- 2** gives the phosphorus coverage at equilibrium segregation equilibrium temperature.

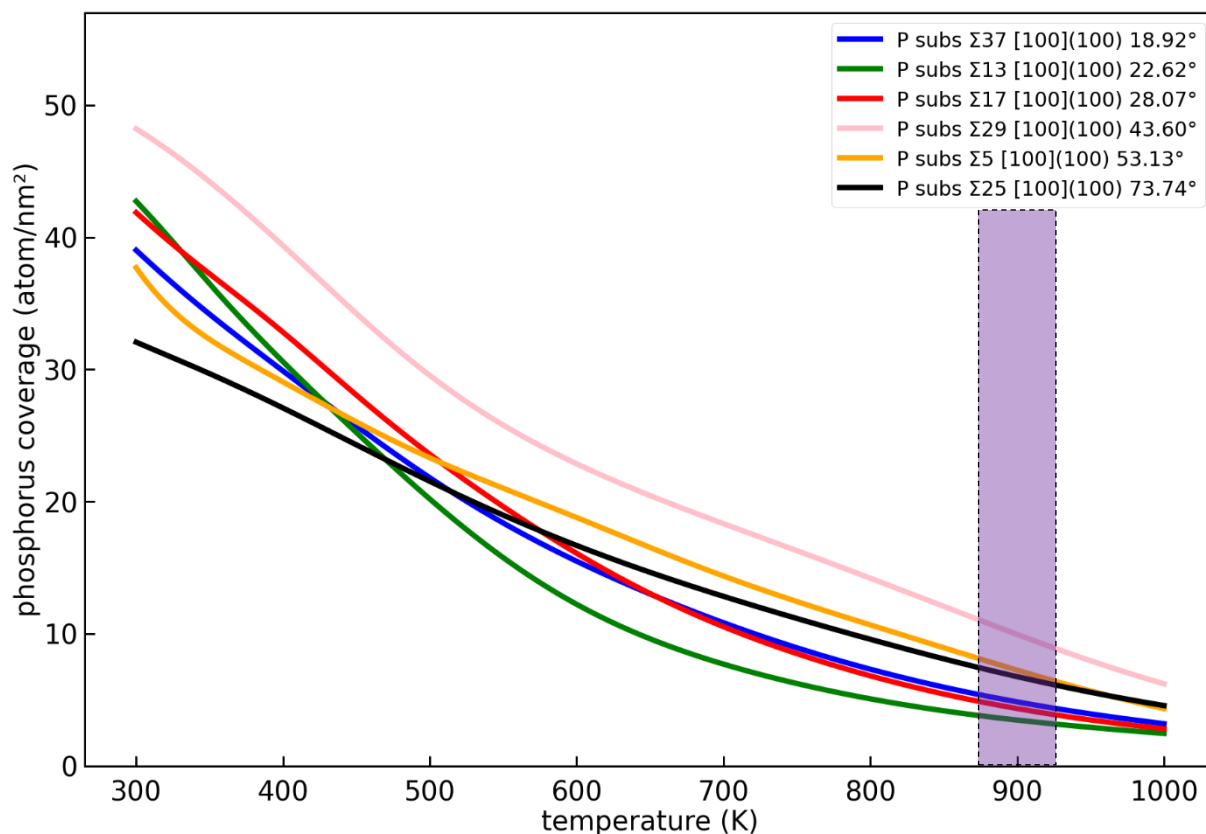


Figure IV- 21: Phosphorus coverage (atoms/nm²) as a function of temperature (K) for GS structures obtained with the **All_trans_method** described in *Chapter III*, for different misorientation angles. The part of GB simulation box considered for the phosphorus coverage calculations is an atomic box with a thickness range from -6 to 6 Å on either side of the GB plane. Phosphorus equilibrium segregation occurs at temperatures colored in purple.

According to **Figure IV- 21** and **Table IV- 2** low energetic GBs such as $\Sigma 5$ do not lead to low phosphorus coverage: $\Sigma 5$ has a higher coverage at 873 K than other GBs except $\Sigma 29$. The initial geometry of GBs and the coverage seem to be independent: less ordered GBs usually associated to high energetic configuration do not necessary conduct to a higher concentration of phosphorus.

GB	$\theta(^{\circ})$	Coverage in atom/nm ² at T = 873 K	Coverage EXP [6] (atom/nm ²)	Coverage in atom/nm ² at T = 923 K	Coverage EXP [15], [30] (atom/nm ²)	Ef (J/m ²)
$\Sigma 37$	18.92	5.4	0.6	4.4	[1.6-2.6]	1.299
$\Sigma 13$	22.62	3.8		3.2		1.288
$\Sigma 17$	28.07	4.9		3.9		1.281
$\Sigma 29$	43.6	11.1		9.0		1.271
$\Sigma 5$	53.13	8.2		6.5		1.142
$\Sigma 25$	73.74	7.5		6.2		1.252

Table IV- 2: Coverage obtained for GB GS structures of **Figure IV- 22** at T = 873K and T = 973K compared with experimental values obtained at the same temperature.

The estimated coverage rate of phosphorus showed in **Figure IV- 21** and summarized **Table IV- 2** is higher than literature experimental values obtained at temperatures between 873 and 923 K for symmetric GBs: between 3.2 and 11.1 atoms/nm². This is greater than MET results from V.Hsu with 2.6 atoms/nm² [30] and atom probe tomography from Akhatova with 1.6 atoms/nm² [15] and from Zhang *et al* [6] who find 0.6 atoms/nm². These discrepancies can probably partly be explained by that all of these experimentalists have studied mixed GBs which are not representative of the twist GBs studied in this work. They have studied mixed GBs. To date no experimental or computational study about phosphorus segregation on twist GB has been performed.

In addition, the methodologies they have used to quantify phosphorus coverage are different from the methodology used in this work:

- Hsu *et al*, used Cliff Lorimer method as known the k-factor method to quantify the phosphorus segregation from STEM-EDX spectrum.
- Akhatova and Zhang *et al*, measured Gibbsian interfacial excess which is converted to a fraction of a monolayer assuming that the phosphorus atoms reside in a single close-packed (110) plane of a BCC α -iron.

More details about these experimental methods and their associated uncertainties are given in **IV-Annex 5**.

An overestimation of phosphorus coverage in our simulations relative to experimental results could be also explained by interactions between solutes that are not taken into account in the simulations in our work as we use White-Coghlan model. A White-Coghlan model which takes into account interactions, has to be introduced to modelize co-segregation. This will be the subject of a future work. Some work, studying the impact of solute-solute interaction on segregation energy has been already done by Jin *et al* [71] for solutes Nb, Mo, and Ti in high symmetric tilt GBs in Fe. Their results are in good agreement with experimental studies, the magnitude of solute segregation increases with the increases of solute atom volume. However, they have not quantified the solute segregation associated with White Coghlan model.

Notice: all of the GBs and results we are using for the coverage calculation comes from calculations at 0 K. The binding energy may change at higher temperatures as a result of harmonic and anharmonic effects. However, the binding energies at 0 K usually provide a good estimate of a lot of GBs for a wide temperature range [72].

IV-3.2.2 Distribution of binding energies

Binding energy distributions for all twist (001) GBs are represented in **Figure IV- 22**. A peak at 0 eV is observed, which corresponds to atomic sites close to the bulk part but also to GB sites. The binding energy doesn't exceed 1.1 eV. $\Sigma 37$, $\Sigma 29$ and $\Sigma 25$ possess a more skewed binding energy distribution than other GBs ($\Sigma 13$, $\Sigma 17$ and $\Sigma 5$) where the binding energies are spread over 3 peaks. Thus, the diversity of segregation sites is greater for these GBs ($\Sigma 37$, $\Sigma 29$ and $\Sigma 25$).

In order to better understand phosphorus segregation phenomenon, we try to find binding energy correlations with physical atomic properties of each GB. The next section is dedicated to this subject.

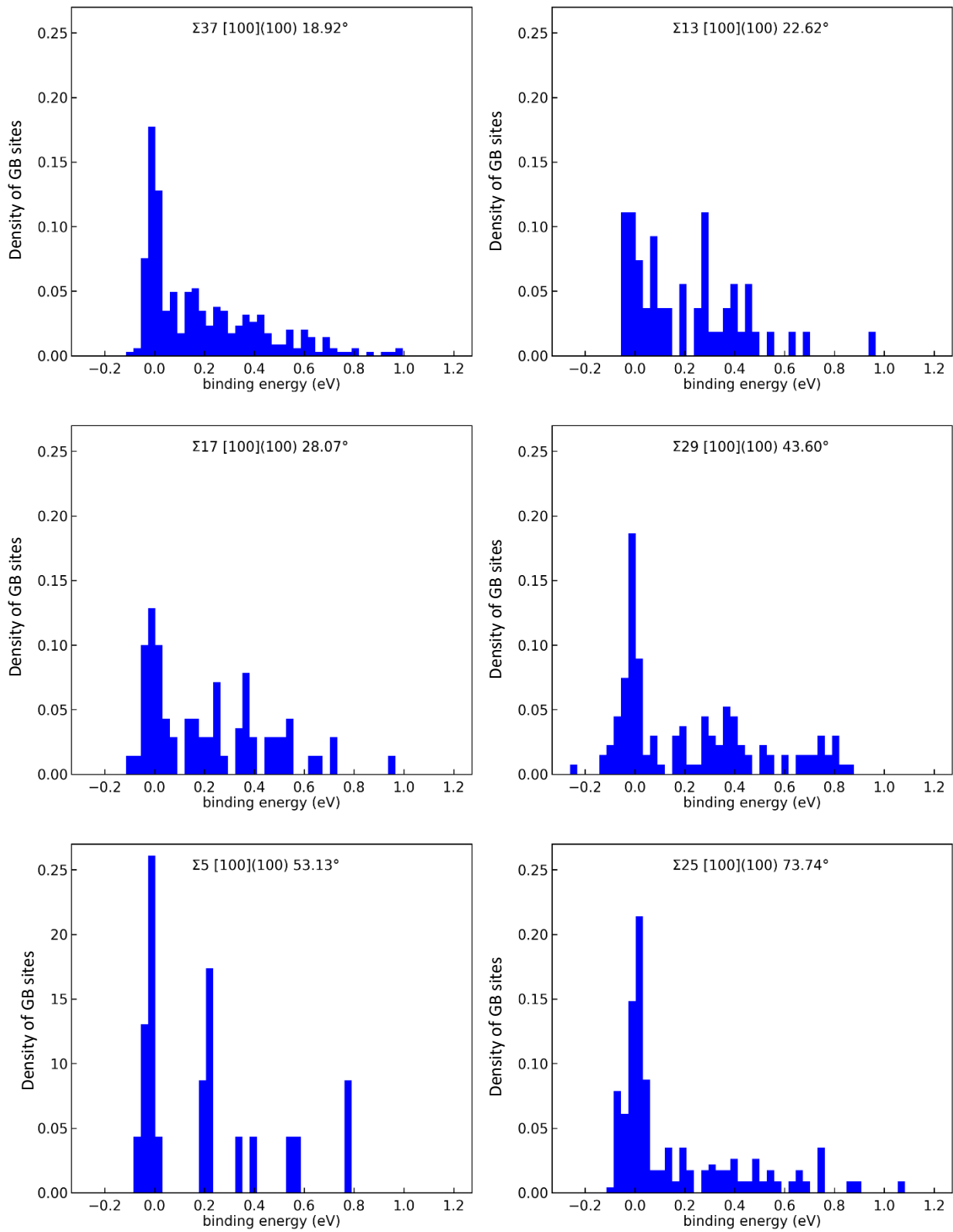


Figure IV- 22: Phosphorus binding energy distributions of GS GBs presented in **Figure IV- 21**.

IV-3.2.3 Relationship between binding energy and GB initial properties

In this section, we present an analysis of the binding energies of GS GBs obtained with **All_trans_method** in *Chapter III*. More precisely, we represent the binding energies as a function of various atomic descriptors to look for correlations: the correlation between binding energy of phosphorus with the binding energy as a function of atomic descriptor.

All atomic descriptors are introduced in *Chapter II*.

IV-3.2.3.1 Binding energy as a function of different atomic descriptors

The binding energy as a function of atomic descriptors of the GB before the introduction of phosphorus, is represented in **Figure IV- 23-27**. The associated microstructures are plotted. A comparison with the binding energy distribution inside the microstructure is given on **Figure IV- 28**. Our observations are presented here:

- **Atomic volume (Figure IV- 23):** highest binding energies are generally associated to atomic segregation sites with small atomic volume ($10-10.5 \text{ \AA}^3$). It seems that the binding energy decreases when the atomic volume increases.
- **Position relative to the GB plane (Figure IV- 24):** highest binding energies are localized close to the GB plane. As expected, the phosphorus binding energy decreases when the distance to the GB plan increases.
- **Smooth Overlap of Atomic Positions (SOAP) (Figure IV- 25):** no evident correlation between binding energy and SOAP has been highlighted.
- **Centrosymmetric parameter (CS) (Figure IV- 26):** we observe that a large part of atomic sites selected correspond to bulk sites ($CS = 0$). The binding energy seems to increase as a function of CS increases.
- **Coordination Number (CN) (Figure IV- 27):** no evident correlation between binding energy and CN can be identified.

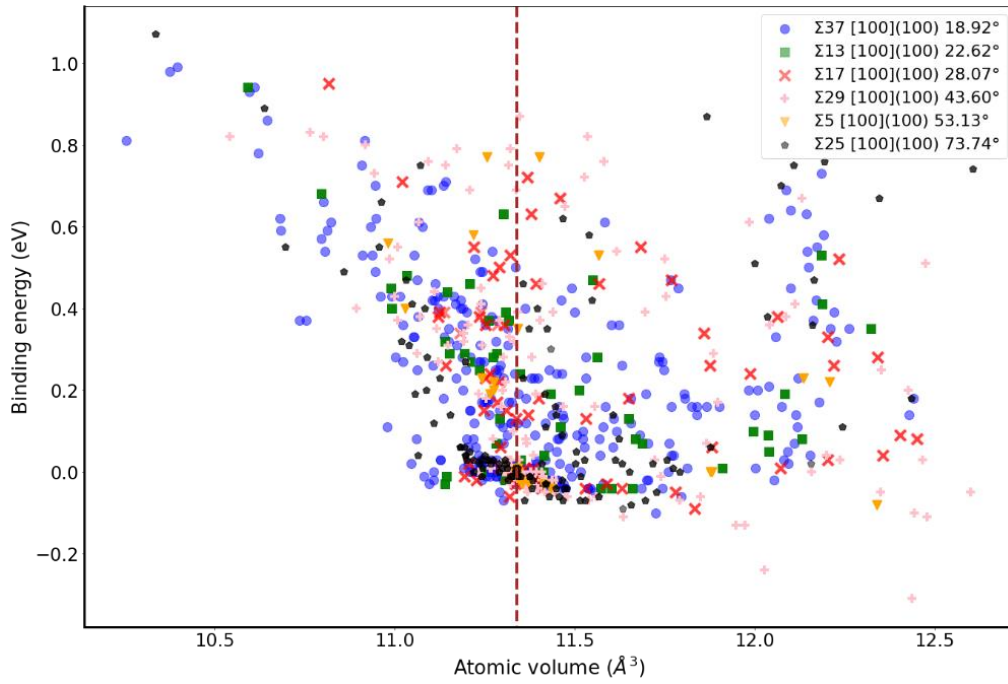


Figure IV- 23: Binding energy of phosphorus with the GB as a function of atomic volume (\AA^3). The atomic volume of a perfect crystal structure is represented by a red dotted line.

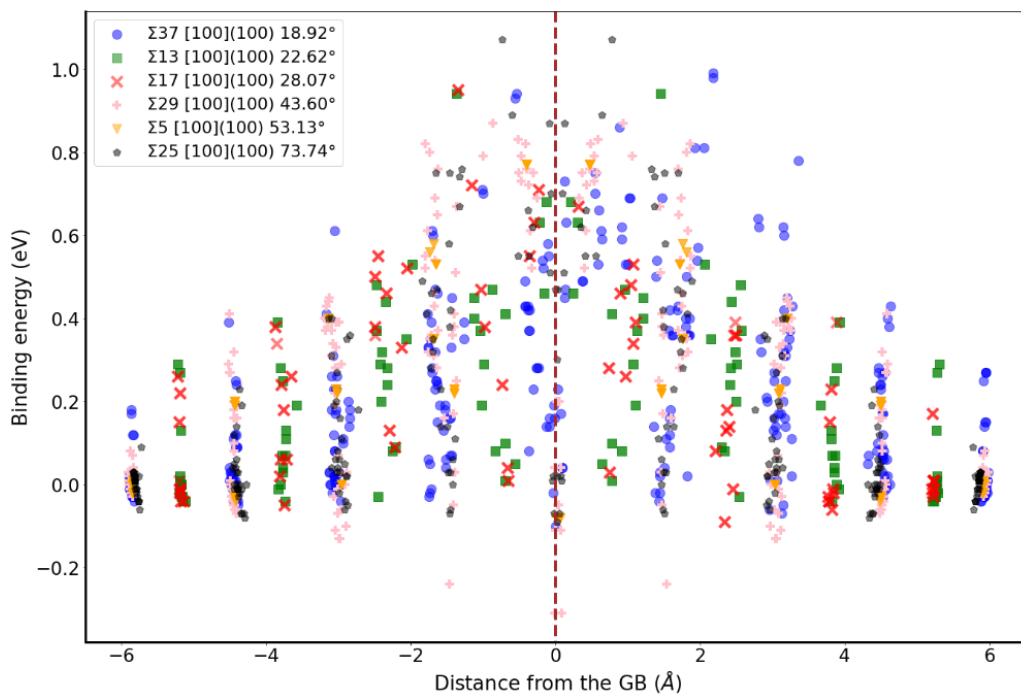


Figure IV- 24: Binding energy of phosphorus with the GB as a function of substitutional phosphorus position. The centre of the GB is represented by a red dotted line.

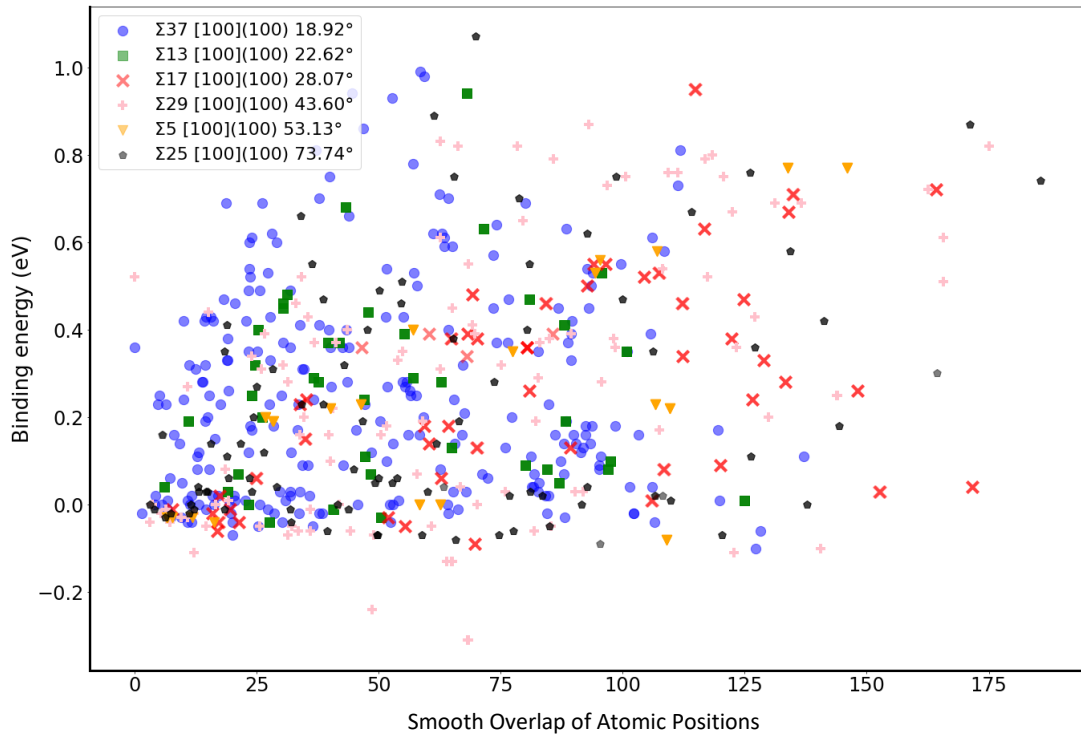


Figure IV- 25: Binding energy of phosphorus with the GB as a function of Smooth Overlap of Atomic Positions (SOAP) atomic descriptor position.

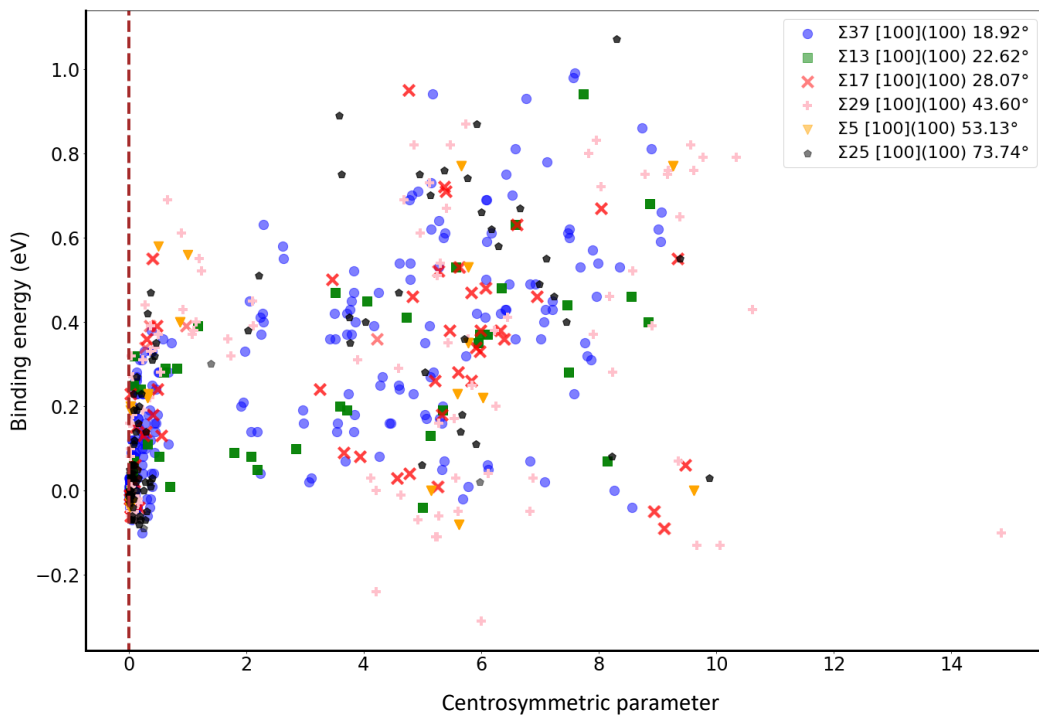


Figure IV- 26: Binding energy of phosphorus with the GB as a function of centrosymmetric atomic parameter. The centrosymmetric parameter of a perfect crystal structure is represented by a red dotted line.

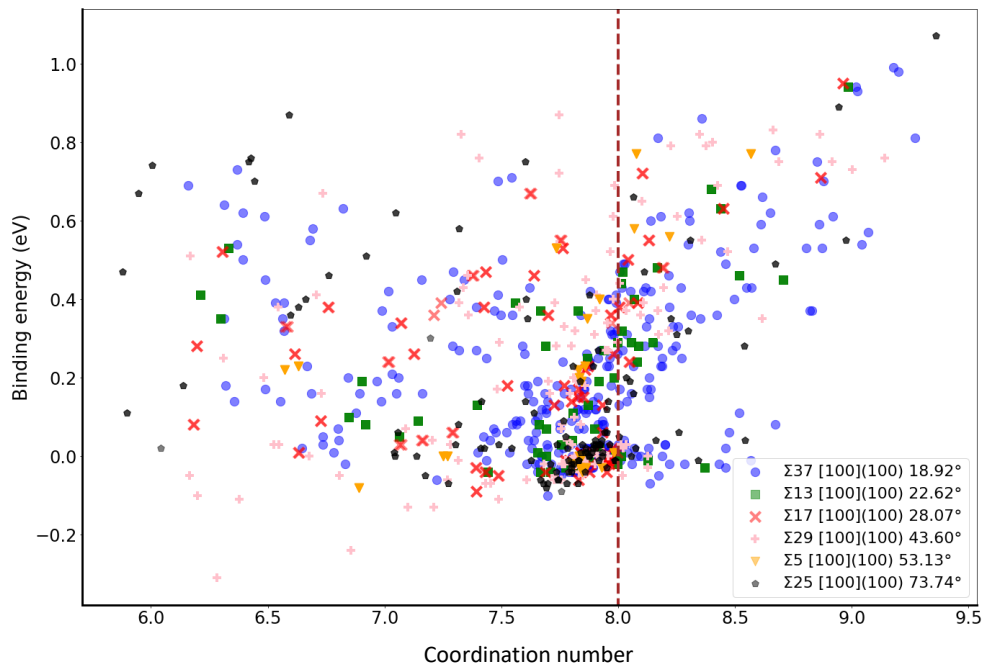


Figure IV- 27: Binding energy of phosphorus with the GB as a function of coordination atomic number. The coordination number of a perfect crystal structure is represented by a red dotted line.

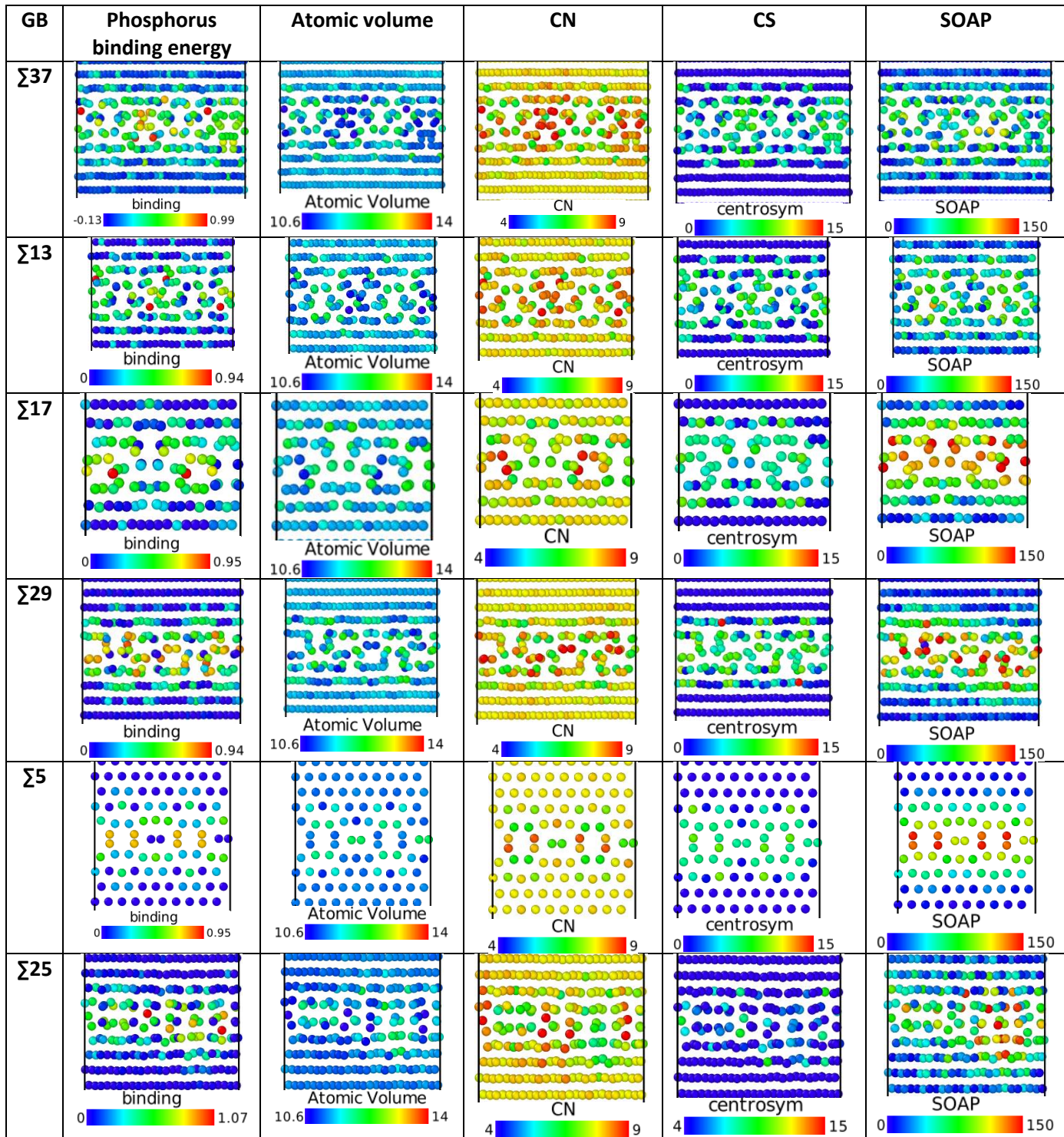


Figure IV- 28: Atomic description of GBs as a function of phosphorus binding energy, atomic volume, CN, CS and SOAP

IV-3.2.3.2 Spearman correlation calculation

In order to quantify the correlation between phosphorus binding energy and atomic descriptors, Spearman correlation coefficient has been calculated using Pandas python module. Spearman correlation evaluates how well can the relationship between paired data be described using a monotonic function. It consists in finding a correlation coefficient, not between the values taken by the two variables but between the ranks of these values. The Spearman correlation will be high when observations have a similar rank between the two variables and low when observations have a dissimilar rank between the two variables.

The strength of the correlation can be described using the following guide in absolute value:

- 0.0-0.19: "very weak"
- 0.20-0.39: "weak"
- -0.40-0.59: "moderate"
- 0.60-0.79: "strong"
- 0.80-1.0: "very strong"

Due to the statistical character of these correlation measures, a sufficiently large database of binding energy is necessary to obtain reliable results. The Spearman plots in **Figure IV- 29** are presented for illustrative purposes because of the lack of sufficient data to conduct a robust statistical study. These representations give however some indications for the analyse and interpretation of the scatter plots.

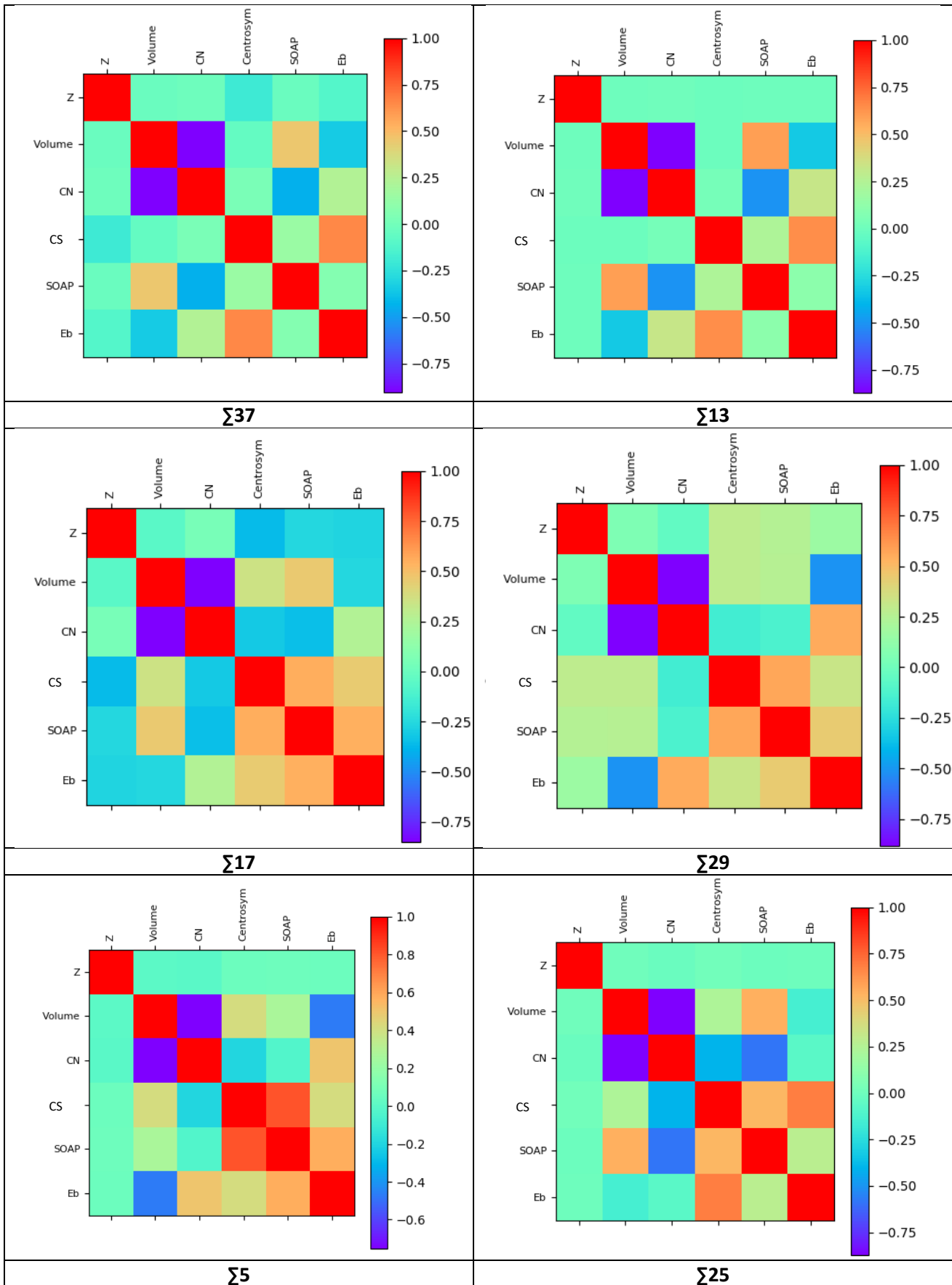


Figure IV- 29: Spearman colorplots for each twist GS GB from **Figure IV- 21.**

Figure IV- 30 corresponds to a Spearman plot containing all the twist GB (001) data. The dataset is composed of 2083 binding energy calculations on different GB sites around the GB. This representation with a larger dataset can give some indications about binding energy correlation in a more general way.

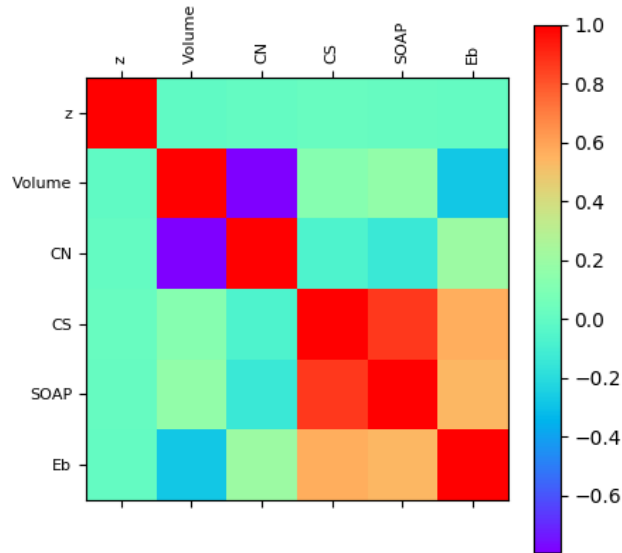


Figure IV- 30: Spearman correlation colorplot for all calculations for all GS GBs from **Figure IV- 21**

Figure IV- 29 shows a strong-moderate correlation between SOAP and CS with binding energy whatever the misorientation angle chosen. The representations of SOAP and CS as a function of binding energy or any descriptors are very similar. It is consistent with the fact that SOAP and CS are correlated according to **Figure IV- 30**. We note that binding energy as a function of atomic volume and CN are anti-correlated which is consistent with their physical definition. These observations are confirmed in a more general way with the Spearman plot **Figure IV- 30**. However, due to the small size of the dataset and binding energy scatterplots (**Figure IV- 24-29** and **IV-Annex 5**), determined an expression of binding energy as a function of atomic descriptors to predict the GB coverage is difficult to establish.

An expression of binding energy as a function of atomic descriptors to predict the GB coverage is difficult to establish.

IV-3.2.4 Evolution of the GB microstructure after phosphorus segregation

The study reported in this part is concerned with determining the influence of solute segregation on the structure of (001) bcc alpha iron GBs. The segregation of phosphorus on GBs causes a change in the GB structure from that present GBs in pure Fe generated previously. The examination of the same GB both in the absence and the presence of the segregation of phosphorus allows us to give some indications about the effects of the segregation process. This study has been carried out briefly because of the restricted time of this PhD. Only three GBs: $\Sigma 13$, $\Sigma 29$ and $\Sigma 25$ have been analyzed.

According to **IV-Annex 7**, the relaxations of phosphorus concerned only Y and Z directions and never exceed 1.1 angströms. Note that a high binding energy not necessary leads to strong relaxations and conversely a small binding energy does not necessary leads to weak relaxations of the GB structure. There is no correlation between atomic strength relaxation and the amplitude of binding energy.

IV-4. Conclusion

- **Phosphorus is expected to be a substitutional segregant** in alpha iron at T=0 K iron up to about 650 - 700°C and an interstitial segregant at higher temperatures.
- Many models derived from McClean model have been developed to predict segregation, and thus also P segregation. **White Coghlan model is the most appropriated for atomic studies.** Therefore, this model has been used to estimate the P coverage on twist GBs.
- **Whatever the method used to construct the GS structure, the phosphorus coverage profile is the same and it is associated to the lowest coverage at 873 K** in comparison to other GB configurations generated during the GB construction with **MQ_method** and **All_trans_method**.
- **The comparison between experimental results and simulation is difficult** because the experimental measurements generally correspond to average segregation contents, whereas atomistic simulations provide a more detailed picture taking into account the precise position of the solute in the GB. → **The estimated coverage rate of phosphorus at segregation phosphorus equilibrium temperature is higher than literature and experimental values for symmetric GBs:** between 3.2 and 11.1 atoms/nm². This is greater than MET results from **V.Hsu** with 2.6 atoms/nm² [30] and atom probe tomography from **Akhatova** with 1.6 atoms/nm² [15] and from **Zhang et al** [6] who find 0.6 atoms/nm². These discrepancies can probably be partly explained by that all the experiments were done on mixed GBs which are not representative of twist GBs studied in this work. In addition, the interactions between solutes are not taken into account in the simulations in our work as we use White-Coghlan model. A White-Coghlan model which takes into account interactions, has to be introduced to modelize co-segregation. This will be the subject of a future work.
- **The segregation energy is not homogenous in the GB.** Segregation is an anisotropic process which depends significantly on the GB structure and on the characteristics of the segregant (the size, the chemical species...). Certain sites in or near GB are more favourable. Binding energy distributions for each misorientation angle tested are all different.
- **Finding correlations between physical atomic descriptors described in Chapter II and binding energy is difficult.** Even if small atomic volumes sites of segregation localized close to the GB plane are generally associated to the highest binding energies, no evident correlation between binding energy and atomic descriptors scatter plots has been found. Spearman correlation plot shows a strong-moderate correlation between SOAP and CS with binding energy whatever the misorientation angle chosen, however the number of data used to construct the Spearman correlation analysis is not sufficient to make a general conclusion.

→ **GB segregation is difficult to understand, measure and predict:** segregation on GBs depends on many physical factors. The wide variety of GB structures makes the establishment of general GB segregation model a hard task. The number of data necessary to set up a good representation of GB segregation is large, an enlargement of EDF GB data base in ferritic steels is thus needed. Twist GBs GS have been generated with **MQ_method** and **All_trans_method**, however, for a given GB, many metastable states close to one another can be reached which should be taken into account to make an exhaustive study of phosphorus segregation with a sufficiently large database. **A better understanding of GB segregation requires a better description of GB atomistic sites**, the generation of a larger GB segregation database and the development of accurate models predicting segregation on the basis of GB physical description by the use of physical descriptors.

IV-5. Bibliography

- [1] P. Lejcek, P. Sandrera, J. Hornikova, P. Rehak, et J. Pokluda, « Grain boundary segregation of elements of 14 and 15 and its consequences for intergranular cohesion of ferritic iron », *Journal of Materials Science*, vol. 52, p. 5822-5834, 2017.
- [2] K. Masuda-Jindo, « On the grain boundary segregation of sp-Valence Impurities in b.c.c. transition metal », *phy. stat. sol. (b)*, vol. 134, p. 545-550, 1986.
- [3] « Effect of Phosphorus on the Properties of Carbon Steels: Part One », *Total Materia*, 2007, [En ligne].
Disponble sur:
<https://www.totalmateria.com/page.aspx?ID=CheckArticle&site=kts&NM=211>
- [4] W.-S. Ko, « Atomistic modeling of an impurity element and a metal-impurity system: pure P and Fe-P system », *J. Phys. : Condens. Matter*, vol. 24, p. 225002, 2012.
- [5] P. D. Styman, J. M. Hyde, K. Wildford, A. Morley, et G. D. W. Smith, « Precipitation in long term thermally aged high copper, high nickel model RPV steel welds », *Progress in Nuclear Energy*, vol. 57, p. 86-92, 2012.
- [6] L. Zhang, « Ségrégation intergranulaire du phosphore dans les aciers des cuves des REP », Université de Rouen Normandie, 2018.
- [7] S. H. Song, H. Zhuang, J. Wu, L. Q. Weng, Z. X. Yuan, et T. H. Xi, « Dependence of ductile-to-brittle transition temperature on phosphorus grain boundary segregation for a 2.25Cr1Mo steel », *Material Science and Engineering A*, vol. 486, p. 433-438, 2008.
- [8] D. Kalderon, « Steam Turbine Failure at Hinkley Point "A" », *Proceedings of Institution of Mechanical Engineers*, vol. 186, p. 341, 1972.
- [9] M. P. Seah et E. D. Hondros, « Grain boundary segregation », *Proc. R. Soc. Lond. A*, vol. 335, p. 191-212, 1973.
- [10] H. Erhart et H. J. Grabke, « Equilibrium segregation of phosphorus at grain boundaries of Fe-P, Fe-C-P, Fe-Cr-P, and Fe-Cr-C-P alloys. », *Metal Science*, vol. 15, p. 401-408, 1981.
- [11] J. Wu, S. H. Song, L. Q. Weng, T. H. Xi, et Z. X. Yuan, « An Auger electron spectroscopy study of phosphorus and molybdenum grain boundary segregation in a 2.225Cr1Mo steel », *Materials Characterisation*, vol. 59, p. 261-265, 2008.
- [12] H. J. Grabke, « Surface and Grain Boundary Segregation on and in Iron and Steels », *ISIJ International*, vol. 29, p. 529-538, 1989.
- [13] T. Sakurai, Y. Kuk, H. J. Grabke, A. K. Birchenall, et H. W. Pickering, « Phosphorus Segregation to Grain Boundaries in A Fe-0.04% P ». 1980.
- [14] Y. Zhao, S. Song, H. Si, et K. Wang, « Effect of Grain Size on Grain Boundary Segregation Thermodynamics of Phosphorus in Interstitial-Free and 2.25Cr-1Mo Steels », *Metals*, vol. 7, p. 470, 2017.
- [15] A. Akhatova, « Méthodologie instrumentale à l'échelle atomique pour une meilleure compréhension des mécanismes de ségrégation intergranulaire dans les aciers : application au phosphore. », Université de Rouen Normandie, 2018.
- [16] W.-S. Ko, « Atomistic modeling of an impurity element and a metal-impurity system: pure P and Fe-P system », *J. Phys. : Condens. Matter*, p. 225002, 2012.
- [17] M. Yamaguchi, Y. Nishiyama, et H. Kaburaki, « Decohesion of iron grain boundaries by sulfur or phosphorous segregation: First-principles calculations », *Physical Review B*, vol. 76, n° 3, Art. n° 3, juill. 2007.
- [18] X. He, S. Wu, L. Jia, D. Wang, Y. Dou, et W. Yang, « Grain Boundary Segregation of Substitutional Solute/Impurities and GB decohesion in BCC Fe », *Energy Procedia*, vol. 127, p. 377-386, 2017.
- [19] M. Hashimoto, Y. Ishida, R. Yamamoto, et M. Doyama, « Atomistic studies of grain boundary segregation in Fe-P and Fe-B alloys-I atomic structure and stress distribution », *Acta Metallurgica*, vol. 1, p. 1-11, 1984.
- [20] K. Masuda-Jindo, « On the grain boundary segregation of sp-Valence Impurities in b.c.c. transition metal », *phy. stat. sol. (b)*, p. 545-550, 1986.

- [21] W.-S. Ko, J. B. Jeon, C.-H. Lee, J.-K. Lee, et B.-J. Lee, « Intergranular embrittlement of iron by phosphorus segregation: an atomistic simulation », *Modelling and Simulation in Materials Science and Engineering*, vol. 21, p. 025012-025028, 2013.
- [22] M. Yamaguchi, « First-Principles Study on the Grain Boundary Embrittlement of Metals by Solute Segregation: Part I. Iron (Fe)-Solute (B, C, P, and S) Systems », *Metallurgical and materials transactions A*, vol. 42A, p. 319-329, 2010.
- [23] M. I. Baskes, « Modified embedded-atom potentials for cubic materials and impurities », *Physical Review B*, p. 2727, 1992.
- [24] G. J. Ackland, M. I. Mendeleev, D. J. Srolovitz, S. Han, et A. V. Barashev, « Development of an interatomic potential for phosphorus impurities in alpha-iron », *arXiv*, 2004.
- [25] M. Rajagopalan, M. A. Tschopp, et K. N. Solanki, « Grain boundary segregation of interstitial and substitutional impurity atoms in alpha-iron », *JOM*, vol. 66, p. 129, 2014.
- [26] E. Wachowicz, T. Ossowski, et A. Kiejna, « Cohesive and magnetic properties of grain boundaries in bcc Fe with Cr additions », *Physical Review B*, vol. 81, n° 9, Art. n° 9, mars 2010.
- [27] H. J. Grabke, « Grain boundary segregation of impurities in iron and steels and effects on steel properties », in *Impurities in Engineering Materials*, C.L. Briant, 1999, p. 143-192.
- [28] X. M. Chen, S. H. Song, L. Q. Weng, S. J. Liu, et K. Wang, « Relation of ductile-to-brittle transition temperature to phosphorus grain boundary segregation for a Ti-stabilized interstitial free steel », *Materials Science and Engineering A*, vol. 528, p. 8299-8304, 2011.
- [29] X. M. Chen, S. H. Song, L. Q. Weng, S. J. Liu, et K. Wang, « Relation of ductile-to-brittle transition temperature to phosphorus grain boundary segregation for a Ti-stabilized interstitial free steel », *Materials Science and Engineering A*, p. 8299-8304, 2011.
- [30] C.-Y. Hsu, J. Stodolna, P. Todeschini, F. Delabrouille, B. Radiguet, et F. Christien, « Accurate quantification of phosphorus intergranular segregation in iron by STEM-EDX », *Micron*, vol. 153, p. 103175, 2022.
- [31] M. Yuasa et M. Mabuchi, « Bond mobility mechanism in grain boundary embrittlement: First-principles tensile tests of Fe with a P-segregated Σ 3 grain boundary », *Physical Review B*, vol. 82, n° 9, p. 094108, sept. 2010.
- [32] M. Yuasa et M. Mabuchi, « Grain boundary embrittlement of Fe induced by P segregation: First-principles tensile tests », *Advanced Materials Research*, p. 455-460, 2011.
- [33] M. Yuasa et M. Mabuchi, « First-Principles Study on Enhanced Grain Boundary Embrittlement of Iron by Phosphorus Segregation », *Materials Transactions*, p. 1369-1373, 2010.
- [34] P. Rez et J. R. Alvarez, « Calculation of cohesion and changes in electronic structure due to impurity segregation at boundaries in iron », *Acta Materialia*, p. 4069-4075, 1999.
- [35] P. Lejcek et S. Hofmann, « Interstitial and substitutional solute segregation at individual grain boundaries of alpha-iron: data revisited », *J. Phys. : Condens. Matter*, vol. 28, p. 064001-064010, 2016.
- [36] Y.-Q. Fen et C.-Y. Wang, « Electronic effects of nitrogen and phosphorus on iron grain boundary cohesion », *Computational Materials Science*, vol. 20, n° 1, Art. n° 1, janv. 2001.
- [37] J. S. Braithwaite et P. Rez, « Grain boundary impurities in iron », *Acta Materialia*, vol. 53, p. 2715-2726, 2005.
- [38] P. Lejcek, « Recent trends and open questions in grain boundary segregation », *Materials Research Society*, vol. 33, n° 18, p. 2647-2660, 2018.
- [39] G. J. Ackland, M. I. Mendeleev, D. J. Srolovitz, S. Han, et A. V. Barashev, « Development of an interatomic potential for phosphorus impurities in alpha-iron », *Journal of Physics: Condensed Matter*, vol. 16, n° 27, p. 1-14, 2004.
- [40] C. Domain, « Solute segregation at (100) and (110) tilt GB in Fe at the atomic scale », présenté à Conference Intergranular and Interphase Boundaries in Materials, Paris, 2019.
- [41] H. J. Grabke, « Surface and Grain Boundary Segregation on and in Iron and Steels », *ISIJ International*, p. 529-538, 1989.
- [42] R. Möller et H. J. Grabke, « Grain boundary segregation of phosphorus in Fe-Nb-P and Fe-Nb-C-P alloys », *Scripta Metallurgica*, vol. 18, p. 527-530, 1984.

- [43] A. Vyrostkova, J. Perhacova, V. Homolova, P. Sevc, J. Janovec, et H. J. Grabke, « Some aspects of carbide precipitation and phosphorus grain boundary segregation in Cr-V low alloy steels », *Kovine, Zlitine, Tehnologije*, vol. 33, p. 423-426, 1999.
- [44] W. T. Geng, A. J. Freeman, R. Wu, et G. B. Olson, « Effect of Mo and Pd on the grain-boundary cohesion of Fe », *Physical Review B*, vol. 62, n° 10, Art. n° 10, sept. 2000.
- [45] R. Möller et H. J. Grabke, « Grain boundary segregation of phosphorus in Fe-Nb-P and Fe-Nb-C-P alloys », *Scripta Metallurgica*, p. 527-530, 1984.
- [46] J. Peerhacova, D. Grman, M. Svoboda, J. Patscheider, A. Vyrostkova, et J. Janovec, « Microstructural aspects of phosphorus grain boundary segregation in low alloy steels », *Materials Letters*, vol. 47, p. 44-49, 2001.
- [47] H. J. Grabke, « Segregation and oxydation », *Materiali in tehnologije*, vol. 40, p. 39-47, 2006.
- [48] D. McLean, « Grain boundaries in metals », *Physics Today*, vol. 11, p. 35, 1958.
- [49] M. P. Seah, « Grain boundary segregation », *J. Phys. F: Metal Phys.*, vol. 10, p. 1043-1064, 1980.
- [50] R. H. Fowler et E. A. Guggenheim, *Statistical Thermodynamics*, CUP. Cambridge, 1939.
- [51] P. Lejcek et S. Hofmann, « Thermodynamics and structural aspects of grain boundary segregation », *Critical Reviews in Solid State and Materials Sciences*, vol. 20, n° 1, p. 1-85, 1995.
- [52] M. Guttman, « Temper Embrittlement and Ternary Equilibrium Segregation », *Material Science and Engineering*, vol. 42, p. 227-232, 1980.
- [53] M. Guttman, « Equilibrium segregation in a ternary solution: a model for temper embrittlement », *Surface Science*, vol. 53, p. 213-227, 1975.
- [54] M. P. Seah, « Grain boundary segregation and the T-t dependence of temper brittleness », *Acta Metallurgica*, vol. 25, p. 345-357, 1976.
- [55] F. L. Carr, M. Goldman, L. D. Jaffe, et D. C. Buffin, « Isothermal Temper Embrittlement of SAE 3140 Steel », *Journal of Metals*, vol. 197, p. 998-998, 1953.
- [56] A. P. Sutton et R. W. Balluffi, « Overview no. 61 On geometric criteria for low interfacial energy », *Acta Metallurgica*, vol. 35, p. 2177, 1987.
- [57] D. Udler et D. N. Seidman, « Solute segregation at [001] tilt boundaries in dilute FCC alloys », *Acta Materialia*, vol. 46, p. 1221-1233, 1998.
- [58] J. Nie, Y. Zhu, J. Liu, et X. Fang, « Periodic Segregation of Solute Atoms in Fully Coherent Twin Boundaries », *Science*, vol. 340, p. 957-960, 2013.
- [59] P. Lejcek, M. Sob, V. Paidar, et V. Vitek, « Why calculated energies of grain boundary segregation are unreliable when segregant solubility is low », *Scripta Materialia*, vol. 68, p. 547-550, 2013.
- [60] P. Lejcek, M. Sob, et V. Paidar, « Interfacial segregation and grain boundary embrittlement: An overview and critical assessment of experimental data and calculated results », vol. 87, p. 83-139, 2017.
- [61] C. L. White et W. A. Coghlan, « The Spectrum of Binding Energies Approach to Grain Boundary Segregation », *Metallurgical transactions A*, vol. 8A, p. 1403-1411, 1977.
- [62] P. Lejcek, L. Zheng, S. Hofmann, et M. Sob, « Applied Thermodynamics: Grain Boundary Segregation », *Entropy*, vol. 16, p. 1462-1483, 2014.
- [63] C. L. White et D. F. Stein, « Sulfur Segregation to Grain (Ni₃)Al and Ni₃(Al,Ti) Alloys », *Metallurgical transactions A*, vol. 9A, p. 13-22, 1978.
- [64] C. L. White et W. A. Coghlan, « The Spectrum of Binding Energies Approach to Grain Boundary Segregation », *Metallurgical transactions A*, p. 1403-1411, 1977.
- [65] L. Huber, B. Grabowski, M. Militzer, J. Neugebauer, et J. Rottler, « Ab initio modelling of solute segregation energies to general grain boundary », *Acta Materialia*, vol. 132, p. 138-148, 2017.
- [66] L. Huber, R. Hadian, B. Grabowski, et J. Neugebauer, « A machine learning approach to model solute grain boundary segregation », *nature partner journals Computational Materials*, vol. 64, p. 1-8, 2018.
- [67] I. A. Vatter et J. M. Titchmarsh, « Measurement of grain-boundary segregation by STEM-EDX analysis », *Ultramicroscopy*, vol. 28, p. 236-239, 1989.
- [68] P. Doig et P. E. J. Flewitt, « Segregation of chromium to prior austenite boundaries during quenching of 21/4%Cr1%Mo steel », *Acta Metallurgica*, vol. 29, p. 1831-1841, 1981.

- [69] R. G. Faulkner, S. Song, et P. E. J. Flewitt, « A Model Describing Neutron Irradiation-Induced Segregation to Grain Boundaries in Dilute Alloys », *Metallurgical transactions A*, vol. 27, p. 3381-3390, 1996.
- [70] V. J. Keast et D. B. Williams, « Quantification of boundary segregation in the analytical electron microscope », *Journal of Microscopy*, vol. 199, n° 1, p. 45-55, 2000.
- [71] H. Jin, F. Elfimov, et M. Militzer, « Study of the interaction of solutes with $\Sigma 5$ (013) tilt grain boundaries in iron using density-functional theory. », *Journal of Applied Physics*, vol. 115, p. 093506, 2014.
- [72] L. Huber, J. Rottler, et M. Militzer, « Atomistic simulations of the interaction of alloying elements with grain boundaries in Mg », *Acta Metallurgica*, vol. 80, p. 194-204, 2014.

Conclusion and perspectives

The main goal of this thesis was to model **the evolution of the microstructure** of the low-alloy ferritic steel 16MND5 under irradiation more accurately by taking better account of the heterogeneities present in RPV steels.

One of the most prominent defects strongly influencing many properties of materials are **grain boundaries (GB)**. In complex materials such RPV steels, containing more than one element, grain boundaries are usually decorated by solutes: solute segregation influences quite significantly the macroscopic properties. Detrimental effects induced by this segregation process can reduce the toughness and ductility of a material. Thus, a particular attention in this thesis has been paid on grain the microstructure of grain boundaries. Modelling the evolution of the microstructure requires a good representation of GBs. Therefore, the aim was to construct the most stable GBs in order to study and quantify the segregation on these GBs.

A lot of atomistic data are currently known only for few high symmetry tilt grain boundaries (e. g. $\Sigma 3$, $\Sigma 5$). In this work, six different **(100) twist grain boundaries** with a more complex structure than tilt grain boundaries, that span low to high angle misorientations generated in for Fe have been constructed and investigated. Due to their complex structure, their minimum ground state structure is difficult to determine.

→ In a first time two GB construction processes have been developed with EP Ackland [1] in this thesis to reach the lowest energetic GB configurations, both of them used three different atomic events:

- the translation of the upper part of the grain boundary along the X and Y direction (moving thus on the γ -surface). This step is done only once, right after the GB has been constructed using the CSL method.
- the insertion of SIA and selecting the position for which the SIA has the highest binding energy with the GB, thus leading to the lowest GB formation energy.
- the heat and the quench of the GB

All of these atomic events applied sequentially permit to reach a ground state. **The first methodology “All_trans_method”**, we have developed at the first time, considers the sequential addition of interstitials on octahedral positions, for all the possible translations found with the γ surface method. In contrast, the second methodology called **“MQ_method”** corresponds to a combination of a melt and quench and addition of SIA as sequential treatments of only one GB generated with the γ surface method.

These two methodologies lead to the construction of equivalent twist GBs. The number of interstitials that have to be added with EP in the vicinity of the GB grain boundary plane is the same whatever the method that have been chose: from 4 to 11 SIAs.

The All_trans_method although faster is less efficient than MQ_method which is slower. The addition of SIA on octahedral positions and the application of MQ treatments permits to explore to some extent the potential energy surface in order to find lower GB energetic states. The application of a translation as it is performed in γ -method is thus not necessary: whatever the initial state chosen; all translated GBs seem to converge to the same minimized GB state. However, **only 20 positions of SIA** near the GB plane have been tested, therefore the introduction of more than 20 positions will perhaps make **All_trans_method** more efficient in finding the GS. Our results for $\Sigma 25$ and $\Sigma 29$ are encouraging.

DFT relaxation of GB structures generated with **MQ_method** and **All_trans_method** leads to the same GB construction scheme (the same number of interstitials) for $\Sigma 17$, $\Sigma 29$ and $\Sigma 5$. However, for more complex microstructures where no clear geometric visual pattern as a function of atomic volume could be found, such as $\Sigma 37$ and $\Sigma 13$ GBs the number of steps is different from EP results. In addition, even if **MQ_method** and **All_trans_method** lead to the same formation energy at the end, for such GB with DFT calculations, **MQ_method** and **All_trans_method** converges to different GB formation energy for these two complex GBs. EP and DFT energetic results are in a good agreement with the literature and their predicted formation energy are always lower than values reported in the literature. Thus, these two methods developed in this thesis permit to construct more stable twist GBs than twist GBs already produced in the literature.

→ In a second time, a particular attention has been paid on the effect of phosphorus segregation, which is mainly implicated in the non-hardening embrittlement causing intergranular fracture. The interaction of twist grain boundary constructed, with phosphorus as a substitutional segregant has been calculated and analyzed based on different descriptors. White Coghlan segregation model [2] which is adapted for atomistic studies has been used to quantify phosphorus segregation

Whatever the method used to construct the GS structure, the phosphorus coverage profile is the same and it is associated to the lowest coverage at 873 K in comparison to other GB configurations generated in **MQ_method** and **All_trans_method**.

The comparison between experimental results and simulation is difficult because the experimental measurements generally correspond to average segregation contents, whereas atomistic simulations provide a more detailed picture taking into account the precise position of the solute in the GB.

The estimated coverage rate of phosphorus is higher than literature and experimental values for symmetric GBs: between 3.2 and 11.1 atoms/nm². This greater than MET results from V.Hsu with 2.6 atoms/nm² [3] and atom probe tomography from Akhatova with 1.6 atoms/nm² [4] and from Zhang *et al* [5] who find 0.6 atoms/nm². These discrepancies can probably partly be explained by that all of these experimentalists have studied mixed GBs which are not representative of twist GBs studied in this work.

An overestimation of phosphorus coverage in our simulations relative to experimental results could be also explained by interactions between solutes that are not taken into account in the simulations in our work as we use White-Coghlan model. A White-Coghlan model which takes into account interactions, has to be introduced to modelize co-segregation.

The segregation energy is not homogenous in the GB. Segregation is an anisotropic process which depends significantly on the GB structure and on the characteristics of the segregant (the size, the chemical species...). Certain sites in or near GB are more favourable to interact with a segregant than others. Binding energy distributions for each misorientation angle tested are all different.

Finding correlations between physical atomic descriptors and binding energy is difficult. Spearman correlation plot shows a strong-moderate correlation between SOAP and CS with binding energy whatever the misorientation angle chosen. However, no evident correlation between binding energy and atomic descriptors scatter plots has been found and the number of data used to construct the Spearman correlation plot is not sufficient to make a general conclusion.

→ **GB segregation is difficult to understand, measure and predict:** segregation on GBs depends on many physical factors. The wide variety of GB structures makes the establishment of general GB segregation model a hard task. The number of data necessary to set up a good representation of GB segregation is large, an enlargement of EDF GB data base in ferritic steels is thus needed. Twist GBs GS have been generated with **MQ_method** and **All_trans_method**, however, for a given GB, many metastable states close to one another can be reached which should be taken into account to make an exhaustive study of phosphorus segregation with a sufficiently large database. **A better understanding of GB segregation requires a better description of GB atomistic sites**, the generation of a larger GB segregation database and the development of accurate models predicting segregation on the basis of GB physical description by the use of physical descriptors.

The integration of the impact phosphorus segregation behavior on microstructure evolution in Kinetic Monte Carlo simulations is the subject of a future work. These advances will permit to envisage more quantitative simulations under PWR-type irradiation conditions over several decades of operation, and to better understand the radiation damage mechanisms of ferritic alloys at different scales.

Bibliography

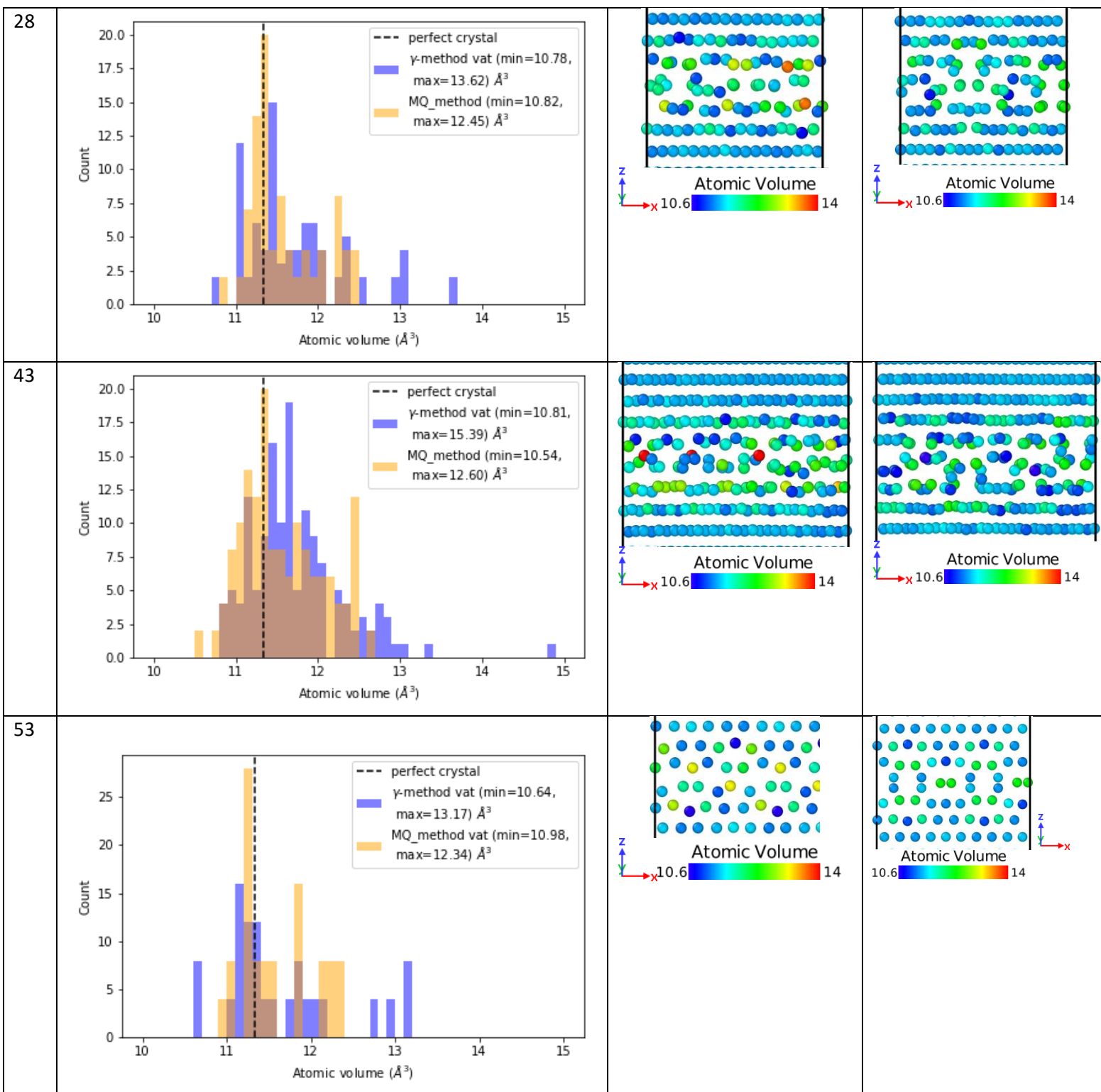
- [1] G. J. Ackland, M. I. Mendeleev, D. J. Srolovitz, S. Han, et A. V. Barashev, « Development of an interatomic potential for phosphorus impurities in alpha-iron », *Journal of Physics: Condensed Matter*, vol. 16, n° 27, p. 1-14, 2004.
- [2] C. L. White et W. A. Coghlan, « The Spectrum of Binding Energies Approach to Grain Boundary Segregation », *Metallurgical transactions A*, vol. 8A, p. 1403-1411, 1977.
- [3] C.-Y. Hsu, J. Stodolna, P. Todeschini, F. Delabrouille, B. Radiguet, et F. Christien, « Accurate quantification of phosphorus intergranular segregation in iron by STEM-EDX », *Micron*, vol. 153, p. 103175, 2022.
- [4] A. Akhatova, « Méthodologie instrumentale à l'échelle atomique pour une meilleure compréhension des mécanismes de ségrégation intergranulaire dans les aciers : application au phosphore. », Université de Rouen Normandie, 2018.
- [5] L. Zhang, « Ségrégation intergranulaire du phosphore dans les aciers des cuves des REP », Université de Rouen Normandie, 2018.

Annexes

III-Annex 1: Atomic volume distribution comparison between GB generated by γ -method and MQ_method, EP Ackland results

The distributions presented here described the atomic volume distributions for atoms positioned near the GB plane: from -4 to 4 Å from the GB plane. The atomic volume corresponding to the bulk is indicated by black dotted lines. The microstructures associated to γ -method and **MQ_method** are represented as a function of the atomic volume in the column γ -method and **MQ_method** in this following table.

Θ°	Distribution of atomic volume	γ -method	MQ_method
18	<p>5</p> <p>Count</p> <p>Atomic volume (Å^3)</p> <p>--- perfect crystal γ-method vat (min=10.79, max=14.50) Å^3 MQ_method (min=10.85, max=13.68) Å^3</p>	<p>Atomic Volume</p> <p>10.6 14</p>	<p>Atomic Volume</p> <p>10.6 14</p>
22	<p>Count</p> <p>Atomic volume (Å^3)</p> <p>--- perfect crystal γ-method vat (min=10.89, max=12.73) Å^3 MQ_method (min=10.59, max=12.32) Å^3</p>	<p>Atomic Volume</p> <p>10.6 14</p>	<p>Atomic Volume</p> <p>10.6 14</p>



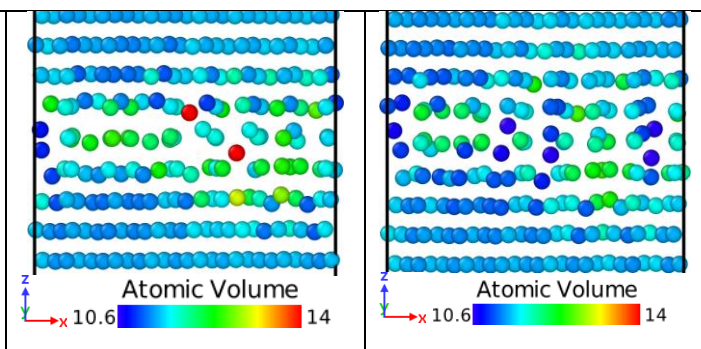
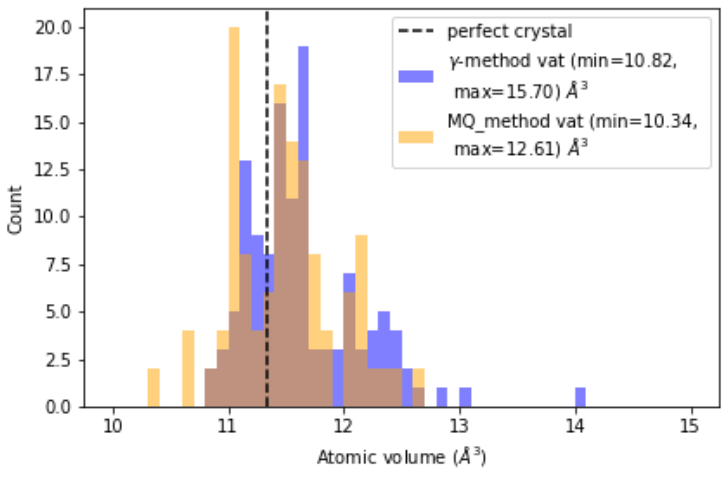


Figure III- 58: Atomic volume distribution and microstructure comparison between GB generated by γ -method and MQ_method, EP Ackland results

III-Annex 2: All_trans method typical evolutions of the formation energy during the process

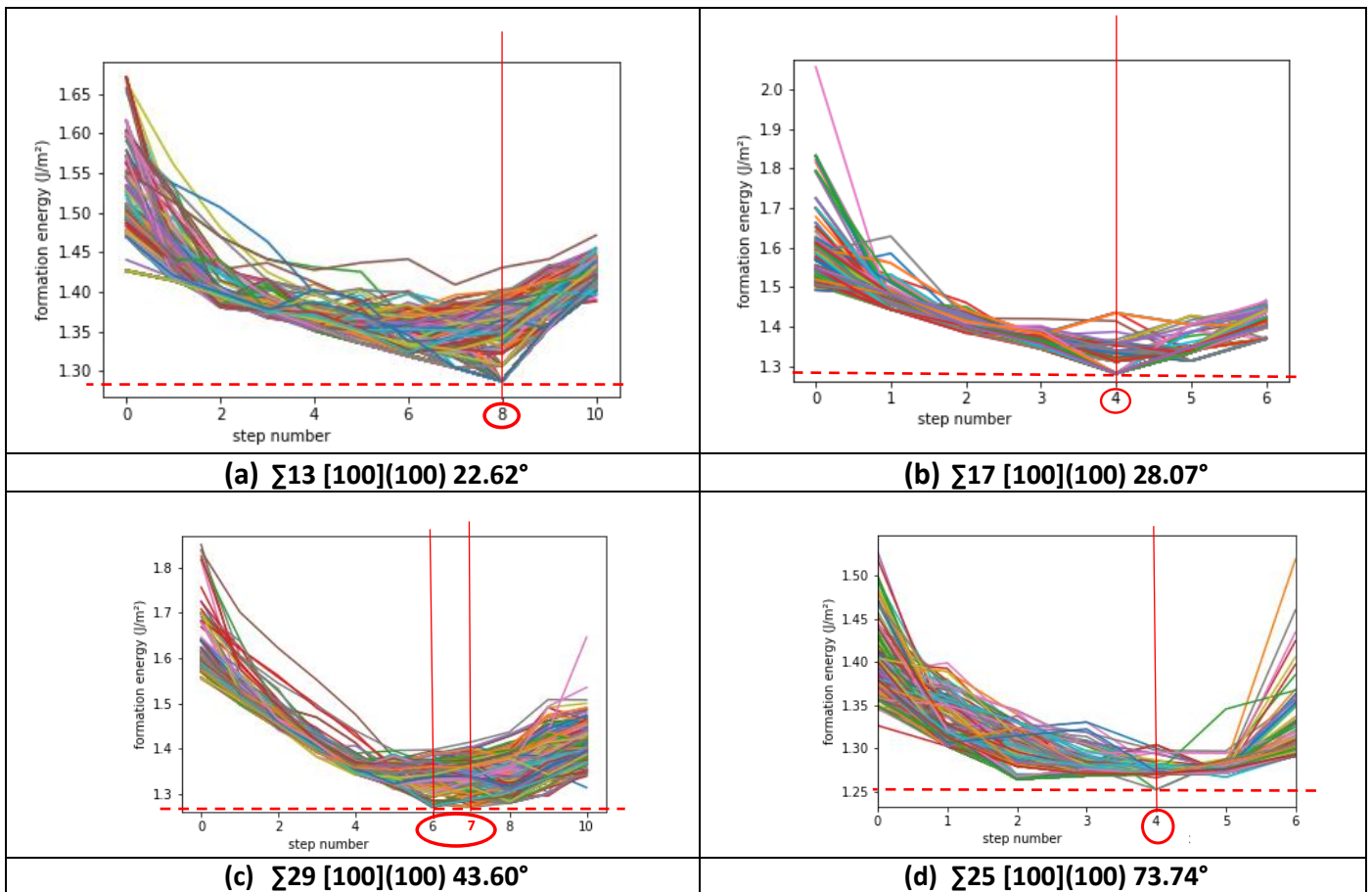


Figure III- 59: Evolution of the grain boundary formation energy versus the number of SIA introduced corresponding here to the step number. The minimum formation energy obtained and its associated number of SIA is indicated by red lines.

III-Annex 3: Minimum formation energies selected at each step of All_trans_method as a function of TX and TY coordinates of the corresponding global translation.

For each following representation the colour scale is adjusted to highlight minimum GB formation energy.

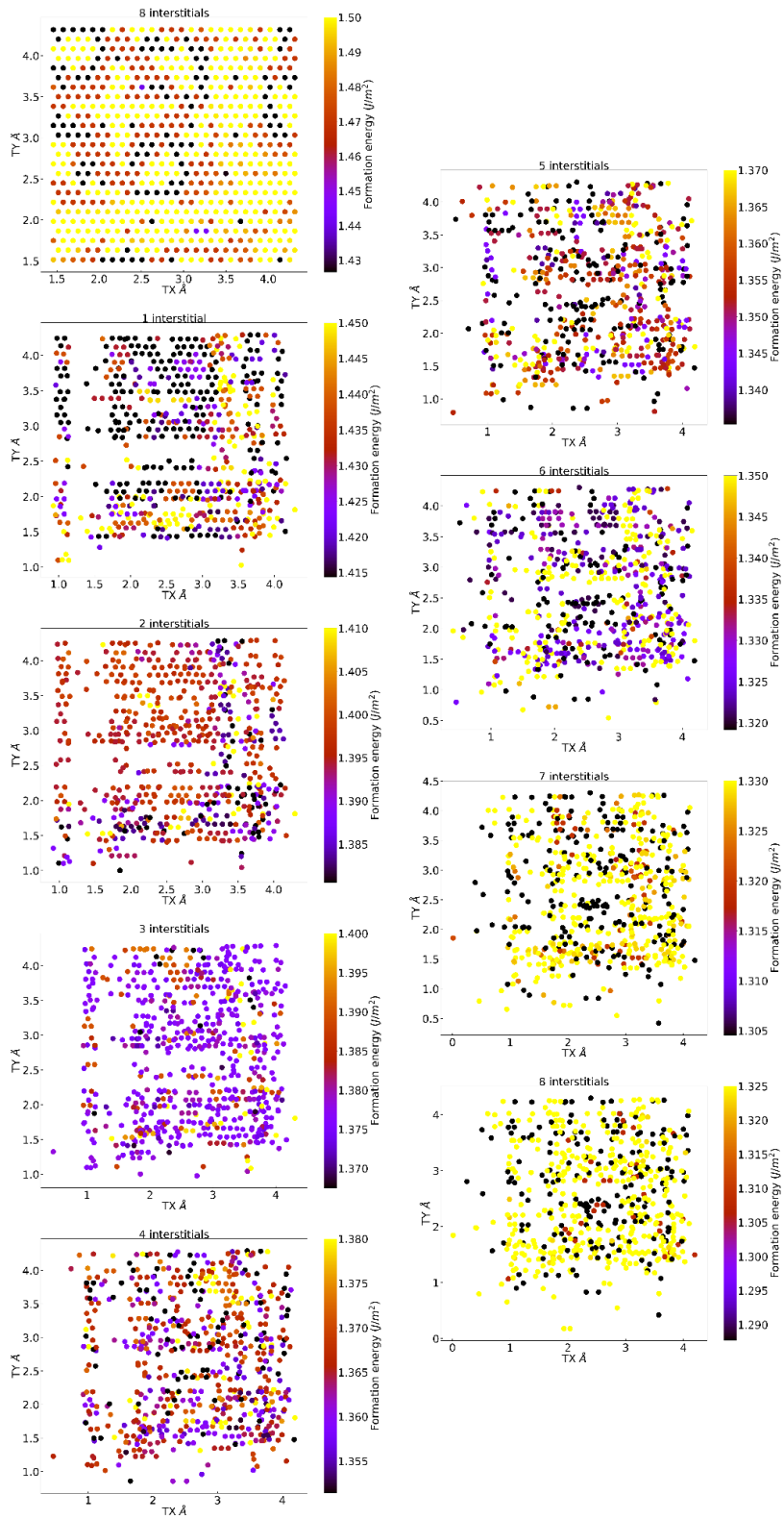


Figure III-60: $\Sigma 13$ minimum formation energies (J/m^2) selected at each step of `All_trans_method` as a function of TX and TY coordinates of the corresponding global translation expressed in Å.

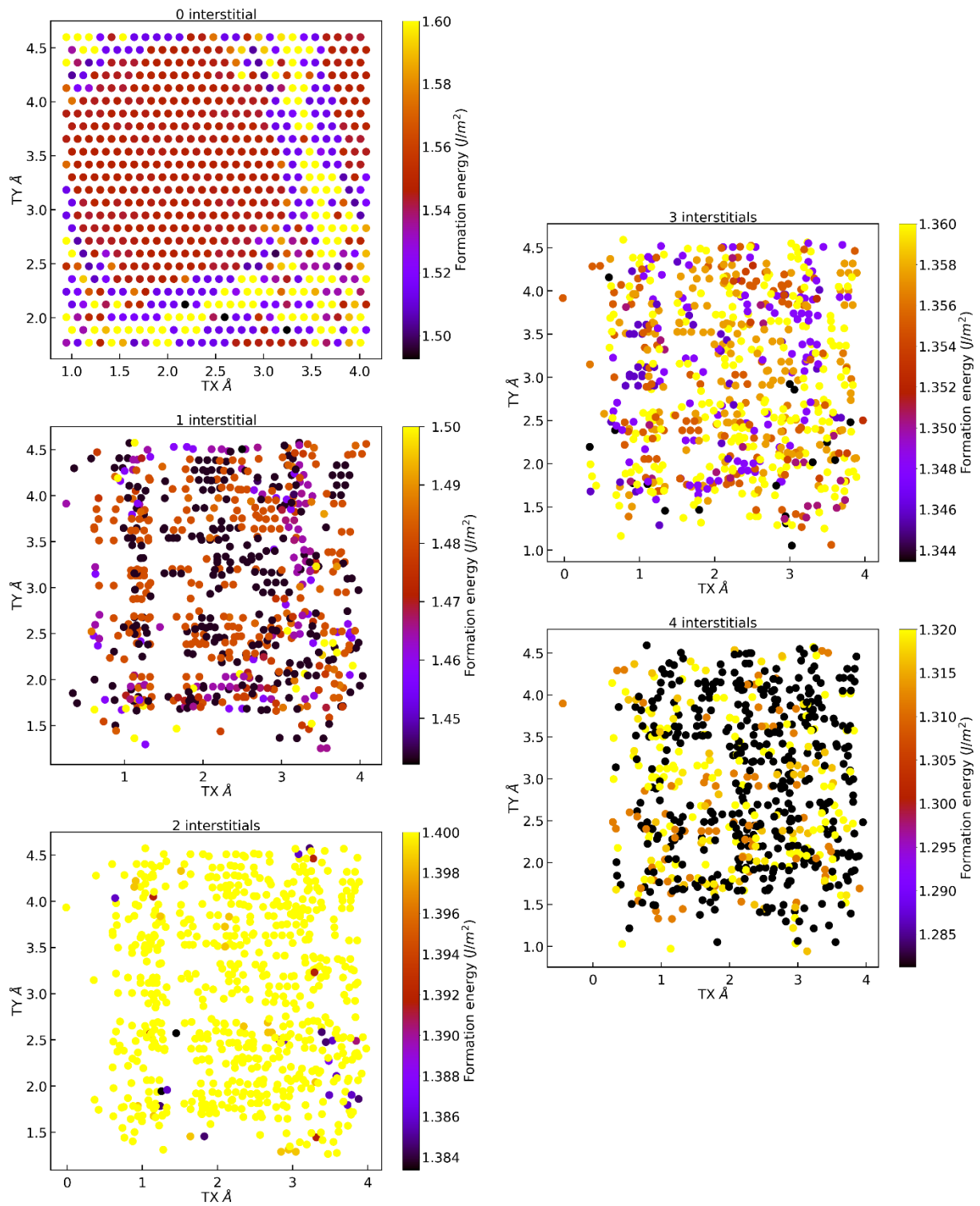


Figure III- 61: $\Sigma 17$ minimum formation energies (J/m^2) selected at each step of `All_trans_method` as a function of TX and TY coordinates of the corresponding global translation expressed in \AA .

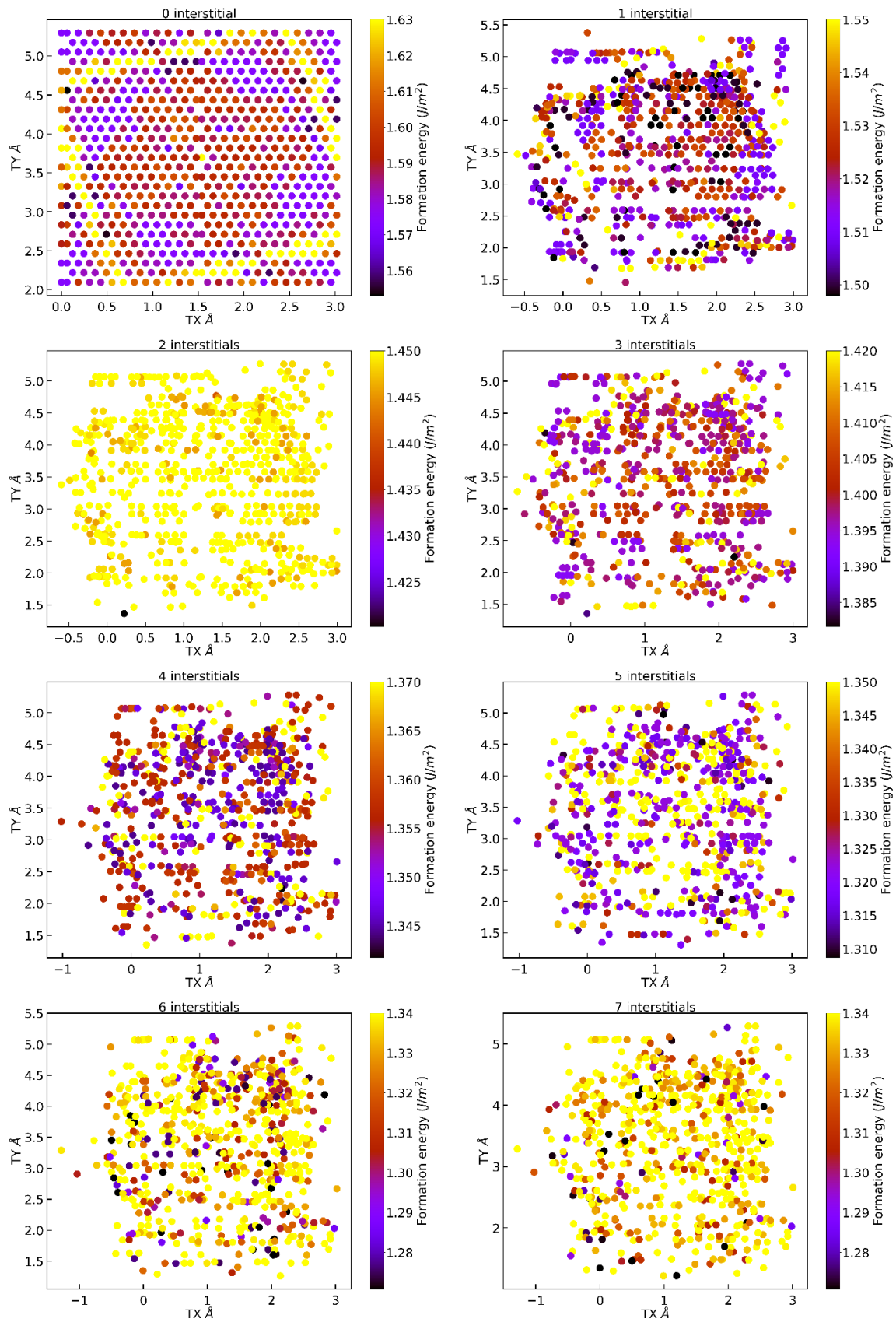


Figure III- 62: $\Sigma 29$ minimum formation energies (J/m²) selected at each step of `All_trans_method` as a function of TX and TY coordinates of the corresponding global translation expressed in Å.

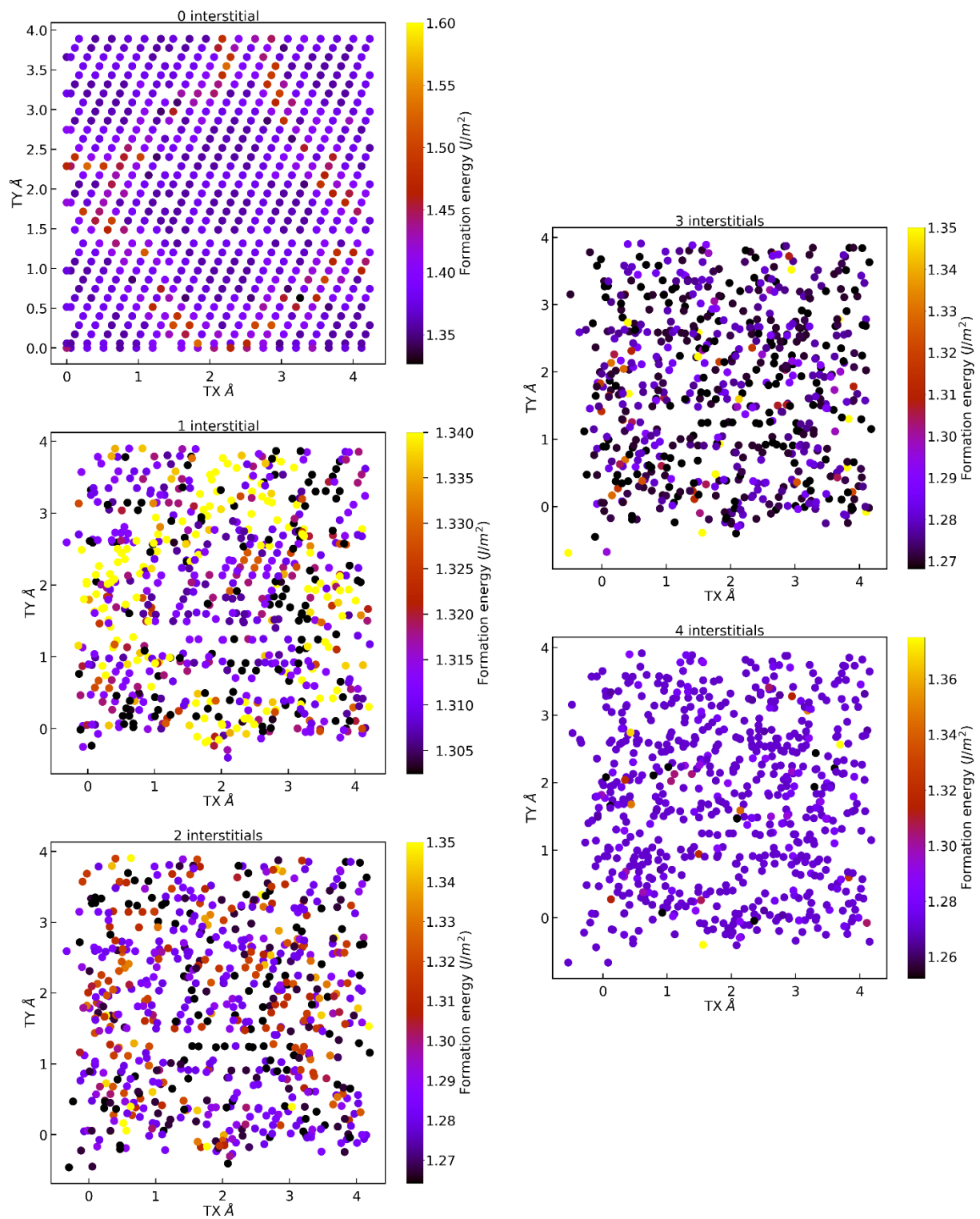


Figure III- 63: $\Sigma 25$ minimum formation energies (J/m^2) selected at each step of **All_trans_method** as a function of TX and TY coordinates of the corresponding global translation expressed in \AA .

III-Annex 4: Distributions of the minimum formation energies selected at each stage of All_trans_method.

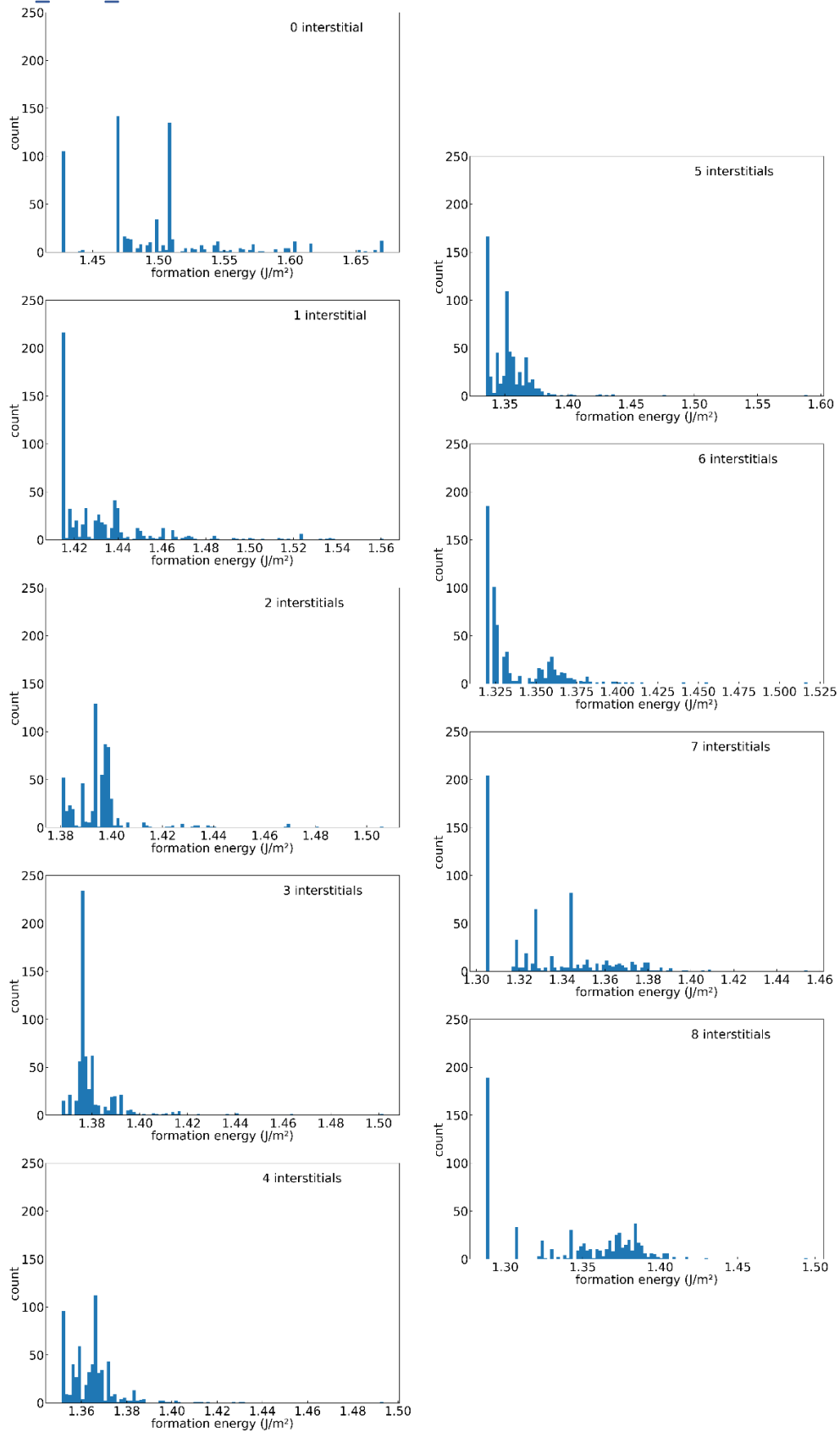


Figure III- 64: Σ 13 distributions of the minimum formation energies selected at each stage of All_trans_method

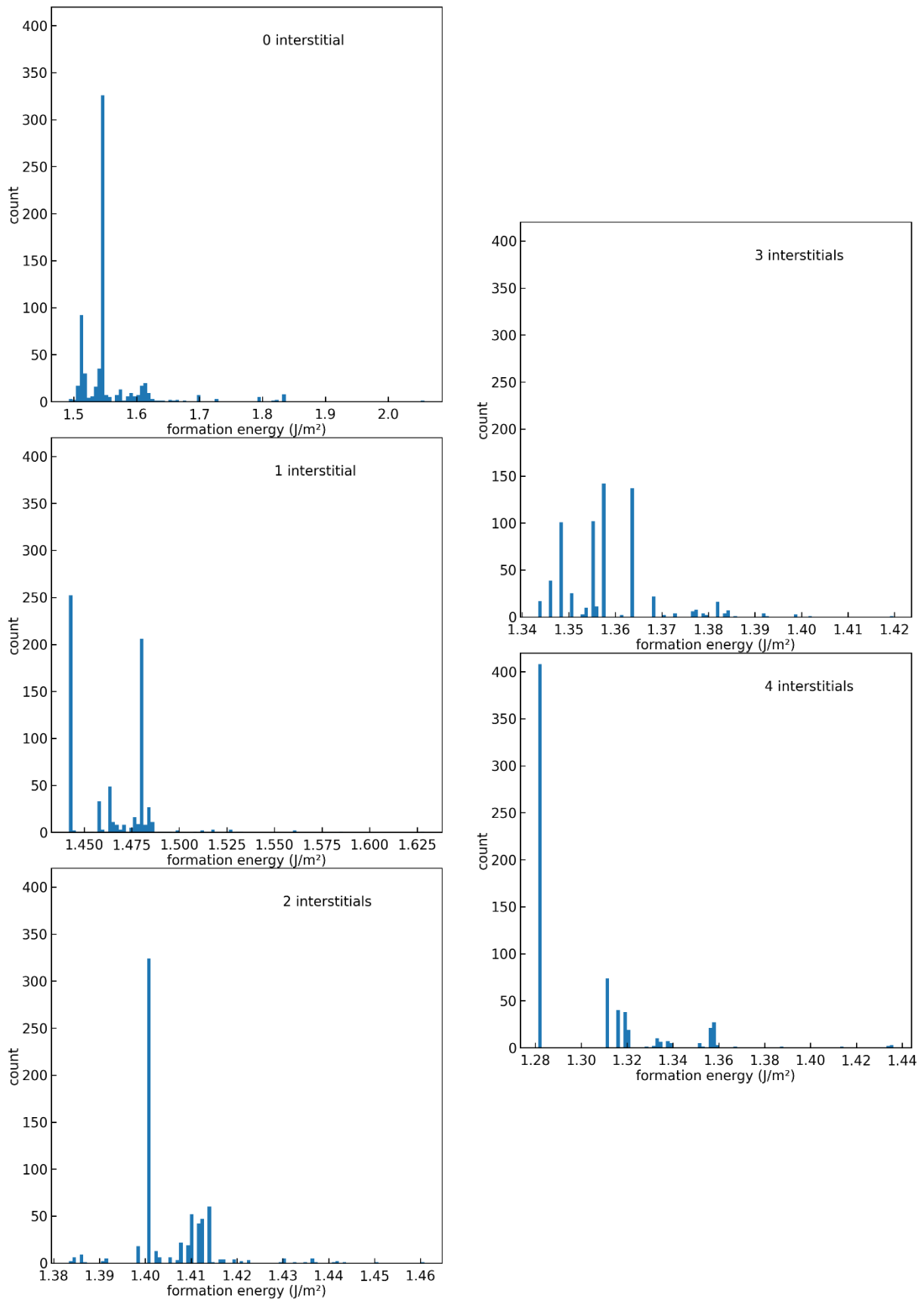


Figure III- 64: $\Sigma 17$ distributions of the minimum formation energies selected at each stage of All_trans_method.

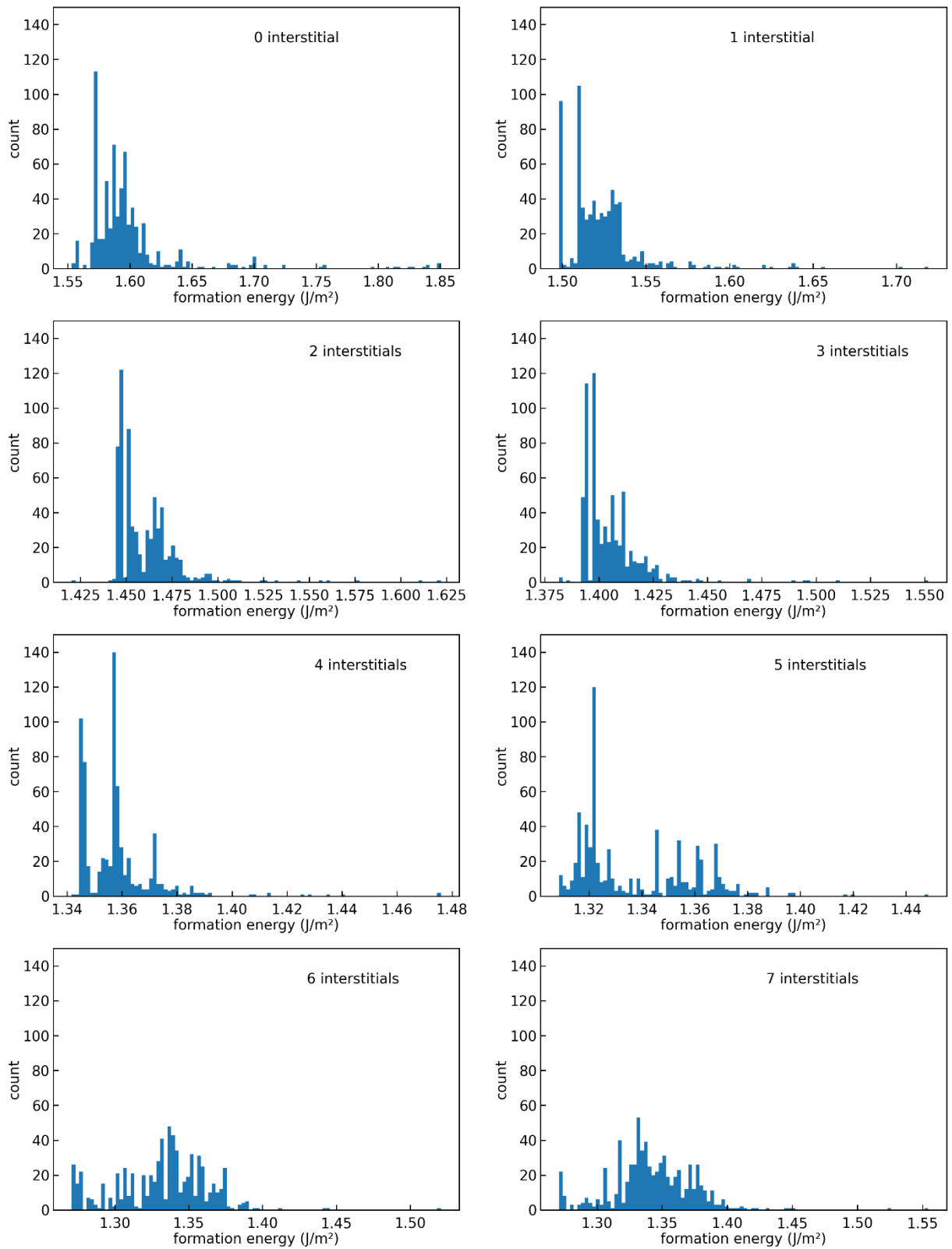


Figure III- 65: Σ_{29} distributions of the minimum formation energies selected at each stage of **All_trans_method**.

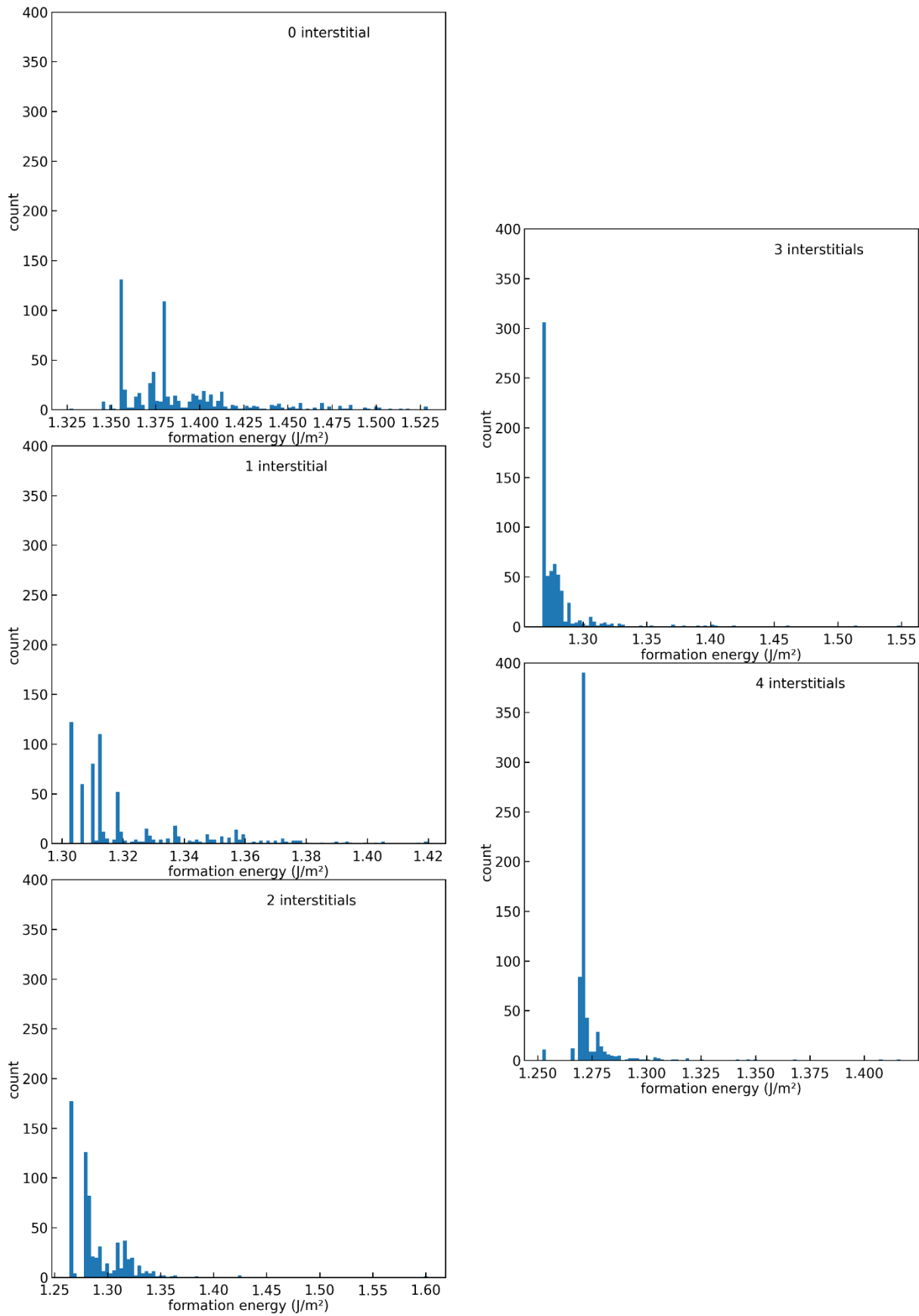
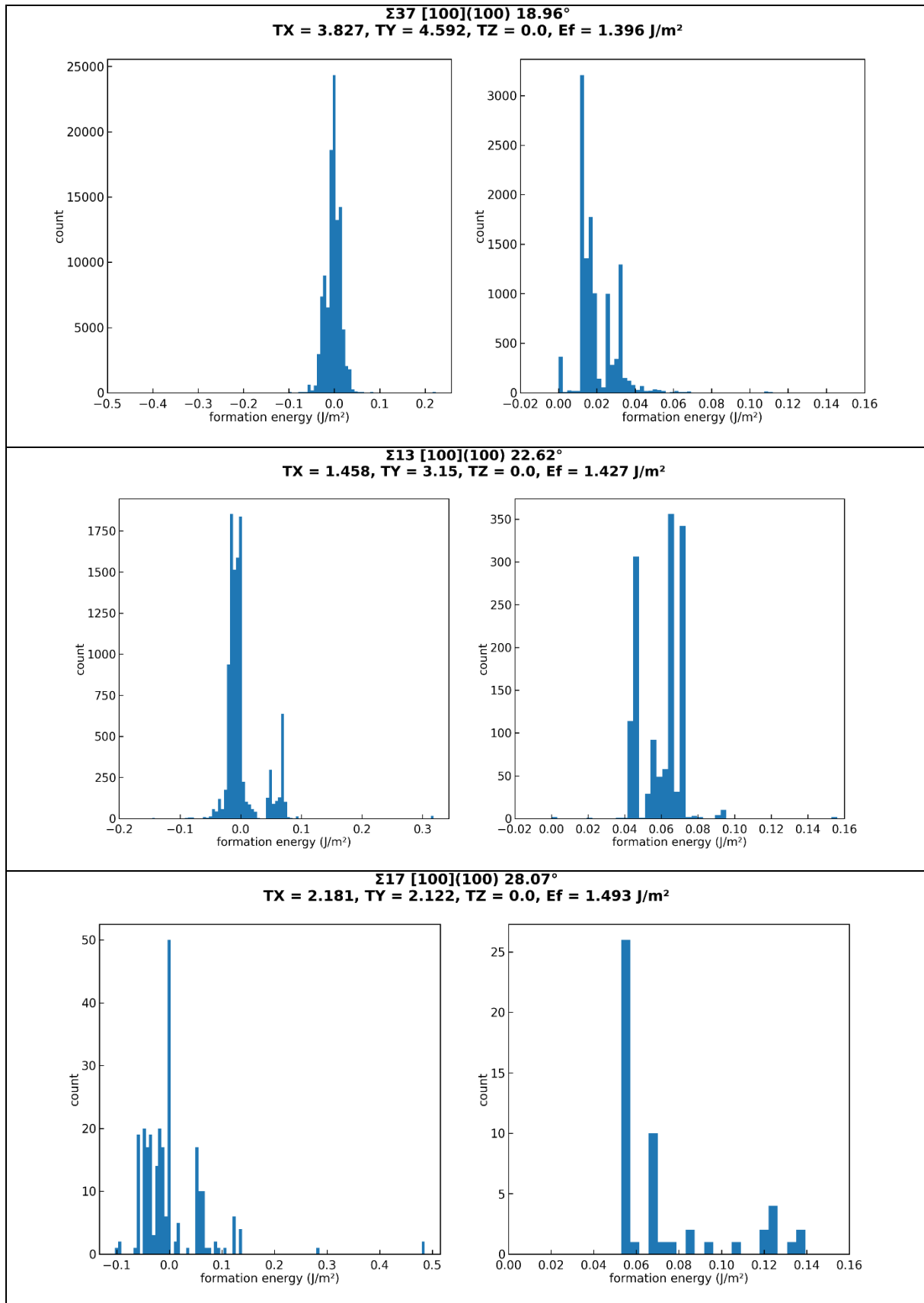


Figure III- 66: Σ_{25} distributions of the minimum formation energies selected at each stage of All_trans_method.

III-Annex 5: Changes in formation energy between two steps with MQ_method



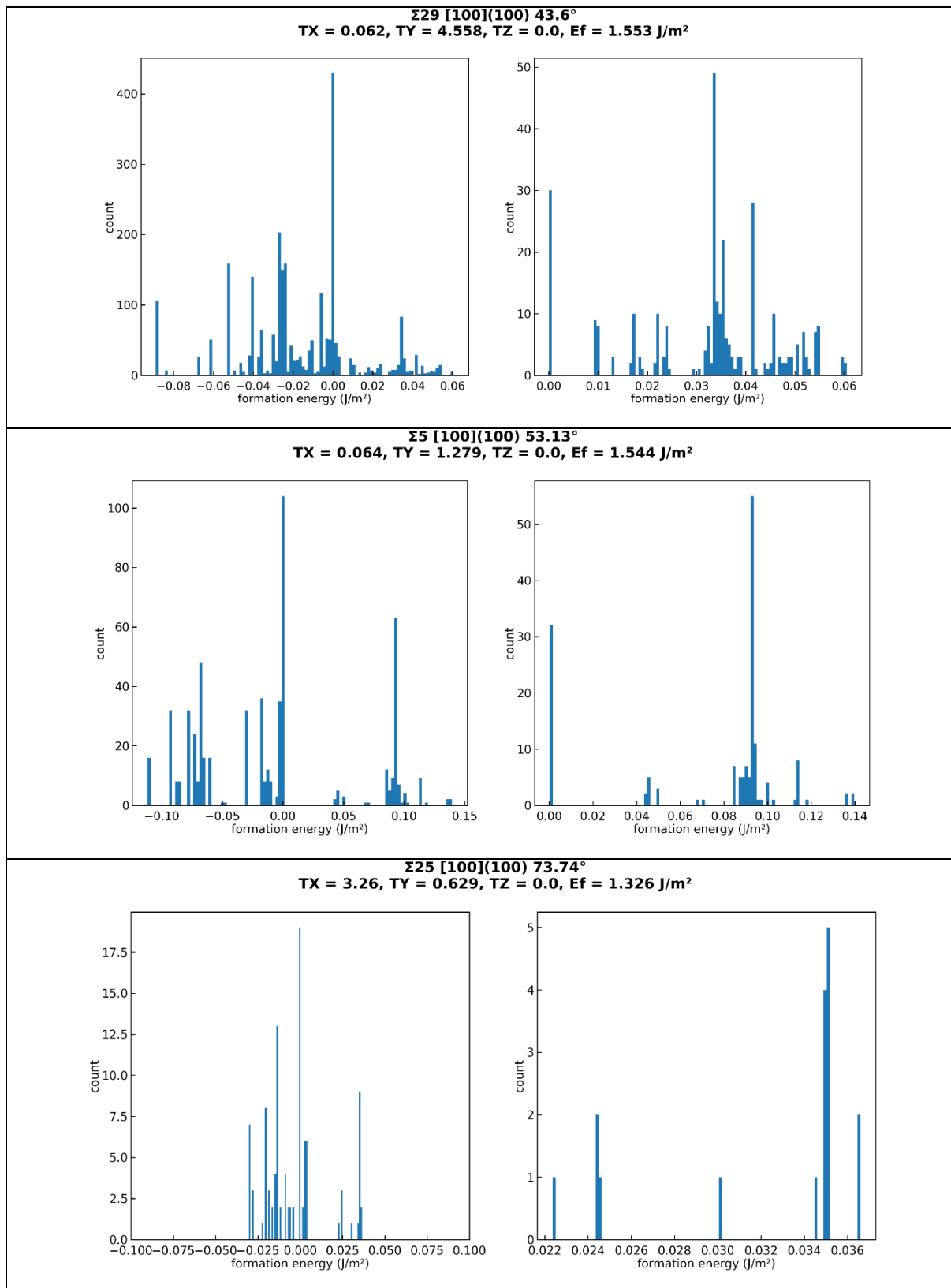


Figure III- 67: changes in formation energy between two steps (of **Figure III- 42** but also for the other branches not represented **Figure III- 42**). Left hand side: all ΔE between two steps, right hand side: positive ΔE before reaching the GS.

III-Annex 6: Impact of GB shift of GB formation energy

GB shift relative to the middle of the GB (Å)	1.42	2.84	4.26	5.68	7.1	8.52	9.94	11.36	12.78
$\Sigma 37$ (100)[100] 18.92° Ef (J/m ²)	1.2987	1.2987	1.2987	1.298	1.297	1.292	1.251	0.326	
$\Sigma 13$ (100)[100] 22.62° Ef (J/m ²)	1.288	1.288	1.288	1.288	1.286	1.284	1.281	1.164	0.54
$\Sigma 17$ (100)[100] 28.08° Ef (J/m ²)	1.281	1.281	1.281	1.281	1.281	1.281	1.28	1.278	1.247
$\Sigma 29$ (100)[100] 43.6° Ef (J/m ²)	1.271	1.271	1.271	1.27	1.27	1.269	1.265	1.251	1
$\Sigma 5$ (100)[100] 53.13° Ef (J/m ²)	1.142	1.142	1.142	1.142	1.142	1.142	1.14	1.139	1.051
$\Sigma 25$ (100)[100] 73.74° Ef (J/m ²)	1.252	1.252	1.252	1.252	1.251	1.247	1.239	1.216	0.13

Table III- 17: GB shift relative to the middle of the GB for each GB misorientation angle in Å

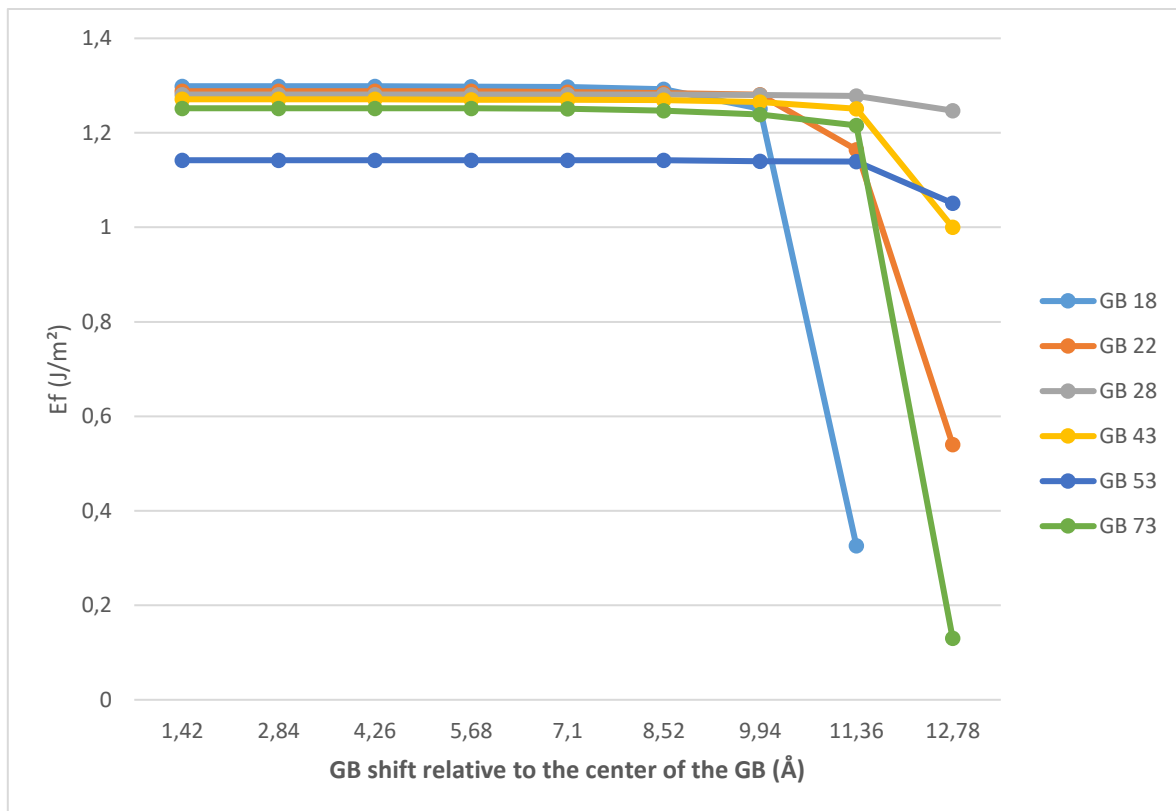


Figure III- 68: GB shift relative to the middle of the GB for each GB misorientation angle in Å

GB shift relative to the middle of the GB often present for MQ method when a step of MQ has been performed, has in most cases a very little or no impact on the final formation energy of the GB i.e. the GB shift generally does not exceed 8.52 Å.

III-Annex 7: Characterisation of final GBs obtained with MQ_method

GB		Initial translation			Global translation			Relative translation						
Σ	$\theta(^{\circ})$	TX_{ini} (Å)	TY_{ini} (Å)	TZ_{ini} (Å)	TXG (Å)	TYG (Å)	TZG (Å)	TX (Å)	TY (Å)	TZ (Å)	Ef_{ini} (J/m ²)	Ef final (J/m ²)	Nb SIA	Nb MQ
<u>$\Sigma 37$</u>	<u>18</u>	<u>0.278</u>	<u>5.079</u>	<u>0</u>	<u>2.397</u>	<u>2.300</u>	<u>0.063</u>	<u>2.119</u>	<u>-2.779</u>	<u>0.063</u>	<u>1.396</u>	<u>1.299</u>	<u>11</u>	<u>7</u>
$\Sigma 37$	18	3.131	4.035	0	1.464	2.129	0.122	-1.667	-1.906	0.122	1.411	1.299	11	7
$\Sigma 37$	18	3.757	2.226	0	2.676	3.291	0.147	-1.081	1.065	0.147	1.495	1.299	11	6
$\Sigma 37$	18	3.618	1.948	0	2.625	0.689	0.119	-0.993	-1.259	0.119	1.525	1.299	11	6
$\Sigma 37$	18	3.896	3.061	0	2.321	2.576	0.111	-1.575	-0.485	0.111	1.538	1.299	11	5
<u>$\Sigma 13$</u>	<u>22</u>	<u>1.458</u>	<u>3.150</u>	<u>0</u>	<u>2.261</u>	<u>5.735</u>	<u>0.081</u>	<u>0.803</u>	<u>2.585</u>	<u>0.081</u>	<u>1.426</u>	<u>1.288</u>	<u>8</u>	<u>1</u>
$\Sigma 13$	22	1.750	3.499	0	3.549	6.435	0.077	1.799	2.935	0.077	1.47	1.288	8	1
$\Sigma 13$	22	3.674	1.516	0	6.258	2.960	0.047	2.584	1.444	0.047	1.477	1.288	8	3
$\Sigma 13$	22	3.849	3.266	0	5.959	4.717	0.101	2.110	1.451	0.101	1.511	1.288	8	3
$\Sigma 13$	22	3.674	4.083	0	6.757	7.598	0.070	3.083	3.515	0.070	1.546	1.288	8	1
$\Sigma 13$	22	3.791	2.916	0	7.128	5.419	0.087	3.337	2.503	0.087	1.603	1.288	8	1
<u>$\Sigma 17$</u>	<u>28</u>	<u>2.181</u>	<u>2.122</u>	<u>0</u>	<u>2.735</u>	<u>3.345</u>	<u>0.049</u>	<u>0.554</u>	<u>1.223</u>	<u>0.049</u>	<u>1.493</u>	<u>1.281</u>	<u>4</u>	<u>3</u>
$\Sigma 17$	28	3.891	2.004	0	7.594	3.443	0.098	3.704	1.439	0.098	1.589	1.281	4	0
$\Sigma 17$	28	3.478	2.358	0	6.668	3.589	0.059	3.190	1.231	0.059	1.643	1.281	4	0
$\Sigma 17$	28	1.415	1.769	0	2.244	3.145	0.103	0.829	1.376	0.103	1.725	1.281	4	0
$\Sigma 17$	28	3.537	3.419	0	6.793	6.321	0.089	3.256	2.901	0.089	1.832	1.281	4	0
<u>$\Sigma 29$</u>	<u>43</u>	<u>0.062</u>	<u>4.558</u>	<u>0</u>	<u>-0.856</u>	<u>8.215</u>	<u>0.070</u>	<u>-0.917</u>	<u>3.657</u>	<u>0.070</u>	<u>1.553</u>	<u>1.271</u>	<u>7</u>	<u>3</u>
$\Sigma 29$	43	2.957	4.065	0	4.216	7.914	0.083	1.260	3.849	0.083	1.756	1.271	6	4
$\Sigma 29$	43	1.971	2.341	0	2.499	3.490	0.071	0.528	1.150	0.071	1.839	1.271	7	4
$\Sigma 29$	43	1.848	5.297	0	2.688	9.817	0.146	0.841	4.520	0.146	1.842	1.271	7	6
$\Sigma 29$	43	0.123	3.449	0	-0.923	5.401	0.000	-1.046	1.951	0.000	1.85	1.271	6	6
<u>$\Sigma 5$</u>	<u>53</u>	<u>0.064</u>	<u>1.279</u>	<u>0</u>	<u>-0.920</u>	<u>1.877</u>	<u>0.044</u>	<u>-0.984</u>	<u>0.598</u>	<u>0.044</u>	<u>1.544</u>	<u>1.142</u>	<u>4</u>	<u>0</u>
$\Sigma 5$	53	1.023	0.831	0	2.023	1.556	0.090	1.000	0.725	0.090	1.586	1.142	4	0
$\Sigma 5$	53	1.599	1.087	0	3.304	1.690	0.056	1.705	0.603	0.056	1.597	1.142	4	0
$\Sigma 5$	53	3.389	3.325	0	6.828	6.624	0.062	3.439	3.299	0.062	1.608	1.142	4	0
$\Sigma 5$	53	1.087	2.302	0	2.192	4.165	0.050	1.105	1.863	0.050	1.611	1.142	4	0
$\Sigma 5$	53	2.366	1.087	0	4.284	1.925	0.057	1.918	0.838	0.057	1.652	1.142	4	0
$\Sigma 5$	53	1.726	0.064	0	2.751	-0.482	0.075	1.025	-0.546	0.075	1.689	1.142	4	0
<u>$\Sigma 25$</u>	<u>73</u>	<u>3.260</u>	<u>0.629</u>	<u>0</u>	<u>6.007</u>	<u>1.131</u>	<u>0.039</u>	<u>2.747</u>	<u>0.502</u>	<u>0.039</u>	<u>1.326</u>	<u>1.252</u>	<u>4</u>	<u>1</u>
$\Sigma 25$	73	1.258	2.402	0	1.492	3.898	0.052	0.233	1.496	0.052	1.345	1.252	4	0
$\Sigma 25$	73	2.974	0.057	0	5.106	-0.384	0.041	2.132	-0.442	0.041	1.351	1.252	4	3
$\Sigma 25$	73	0.515	0.972	0	1.021	1.826	0.047	0.506	0.853	0.047	1.366	1.252	4	1
$\Sigma 25$	73	0.858	3.432	0	0.521	5.942	0.041	-0.337	2.511	0.041	1.374	1.252	4	5
$\Sigma 25$	73	3.717	1.487	0	6.560	2.129	0.051	2.843	0.642	0.051	1.381	1.252	4	3
$\Sigma 25$	73	3.432	2.288	0	6.089	3.803	0.042	2.657	1.515	0.042	1.413	1.252	4	4
$\Sigma 25$	73	3.775	1.201	0	6.472	1.952	0.051	2.697	0.751	0.051	1.481	1.252	4	2
$\Sigma 25$	73	2.230	3.546	0	2.613	6.820	0.036	0.383	3.274	0.036	1.529	1.252	4	5

Table III- 18: Initial translations (TX_{ini} , TY_{ini} and TZ_{ini}) applied during the γ -method and global translations (TXG , TYG and TZG) obtained for each translated GB. The data in red correspond to the simulations of **Figure III- 42**. Ef_{ini} is the initial formation energy obtained after the γ -surface method; the relative translation between initial and global translation is indicated in the third column. The number of interstitials and MQ that have to be added to reach the lowest energetic configuration are indicated in the two last columns.

III-Annex 8: Final microstructures associated to the configurations obtained in III-Annex 7

				Atomic Volume 10.7 14.5		
$\Sigma 37$						
	TX=0.016; TY=0.295; $E_{f_{ini}} = 1.396$	TX=0.182; TY=0.234; $E_{f_{ini}} = 1.411$	TX=0.222; TY=0.267; $E_{f_{ini}} = 1.495$			
	TX=0.210; TY=0.113; $E_{f_{ini}} = 1.525$		TX=0.226; TY=0.178; $E_{f_{ini}} = 1.538$			
$\Sigma 13$						
	TX=0.101; TY=0.218; $E_{f_{ini}} = 1.427$	TX=0.121; TY=0.242; $E_{f_{ini}} = 1.4696$	TX=0.255; TY=0.105; $E_{f_{ini}} = 1.477$			
	TX=0.267; TY=0.226; $E_{f_{ini}} = 1.511$	TX=0.255; TY=0.283; $E_{f_{ini}} = 1.546$	TX=0.263; TY=0.202; $E_{f_{ini}} = 1.603$			
$\Sigma 17$						
	TX=0.187; TY=0.182; $E_{f_{ini}} = 1.493$	TX=0.333; TY=0.172; $E_{f_{ini}} = 1.589$	TX=0.297; TY=0.202; $E_{f_{ini}} = 1.6429$			

$\Sigma 17$					
	TX=0.121; TY=0.152; Ef _{ini} =1.832		TX=0.303; TY=0.293; Ef _{ini} =1.8320		
$\Sigma 29$					
	TX=0.004; TY=0.299; Ef _{ini} =1.553	TX=0.194; TY=0.267; Ef _{ini} =1.756	TX=0.129; TY=0.154; Ef _{ini} =1.839	TX=0.121; TY=0.347; Ef _{ini} =1.8415	TX=0.008; TY=0.226; Ef _{ini} =1.8504
$\Sigma 5$					
	TX=0.005; TY=0.101; Ef _{ini} =1.544	TX=0.081; TY=0.066; Ef _{ini} =1.586	TX=0.126; TY=0.086; Ef _{ini} =1.597	TX=0.268; TY=0.263; Ef _{ini} =1.608	TX=0.086; TY=0.182; Ef _{ini} =1.611

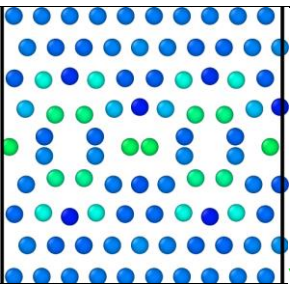
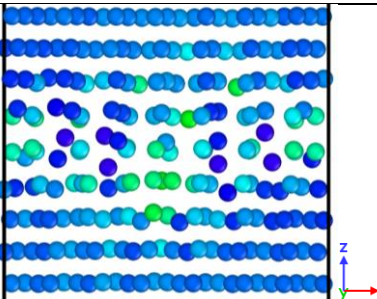
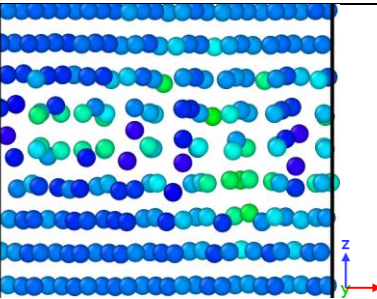
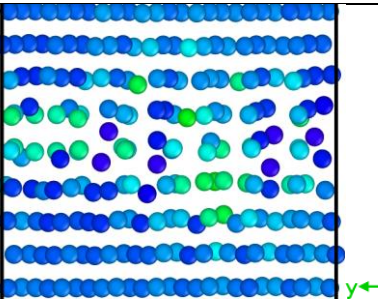
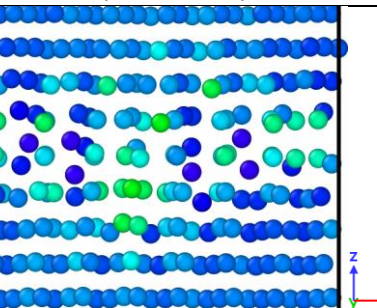
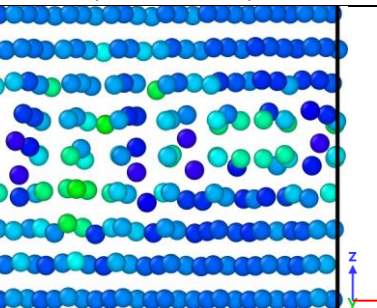
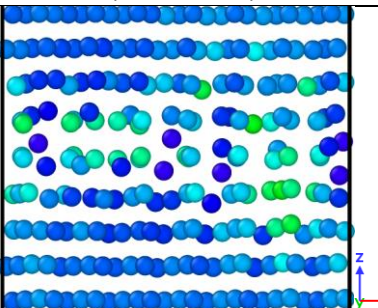
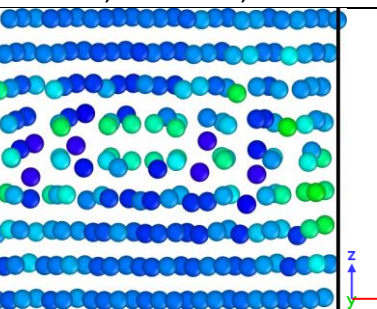
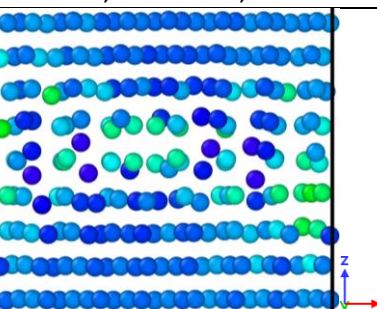
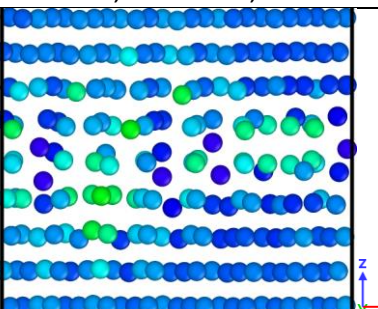
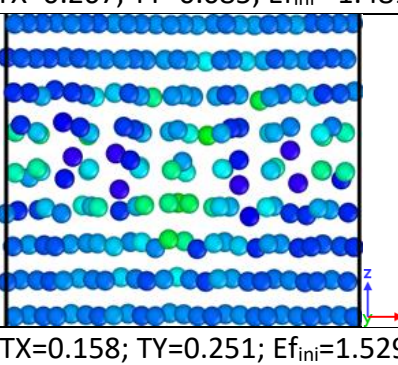
$\Sigma 5$			
	TX=0.136; TY=0.005; $E_{f_{ini}}=1.689$		
$\Sigma 25$			
	TX=0.230; TY=0.044; $E_{f_{ini}}=1.326$	TX=0.089; TY=0.1697; $E_{f_{ini}}=1.345$	TX=0.210; TY=0.004; $E_{f_{ini}}=1.351$
			
	TX=0.036; TY=0.069; $E_{f_{ini}}=1.366$	TX=0.061; TY=0.242; $E_{f_{ini}}=1.374$	TX=0.263; TY=0.105; $E_{f_{ini}}=1.381$
			
	TX=0.242; TY=0.162; $E_{f_{ini}}=1.413$	TX=0.267; TY=0.085; $E_{f_{ini}}=1.481$	TX=0.073; TY=0.170; $E_{f_{ini}}=1.4998$
			
	TX=0.158; TY=0.251; $E_{f_{ini}}=1.529$		

Table III- 19: Final microstructures obtained for different initial translations corresponding to different formation energy, by performing **MQ_method**. The Initial translations are expressed in reduced coordinates and the initial formation energy is expressed in J/m².

III-Annex 9: Formation energy of GBs generated with EP Ackland and relaxed with DFT.

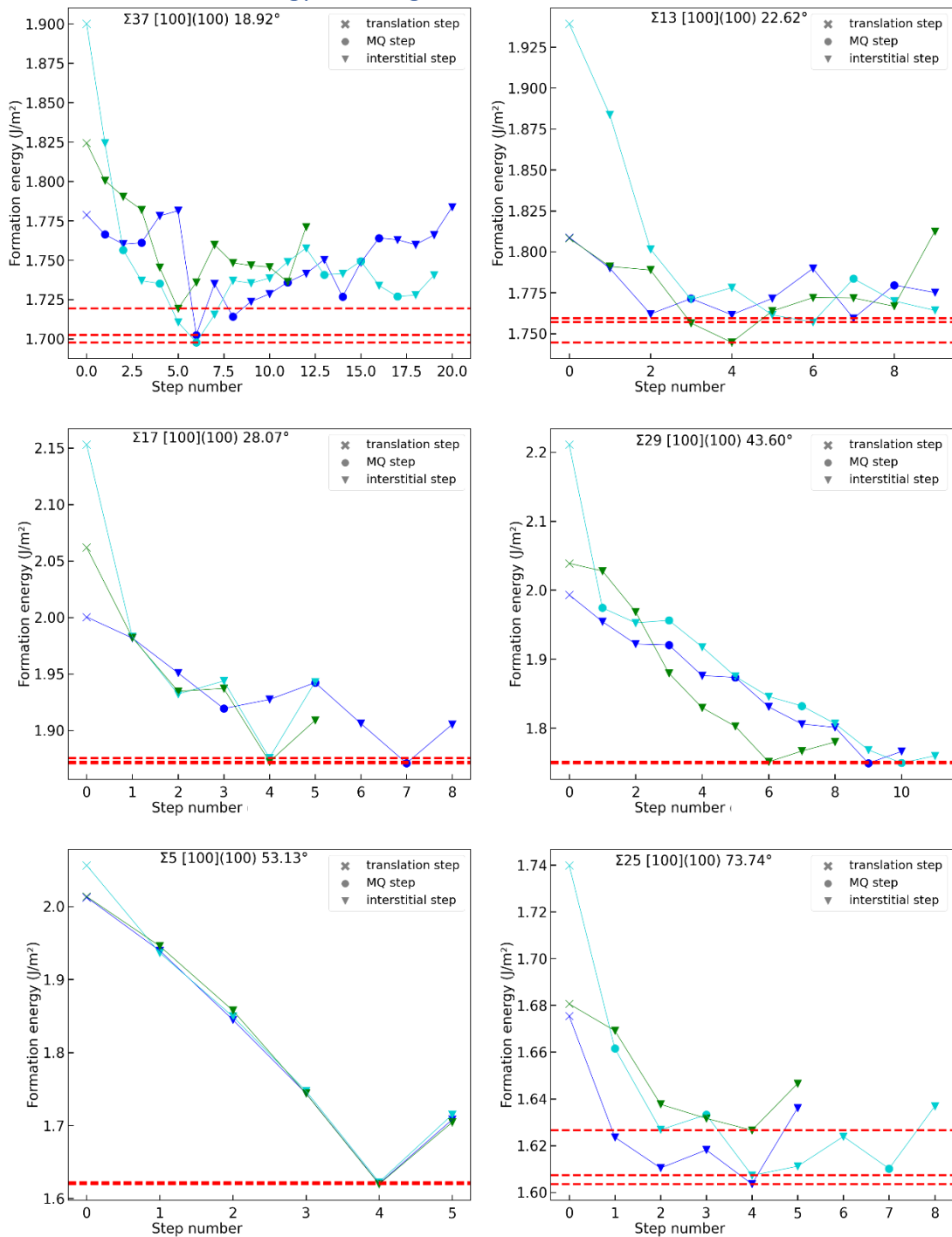
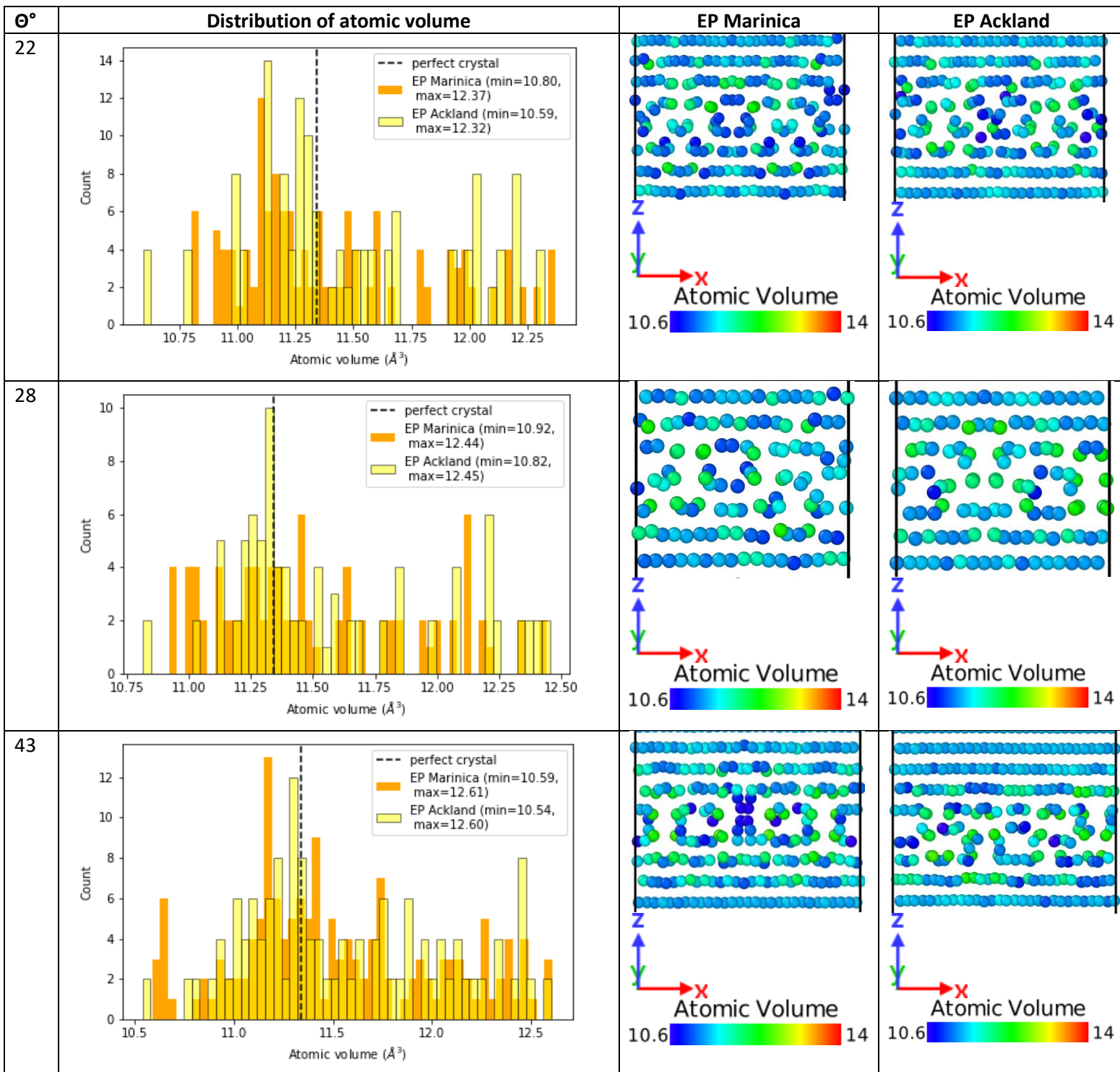


Figure III- 69: Formation energy calculated with DFT for twist GBs obtained with **MQ_method** and **All_trans_method** as a function of step number. Several initial configurations have been tested for **MQ_method** and are indicated by a blue colour. **All_trans_method** is green. A translation event is indicated by a cross, a MQ event by a circle and the introduction of an interstitial event by a triangle. The color indicates the corresponding misorientation angle. The red-dotted line indicates the minimum GB formation energy obtained with this method.

III-Annex 10: Atomic volume distribution comparison between GB generated with EP Ackland and EP Marinica with MQ_method

The distributions presented here described the atomic volume distributions for atoms positioned near the GB plane: from -4 to 4 Å from the GB plane. The atomic volume corresponding to the bulk is indicated by black dotted lines. Atomic volume distributions associated to GBs relaxed with EP Marinica [80], [81] are represented in orange and those associated to GBs relaxed with EP Ackland [70] are coloured in yellow. The microstructures associated to these distributions are represented as a function of the misorientation angle in the two remains columns.



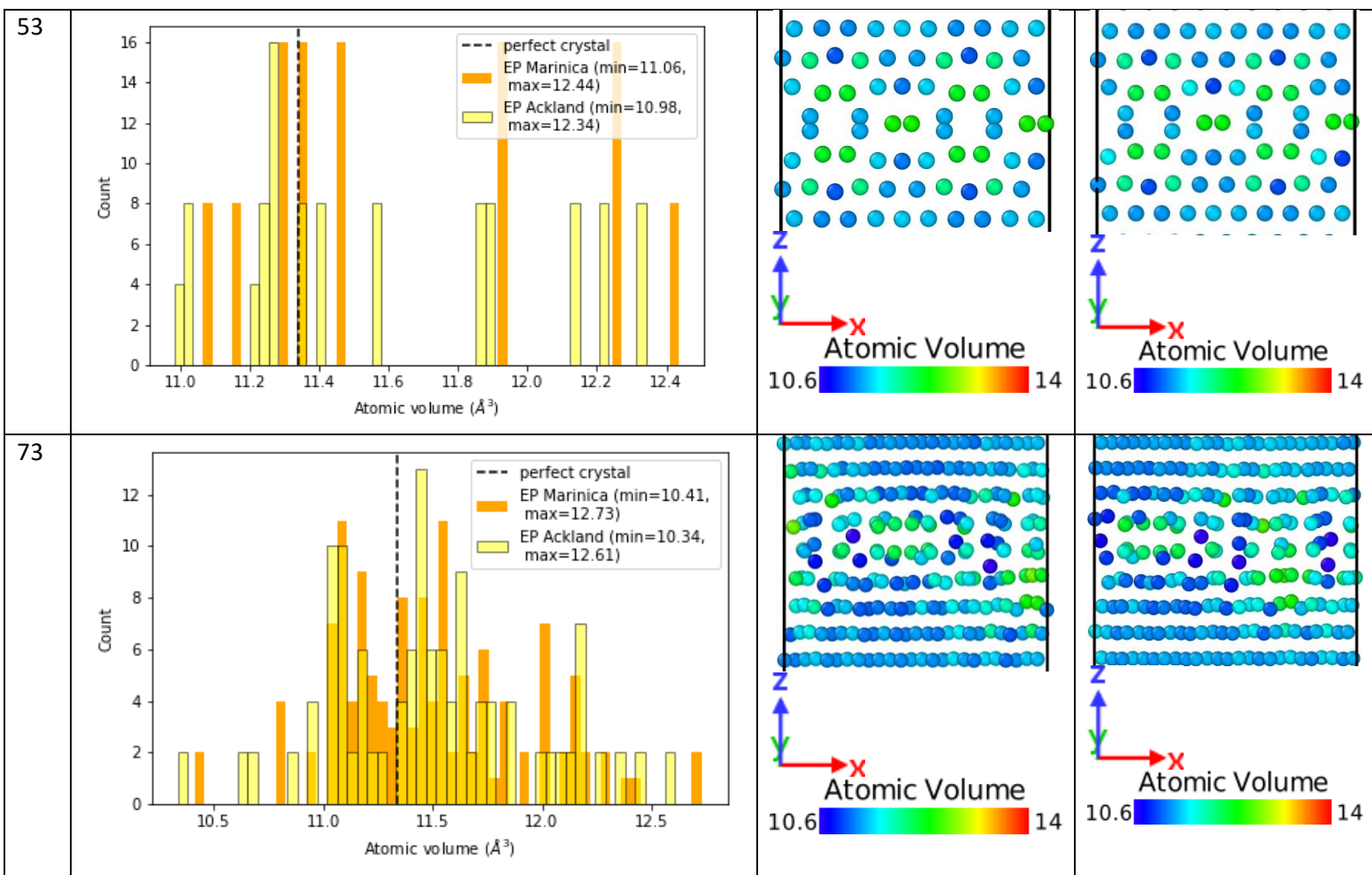
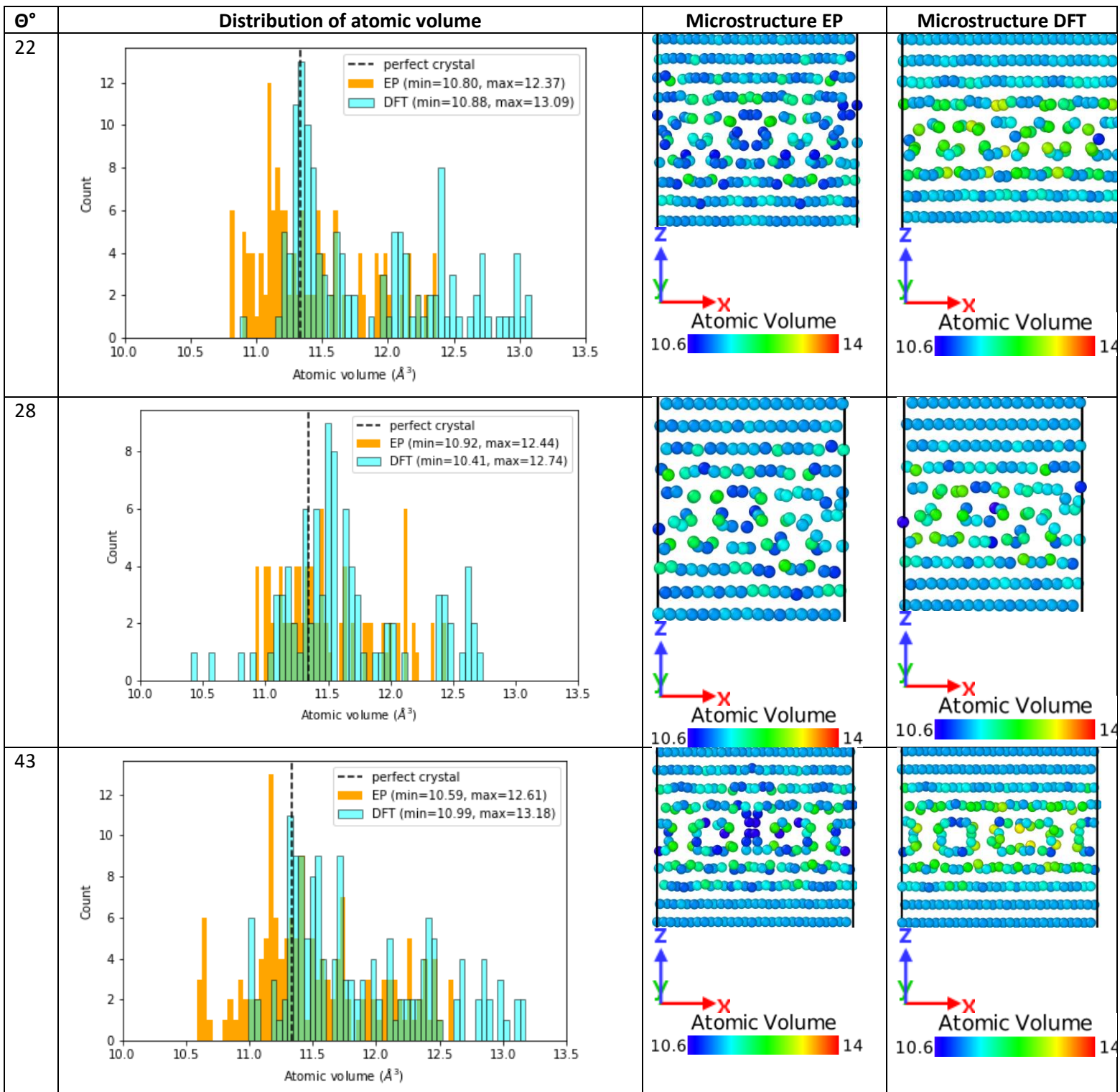


Figure III- 70: Atomic volume distribution and microstructure comparison between GB generated with EP Ackland and EP Marinica with **MQ_method**.

III-Annex 11: Atomic volume distribution comparison between GBs generated with MQ_method with EP Marinica and with EP Marinica then relaxed with DFT

The distributions presented here described the atomic volume distributions for atoms positioned near the GB plane: from -4 to 4 Å from the GB plane. The atomic volume corresponding to the bulk is indicated by black dotted lines. Atomic volume distributions associated to GBs relaxed with EP Marinica [80], [81] are represented in orange and those GBs relaxed with DFT with are coloured in cyan. The microstructures associated to these distributions are represented as a function of the misorientation angle in the two remains columns.



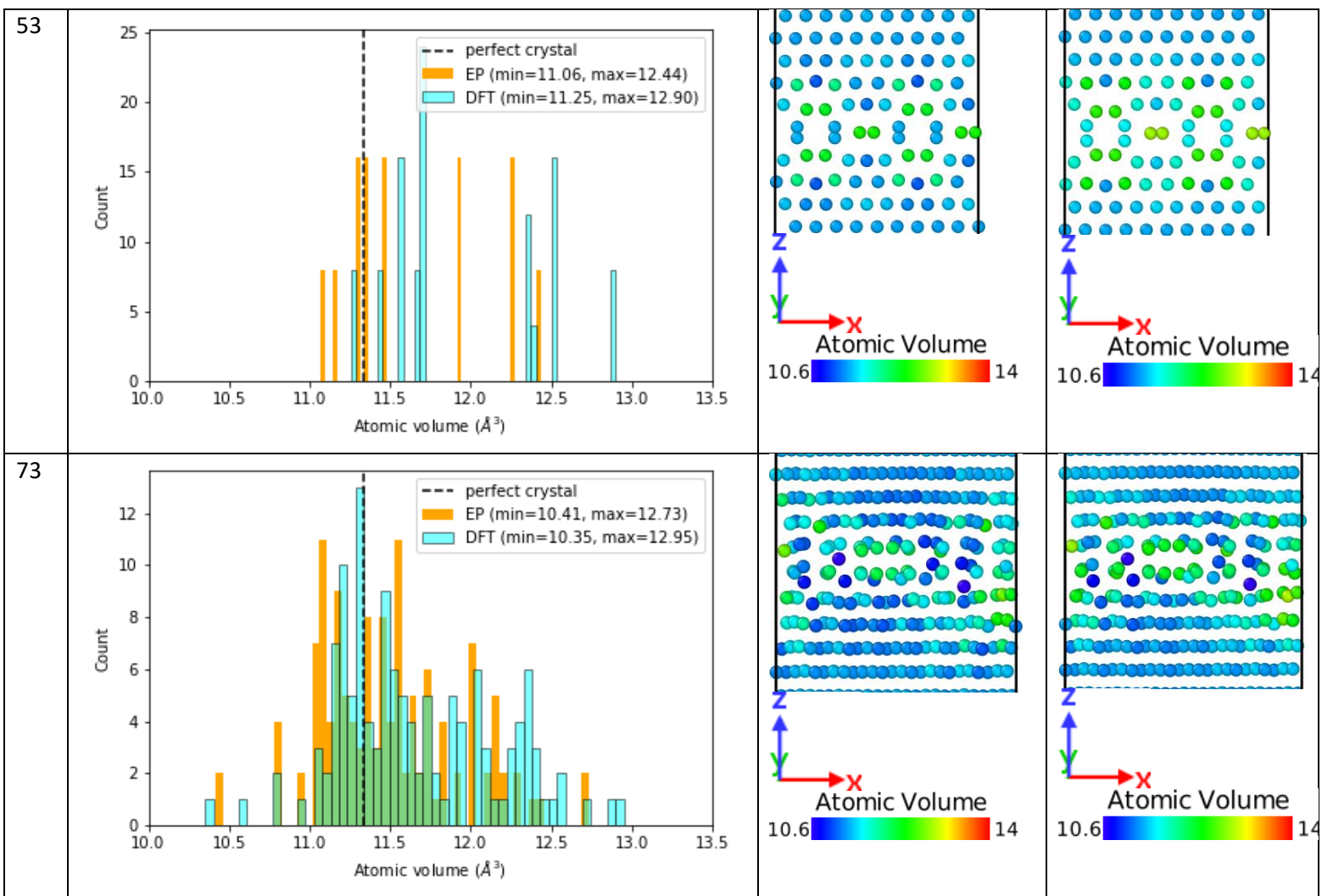
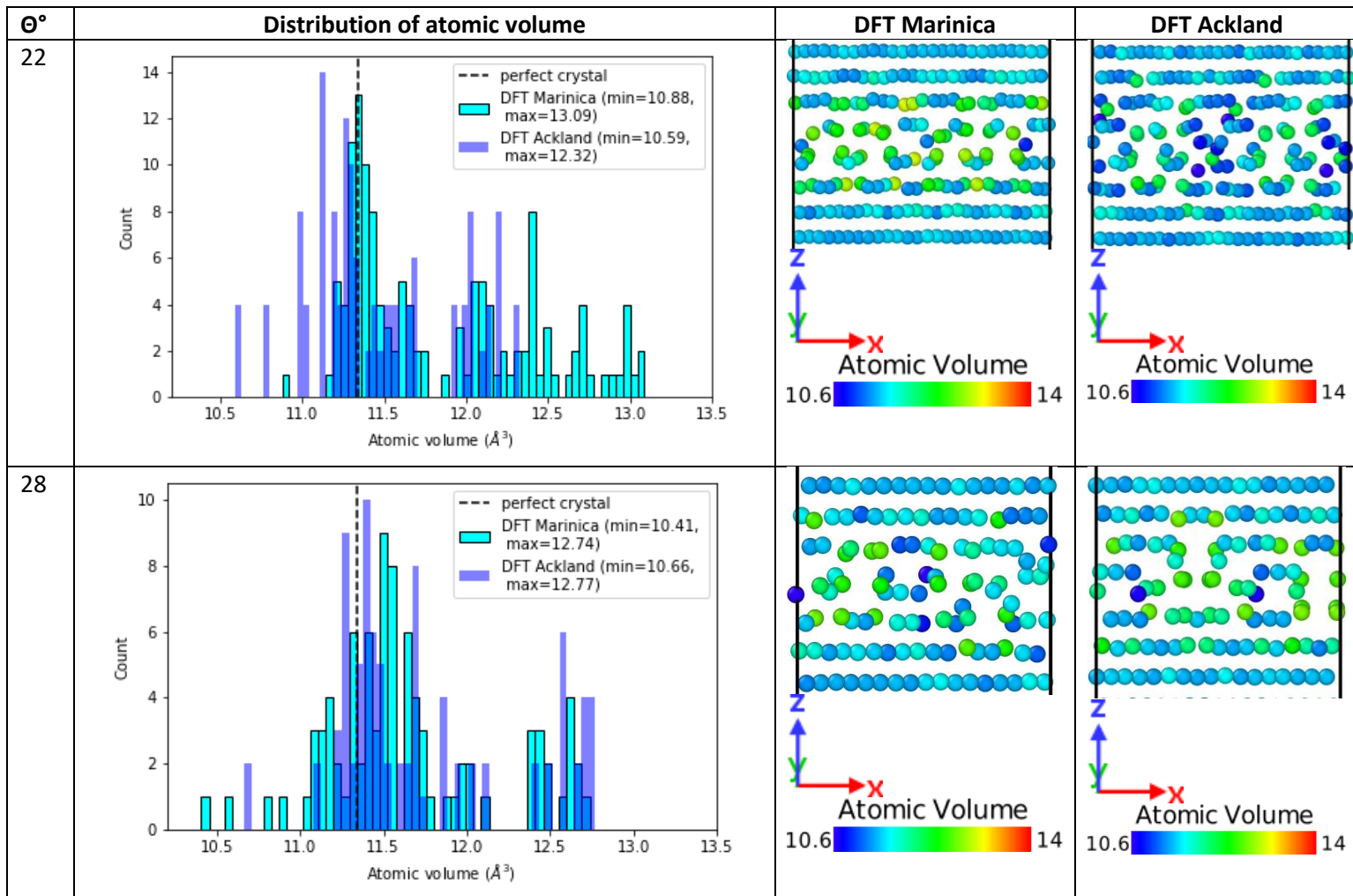


Figure III- 71: Atomic volume distribution and microstructure comparison between GBs generated with **MQ_method** with EP Marinica and with EP Marinica then relaxed with DFT.

III-Annex 12: Atomic volume distribution comparison between GBs generated with MQ_method with EP Ackland and then relaxed with DFT and with EP Marinica and then relaxed with DFT

The distributions presented here described the atomic volume distributions for atoms positioned near the GB plane: from -4 to 4 Å from the GB plane. The atomic volume corresponding to the bulk is indicated by black dotted lines. Atomic volume distributions associated to GBs initially relaxed with EP Marinica [80], [81] and then relaxed with DFT are represented in cyan and GBs relaxed with EP Ackland [70] then relaxed with DFT with are coloured in blue. The microstructures associated to these distributions are represented as a function of the misorientation angle in the two remains columns.



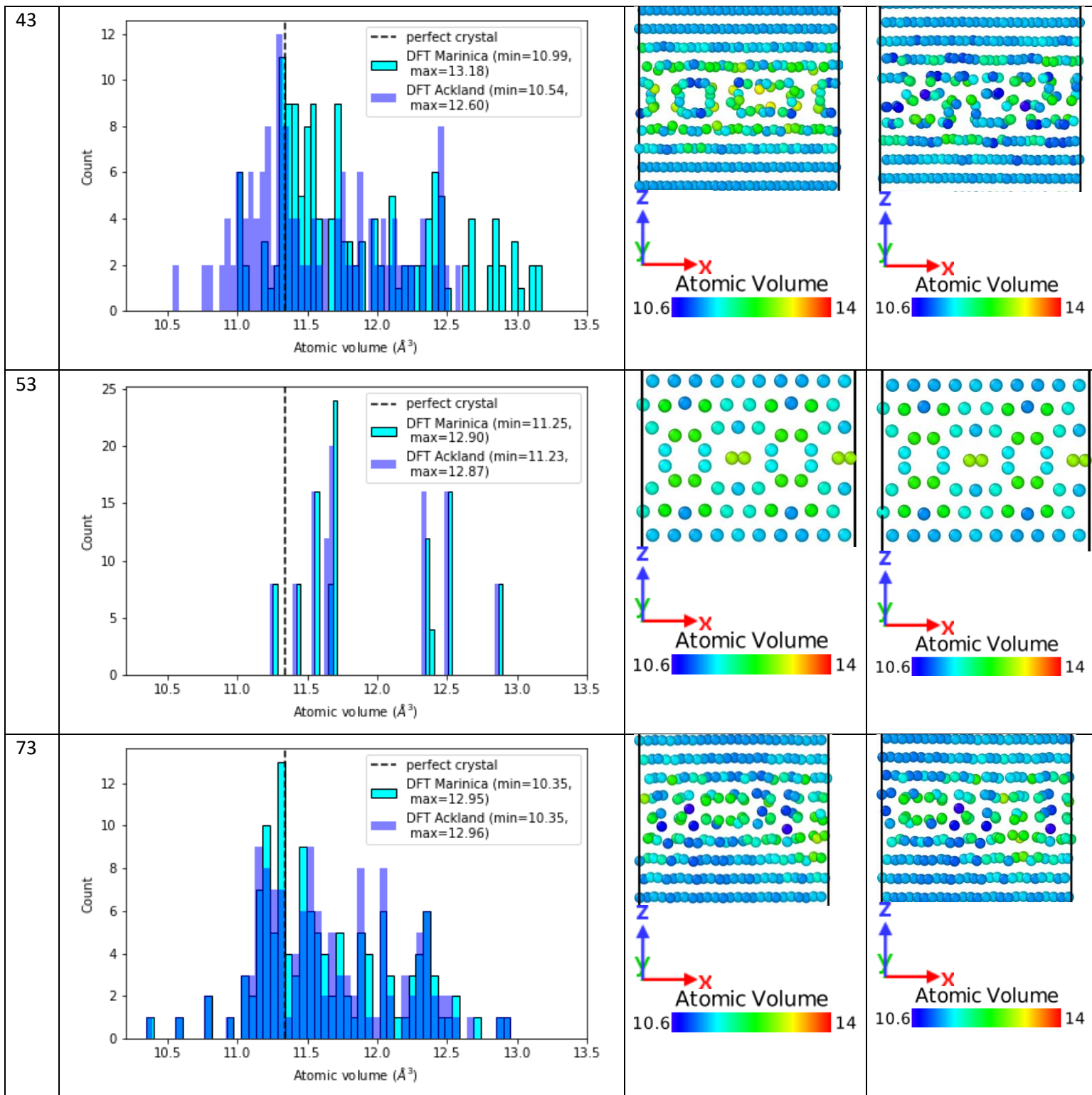


Figure III-72: Atomic volume distribution and microstructure comparison between GBs generated with **MQ_method** with EP Ackland and then relaxed with DFT and with EP Marinica and then relaxed with DFT.

IV-Annex 1: Experimental techniques used for the study of GBs

Studying the chemical composition of the GB and thus segregation requires both **experimental and computational investigations**. More than 30 years ago, **Hondros [1]** defined the necessary requirements for experimental techniques to provide accurate data about the chemical composition of GB:

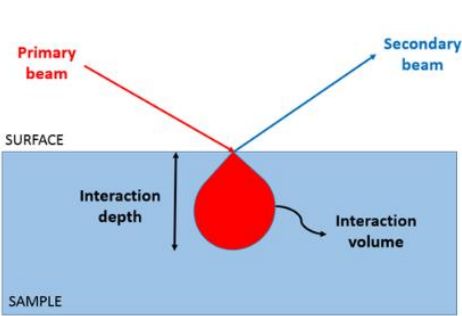
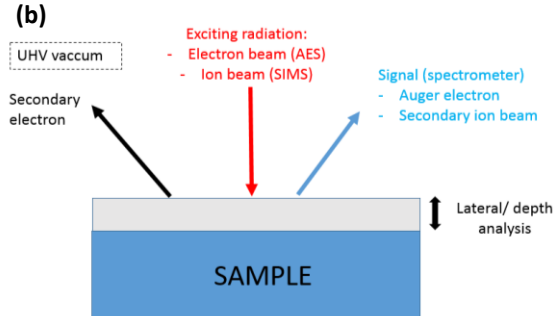
- High spatial and depth resolution
- Elemental detection and identification without a priori knowledge of segregating elements
- Quantitative measurement
- Non-exposure operation of a GB by fracture in order to study weakly embrittling as well as non-embrittling species
- Determination of the chemical binding of the segregating species

Based on these criteria, sophisticated **surface analysis and microscopic** techniques have been developed in the last decades.

- **Surface spectroscopic techniques** permit to evaluate the GB chemical composition and segregation. **AES GB analysis** is the most popular method that permits to quantify GB segregation of a specific chemical element. SIMS GB analysis principle is the same as AES analysis, but uses ions instead of electrons. This technique is more adapted for the analysis of molecules but its spatial resolution is lower than AES. Other spectroscopic techniques exist, but the principle remains the same. The only difference is the nature of the primary beam which interacts with the sample. These methods are limited by their spatial resolution which depends on the beam characteristics and GB composition. Moreover, there are **deconvolution problems** because of the complex shapes of the spectroscopic peaks, and to prepare the sample requires a destructive **fracture process**.
- **Non-destructive methods** can also be used: **microscopic techniques** permit characterization of GB and GB segregation. A primary beam is focused on the sample. Depending on its wavelength and the sample thickness, it is reflected or transmitted, giving rise to different imaging techniques. The analysis of electrons of the primary beam leads to **analytical electron microscopy (AEM): scanning electron microscopy (SEM)** methods extract surface topography and composition from reflected electrons of a sample whereas **transmitted electron microscopy (TEM)** method constitutes a more accurate technique in terms of spatial resolution and extracts crystal structure, morphology. These techniques are often **coupled with spectroscopic techniques** to extract at the same time the GB characteristics and chemical composition. Coupling with EBSD technique allows to get more accurate structural information about the orientation of the GB plane; coupling with EDXS technique allows to a quantification of the chemical composition using Cliff Lorimer equation.

Another method consists in evaporating atoms one by one with the help of an electrical field and reconstructing the volume. This technique is **the field ion microscopy (FIM)**, a 1-dimensional atomistic representation of the sample. This technique gave rise to the tomographic **atom probe tomography (APT)** which produces a 3-dimensional atomistic orientation representation of the sample. It provides chemical analysis of the atoms detected in the sample and gives access to the GB crystallography properties and chemical identity of individual atoms. However, APT results depend crucially on the curvature of the tip which influences the ion trajectory and the 3D reconstruction.

A more detailed description of these experimental techniques is developed in the following table.

Technique	Principle	GB features extracted	Limitations
Surface techniques	<p>A lot of surface techniques are based on the spectrometry of particles and rays emitted by the surface when excited. These methods rely on the emission of primary beams which interact with a sample characterised by a certain interaction volume and depth generating secondary beams (Figure a)</p> <p>(a) </p> <p>(b) </p> <p>Two main classes of these techniques are often used to characterise GB segregation: the Auger electron spectroscopy (AES) and the secondary ion mass spectroscopy (SIMS) (Figure b). Focusing electron or ion beam, in ultra-high vacuum (UHV) environment with a pressure on the order of 10^{-8} Pa, provides the emission of a characteristic Auger electron or secondary ion beam which can be recorded by a spectrometer to extract a chemical composition and quantification of the sample.</p> <p>Other spectroscopic techniques exist with their principles remaining the same, the only difference is the nature of primary beam which interacts with the sample (for example X-rays beam for X-ray photoelectron spectroscopy), or for ion spectroscopy techniques based on ion scattering (ISS), on the quantification method.</p> <p>-> The main drawback is the fracture process [2]–[4] necessary to prepare the GB sample: the GB sample can be damaged and not be representative of the real GB and in some cases, fracture of grain boundaries can be difficult to obtain.</p>		
AES: Auger electron microscopy	Focusing electron of in a 1 – 30 keV energy, recorded Auger electron.	Chemical quantification by Auger peak-to-peak heights standard method (APPHs). The height of a characteristic peak of an element corresponds to the number of Auger electrons homogeneously distributed in the analysis sample volume, which is proportional to its chemical element concentration.	<ul style="list-style-type: none"> - Fracture process [2]–[4] - Spatial resolution depends on the electron beam characteristics and GB composition [5] (10 - 100 nm [6]) - Concerns only the outermost atomic layers of a solid [7]: Auger electrons ejected from atoms located at depths greater than few atomic layers (4-50 nm) are absorbed in the material and do not contribute to the emitted line spectrum - Deconvolution problems because of the complex shape of the Auger peaks [6].

SIMS: Secondary ion mass spectroscopy	Focusing ion beam of energy in a range of 1-3 keV, recorded secondary ion beam.	Chemical quantification More adapted to the analysis of complexes, and molecules than AES More sensitive than AES,	<ul style="list-style-type: none"> - Fracture process [2]–[4] - Spatial resolution is lower than AES: on the order of 100 nm [8] even with high resolution imaging secondary ion mass spectrometry (HRI-SIMS) which allow to increase the resolution to about 20-50 nm [9]. - Spectra are more complicated to analyse than AES and the quantification of the data obtained requires to use standards.
--	--	---	--

Microscopic techniques	<p>Microscopic techniques are non-destructive techniques using a primary beam which is focused on the sample. Depending on its wavelength and the sample thickness, the primary beam is reflected or transmitted giving rise to different imaging techniques (Figure c).</p> <div data-bbox="331 835 1516 1283" data-label="Diagram"> </div> <p>To be able to distinguish at the nanoscale, one needs to use electrons for the primary beam leading to Analytical electron microscopy (AEM). AEM methods refer usually to two main techniques: scanning electron microscopy and Transmitted electron microscopy. The spatial resolution and the interaction volume of each technique are represented on figure (d).</p> <p>These techniques are often coupled to a surface technique (spectroscopic technique) to extract at the same time the GB characteristics and chemical composition: the most used techniques are the energy dispersive X-ray spectroscopy (EDXS) measuring the energy released during the sample relaxation via the emission of a characteristic photon and the electron energy loss spectroscopy (EELS) measuring the electron energy loss once transmitted through the sample. EDXS permits to get a qualitative fast overview of the sample composition, the whole energy range of interest (signal) is recorded whereas EELS does not cover a sufficient energy range to detect all elements present. Moreover, EDXS is simple to use: the data is easily interpretable compared to EELS because of the problem of background arising from non-elastic scattering for EELS. Therefore, EDXS is the often used technique to study the GB segregation [10]. The relative concentration between two elements from the integrated EDXS peak intensities, for a binary or a multicomponent system, is given by the Cliff-Lorimer equation [11]</p>		
-------------------------------	--	--	--

	<p>Moreover, Electron Backscatter Diffraction (EBSD) technique can be coupled with AEM techniques to get more accurate structural information about the orientation of the GB plane. <i>EBSD camera records the incident beam diffracted by crystal plane. If backscattered electrons satisfy the Bragg's law for a given plane, two diffracting large cones are formed. The cones intersecting the screen involve the formation of numerous thin bands (called EBSD pattern) which refers to the Kikuchi lines. These patterns correspond to the projections of the geometry of the lattice planes in the crystal and permit to access the structure and crystallographic orientation of the sample. Then, the EBSD algorithm indexes the lines and thus, creates a crystal orientation map by a comparison of the observed lines with the theoretical Kikuchi lines database</i></p> <p>Another microscopic method consists in evaporating atoms one by one with the help of an electrical field and reconstructing the volume. This technique is the field ion microscopy (FIM) which gave rise to the tomographic atom probe tomography (APT).</p>		
<p>SEM: Scanning electron microscopy</p>	<p>Analyses reflected electrons (elastically scattered interaction between the sample and the electron beam).</p> <p><i>Samples are positioned at the bottom of the electron column and the scattered electrons are captured by electron detectors. Photomultipliers then convert this signal into an electric signal.</i></p>	<p>Chemical composition</p> <p>Surface topography</p>	<p>Spatial resolution limited in comparison with TEM (0.5 nm) [12]</p>
<p>TEM: Transmitted electron microscopy</p>	<p>Analyses the transmitted electrons.</p> <p><i>The sample image is created from the interaction of the electrons with the sample as the beam is transmitted through the specimen. Electrons passing through the sample and through a strong magnetic field that acts as a series of intermediate and projector lenses below the sample, create a picture on a fluorescent screen or by a sensor via a charge-coupled device (CCD) camera, onto a PC screen, before they are collected.</i></p>	<p>Information about the inner structure such as the crystallography, morphology and stress state as well as the defects.</p>	<ul style="list-style-type: none"> - Spatial resolution (50 pm) - Requires thin enough samples - Preparation of the samples with the Focused ion beam technique [13] remains difficult and time consuming; noise is present for each spectrum measurement because of small shifts of the sample, which leads to an underestimated GB segregation. - Compromise between the probe size, the intensity of electron beam and the spatial resolution has to be found. The increased intensity of the probe enhances the electron count but could involve a destruction or transformation of the sample and difficulties to focus the probe.

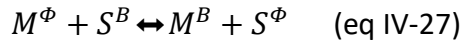
HRTEM: High resolution TEM	<p style="text-align: center;">Same features as TEM but higher spatial resolution (Figure d)</p> <p><i>A symmetrical multi-beam illumination is applied on the sample, the transmitted and diffracted beams pass through a large objective aperture which create interferences between the transmitted and diffracted beam. Both direct and diffracted electron waves are used to form the image leading to a much higher resolution.</i></p>		
<p>AP-FIM: Atom-probe field ion microscopy and Atom-probe tomography ATP</p> <p><i>AP-FIM gives a 1-dimensional atomistic representation of the sample, whereas the improvement of APT device leads to more accurate results and a 3-dimensional atomistic orientation representation.</i></p>	<p>Relies on ionization and subsequent field evaporation of individual atoms/atomic clusters from a specimen surface.</p> <p><i>The field ion microscope [14], [15] is constituted of a ultra high vacuum (UHV) chamber, where the sample of interest, in the form of a sharp tip is placed. This tip is maintained at extremely low temperature, around 5-80 K, to obtain a high spatial resolution. Then, an electric positive potential (5-10 kV) is applied at the surface of the tip, in front of a screen. An inert gas is introduced in the chamber, called "image gas", and atoms of this inert gas (helium or neon) are subsequently ionized. A strong ionisation field is thus created, which corresponds to the field induced by the removal of an electron from the outer shell of the gas atom to an empty energy level at the metal surface, via electron tunnelling. The probability of an electron to overcome the energy barrier, which leads to ionisation depends on the relative width of the potential barrier. Then each imaging-gas ion that strikes the tip, is exposed to this intense electric field surrounding the tip. The electric field accelerates the ions which are ejected from the positively charged surface formed by the sharp tip surface to the microscope chamber and eventually strikes a screen which is equipped with a detection system and provides thus a magnified 2D reconstruction of the sample surface</i></p>	<p>Chemical quantification of atoms.</p> <p>GB misorientation angle can be measure with Transmission Kikuchi Diffraction mapping (TKD)</p>	<p>Curvature of the tip influences the ion trajectory and the 3D reconstruction.</p> <p>Atomic concentrations measured with APT are expressed as atomic averages.</p>

**The most common used techniques are indicated in orange*

- [1] E. D. Hondros, « Grain boundary segregation assessment of investigative techniques », in *Grain Boundary Structure and Properties*, London: G.A. Chadwick, D.A. Smith, 1976, p. 265-298.
- [2] P. Lejcek, M. Koutnik, J. Bradler, V. Paidar, et A. Potmesilova, « Anisotropy of grain boundary segregation in as-grown Fe-6at%Si alloy bicrystals », *Applied Surface Science*, vol. 44, p. 75-86, 1990.
- [3] P. Lejcek, J. Bradler, et V. Paidar, « Segregation at the {013} symmetrical tilt grain boundary in dilute Fe-Si alloy bicrystals », *Journal of Materials Science*, vol. 22, p. 3974-3982, 1987.
- [4] P. Lejcek et S. Hofmann, « The effects of the fracture surface on the measurements of grain-boundary segregation by AES », *Journal of Materials Science Letters*, vol. 7, p. 646-648, 1988.
- [5] M. M. El Gomati et M. Prutton, « Monte Carlo calculations of the spatial resolution in a scanning auger electron microscope », *Surface Science*, vol. 72, p. 485-494, 1978.
- [6] F. Reiners et C. Tewell, « New improvements in energy and spatial (x, y, z) resolution in AES and XPS application », *Journal of Electron Spectroscopy and Related Phenomena*, vol. 142, p. 1-25, 2005.
- [7] M. P. Seah, « Grain boundary segregation », *J. Phys. F: Metal Phys.*, vol. 10, p. 1043-1064, 1980.
- [8] P. E. J. Flewitt et R. K. Wild, *Grain Boundaries: Their Microstructure and Chemistry*. 2001.
- [9] K. L. Gavrilov, S. J. Bennison, K. R. Mikeska, et R. Levi-Setti, « Grain boundary chemistry of alumina by high-resolution imaging SIMS », *Acta Metallurgica*, vol. 47, p. 4031-4039, 1999.
- [10] H. Müllejans et J. Bruley, « Electron energy-loss spectroscopy (EELS); comparison with X-ray analysis », *Journal de Physique IV Colloques*, vol. 03, p. C7-2083-C7-2092, 1993.
- [11] G. Cliff et G. W. Lorimer, « The quantitative analysis of thin specimens », *Journal of Microscopy*, vol. 103, p. 203-207, 1975.
- [12] D. B. Williams et C. B. Carter, *Transmission Electron Microscopy A Textbook for Material Science*. 1986.
- [13] J. Mayer, L. A. Giannuzzi, T. Kamino, et J. Michael, « TEM Sample Preparation and FIB Induced Damage », *MRS Bulletin*, vol. 32, p. 400-407, 2017.
- [14] A. Merand, C. Martin, et J. Gallot, « Réalisation d'un microscope ionique à champ », *Revue de Physique Appliquée*, vol. 7, p. 177-180, 1972.
- [15] B. Gault, M. P. Moody, J. M. Cairney, et S. P. Ringer, « Atom probe crystallography », *Materials today*, vol. 15, p. 378-386, 2012.

IV-Annex 2: Derivation of the general Langmuir-McLean isotherm for regular binary solutions

Segregation is viewed as an exchange between component M and S at the interface Φ and the bulk B:



This exchange is associated to an **enthalpy of "reaction"** ΔG_r . This quantity can be expressed as the change of the free energy that can be absorbed or released due to the change of the particle number M and S between the bulk and the interface which corresponds to the difference of chemical potentials of M and S at the interface and in the bulk.

$$\Delta G_r = (\mu_S^\Phi + \mu_M^B) - (\mu_S^B + \mu_M^\Phi) \quad (\text{eq IV-28})$$

where μ_j^x is the chemical potential of atom j (M or S) in x phase (in Φ or B) which can be expressed as a function of standard chemical potential at temperature T $\mu_j^{x,0}$ corresponding to the chemical potential of the pure component and as a function of the activity of the compound a_j^x in the different phases.

$$\mu_j^x = \mu_j^{x,0} + RT \ln(a_j^x) \quad (\text{eq IV-29})$$

The total number of particles of components M and S has to be conserved between the bulk and the interface, therefore the change of particle number at the interface must be the same as in the bulk. The equilibrium condition of both elements M and S leads to equations:

$$\mu_M^B = \mu_M^\Phi \text{ and } \mu_S^B = \mu_S^\Phi \quad (\text{eq IV-30})$$

The basic conditions for the chemical equilibrium between the interface (GB) and the bulk for species M and S are given by

$$\Delta G_r = 0 :$$

$$\begin{aligned} \mu_M^B + \mu_S^\Phi &= \mu_M^\Phi + \mu_S^B \\ (\mu_S^{\Phi,0} + \mu_M^{B,0}) - (\mu_S^{B,0} + \mu_M^{\Phi,0}) + RT[(\ln(a_S^\Phi) + \ln(a_M^B)) - (\ln(a_S^B) + \ln(a_M^\Phi))] &= 0 \\ \Rightarrow \Delta G_S^0 + RT \ln\left(\frac{a_S^\Phi a_M^B}{a_M^\Phi a_S^B}\right) &= 0 \end{aligned}$$

$$\text{Where } \Delta G_S^0 = (\mu_S^{\Phi,0} + \mu_M^{B,0}) - (\mu_S^{B,0} + \mu_M^{\Phi,0})$$

$$\Rightarrow -\frac{\Delta G_S^0}{RT} = \ln\left(\frac{a_S^\Phi a_M^B}{a_M^\Phi a_S^B}\right) \Rightarrow \frac{a_S^\Phi}{a_M^\Phi} = \frac{a_S^B}{a_M^B} e^{-\frac{\Delta G_S^0}{RT}} \quad (\text{eq IV-31})$$

Activities which corresponds to a measure of the "effective concentration" of species, can be replaced by concentrations, where γ_j^x are the activity coefficients, and X_j^x are the concentration for components j at the interface or in the bulk.

Since $a_j^x = \gamma_j^x X_j^x$

$$\frac{X_S^\Phi X_M^B}{X_M^\Phi X_S^B} = \frac{\gamma_S^\Phi \gamma_M^B}{\gamma_M^\Phi \gamma_S^B} e^{-\frac{\Delta G_S^0}{RT}} \quad (\text{eq IV-32})$$

The interfacial excess is represented by the effective concentration of species, associated to their activity coefficients. The extra contribution of interfaces with respect to the bulk can be quantified by the excess Gibbs free energy ΔG_S^E which is expressed as $RT \ln \left(\frac{\gamma_S^\Phi \gamma_M^B}{\gamma_M^\Phi \gamma_S^B} \right)$

For a regular binary dilute solid solution with an ideal random distribution of different species (ideal entropy mixing), the activity coefficients are equal to 1, for all species both at the interface and in the bulk. All substitutional sites are occupied by an atom of type S when saturation is reached. Thus, the classical Langmuir-McLean isotherm is retrieved and $\Delta G_S^E = 0$

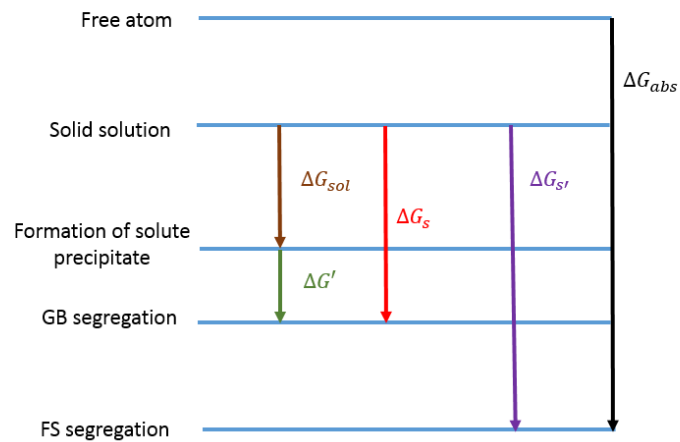
As

$$\frac{X_S^\Phi}{1-X_S^\Phi} = \frac{X_S^B}{1-X_S^B} e^{-\frac{(\Delta G_S^0 + \Delta G_S^E)}{RT}} \quad (\text{eq IV-33})$$

ΔG_S^0 is the Gibbs standard free energy which corresponds to free enthalpy when one solute atom replaces another.

ΔG_S^E is the Gibbs excess free energy which represents the surface excess of the solute with respect to bulk concentration: the interfacial enrichment. It corresponds to the deviation between ideal and real behaviour of any thermodynamic system due to the presence of a GB which can be considered as a defect in the crystal lattice.

IV-Annex 3: Solubility limit Seah and Hondros model



Schematic free energy diagram for the solute atoms, showing the relation between adsorption ΔG_{abs} at a free surface, free surface segregation $\Delta G_{s'}$, GB segregation ΔG_s and solubility ΔG_{sol} [1], [2]

[1] P. A. Dowben et A. Miller, *Surface Segregation Phenomena*, CRC Press. 1990.

[2] E. D. Hondros et M. P. Seah, *Interfacial and surface microchemistry in Physical Metallurgy*, RW Cahn and P. Haansen., vol. 856. 1983.

IV-Annex 4: Derivation of Lejcek model

At the solubility limit X_S^* , the chemical potential μ_S^* of the solute S is related to its activity a_S^* i.e. the effective concentration of solute as:

$$\mu_S^* = \mu_S^{0gb} + RT \ln(a_S^*) \quad (\text{eq IV-34})$$

where μ_S^{0gb} is the standard chemical potential at the GB, and a_S^* is the activity at the solute solubility limit which is expressed as an empirical law:

$$a_S^* = (X_S^*)^\lambda \quad (\text{eq IV-35})$$

where λ is a constant describing the non-ideality of binary systems with the same matrix element M at the solute solubility limit X_S^* , adjusted to fit experimental results.

The Gibbs free energy segregation of the solute at the solubility limit is then given by:

$$\Delta G_S^* = (\mu_S^{0\Phi} - \mu_S^*) - (\mu_M^{0\Phi} - \mu_M^{0B}) = \Delta G_S^0 - RT \ln(a_S^*) \quad (\text{eq IV-36})$$

Thus, the standard segregation energy is expressed as:

$$\Delta G_S^0 = \Delta G_S^* + RT \ln(a_S^*) = \Delta H_S^* - T \Delta S_S^* + RT \ln(a_S^*) \quad (\text{eq IV-37})$$

The segregation entropies ΔS_S^* and ΔS_S^0 can be written as:

$$\Delta S_S^* = \left(\frac{\partial \Delta G_S^*}{\partial T} \right)_{P, X_S^B} \quad \Delta S_S^0 = \left(\frac{\partial \Delta G_S^0}{\partial T} \right)_{P, X_S} \quad (\text{eq IV-38})$$

Combining equation (IV-37) and (IV-38) leads to:

$$\Delta S_S^* = \Delta S_S^0 - R \left(\frac{\partial [T \ln a_S^*]}{\partial T} \right)_{P, X_S} \quad (\text{eq IV-39})$$

$$\text{Or } \Delta S_S^* = \Delta S_S^0 - \lambda R \left(\frac{\partial [T \ln X_S^*]}{\partial T} \right)_{P, X_S} \quad (\text{eq IV-40})$$

The entropy is expressed as a sum of two terms i.e. the configurational entropy (standard entropy) ΔS_S^0 and an entropy term depending on the activity relative to the solubility limit of the solute in the solid solution.

Lejcek *et al* [1] showed for different solutes in Fe, the term $[T \ln X_S^*]$ is approximately constant with the temperature as shown on **Figure IV- 31**,

$$\left(\frac{\partial [T \ln X_S^*]}{\partial T} \right)_{P, X_S} = 0 \quad (\text{eq IV-41})$$

$\Delta S_S^* \approx \Delta S_S^0$ and

$$\Delta H_S^0 = \Delta H_S^* + RT \ln(a_S^*) = \Delta H_S^* + \lambda RT \ln(X_S^*) \quad (\text{eq IV-42})$$

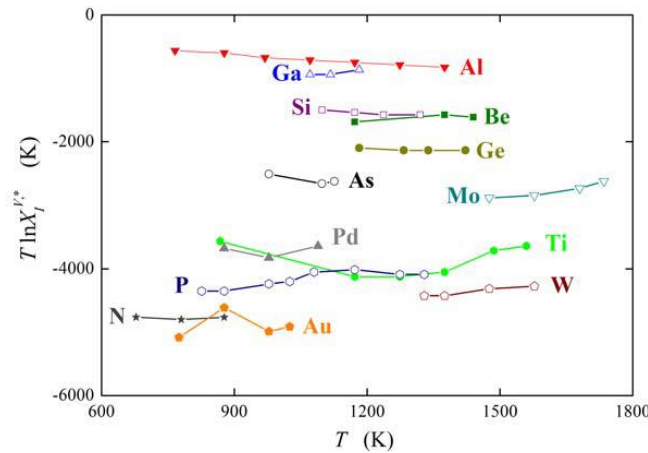


Figure IV- 31: Temperature dependence $[T \ln X_S^*]$ of the product for various solutes in α -iron [1]

Extrapolating equation (IV-42) to $X_S^* \rightarrow 1$, gives $[T \ln X_S^*] \rightarrow 0$ and

$$\Delta H_S^0(\Phi, X_S^*) = \Delta H_S^*(\Phi, X_S^* = 1) + RT \ln(a_S^*) = \Delta H_S^* + \omega RT \ln(X_S^*) \quad (\text{eq IV-43})$$

where $\Delta H_S^*(\Phi, X_S^* = 1)$ is the structurally dependent segregation enthalpy of a soluble solute in a matrix M characterised by the parameter ω which is expressed in what follows as $\Delta H_{\text{CSS}}^*(\Phi)$.

To tackle the entropy issue, Lejcek *et al* [1] have developed a concept to estimate the standard segregation entropy ΔS_S^0 from experimental data. Segregation is characterized by a change of the free energy $\Delta G(\Omega_j)$, that depends on N independent intensive variables Ω_j (concentration, magnetic field, specific defect energy, solubility ...):

$$d\Delta G_S^0 = \sum_{j=1}^N \left(\frac{\partial \Delta G}{\partial \Omega_j} \right) \partial \Omega_j \quad (eq IV-44)_{T,P,\Omega_j \neq \Omega_I}$$

The same applies to enthalpy and entropy:

$$d\Delta H_S^0 = \sum_{j=1}^N \left(\frac{\partial \Delta H}{\partial \Omega_j} \right) \partial \Omega_j \quad (eq IV-45)_{T,P,\Omega_j \neq \Omega_I}$$

and

$$d\Delta S_S^0 = \sum_{j=1}^N \left(\frac{\partial \Delta S}{\partial \Omega_j} \right) \partial \Omega_j \quad (eq IV-46)_{T,P,\Omega_j \neq \Omega_I}$$

They define a temperature T_{CE} at which no change of $d\Delta G_S^0$ with a change of Ω_j takes place i.e. $d\Delta G_S^0 = 0$:

$$T_{CE} = \frac{d\Delta H_S^0}{d\Delta S_S^0} = \frac{\sum_{j=1}^N \left(\frac{\partial \Delta H}{\partial \Omega_j} \right) \partial \Omega_j}{\sum_{j=1}^N \left(\frac{\partial \Delta S}{\partial \Omega_j} \right) \partial \Omega_j} \quad (eq IV-47)_{T,P,\Omega_j \neq \Omega_I}$$

A linear relationship between the segregation entropy and enthalpy emerges from the integration of (47): **the enthalpy-entropy compensation effect** [2] [3] [4], which leads to

$$\Delta S_S^0 = \frac{\Delta H_S^0}{T_{CE}} + \Delta S' \quad (eq IV-48)$$

where ΔH_S^0 is the standard enthalpy of segregation which depends on the nature of the solute, ΔS_S^0 the standard entropy, $\Delta S'$ the integration constant and T_{CE} the temperature limit related to a change of the slope of the enthalpy-entropy compensation effect. Its value is around 900 K for ferritic iron.

Figure IV- 32 highlights the linear relationship between segregation entropy and enthalpy as well as the impact of the nature of the segregation sites (substitutional or interstitial) as shown by the split into two branches, one for substitutional segregating solutes and the other for interstitial segregating solutes. One needs thus to be careful when using this compensation effect that one single segregation mechanism is active.

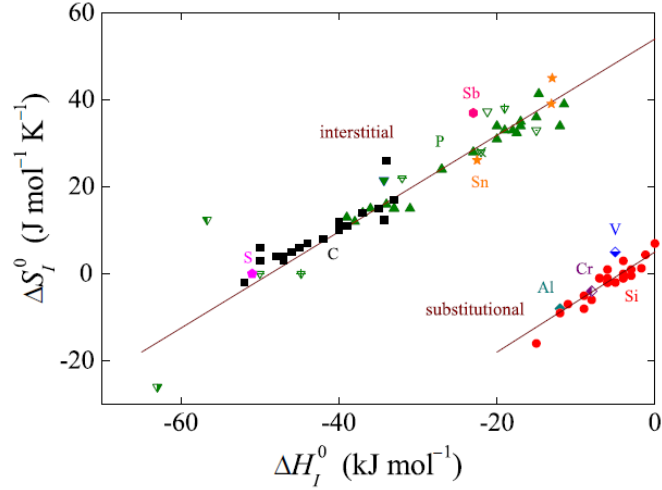


Figure IV- 32: Enthalpy-entropy compensation effect for GB segregation in alpha-Fe. Full symbols the segregation at individual GB, other symbols are literature data for polycrystalline alpha-Fe [5]

The determination of $\Delta S'_S$ and $\Delta H'_S$ by experimental or computational methods permit to Lejcek *et al* to determine first ΔH_{CSS}^* and secondly $\Delta S'_S$, by fitting experimental and computational data. They express the dependence of $\Delta S'_S$ on the segregation site and solubility limit as:

$$\Delta S'_S(\Phi, site, X_S^*) = \left[\Delta S^{0,CE}(\Phi, site) + \frac{\Delta H_{CSS}^*(\Phi)}{T_{CE}} \right] + \frac{\omega R}{T_{CE}} [T \ln X_S^*(T)] \quad (\text{eq IV-49})$$

where site refers to the type of the segregation site (interstitial or substitutional), Φ corresponds to the GB orientation, and X_S^* is the solute solubility limit in the matrix. $\Delta S^{0,CE}$ corresponds to $\Delta S'_S$ the standard entropy associated to a given T_{CE} and ΔH_{CSS}^* is the standard enthalpy of the segregation of a completely soluble solute. **For an interstitial segregation in iron** $\Delta S^{0,CE}$ is equal to 56 J/(mol.K) and for substitutional segregation in iron $\Delta S^{0,CE}$ is lower and equal to 5 J/(mol.K) at $T_{CE} = 930K$. ΔH_{CSS}^* varies with the GB character: a lower value corresponds to highly segregated general GBs while a higher value corresponds to the special GBs characterized by a low segregation level.

- [1] P. Lejcek, L. Zheng, S. Hofmann, et M. Sob, « Applied Thermodynamics: Grain Boundary Segregation », *Entropy*, vol. 16, p. 1462-1483, 2014.
- [2] P. Lejcek, P. Sandrera, J. Hornikova, P. Rehak, et J. Pokluda, « Grain boundary segregation of elements of 14 and 15 and its consequences for intergranular cohesion of ferritic iron », *Journal of Materials Science*, vol. 52, p. 5822-5834, 2017.
- [3] Y. Zhao, S. Song, H. Si, et K. Wang, « Effect of Grain Size on Grain Boundary Segregation Thermodynamics of Phosphorus in Interstitial-Free and 2.25Cr-1Mo Steels », *Metals*, vol. 7, p. 470, 2017.
- [4] P. Lejcek, « Recent trends and open questions in grain boundary segregation », *Materials Research Society*, vol. 33, n° 18, p. 2647-2660, 2018.
- [5] P. Lejcek et S. Hofmann, « Interstitial and substitutional solute segregation at individual grain boundaries of alpha-iron: data revisited », *J. Phys. : Condens. Matter*, vol. 28, p. 064001-064010, 2016.

IV-Annex 5: Microscopic techniques and ATP, GB segregation quantification methods and uncertainties.

1. Microscopic techniques: GB and GB segregation characterisation

Microscopic techniques use a primary beam which is focused on the sample. Depending on its wave length and the sample thickness, it is reflected or transmitted giving rise to different imaging techniques.

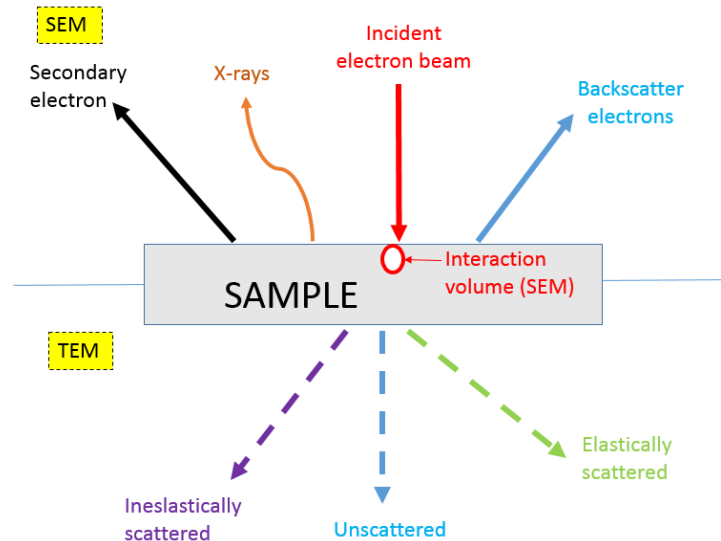


Figure IV- 33: Type of scattering events when a primary-beam electron collides with a sample.

To be able to distinguish at the nanoscale, one needs to use electrons for the primary beam leading to Analytical electron microscopy (AEM). These techniques are often coupled to a surface technique (spectroscopic technique) to extract at the same time the GB characteristics and chemical composition.

Another method consists in evaporating atoms one by one with the help of an electrical field and reconstructing the volume. This technique is the field ion microscopy (FIM) which gave rise to the tomographic atom probe tomography (APT).

1.1. Analytical electron microscopy (AEM)

1.1.1 AEM basic principles

Analytical electron microscopy (Figure IV- 33) relies on focusing a primary high energetic, 100-1000 keV, electron beam on a sample, where numerous interactions of electrons with the sample volume currently known as the **interaction volume (Figure IV- 34)** take place.

The electrons lose energy by repeated random scattering and absorption within the volume of the specimen and can be deviated from their original trajectory. Two main exchange energy interaction mechanisms, based on **electron scattering (Figure IV- 34)** occur:

- Reflection of high energy electrons by **elastic scattering**: the total kinetic energy of the system is conserved; thus, the internal states of each electron remain unchanged. There is no energy loss of electrons but the interaction with other particles can shift the electron direction of propagation.
- Emission of secondary electrons by **inelastic scattering**: in contrast to elastic scattering, the internal state of electrons has changed, and some energy of the incident electron is lost. Thus, inelastically scattered electrons generally have a low scattering angle while elastically scattered electrons refer to much higher scattering angles.

As a consequence, the size of the interaction volume depends on the electron landing energy, the atomic number of the specimen and the specimen density.

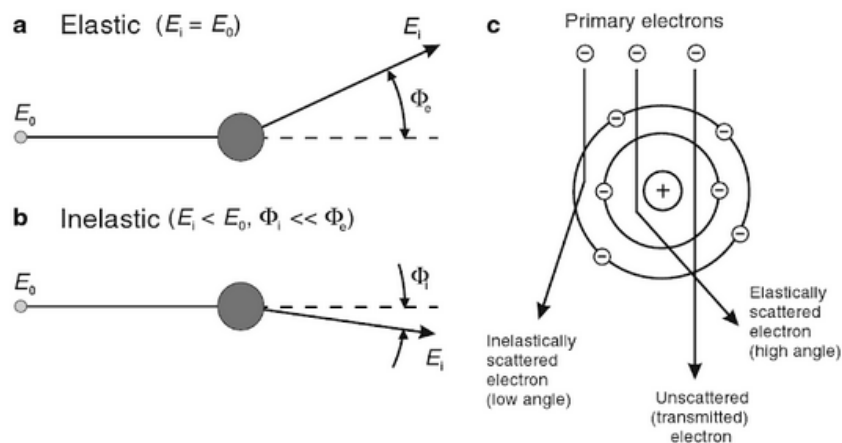


Figure IV- 34: (a) Elastic and inelastic scattering comparison. E_0 refers to the energy of the incident electron, E_i corresponds to the energy of the electron after scattering, Φ_e is the elastic scattering angle and Φ_i is the inelastic scattering angle. (b) Schematic drawing of electron scattering mechanism within an atom [1]

AEM methods refer usually to two main techniques: **scanning electron microscopy** and **Transmitted electron microscopy**:

- **Scanning electron microscopy (SEM)** permits to analyse reflected electrons (elastically scattered interaction between the sample and the electron beam). Samples are positioned at the bottom of the electron column and the scattered electrons are captured by electron detectors. Photomultipliers then convert this signal into an electric signal. This technique **provides information on the sample surface topography and composition**
- **Transmitted electron microscopy (TEM)** analyses the transmitted electrons. The sample image is created from the interaction of the electrons with the sample as the beam is transmitted through the specimen. A monochromatic beam of electrons is accelerated through a potential of 40 to 100 kilovolts (kV).

Electrons passing through the sample and through a strong magnetic field that acts as a series of intermediate and projector lenses below the sample, create a picture on a fluorescent screen or by a sensor via a charge-coupled device (CCD) camera, onto a PC screen, before they are collected.

The spatial resolution is considerably improved compared to SEM (50 pm while 0.5 nm for SEM) with respect to the size of the beam specimen and the interaction volume which is expected to be lower than that of SEM (**Figure IV- 35**). **TEM provide information about the inner structure such as the crystallography, morphology and stress state as well as the defects.**

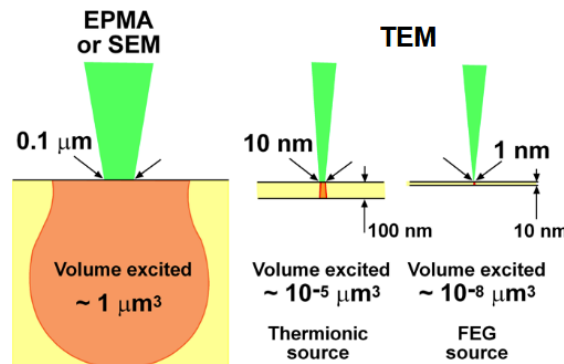


Figure IV- 35: Comparison of the relative size of the beam-specimen and interaction volume in SEM and TEM techniques [2]

TEM is a good choice to study possible structural defects like GB in iron steels and solutes and impurities on GB.

To improve the resolution, **High resolution TEM (HRTEM) imaging** has been developed: a symmetrical multi-beam illumination is applied on the sample, the transmitted and diffracted beams pass through a large objective aperture which create interferences between the transmitted and diffracted beam. Both direct and diffracted electron waves are used to form the image leading to a much higher resolution.

The multi-beam illumination accounts for higher spatial frequencies and thus reaches a **higher spatial resolution**. Only electrons scattered at small angles and without loss of energy are taken into account in HRTEM images, but those with significant energy loss and which have been scattered at a high angle contain also significant information about the sample. Furthermore, recently, the advances in aberration correction have been able also to reduce spherical aberrations to achieve an improved spatial resolution [3]–[5]. In 2008, the highest point resolution realised in phase contrast TEM was around 0.050 nm according to Kisielowski *et al.* [6]

AEM methods can be equipped **with Electron Backscatter Diffraction (EBSD) camera** which provide access to GB plan orientation. It records the incident beam diffracted by crystal plane. If backscattered electrons satisfy the Bragg’s law for a given plane, two diffracting large cones are formed. The cones intersecting the screen involve the formation of numerous thin bands

(called EBSD pattern) which refers to the Kikuchi lines (**Figure IV- 36**Figure IV- 36: The formation of Kikuchi lines and the electron backscatter diffraction pattern.).

These patterns correspond to the projections of the geometry of the lattice planes in the crystal and permit to access the structure and crystallographic orientation of the sample. Then, the EBSD algorithm indexes the lines and thus, creates a crystal orientation map by a comparison of the observed lines with the theoretical Kikuchi lines database

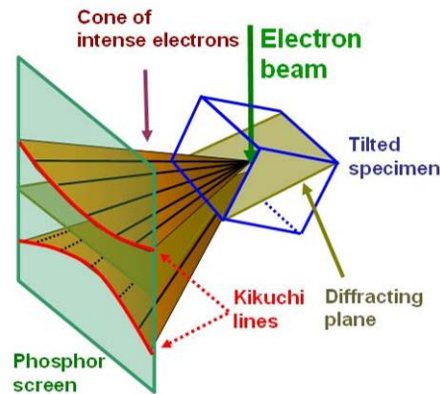


Figure IV- 36: The formation of Kikuchi lines and the electron backscatter diffraction pattern.

1.1.2 GB segregation/chemical composition characterisation

Various signals generated following the inelastic interaction of the incident electron beam with the sample can be used to identify and quantify the concentration of the elements present in the sample.

AEM methods can be combined with highly localised analytical tools based on the detection of X-ray signals such as the electron energy loss spectroscopy (EELS) or the energy dispersive X-ray spectroscopy (EDXS) (**Figure IV- 37**):

- **EDXS** measuring the energy released during the sample relaxation via the emission of a characteristic photon
- **EELS** measuring the electron energy loss once transmitted through the sample. The main electrons pass through the sample without losing energy. The remaining fraction of electrons undergo inelastic scattering, lose energy as they interact with the sample and leave the sample in an excited state. The energy and momentum of these electrons change permit to detect them with a spectrometer and give rise to the electron energy loss signal and thus the chemical composition of the sample (by the identification of spectrum peaks).

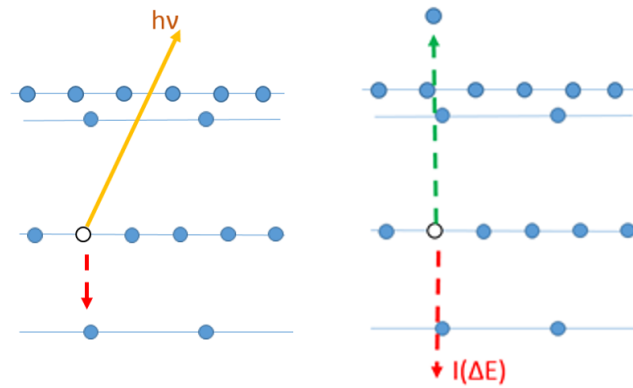


Figure IV- 37: EDXS and EELS comparison

EDXS permits to get a qualitative fast overview of the sample composition. Indeed, the whole energy range of interest (signal) is recorded whereas **EELS** does not cover a sufficient energy range to detect all elements present. Moreover, **EDXS** is simple to use: the data is easily interpretable compared to **EELS** because of the problem of background arising from non-elastic scattering for EELS. Therefore, **EDXS** is the often used technique to study the GB segregation [7].

HRTEM could be combined with **EDXS technique**, it permits to provide the chemical composition of the GB segregation sites of impurities and solutes of a thin foil sample.

The layers and precipitates in GB are commonly analysed by X-ray and electron diffraction. Detectors are placed around the sample and pick up the X-ray produced by the interaction between the impinging electrons and atoms within an interaction volume. If the sample is thin enough to neglect absorption or fluorescence effects, the relative concentration between two elements from the integrated EDXS peak intensities, for a binary or a multicomponent system, is given by the **Cliff-Lorimer** equation [8]:

$$\frac{X_A}{X_B} = \frac{k_{AB}^{AEM} I_A}{I_B} \text{ (eq IV-50)}$$

This equation depends on the knowledge of the interaction volume where X_A and X_B are the concentration in the interaction volume depending on the intensities above background in the X-ray spectrum of the element A and B respectively and I_A and I_B are the integrated EDXS peak intensity of the element A and B respectively.

The **k-factor** corresponds to a **sensitivity factor** which takes into account the differences in the generation and detection characteristic of the X-rays from different elements. This factor depends on the materials, the choice of elements A and B and the atomic number (Z). It neglects, in a first approximation the effects of absorption and fluorescence. The k-factor can be determined experimentally by calibration with a standard sample.

Variations of composition can be obtained easily with EDXS techniques, but it should be borne in mind that the EELS spatial resolution is higher than the EDXS, due to the aperture limitation of the spectrometer and EELS is more sensitive to light elements. Moreover, the k-factor method is also used in EELS spectrum analysis [7]. Therefore, EELS and EDXS can be seen as complementary techniques to study GB: the EDXS quantification can be complemented by EELS technique in order to make an accurate measurement of light elements.

1.1.3 Limitations and solutions

In order to obtain reliable thin enough samples for TEM analysis, specific preparation methods have been developed. The lift out method is the most commonly used. A focused ion beam permits to remove thin cross-sections from sites specific location, large uniformly thick, and to transfer it to a grid.

Nevertheless, the preparation of the samples with the **Focused ion beam** technique [9] remains difficult and time consuming; noise is present for each spectrum measurement because of small shifts of the sample, which leads to an underestimated GB segregation.

Other problems remain significant: a compromise between the probe size, the intensity of electron beam and the spatial resolution has to be found. Indeed, the increased intensity of the probe enhances the electron count but could involve a destruction or transformation of the sample and difficulties to focus the probe. Moreover, the optimum sensitivity is not achieved with smallest probe sizes as it can be expected [10].

AEM techniques are useful accurate methods to characterize GBs, from a structural and chemical point of view. SEM methods extract surface topography and composition from reflected electrons (interacted with the sample) of a sample. TEM method constitutes a more accurate technique in terms of spatial resolution (related to the interaction volume and the probe size) which extracts crystal structure, morphology and stress information from transmitted electrons. Thus, TEM is more adapted to study GB structure. EBSD technique can be coupled with AEM techniques to get more accurate structural information about the orientation of the GB plane. The quantification of the chemical composition is determined by EDXS or EELS.

2. Atom-probe field ion microscopy (AP FIM)

This technique can be represented as a combination of the **field ion microscope (FIM)** possessing an atomic spatial resolution, with a **mass spectrometer** which **provides a chemical analysis of selected atoms of the sample**.

The field ion microscope (Figure IV- 38) [11], [12] is constituted of a ultra high vacuum (**UHV chamber**), where the sample of interest, in the form of a **sharp tip** is placed. This tip is maintained at extremely low temperature, around 5-80 K, to obtain a high spatial resolution. Then, an electric positive potential (5-10 kV) is applied at the surface of the tip, in front of a screen. An inert gas is introduced in the chamber, called "image gas", and atoms of this inert gas (helium or neon) are subsequently ionized. **A strong ionisation field** is thus created, which corresponds to the field induced by the removal of an electron from the outer shell of the gas atom to an empty energy level at the metal surface, via electron tunnelling. The probability of an electron to overcome the energy barrier, which leads to ionisation depends on the relative width of the potential barrier. Then each imaging-gas ion that strikes the tip, is exposed to this intense electric field surrounding the tip. The electric field accelerates the ions which are ejected from the positively charged surface formed by the sharp tip surface to the microscope

chamber and eventually strikes a screen which is equipped with a detection system and provides thus a magnified 2D reconstruction of the sample surface.

The curvature of the surface near the tip causes a natural magnification which causes gas ion repelling from the tip surface. Since the electric field is nearly normal to the surface, the ions are projected along the electric field lines and behave as if they were projected away from the surface.

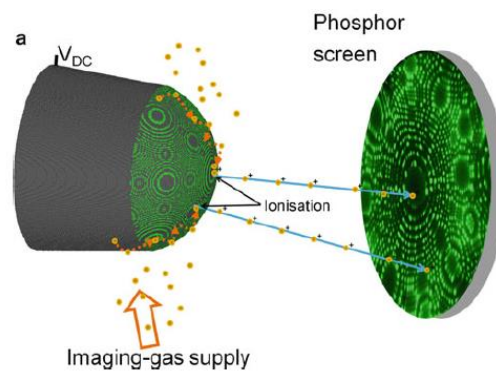


Figure IV- 38: Schematic view of a field ion microscope, V_{DC} corresponds to the electric potential applied to the surface of the tip to ionised gas atoms [11]

This method creates thus a two-dimensional representation of the **arrangement of individual atoms** at the end of the sharp tip by stereographic projection. Relatively small volume, around 10^3 cubic nm, can be analysed, therefore, GB and solute atoms or precipitates may be analysed and counted.

The chemical nature of each ion is obtained by the **time of flight mass spectrometry**: the starting time and arrival time of ions are given by electrical pulses transmitted to the tip and to the detector respectively. Therefore, a chemical atomic map distribution of the sample with an atomic resolution can be extracted. The impact position of ions and an inverse stereographic projection permit to get the initial position of atoms in the sample.

The electric field at the top of the tip F_{tip} depends on the radius curvature of the surface tip R_{tip} , the voltage u and a field factor k_{ftip} that takes into account the tip shape and electrostatic environment. This parameter is often given by the expression [11]:

$$F_{tip} = \frac{u}{k_{ftip}R_{tip}} \text{ (eq IV-51)}$$

The AP FIM is the earlier design of the APT technique, and corresponds to only one-dimensional atom probe. It provides a linear compositional measurement in the depth of the sample. Large progress of AP FIM technical characteristics (the introduction of position-sensitive and time-resolved particle detectors and systems which enhance the electric field in a very confined region like electrodes ...) has been made and conducted to the emergence **of the Atom probe tomography (APT 3D)**. APT data can be separated into raw data, the direct output from the microscope, and a point cloud where every ion has been identified and allocated a position in the three-dimensional (3D) reconstruction. This reconstruction from

atom-probe data permits then the assessment of the **GB crystallography** details with the construction of a three-dimensional mapping of the orientation of the nanoscale grains. These improvements lead to **identify more precisely the chemical and crystallographic properties of individual atom** in a cylinder of material on an atomic layer-by-layer basis [11], [13]–[18]. The thickness of the specimen, that can be investigated is on the order of 50 to 100 nm [11].

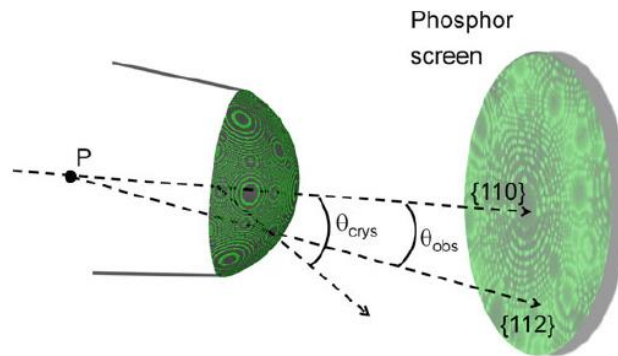


Figure IV- 39: Schematic view of the projection of the atoms from the surface [11]

In comparison to optical and electron microscopes the magnification effects come from the magnification produced by a high curved electron field. The apparent size of the GB projected image is enlarged. This enlargement is quantified by a magnification number M_{proj} .

This quantity depends on the ratio $\zeta = \frac{\theta_{crys}}{\theta_{obs}}$ between the two crystallographic directions on the projected image θ_{obs} and the theoretical value θ_{crys} (**Figure IV- 40**), the tip radius R and the distance between the screen and the tip L_{tip} [19]:

$$M_{proj} = \frac{L_{tip}}{\zeta R_{tip}} \text{ (eq IV-52)}$$

$M_{proj} < 1$ corresponds to a reduction of the apparent size of the GB projected image.

The projection of the atom distribution depends on the ion trajectory, directly associated to the tip curvature. **In the case of GB analysis, the trajectory of ions is modified (Figure IV- 40):** a high evaporation field at GB can be explained by a smaller local curvature of the tip surface which leads to a defocusing of ion trajectories and the estimation of GB atomic density is lower than expected; a lower evaporation field at the GB than at the matrix, results from an over focusing of ions which leads to overestimate the density of atoms at GB.

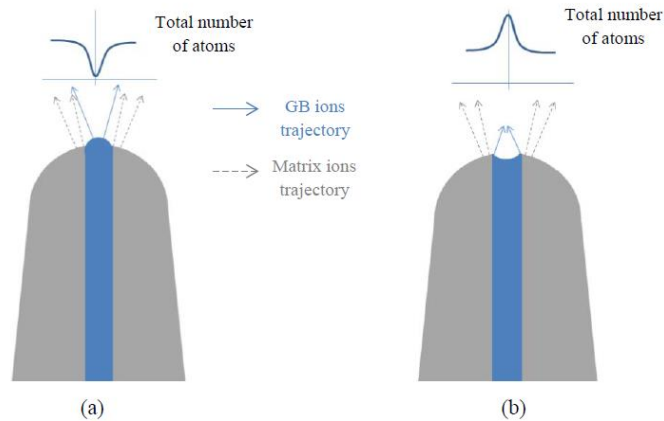


Figure IV- 40: Schematic representation of the trajectory of ions from (a) low-field GB and (b) high-field GB and the atomic density at GB in the reconstructed volume [20]

To overcome these local magnification effects, the **GB planes have to be placed perpendicular to the analysis direction.**

Since GB present numerous point-defects, they are expected to have a lower evaporation field than the perfect BCC crystal. Nevertheless, it was shown that GB that contain phosphorus are characterized by a higher evaporation field (103 V/nm) [18] than the matrix of iron which leads to some aberrations.

In order to minimize the reconstruction artefacts, the GB system can be considered as two phases α and β separated by a surface. Then the interface excess can be described by **Gibbs approach** [21].

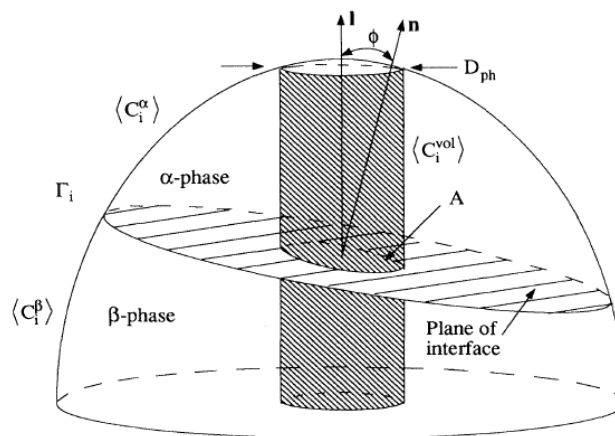


Figure IV- 41: Three-dimensional schematic drawing of the volume analysed via APT [22]

Since APT determines the chemical identity of individual atoms, one at a time, in the surface tip layer-by-layer, the number of solute and matrix atoms are directly accessible from a reconstructed volume. Therefore, the number of segregated atoms or interfacial excess can be defined by the plot of the difference between the number of solute atoms in the grains before and after the GB (Gibbs dividing surface ξ). It can be expressed as function of the number of element i in phases α and β , N_i^α and N_i^β with respect to the number of element i in the whole system including the GB interface and α and β phases, N_i^{vol} .

$$N_i^{excess, APT} = N_i^{vol} - N_i^\alpha - N_i^\beta \quad (\text{eq IV-53})$$

In terms of atomic fraction with respect to the position of the Gibbsian interface ξ , $N_i^{excess, APT}$ can be expressed as:

$$N_i^{excess, APT} = N_{vol} (X_i^{vol} - X_i^\alpha \xi - X_i^\beta (1 - \xi)) \quad (\text{eq IV-54})$$

where N_{vol} is the total number of all elements in the whole system (the system including the GB interface and α and β).

A cumulative profile can then be obtained as shown **Figure IV- 42**. If there is no segregation, the cumulative number of atoms i will increase proportionally to the cumulative number of all atoms, whereas the intergranular segregation happens when inflexion occurs. The slopes between A and B, for the α phase, C and D for the β phase and B and C for the GB region, correspond to the average atomic composition of element i region considered. Thus, the atomic concentrations/fractions measured by APT are expressed as **atomic averages**: $\langle X_i^{vol} \rangle$ corresponds to the average atomic fraction of the interfacial excess contained in the whole interface, and $\langle X_i^\alpha \rangle$ and $\langle X_i^\beta \rangle$ are the average atomic fraction of the interfacial excess in the grain phase α and β respectively.

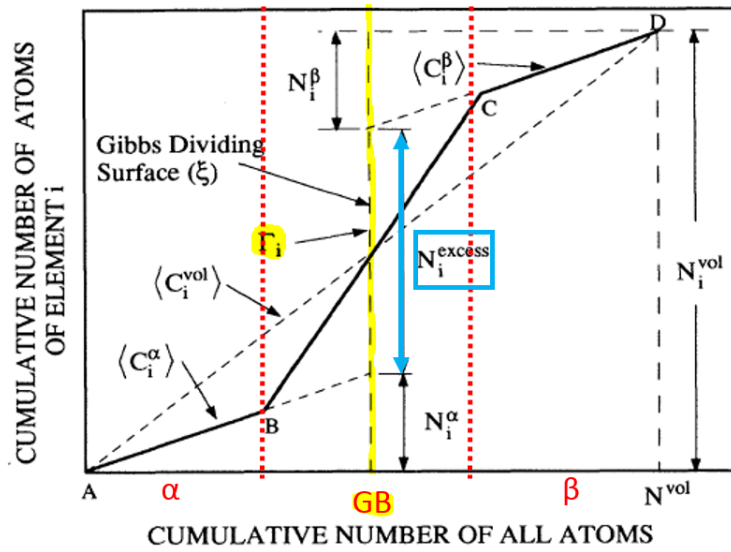


Figure IV- 42: Cumulative concentration profiles of atoms i determined from a parallelepiped region perpendicular to a GB [22]

Therefore, Gibbs interfacial excess of the element i which can be converted as a fraction of a monolayer segregation, is given by:

$$\Gamma_i = \frac{N_i^{excess, APT}}{\eta_{detect} A} = \frac{N_{vol} (\langle X_i^{vol} \rangle - \langle X_i^\alpha \rangle \xi - \langle X_i^\beta \rangle (1 - \xi))}{\eta_{detect} A_{surf}} \quad (\text{eq IV-55})$$

Where ξ indicates the position of the interface, and η_{detect} is the detection efficiency of the APT detector which can be defined as the probability of a single ion to strike successfully the surface detector, its typical value being 0.55. This quantity is theoretically limited by the open

area of the detector (i.e. the fraction of the surface area of the detector reached successfully by a single ion). A_{surf} is the interfacial area which can be seen as an ellipsoid projection of the probe onto the GB plane expressed in function of atom probe parameters (**Figure IV- 42**):

$$A_{surf} = \frac{\pi D_{ph}^2}{4 \cos \Phi} \quad (\text{eq IV-56})$$

where D_{ph} is the diameter of the probe projected onto a tip sample surface, and Φ is the angle between the vector \mathbf{n} normal to the interface plane and \mathbf{l} the vector parallel to the direction of APT analysis (**Figure IV- 41**)

$$\Phi = \cos^{-1}(\mathbf{n}\mathbf{l}) \quad (\text{eq IV-57})$$

AEM techniques and EBSD combined with APT [23] [24] [25] allow to access all GB five degrees of freedom. The crystal orientation map can be made by EBSD measurements. For that purpose, TEM and EBSD techniques coupled with APT reconstruction need a high spatial resolution to obtain a high angular resolution with a high diffraction pattern resolution (usually on the order of 1-3°)[26].

The misorientation angle can be also obtained by a combination of **Transmission Kikuchi Diffraction mapping (TKD)** and APT reconstruction[27]. This method can be considered as a variation of EBSD analysis with an improved spatial resolution, to be used with sufficiently thin samples. The main difference between classical EBSD and this method is that TKD operate with diffracted transmitted electrons [28].

One of the main problem of using APT is that the preparation of the sample, in form of a thin needle with the chosen interface just located within the tip, is difficult. Furthermore, there can be some **mechanical problems because of the high stress induced by the high electric field** applied for the evaporation during the analysis [29], [30].

The main drawback of these quantitative microscopic methods (AEM, TEM and APT) is the lack of exact atomistic knowledge of the segregation process [31]–[33]. TEM exact quantification is difficult because of its complex spectra which requires deconvolution methods. Moreover, this type of method depends also on optical parameters which have a significant impact on spatial resolution. Furthermore, APT leads only to an average atomic quantification of the GB interfacial excess because ATP quantification uses Gibbs approach where the atomic concentrations/fractions are expressed as **atomic averages**. Therefore, complementary to the experimental investigations [34], computational methods have been used to study the GB segregation, from an atomic point of view.

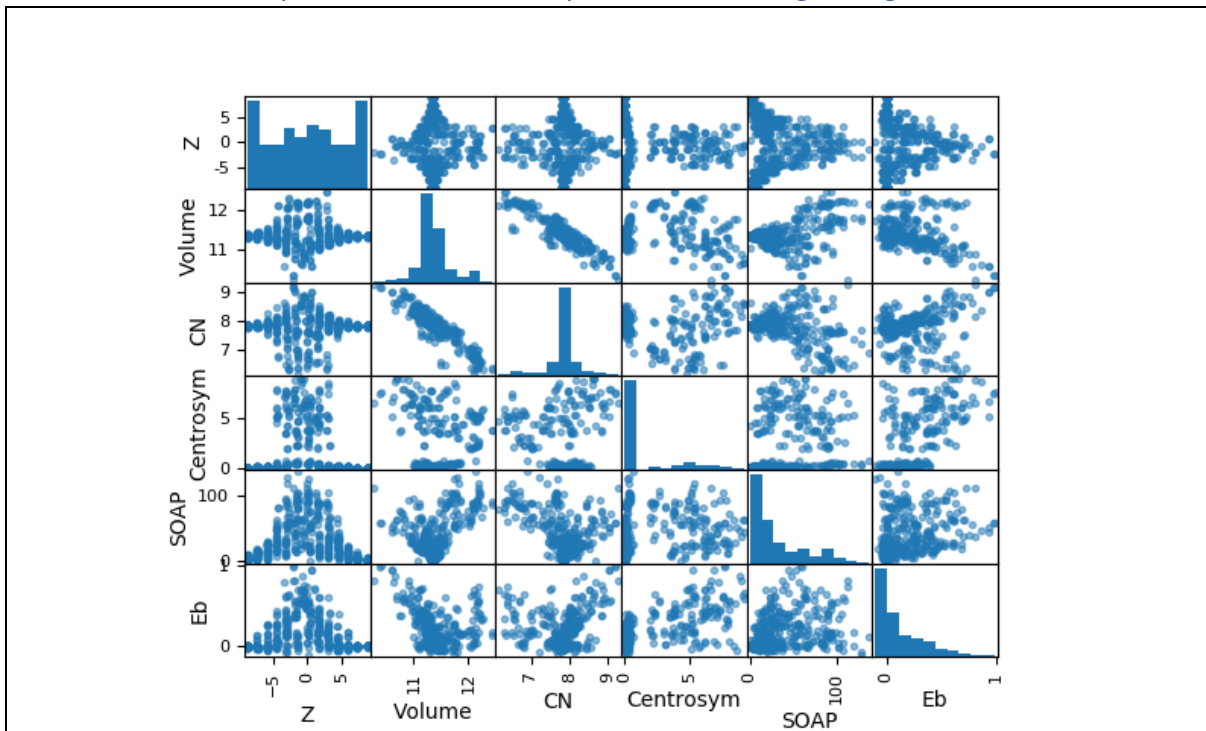
Atom probe techniques provide chemical analysis of atoms which are detected in a sample. AP-FIM gives a 1-dimensionnal atomistic representation of the sample, whereas the improvement of APT device leads to more accurate results and a 3-dimensionnal atomistic orientation representation. APT gives access to the GB crystallography properties and chemical identity of individual atoms. However, it depends on the curvature of the tip which influences the ion trajectory and the 3D reconstruction. APT gives an atomistic point of view of a GB but it must be borne in mind that atomic concentrations measured with APT are expressed as atomic averages.

- [1] G. E. Christidis, *Advances in the characterization of industrial minerals*, European mineralogical union., vol. 9. 2011.
- [2] D. B. Williams et C. B. Carter, *Transmission Electron Microscopy A Textbook for Material Science*. 1986.
- [3] Z. Yu, Q. Wu, J. M. Rickman, H. M. Chan, et M. P. Harmer, « Atomic-resolution observation of Hf-doped alumina grain boundaries », *Scripta Materialia*, vol. 68, p. 703-706, 2013.
- [4] M. P. Harmer, « The Phase Behavior of Interfaces », *Science*, vol. 332, p. 182-183, 2011.
- [5] S. J. Dillon et M. P. Harmer, « Direct Observation of Multilayer Adsorption on Alumina Grain Boundaries », *Journal of American Ceramic Society*, vol. 90, p. 996-998, 2007.
- [6] C. Kisielowski *et al.*, « Detection of Single Atoms and Buried Defects in Three Dimensions by Aberration-Corrected Electron Microscope with 0.5 Angstroms Information Limit », *Microscopy Society of America*, vol. 14, p. 469-477, 2008.
- [7] H. Müllejans et J. Bruley, « Electron enegy-loss spectroscopy (EELS); comparison with X-ray analysis », *Journal de Physique IV Colloques*, vol. 03, p. C7-2083-C7-2092, 1993.
- [8] G. Cliff et G. W. Lorimer, « The quantitative analysis of thin specimens », *Journal of Microscopy*, vol. 103, p. 203-207, 1975.
- [9] J. Mayer, L. A. Giannuzzi, T. Kamino, et J. Michael, « TEM Sample Preparation and FIB Induced Damage », *MRS Bulletin*, vol. 32, p. 400-407, 2017.
- [10] V. J. Keast et D. B. Williams, « Quantification of boundary segregation in the analytical electron microscope », *Journal of Microscopy*, vol. 199, n° 1, p. 45-55, 2000.
- [11] B. Gault, M. P. Moody, J. M. Cairney, et S. P. Ringer, « Atom probe crystallography », *Materials today*, vol. 15, p. 378-386, 2012.
- [12] A. Merand, C. Martin, et J. Gallot, « Réalisation d'un microscope ionique à champ », *Revue de Physique Appliquée*, vol. 7, p. 177-180, 1972.
- [13] P. J. Felfer, T. Alam, S. P. Ringer, et J. M. Cairney, « A Reproducible Method for Damage-Free Site-Specific Preparation of Atom Probe Tips from Interfaces », *Microscopy research and technique*, vol. 75, p. 484-491, 2012.
- [14] M. P. Moody, F. Tang, B. Gault, S. P. Ringer, et J. M. Cairney, « Atom probe crystallography: Characterization of grain boundary orientation relationships in nanocrystalline aluminium », *Ultramicroscopy*, vol. 11, p. 493-499, 2011.

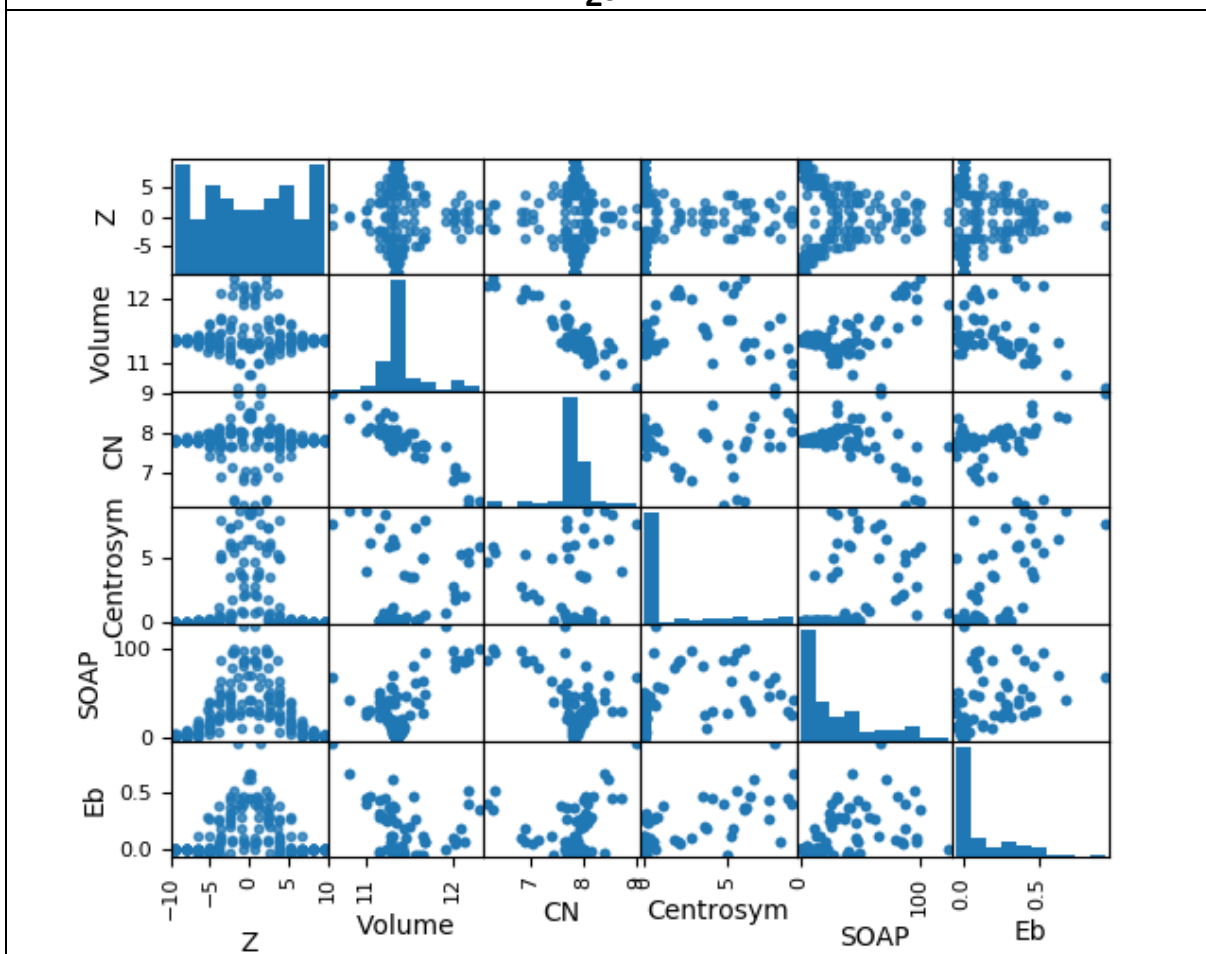
- [15] M. P. Moody, B. Gault, L. T. Stephenson, D. Haley, et S. P. Ringer, « Qualification of the tomographic reconstruction in atom probe by advanced spatial distribution map techniques », *Ultramicroscopy*, vol. 109, p. 815-824, 2009.
- [16] V. J. Araullo-Peters *et al.*, « Atom probe crystallography: Atomic-scale 3-D orientation mapping », *Scripta Materialia*, vol. 66, p. 907-910, 2012.
- [17] A. Akhatova *et al.*, « Investigation of the dependence of phosphorus segregation on grain boundary structure in Fe-P-C alloy: cross comparison between Atom Probe Tomography and Auger Electron Spectroscopy », *Applied Surface Science*, vol. 463, p. 203-210, 2019.
- [18] A. Akhatova, « Méthodologie instrumentale à l'échelle atomique pour une meilleure compréhension des mécanismes de ségrégation intergranulaire dans les aciers : application au phosphore. », Université de Rouen Normandie, 2018.
- [19] B. Gault, M. P. Moody, J. M. Cairney, et S. P. Ringer, « Chapter 2: Field Ion Microscopy », in *Atom Probe Microscopy*, Hardcover., 2012, p. 396.
- [20] A. Akhatova, « Méthodologie instrumentale à l'échelle atomique pour une meilleure compréhension des mécanismes de ségrégation intergranulaire dans les aciers : application au phosphore. », Université de Rouen Normandie, 2018.
- [21] B. Krakauer et D. N. Seidman, « Absolute atomic-scale measurements of the Gibbsian interfacial excess of solute at internal interfaces », *Physical Review B*, vol. 48, p. 6724-6727, 1993.
- [22] B. Krakauer et D. N. Seidman, « Absolute atomic-scale measurements of the Gibbsian interfacial excess of solute at internal interfaces », *Physical Review B*, p. 6724-6727, 1993.
- [23] Y. Toji, H. Matsuda, M. Herbig, P.-P. Choi, et D. Raabe, « Atomic-scale analysis of carbon partitioning between martensite and austenite by atom probe tomography and correlative transmission electron microscopy », *Acta Materialia*, vol. 65, p. 215-228, 2014.
- [24] S. Mandal, K. G. Pradeep, S. Zaeferrer, et D. Raabe, « A novel approach to measure grain boundary segregation in bulk polycrystalline materials in dependence of the boundaries' five rotational degrees of freedom », *Scripta Materialia*, vol. 81, p. 16-19, 2014.
- [25] P. Lejcek, « Recent trends and open questions in grain boundary segregation », *Materials Research Society*, vol. 33, n° 18, p. 2647-2660, 2018.
- [26] D. Raabe, « Grain boundary segregation engineering in metallic alloys : A pathway to the design of interfaces », *Current Opinion in Solid State and Material Science*, vol. 18, p. 253-261, 2014.
- [27] A. Akhatova *et al.*, « Investigation of the dependence of phosphorus segregation on grain boundary structure in Fe-P-C alloy: cross comparison between Atom Probe Tomography and Auger Electron Spectroscopy », *Applied Surface Science*, p. 203-210, 2019.
- [28] R. R. Keller et R. H. Geiss, « Transmission EBSD from 10nm domains in a scanning electron microscope », *Journal of Microscopy*, vol. 245, p. 245-251, 2012.
- [29] P. Lejcek, « Grain Boundaries: Description, Structure and Thermodynamics », in *Grain Boundary Segregation in Metals*, 2010.
- [30] Craig et M. Eucken, *Zirconium in the Nuclear Industry: Ninth International Symposium*, vol. STP 1132. Eucken.

- [31] S. H. Song, H. Zhuang, J. Wu, L. Q. Weng, Z. X. Yuan, et T. H. Xi, « Dependence of ductile-to-brittle transition temperature on phosphorus grain boundary segregation for a 2.25Cr1Mo steel », *Material Science and Engineering A*, vol. 486, p. 433-438, 2008.
- [32] A. Andrieu, A. Pineau, P. Joly, et F. Roch, « On Modeling of Thermal Embrittlement in PWR Steels using the Local Approach to Fracture », *13th International Conference on Fracture*, 2013.
- [33] X. M. Chen, S. H. Song, L. Q. Weng, S. J. Liu, et K. Wang, « Relation of ductile-to-brittle transition temperature to phosphorus grain boundary segregation for a Ti-stabilized interstitial free steel », *Materials Science and Engineering A*, vol. 528, p. 8299-8304, 2011.
- [34] W.-S. Ko, « Atomistic modeling of an impurity element and a metal-impurity system: pure P and Fe-P system », *J. Phys. : Condens. Matter*, vol. 24, p. 225002, 2012.

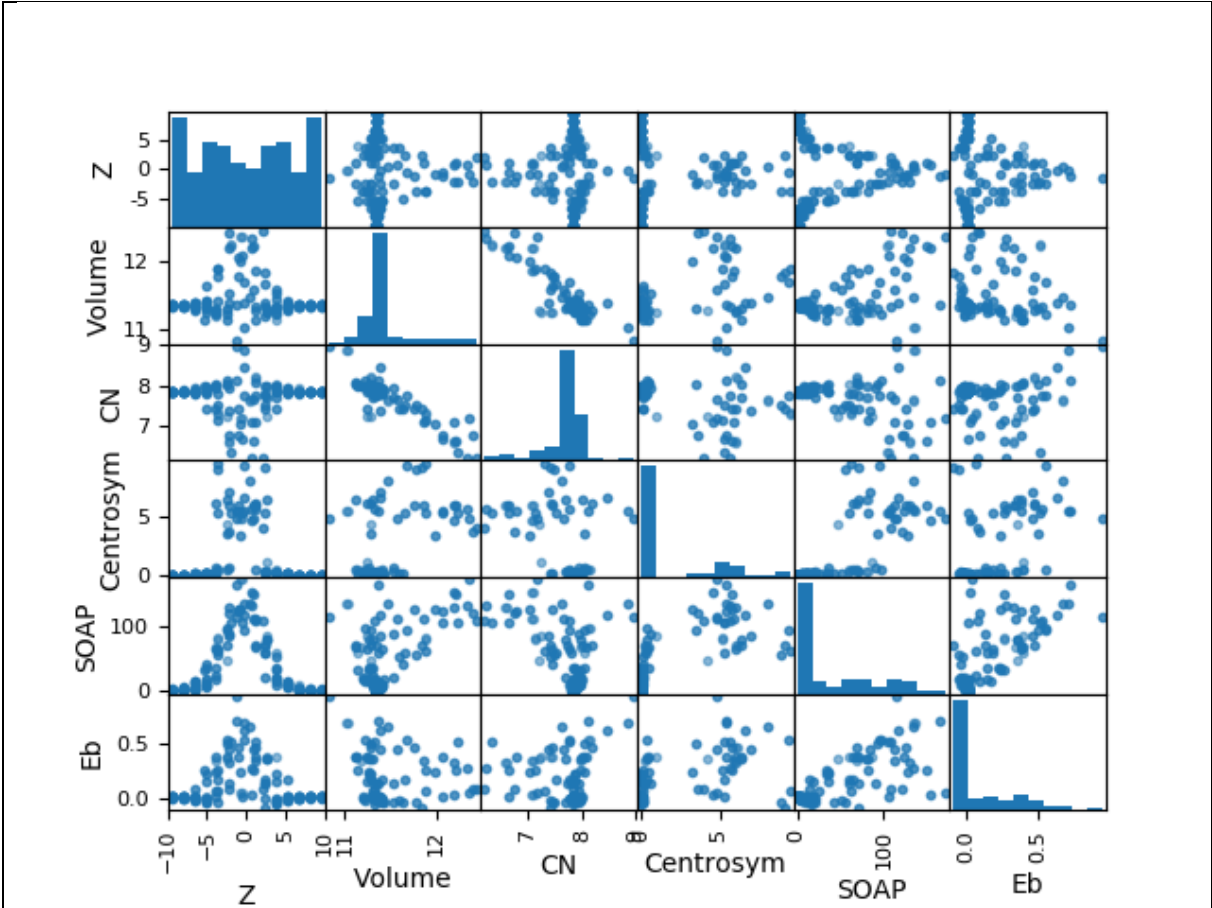
IV-Annex 6: Scatter plot of atomic descriptors and binding energies of each twist GB.



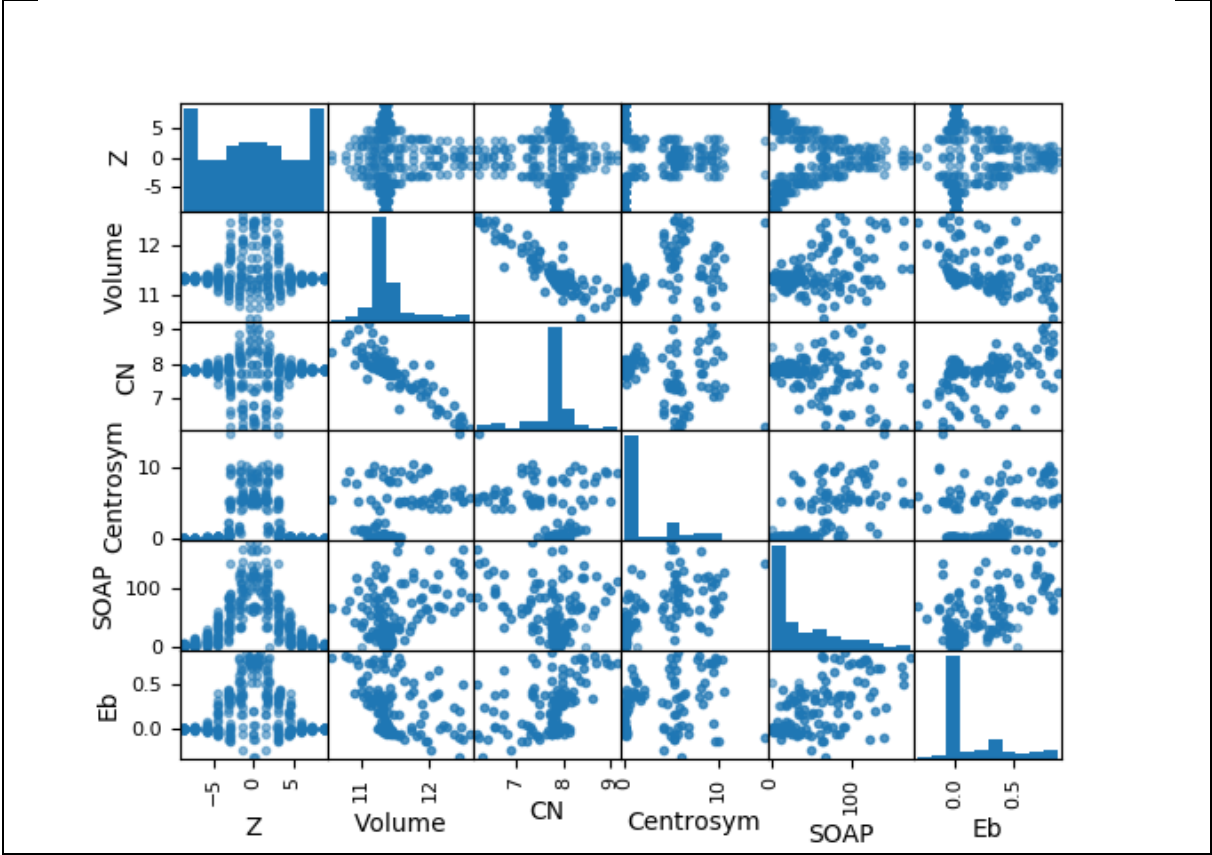
$\Sigma 37$



$\Sigma 13$



$\Sigma 17$



$\Sigma 29$

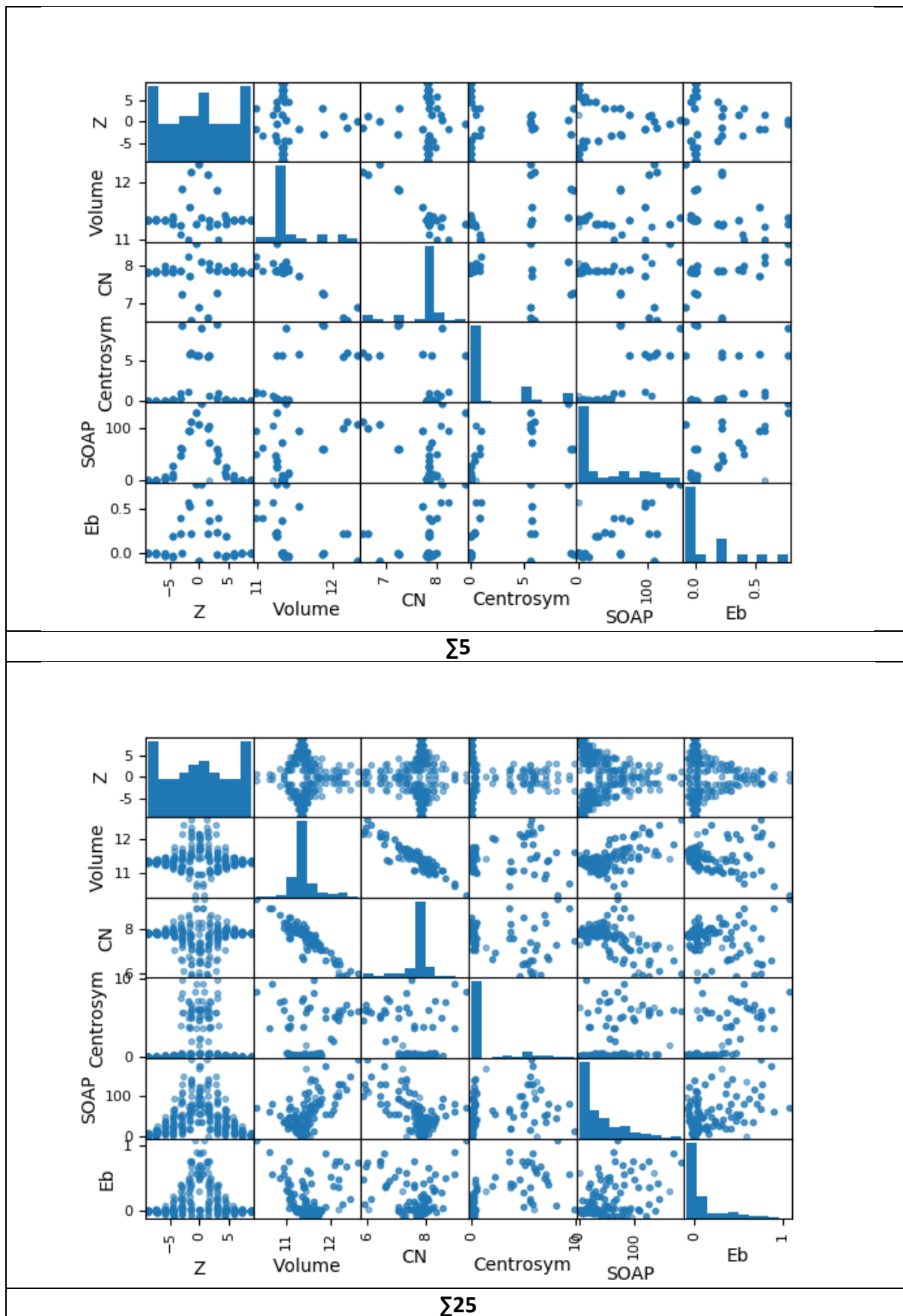
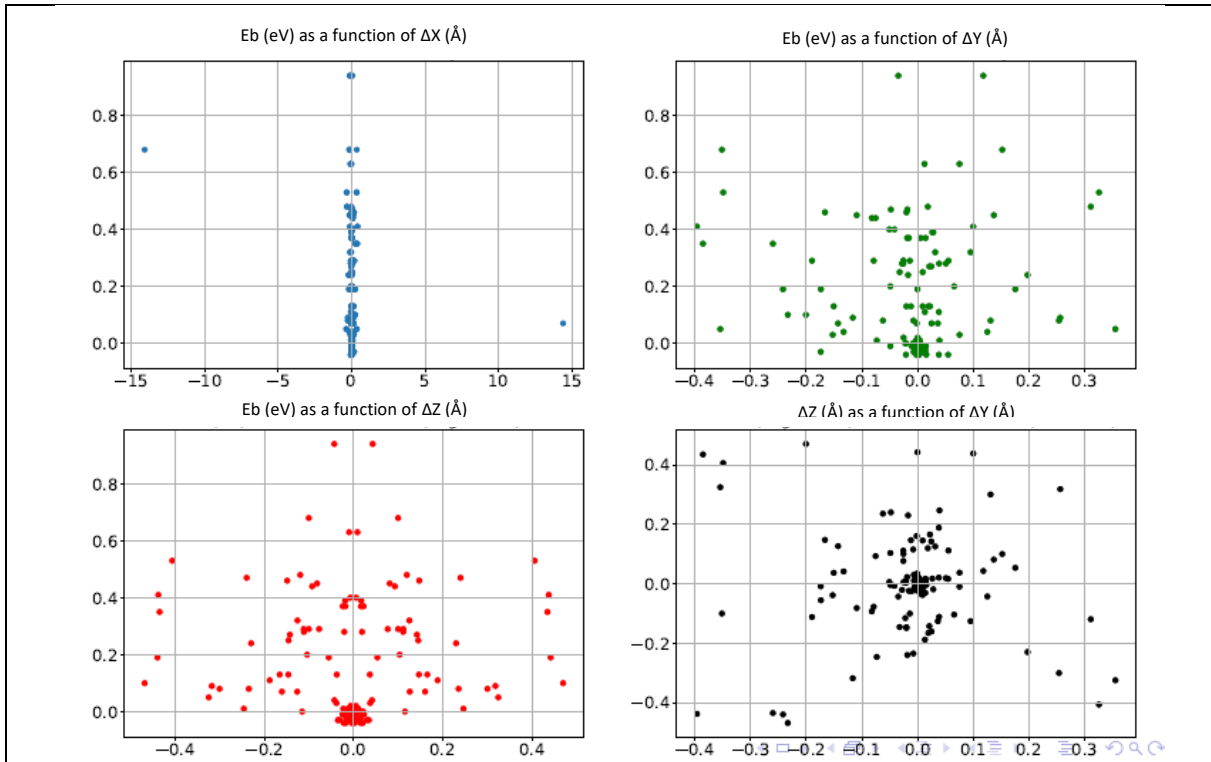
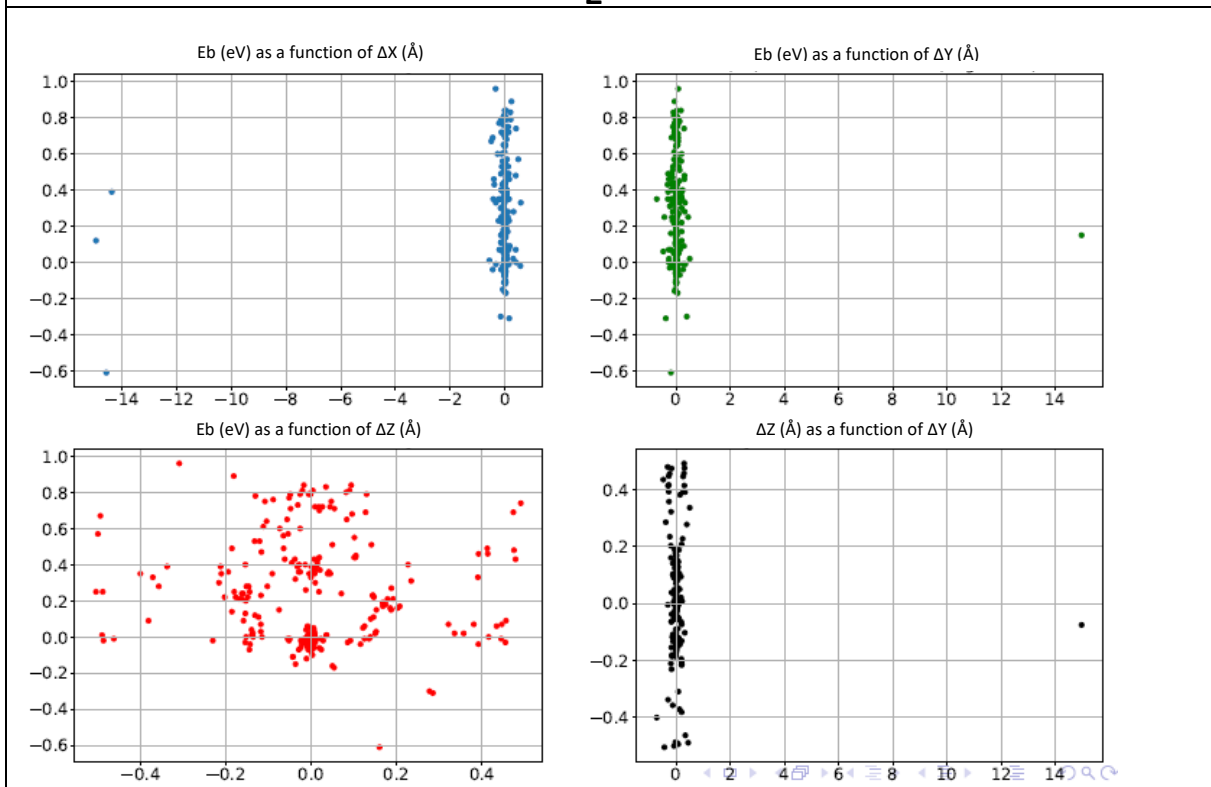


Figure IV- 43: Scatter plot of atomic descriptors and binding energies of each twist GB. Centrosym corresponds to CS and volume to the atomic volume.

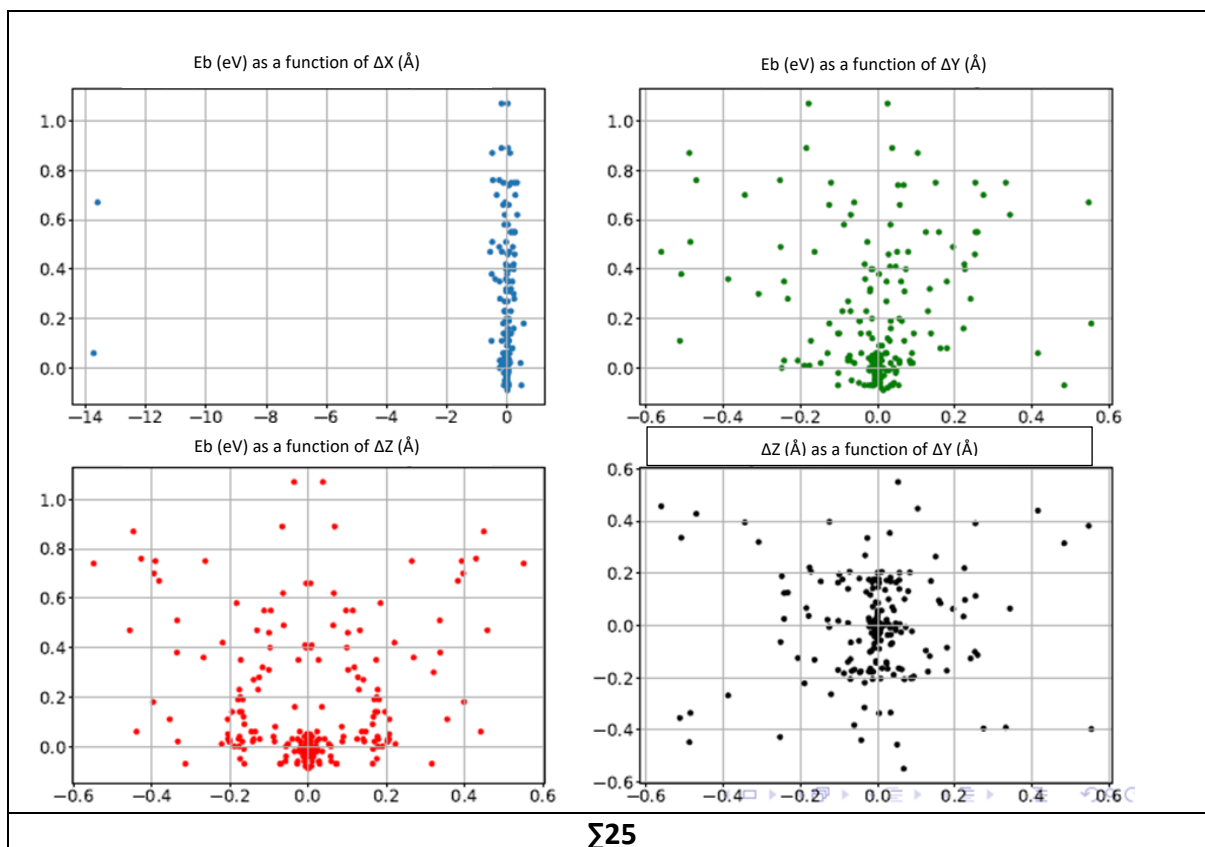
IV-Annex 7: Binding energy of substitutional phosphorus as a function of the difference between initial and final positions (ΔX , ΔY , ΔZ), and representation of ΔZ as a function of ΔY .



Σ13



Σ29



Σ25

Figure IV- 44: Binding energy of substitutional phosphorus as a function of the difference between initial and final positions (ΔX , ΔY , ΔZ), and representation of ΔZ as a function of ΔY .

Prévisions de l'évolution micro structurale jusqu'à fin de vie sous irradiation d'alliages ferritiques par simulations numérique - vers une simulation quantitative et la prise en compte des hétérogénéités

Résumé :

Le but de cette thèse est de mettre en œuvre une description plus réaliste des hétérogénéités structurales et chimiques. Dans de nombreux alliages comme les aciers utilisés en tant que matériaux de structure dans les réacteurs sous pression des centrales nucléaires, les solutés peuvent venir ségréger au niveau des joints de grains par vieillissement thermique ou irradiation. Ces ségrégations de solutés peuvent affecter les propriétés mécaniques des matériaux, soit en renforçant la cohésion de la limite du joint de grain (comme le carbone) ou en la réduisant (comme le phosphore). Afin de prédire la ségrégation de ces solutés, les modèles tels que ceux dérivés par Mac Lean pour les systèmes binaires ou Guttman pour les systèmes multi-composants, nécessitent la connaissance des énergies soluté – joint de grain, qui dépendent des caractéristiques des joints de grain. Ces données peuvent être obtenues par simulation à l'échelle atomique et ne sont actuellement connues que pour quelques joints de grain de flexion à symétrie élevée (par exemple : $\Sigma 3$ et $\Sigma 5$). Dans ce travail, on a étudié six joints de grain de torsion (100) différents, dont la structure est par définition plus complexe que les joints de grain de flexion, qui s'étendent sur des désorientations de faibles à élevées, générés pour Fe. En raison de leur structure complexe, les microstructures de plus basse énergie sont difficiles à déterminer. Une grande partie de cette thèse a été consacrée à l'établissement de méthodologies de construction des joints de grains de torsion. Ce travail s'appuie fortement sur les calculs en potentiel empiriques et l'analyse la diversité des joints de grain de torsion construits. La γ -méthode est la méthode la plus communément utilisée pour trouver un joint de grain de plus basse énergie. Dans cette thèse, deux méthodes utilisant la méthode γ comme première étape de construction, ont été développées. L'ajout de SIA séquentiellement à l'intérieur d'une structure de joint de grain de torsion permet d'approcher l'état de minimum d'énergie, mais une combinaison d'un traitement de fusion et de trempe et l'ajout de SIA séquentiellement semble être plus efficace pour déterminer une microstructure de plus basse énergie. L'interaction d'un joint de grain de torsion avec le phosphore a été calculée et analysée à partir de différents descripteurs. Le modèle de ségrégation de White Coghlan, adapté aux études atomistiques, a été utilisé pour quantifier la ségrégation du phosphore. L'intégration de l'impact du comportement de ségrégation du phosphore sur l'évolution de la microstructure dans les simulations de Monte Carlo Cinétique fera l'objet de futures études. Ces avancées permettront d'envisager des simulations plus quantitatives dans des conditions d'irradiation de type REP sur plusieurs décennies d'exploitation, et de mieux comprendre les mécanismes de dommages par rayonnement des alliages ferritiques à différentes échelles.

Mots-clefs : simulation numérique, irradiation d'alliages ferritiques, évolution microstructurale, vieillissement

Predictions of micro-structural evolution to the end of life under irradiation of ferritic alloys by numerical simulations - towards quantitative simulation and consideration of heterogeneities

Abstract:

The aim of this thesis is to implement a more realistic description of the structural and chemical heterogeneities. In many alloys and for instance in the steels used as structural materials in nuclear power plant pressurized reactors, solute can segregate to grain boundaries under thermal ageing or irradiation. These solute segregations can affect the mechanical properties of the materials, by either reinforcing the grain boundary cohesion (like carbon) or reducing it (like phosphorus). In order to predict the segregation of these solutes, models such as the ones derived by Mac Lean for binary systems or Guttman for multi-component systems, require the knowledge of solute – grain boundary energies, which depend on the grain boundary characteristics. These data can be obtained by simulation at the atomic scale and are currently known only for few high symmetry tilt grain boundaries (e. g. $\Sigma 3$, $\Sigma 5$). In this work, six different (100) twist grain boundaries with more complex structure than tilt grain boundaries, that span low to high angle misorientations generated in for Fe have been investigated. Due to their complex structure, their minimum ground state structure is difficult to determine. A large part of this thesis has been dedicated to the establishment of twist grain boundary construction methodologies. This work relies heavily on EP calculations made and analyses the diversity of grain boundaries constructed. Usually, classical γ -method is used. In this thesis two methods using γ -method as an initial step have been developed. The addition of SIA sequentially inside a twist grain boundary structure, permits to approach a ground state, however a combination of a melt and quench treatment and addition of SIA seems to be more efficient to find a ground state grain boundary microstructure. The interaction of twist grain boundary constructed, with phosphorus has been calculated and analyzed based on different descriptors. White Coghlan segregation model which is adapted for atomistic studies has been used to quantify phosphorus segregation. The integration of the impact phosphorus segregation behavior on microstructure evolution in Kinetic Monte Carlo simulations is the subject of a future work. These advances will permit to envisage more quantitative simulations under PWR-type irradiation conditions over several decades of operation, and to better understand the radiation damage mechanisms of ferritic alloys at different scales.

Keywords: numerical simulation, irradiation of ferritic alloys, micro-structural evolution, aging